

Spreading and Epidemic Interventions

—

Effects of Network Structure and Dynamics

Abbas K. Rizi



Spreading and Epidemic Interventions

Effects of Network Structure and Dynamics

Abbas K. Rizi

A doctoral thesis completed for the degree of Doctor of Science (Technology) to be defended, with the permission of the Aalto University School of Science, at a public examination held at the lecture hall T2 of the school on 15 March 2024 at noon.

Aalto University
School of Science
Department of Computer Science
Complex Systems Group

Supervising professor

Prof. Mikko Kivelä, Assistant Professor at Aalto University, Finland

Preliminary examiners

Prof. Clara Stegehuis, Associate Professor at Twente University, Netherlands

Dr. Riccardo Gallotti, Head of the Complex Human Behaviour, FBK, Italy

Opponent

Prof. Nicola Perra, Reader in Applied Mathematics, Queen Mary University of London, UK

Aalto University publication series

DOCTORAL THESES 48/2024

© 2024 Abbas K. Rizi

ISBN 978-952-64-1704-2 (printed)

ISBN 978-952-64-1705-9 (pdf)

ISSN 1799-4934 (printed)

ISSN 1799-4942 (pdf)

<http://urn.fi/URN:ISBN:978-952-64-1705-9>

Images: The front cover's illustration portrays a Plague Doctor engaging with a modern contact tracing app, a fusion of historical imagery and contemporary technology. It was crafted using advanced AI through a specific 'prompt' command.

Unigrafia Oy
Helsinki 2024

Finland



Author

Abbas K. Rizzi

Name of the doctoral thesis

Spreading and Epidemic Interventions

Publisher School of Science**Unit** Department of Computer Science**Series** Aalto University publication series DOCTORAL THESES 48/2024**Field of research** Network Science, Computational Epidemiology, Complex Systems, Statistical Physics**Manuscript submitted** 5 December 2023**Date of the defence** 15 March 2024**Permission for public defence granted (date)** 13 February 2024**Language** English **Monograph** **Article thesis** **Essay thesis****Abstract**

The COVID-19 pandemic has highlighted the critical importance of understanding epidemic dynamics, particularly the significant gaps in our knowledge that need addressing to better prepare for future pandemics. This thesis delves into the intricacies of disease spread within complex human interaction networks, underlining the pivotal role of individual connectedness in influencing epidemic outcomes. By developing theoretical models inspired by real-world epidemiological data, this work provides a nuanced exploration of disease transmission dynamics across networked populations, emphasizing the heterogeneous, spatial, homophilic, and temporal characteristics inherent in human social structures.

A primary focus of this research is the investigation of intervention strategies, encompassing pharmaceutical measures, such as vaccination campaigns, and non-pharmaceutical interventions, including contact tracing techniques. These interventions are evaluated within more realistic network topologies, characterized by degree heterogeneity and group structures, to assess their effectiveness in mitigating epidemic spread. The thesis leverages mathematical and computational epidemiology to offer profound insights into optimizing intervention strategies within the complex web of human interactions, thereby contributing to the academic discourse and providing actionable intelligence for public health policy formulation and epidemic preparedness.

The avenues of research opened by this work offer deeper insights into the mechanisms of epidemic spread in social networks. By using stylized modeling, the study was able to delve into the non-trivial ways epidemics spread through social networks. This modeling approach simplified the real-world dynamics into more analytically tractable forms, allowing the researchers to capture the essence of contact network structures and their crucial role in transmitting infectious diseases. The primary objective of this study was to identify new pathways for academic exploration and offer valuable perspectives that can enhance public health policies and epidemic response strategies. Ultimately, this work seeks to contribute to a better understanding of epidemic dynamics by bridging knowledge gaps and fostering a more resilient response to public health challenges in the face of complex human interactions.

Keywords Complex Systems, Network Science, Spreading Phenomena, Computational Epidemiology, Digital Epidemiology, Complex Networks, Temporal Networks, Reachability, Phase Transitions, Percolation, Covid-19, Vaccination, Contact Tracing

ISBN (printed) 978-952-64-1704-2**ISBN (pdf)** 978-952-64-1705-9**ISSN (printed)** 1799-4934**ISSN (pdf)** 1799-4942**Location of publisher** Helsinki**Location of printing** Helsinki **Year** 2024**Pages** 183**urn** <http://urn.fi/URN:ISBN:978-952-64-1705-9>

بِسْمِ اللَّهِ الرَّحْمَنِ الرَّحِيمِ

*In loving memory of Grandpa,
Mohammad Karimi (1944 – 2023)*

Preface

It is now time to recap this rather extensive journey. To all who made my research possible, I am deeply grateful, and on top of that endless list comes my supervisor, Mikko Kivelä. Working with Mikko has been one of the few things I always count myself lucky for. I value how he walked me through my doctorate with his serene demeanor and unwavering patience. Thanks to Mikko, I worked with many excellent people in and out of Aalto. I am profoundly thankful to all my coauthors, especially Jari Saramäki, Márton Karsai, Ali Faqeeh, David O’Sullivan, and Zahra Ghadiri. With special thanks to Arash Badie-Modiri and Takayuki Hiraoka, with whom I had the most fruitful conversations while preparing our work.

In my doctoral studies, I participated in the NordicMathCovid Project, benefiting greatly from insightful discussions with Lasse Leskelä, Tom Britton, Pieter Trapman, Arnaldo Frigessi, Gianpaolo Scalia Tomba, and Lasse Engbo Christiansen. My sincere gratitude goes to each of them. My appreciation also extends to Petter Holme. Although we never got to work on something together, I have always enjoyed conversing with him and reading his remarkable blog. I also want to devote some words of gratitude to Yasser Roudi. With Yasser, I have engaged in the most vital discussions about the pursuit of science over the past four years.

In the dreary hallways of Aalto’s CS building, where conversations were sparse, I was fortunate to have kind-hearted colleagues like Vesa Vahermaa, Yan Xia, Zhiren Huang, Hasti Narimanzadeh and Tarmo Nurmi. Their presence added a touch of warmth to the workspace, making it a more pleasant environment. My sincere thanks go to them for making my time there enjoyable. I also wholeheartedly thank my Iranian friends in Finland, who made my stay more welcoming: Morteza Shiripour, Babak Nasrinpay, Minoos Zarsav, Amirreza Akbari, and Mehdi Saman Booy. On this note, I want to thank those who came into my life as colleagues but remained friends. If this is not nice, I do not know what is! Sergei Kozlukov, Pegah Pournajafi, Pourya Toranj Simin, Aymara Baumann, and Rouzbeh Hasheminezhad, you are all stars!

A list of appreciation is complete with acknowledging my family, particu-

larly my mom and dad, to whom I am most indebted. I owe a great deal of thanks to my late grandpa and my uncle, Saïd, for his generous financial support. I will never forget my uncle, Masoud, for his candid advice; "You know, don't take it personal, but business is not your thing. Go all in with science; you're pretty good at math."

Looking back now, there is something more that I need to document here. It may reveal the ambiance of my thesis. In the middle of my doctoral studies, something happened in my personal life that brought hope to my perspective and color to my life. It was a beautiful mess but did not last long. It radiated away all its energy, leaving a void that could never be filled. Most of my doctoral studies have been spent with no genuine smile on my face. I was just traveling through the dark like in a Franz Kafka story. There were nights if a close friend had opened his arms to me, I would have wept like a child. Oh man, I should thank Reza Heydari and Omid MnZ. Without our conversations, my nights could have been much longer and my life darker. I owe them big time. Anyway, life did not get any better for me whatsoever. With my grandpa's passing, I remained a regular at the house of despair.

(In my sleep I dreamed this poem)
Someone I loved once gave me a box full of darkness.
It took me years to understand that this, too, was a gift.

Mary Oliver, "*Thirst: Poems*", 2007

All these nightmares, however, had nothing to do with the fulfillment of doing research. If there was no formula to derive or code to implement, I could find no good reason to leave my bed in the morning. Science has been the axe for the frozen sea within me. In these years, whenever I wanted to seek shelter from the world or its indifferent population, I came to the temple of science. If this work is now done, it just means I have put too much effort into making it through. If it were another time that an air of melancholy did not surround me, I could do it with much more ease, less pain, and perhaps in a different class. What comes next is a pure result of my faith in doing science and some discipline I grew up with since my whole life was a sink or swim. Come what may!

Lauttasaari, February 13, 2024,

Abbas K. Rizzi

Contents

Preface	7
Contents	9
List of Publications	11
Author's contributions	13
List of Figures	17
0. About This Work	19
0.0.1 Motivation behind the thesis	19
0.0.2 Structure of the thesis	21
0.0.3 Scope of the thesis	21
1. Mathematical Epidemiology in One Sitting	23
1.1 Things to Consider When Modeling Epidemics	24
1.1.1 Continuous and Discrete Time Modeling	26
1.2 Compartmental Models in Epidemiology	26
1.2.1 The SI Model	27
1.2.2 The SIR Model	29
1.2.3 The Basic Reproduction Number	33
1.2.4 The SIS Model	34
1.2.5 The SEIR Model	35
1.2.6 The Next-generation Method and R_0	37
1.2.7 The Next-generation Matrix for Compartmental Models	38
1.2.8 Beyond the SIR Model	40
1.3 Herd Immunity and Failures of Simple Models	41
1.3.1 Herd Immunity after Vaccination	42
1.3.2 Herd Immunity through Natural Infection	43
2. Structured Populations and Networks	47
2.1 Random Graph Theory: Key Concepts and Definitions . . .	48

2.2	Erdős–Rényi Networks	50
2.2.1	Emergence of the Giant Component	52
2.2.2	Shortcomings of ER Networks in Modeling Contact Networks	54
2.3	The Configuration Model	56
2.3.1	Existence of the Giant Component	58
2.3.2	Size of Giant Component and Generating Functions	58
2.4	Random Graph Models For Networks with Group Structure	59
2.4.1	Bipartite Network	60
2.4.2	Random Clique Networks	60
2.4.3	Stochastic Block Models	61
2.4.4	Networks with Homophily	62
2.5	Spatial Random Graphs	63
2.5.1	Random Geometric Graphs	63
2.6	Lattices	64
2.7	Temporal Networks	64
2.8	Percolation Theory	67
2.8.1	Bond Percolation	67
2.8.2	Site Percolation	69
2.8.3	Percolation as a Critical Phenomenon	69
2.8.4	Directed Percolation	70
3.	Epidemics on Networks	73
3.1	Identifying Key Nodes in Networks	73
3.2	Modeling Epidemics on Networks	74
3.3	Mean-field Approximations	75
3.4	From the Contact Networks to Transmission Networks . .	75
3.5	Mapping Epidemics to Percolation	77
3.5.1	SIR Model and the Configuration Model	77
3.6	Spreading on Temporal Networks	78
3.6.1	Directed Percolation and Spreading Phenomena . .	79
3.7	Homophily and Herd Immunity Threshold	80
3.8	Disease-induced Herd Immunity	82
3.9	Epidemic Spreading and Contact Tracing	84
3.9.1	Digital Contact Tracing	85
3.9.2	Contact Tracing and Social Groups	87
4.	Conclusion	91
	References	93
	Publications	107

List of Publications

This thesis consists of an overview and of the following publications which are referred to in the text by their Roman numerals.

- I** T. Hiraoka, A. K. Rizi, J. Saramäki and M. Kivelä. Herd immunity and epidemic size in networks with vaccination homophily . *Physical Review E*, 105(5) L052301, May 2020.
- II** T. Hiraoka, A. K. Rizi, Z. Ghadiri, J. Saramäki and M. Kivelä. The strength and weakness of disease-induced herd immunity. *Presented at NetSci 2023 Conference*, pre-print: arXiv:2307.04700, Jul 2023.
- III** A. K. Rizi, L. A. Keating, J. P. Gleeson, David J.P. O’Sullivan and M. Kivelä. Effectiveness of Contact Tracing on Networks with Cliques. *Physical Review E*, 109, 024303, Feb 2024.
- IV** A. K. Rizi, A. Faqeeh, A. Badie-Modiri and M. Kivelä. Epidemic spreading and digital contact tracing: Effects of heterogeneous mixing and quarantine failures. *Physical Review E*, 105(4) 044313, April 2022.
- V** A. Badie-Modiri, A. K. Rizi, M. Karsai and M. Kivelä. Directed percolation in random temporal network. *Physical Review Research*, 4(7) L022047, May 2022.
- VI** A. Badie-Modiri, A. K. Rizi, M. Karsai and M. Kivelä. Directed percolation in random temporal network models with heterogeneities. *Physical Review E*, 105(17) 054313, May 2022.

Author's contributions

Publication I: “Herd immunity and epidemic size in networks with vaccination homophily ”

A. K. Rizi played a pivotal role in the development of this work and in shaping the core aspects of the research alongside the primarily responsible author, T. Hiraoka. A. K. Rizi and T. Hiraoka jointly conducted the majority of simulations and mean-field calculations. A. K. Rizi participated in conceptualizing the idea, conducting an extensive literature review, and composing significant sections of the manuscript. M. Kivelä and J. Saramäki supervised the project. The refinement of the manuscript was a collaborative effort, with all project members contributing valuable input. J. Saramäki revised the final version of the manuscript.

Publication II: “The strength and weakness of disease-induced herd immunity”

A. K. Rizi played a crucial role in shaping the research's foundational aspects and its development. He was responsible for originating the research concept, conducting a comprehensive literature review, designing the initial simulations, and building the frameworks and necessary pipelines for the project. Moreover, A. K. Rizi contributed to writing key sections of the manuscripts. T. Hiraoka, the principal author, primarily handled the analytical calculations and led the project. Z. Ghadiri's extensive involvement included model implementation, measure design, and simulation execution. This project was done under the supervision of M. Kivelä and J. Saramäki. The refinement of the manuscript was a collective effort, with all members contributing.

Publication III: “Effectiveness of Contact Tracing on Networks with Cliques”

The primary author of this paper, A. K. Rizi, led the comprehensive development of the research, encompassing the initiation of the initial manuscript, software implementation, analytical and mean-field derivations, practical execution of experiments, literature review, and composition of the dedicated manuscript section. D. O’Sullivan contributed to the analytical calculations, simulation implementation, literature review, and manuscript writing. Additionally, D. O’Sullivan was actively involved in crafting relevant content within the manuscript. M. Kivelä played a significant role by contributing to the numerical calculations for the M matrix and providing a theoretical rationale for the results. L. Keating participated in the revision process of the paper. The project benefited from the oversight of D. O’Sullivan, J. Gleeson, and M. Kivelä. Notably, all project members actively participated in the rigorous revision process of the manuscript.

Publication IV: “Epidemic spreading and digital contact tracing: Effects of heterogeneous mixing and quarantine failures”

A. K. Rizi served as the primary author of this paper, having undertaken initial manuscript drafting, software implementation, and analytical calculations. A. K. Rizi and M. Kivelä had played integral roles in mean-field derivations, analytical outcomes, literature review, and the composition of the dedicated manuscript section. A. Badie-Modiri contributed to the compartmental model section of the article, encompassing model implementation, measure design, simulation execution, and the corresponding manuscript section. The overall project was conducted under the guidance of A. Faqeeh and M. Kivelä, with A. Faqeeh also contributing partially to software implementation. The refinement of the manuscript involved input from every project member.

Publication V: “Directed percolation in random temporal network”

A. Badie-Modiri led the paper’s creation, undertaking initial manuscript drafting, software implementation, and experimental execution. A. K. Rizi and M. Kivelä contributed to mean-field derivations, analytical results, literature review, and manuscript composition for that section. The research idea was conceived by M. Karsai and M. Kivelä, building upon previous work. Manuscript refinement was done by all the authors, and project guidance was collectively overseen by M. Karsai and M. Kivelä.

Publication VI: “Directed percolation in random temporal network models with heterogeneities”

A. Badie-Modiri led the paper's creation, undertaking initial manuscript drafting, software implementation, and experimental execution. A. K. Rizi and M. Kivelä contributed to analytical results, literature review, and manuscript composition for that section. The research idea was conceived by M. Karsai and M. Kivelä, building upon previous work. Manuscript refinement was done by all the authors, and project guidance was collectively overseen by M. Karsai and M. Kivelä.

List of Figures

1.1	Logistic growth curve in the SI Epidemic Model	28
1.2	Evolution of compartments in SIR model	30
1.3	Flattening The Curve Strategy	31
1.4	Distribution of Recovery Time	33
1.5	Epidemic Phase Transition	34
1.6	Fraction of infected people in the SIS model	35
1.7	Epidemic Size in the SIS and SIR model	36
1.8	Incubation Period	37
1.9	Vaccination Homophily	43
1.10	Localized Immunity	44
2.1	Disconnected graph with two cliques	49
2.2	Phase transition in ER network	53
2.3	Divergence in the size of small components	54
2.4	r -regular c -clique networks	61
2.5	Visual representation of a temporal network	66
2.6	Percolation Phase Transition	68
3.1	Herd Immunity Threshold with Homophily	82
3.2	Degree Heterogeneity and Spatiality Space	83
3.3	Contact Tracing with Loops	87
3.4	Diffusion Patterns of a 3-clique	88
3.5	Phase diagrams for Clique Networks	90

0. About This Work

The sciences do not try to explain, they hardly even try to interpret, they mainly make models. By a model is meant a mathematical construct which, with the addition of certain verbal interpretations, describes observed phenomena. The justification of such a mathematical construct is solely and precisely that it is expected to work - that is correctly to describe phenomena from a reasonably wide area. Furthermore, it must satisfy certain esthetic criteria - that is, in relation to how much it describes, it must be rather simple.

John von Neumann, "*Method in the Physical Sciences*",
in *The Unity of Knowledge* (1955)

This chapter offers an overview of the thesis. This thesis includes a didactic introduction that precedes the six featured publications.

0.0.1 Motivation behind the thesis

The COVID-19 pandemic, a stark reminder of our vulnerability to infectious diseases, was neither the first nor will it be the last pandemic humanity confronts. This recent global health crisis underscores the urgent need for preparedness against future pandemics. Pandemics, by their very nature, can be devastatingly deadly, rapidly overwhelming health-care systems and causing widespread social and economic disruptions. The unpredictable nature of viral mutations and the interconnectedness of our world only exacerbate these risks. Therefore, understanding the mechanisms of pandemic spread, including the role of social networks and human behavior, is crucial [164, 165, 158, 115]. This knowledge not only aids in developing effective intervention strategies [163] but also helps mitigate the severe consequences that unchecked pandemics can impose on

global health, economies, and societies [124]. Our future resilience lies in learning from past experiences, investing in public health infrastructure, advancing scientific research, and fostering global cooperation to manage and ultimately prevent the devastating impact of pandemics.

This research explores the intricate dynamics of how diseases spread through the complex networks of human societies [151], evaluating the effectiveness of different interventions within these interconnected populations [113, 112, 80, 78]. It emphasizes the critical role that the detailed connections between individuals play in influencing the spread and severity of epidemics [150]. The study introduces theoretical frameworks that better reflect certain aspects of real-world situations. A significant aspect of *network epidemiology* [53] examined in this work is how the structural and spatial characteristics of networks influence the effectiveness of herd immunity [92]. The focus is on deciphering the structure and dynamics of contact networks [177, 13, 12], particularly in understanding how specific health behaviors influence disease transmission [105, 93]. The research employs stylized models to demonstrate the significant impact of homophily in hesitancy in adopting Contact Tracing Apps and vaccine reluctance on achieving herd immunity [184, 105, 93]. The aim of these models is not to comprehensively represent the complexities of actual epidemics but to illustrate the potential effects of certain network structures and health behaviors, as well as non-pharmaceutical interventions like contact tracing, on the outcomes of epidemics.

Building on this foundation, the ultimate goal of this thesis is to highlight the importance of the contact network structure in modeling disease spreading and act as a guide for showing what kind of network structures can be crucial in building epidemic models. It's important to note that our approach to understanding the spread of infectious diseases follows a "modeling for insight" methodology. Our goal is to gain a deeper understanding of the underlying dynamics of these diseases, so we can provide insights into more effective public health strategies and interventions. I want to emphasize that our *spherical cow* models [30] are not intended to fit data directly. Instead, they aim to broaden the conceptual framework within which we understand and respond to epidemics. For readers keen on exploring a data-driven approach to modeling and predicting the global spread of infectious diseases using real-world data, I suggest diving into "Charting the Next Pandemic" by y Piontti et al. [206]. Our work contributes to academic discourse and provides a foundation for future empirical research in support of society's ongoing efforts to enhance resilience against infectious diseases.

0.0.2 Structure of the thesis

In Chapter 1, I present an introductory survey of Mathematical Epidemiology, focusing on compartmental models. The chapter delves into the historical context of translating epidemiological challenges into mathematical frameworks. Central to this exploration is the mass-action or fully-mixed population hypothesis, which enables the application of calculus tools to model population dynamics using differential equations. I comprehensively review essential epidemiological concepts and demonstrate their translation into mathematical terms. This chapter lays the groundwork for our understanding of how to formalize models that describe the spread of epidemics. I conclude with a discussion on the limitations of the models discussed, particularly the inadequacy of the fully-mixed population assumption for complex, structured human populations. I illustrate this point by examining vaccination strategies, showing how conventional infectious disease models fall short of accurately predicting vaccine quantities required for achieving herd immunity to ensure the safety of an entire population, including the unvaccinated.

In Chapter 2, I provide an accessible introduction to network science, outlining the essential concepts and methodologies that will be applied to more accurately model infectious diseases. I explore the critical aspects of human population structure that can significantly influence epidemic outcomes. The chapter navigates various random network models, their characteristics, and the phase transition phenomena observable in static and temporal network contexts.

Equipped with the insights and techniques from these two chapters, we embark on a detailed study of epidemic modeling on complex networks. In Chapter 3, I discuss how our foundational knowledge of spreading and diffusion processes can be applied to quantify epidemic behavior on networks. The chapter introduces various mean-field approximations and other modeling techniques. I emphasize that epidemic modeling on networks can reveal non-trivial dynamics, which are crucial for understanding effective epidemic control.

0.0.3 Scope of the thesis

A patient reader with a good background in science can follow the research papers presented in this work after reading the following three chapters. The theoretical minimum required for understanding them is a working knowledge of probability theory, calculus, and linear algebra. I also recommend Newman's book [151] as a network textbook and Diekmann et al. book [55] for a general understanding of mathematical epidemiology.

On another note, you should know that I grew up in the physics culture, and I like borrowing the tools and perspectives of that field and trying to

combine them with new ideas and techniques to tackle interdisciplinary problems. So, in terms of technicality and jargon, what follows in this work is not only written with the notation that is the best to the taste of a physicist but also the mathematical rigor that I have gone through is more physics-friendly than mathematics-friendly. A background in physics, with a focus on statistical mechanics, ideally equips you to engage with and understand the complexities of this work.

This is not a *theorem and proof* thesis, but I have mentioned resources where you can find more rigorous mathematical arguments. So, if you have a math background, you will have many exciting puzzles to think about after reading each chapter. I also invite you to delve into some proof to turn this work into an even better investment in your time. For a more mathematical approach to networks, I recommend referring to *Random Graphs and Complex Networks* by Van der Hofstad [194]. Depending on their particular field of study, computer scientists should also be capable of comprehending this work, albeit not as effortlessly as physicists. If you are more from an engineering background, you will find simulations in our papers very interesting. While this work leans heavily on mathematical modeling, it stands as an inviting challenge for epidemiologists keen on extending their professional skill set in this exciting direction. Moreover, they may find some of our models not precisely suitable to describe some particular phenomenon, as in this work, we have done our best to come up with reasonably simple mathematical models to explain the physics behind spreading phenomena and, more importantly, get the phenomenology right. Believe me, it is no less deserving of scrutiny!

In conclusion, writing this work has been a thoroughly enjoyable experience for me. Above all, I sincerely hope you find equal pleasure in reading it.

Like most mathematicians, he takes the hopeful biologist to the edge of a pond, points out that a good swim will help his work, and then pushes him in and leaves him to drown.

C. Elton, 1935 review on the mathematical ecology work of Lotka.

What is physics? To me, ... the central idea was that the world is understandable, that you should be able to take anything apart, understand the relationships between its constituents, do experiments, and on that basis be able to develop a quantitative understanding of its behavior.

John Hopfield, 2018, *Now What?*

1. Mathematical Epidemiology in One Sitting

I simply wish that, in a matter which so closely concerns the well-being of the human race, no decision shall be made without all knowledge which a little analysis and calculation can provide.

D. Bernoulli, 1760, on smallpox inoculation

It is not easy to say precisely when and by whom the foundations of Mathematical Epidemiology were established. Here, by Mathematical Epidemiology, I primarily refer to a rigorous quantitative framework for studying how infectious diseases spread, predicting what might happen during an outbreak, and figuring out how to control it. One can argue that John Graunt, a businessman admitted to the Royal Society, lit the torch in the 17th century with a new approach to the analysis of causes of death in London [145]. Graunt did an excellent job of bookkeeping the so-called “Bills of Mortality” which were weekly records of numbers and causes of death in London parishes from 1592 to 1603 and tried to quantify causes of death in a systematic way [84]. Based on real data, he predicted the percentage of people who would live to different ages and their year-by-year life expectancy. Among his observations, he also noticed that in cities, more people died than in rural areas, and while more boys were born than girls, higher male mortality balanced it out, resulting in a nearly equal gender distribution in the population [171].

I admire Graunt’s contribution to the field of epidemiology. His innovative analysis of the tables of health data (Bills of Mortality) is commendable, and from a technical perspective, his work can be recognized as seminal in *Quantitative* Epidemiology. However, when we consider the monumental significance of Daniel Bernoulli’s 1766 paper, it becomes clear that this work forms the cornerstone of *Mathematical* Epidemiology. Graunt may have lit the torch, but Bernoulli’s work led to a wildfire! Bernoulli introduced the first compartmental model of infectious disease in that work and used mathematical reasoning to argue for universal inoculation

against smallpox. Compartmental models in epidemiology allow us to strip unnecessary complicating factors away from disease dynamics to gain a reasonable understanding of such spreading phenomena. I will explain compartmental models and the effectiveness of interventions in a more pedagogical way in this section. For a more historical note on Bernoulli's epidemiological model, I recommend referring to Ref. [60]. Ref. [55] also serves as an excellent guide for those aiming to learn the formulation and analysis of mathematical models in infectious disease epidemiology.

As a matter of fact all epidemiology, concerned as it is with variation of disease from time to time or from place to place, **must** be considered mathematically, if it is to be considered scientifically at all. And the mathematical method of treatment is really nothing but the application of careful reasoning to the problems at hand.

Sir Ronald Ross, 1911, *The Prevention of Malaria*

1.1 Things to Consider When Modeling Epidemics

Let us begin with the epidemic in a closed population in a demographic steady state, with no history of a given infection or introduction of any intervention. We are also interested in spreading phenomena that take place in *naive* populations at particular time scales, often much smaller than fluctuations in population due to the birth or death of people out of epidemiological reasons. By naive, we mean every individual lacks immunity or immunologic memory to a disease and is susceptible to infection.

Imagine a population with only one infected person (seed of infection) at day zero. If an infected person can infect $R_0 > 1$ more susceptible people, this process would undergo a deterministic exponential growth such that the number of infected people after t generations, ε_t , would be given by the following geometric series:

$$\varepsilon_t = 1 + R_0 + R_0^2 + \dots + R_0^t = \frac{R_0^{t+1} - 1}{R_0 - 1}. \quad (1.1)$$

We call ε_t the epidemic size after t generations. The first lesson from the mathematics of this equation is that if $R_0 < 1$, then in finite time, the disease spreading will die out. Compared to the population size, the epidemic size would be negligible even if we start with more than one infected person. For mathematical tractability, we model the epidemics in the thermodynamic limit, meaning that we assume the size of the population, a.k.a. the system size, N , is large enough so that we can follow the problem in the limit that $N \rightarrow \infty$. Therefore, the size of the

epidemic compared to the population size will be zero when $R_0 < 1$. Even if we consider that every person can, on average, infect R_0 susceptible people and R_0 is drawn from some distribution with finite first and second moments, one can easily show we again end up with a similar conclusion, this time through a stochastic growth known as Galton–Watson process [55].

However, since R_0 , here, represents the expected number of people secondarily infected, which is an integer, the epidemic's size will increase monotonically without an epidemic threshold. According to this model, a massive outbreak comparable in scale to the population size will invariably occur swiftly.

Disease	Basic Reproduction Number
Measles	12–18
Chickenpox (Varicella)	10–12
Mumps	10–12
Rubella	6–7
Polio	5–7
Pertussis (Whooping Cough)	5.5
Smallpox	3.5–6.0
HIV/AIDS	2–5
COVID-19 (Ancestral Strain)	2.9 (2.4–3.4)
SARS	2–4
Diphtheria	2.6 (1.7–4.3)
Common Cold (e.g., Rhinovirus)	2–3
Mpox	2.1 (1.5–2.7)
Ebola (2014 Outbreak)	1.8 (1.4–1.8)
Influenza (Seasonal Strains)	1.3 (1.2–1.4)
Andes Hantavirus	1.2 (0.8–1.6)
Nipah Virus	0.5
MERS	0.5 (0.3–0.8)

Table 1.1. Basic Reproduction Numbers of Various Infectious Diseases [59, 54, 27].

Table 1.1 compares the average number of secondary infections, commonly referred to as the basic reproduction number, for various diseases. Assume a hypothetical scenario such that $R_0 = 3$, which is a reasonable number for some severe infectious diseases [59, 54] as it was estimated for some analysis during the COVID-19 pandemic [27]. Then, when $t = 10$, more than 88,000 people will be infected, and after 30 generations, it will reach more than 100 trillion people, much larger than the entire earth's

population. This astronomically big number does not make sense at all, as, in reality, many boundary conditions control such exponential growth. Obviously, there should be a cut-off; the process must cease when everyone is infected. We explicitly did not account for reinfection or recovery in this model. People may recover from the disease in a different time scale and gain immunity against reinfection. Therefore, in practice, every infected person cannot keep infecting R_0 more people as the spreading process unfolds. Not everyone has access to enough susceptible cases after the epidemic's early stages. Ultimately, the exponential growth should be saturated as we run out of susceptible people. On top of these, people change their social behavior [176] as they face a wave of infection, so either individuals on their own try to protect themselves from infection or some external effects such as seasonality or high-level social constructs such as governments will impose regulations and apply interventions to curb the epidemic. Therefore, for more realistic modeling, we need to consider all these scenarios, one at a time, and then try to consider them all together to the extent that we can handle the arising complexity of the problem.

1.1.1 Continuous and Discrete Time Modeling

Epidemic modeling on networks employs continuous and discrete time models, each with distinct advantages [161, 42, 198]. Continuous-time models, often formulated with non-linear differential equations, are helpful for uninterrupted changes but may not always accurately represent the epidemic spread [152]. On the other hand, discrete-time models, described by difference equations, align better with the discrete nature of epidemic data collection and are easier to implement in computer simulations. They may also offer a more granular view of the spread, accounting for specific time intervals and potentially capturing the spatial dependencies between individuals more accurately. Both methods are valuable, and we will use them in modeling epidemics on networks depending on our modeling requirements and objectives. In this section, we will continue with continuous-time compartmental models as they are beneficial for pedagogical purposes, leveraging calculus tools to elucidate the dynamics of disease spread. We will later show how we can formulate such models within discrete-time settings. In our publications, we utilize both continuous and discrete-time modeling approaches to capture the nuances of disease spread in networks.

1.2 Compartmental Models in Epidemiology

A convenient way to model epidemics is to divide people into groups, commonly known as compartments, and develop equations that govern how

one person leaves one and joins the other. Compartmental models provide a useful abstraction of disease dynamics by making it easier to track and predict the course of an epidemic, as the equations describe the rate at which people move from one compartment to another.

1.2.1 The SI Model

In the previous example, every individual was either susceptible or infected in a population of size, say, N and preferably $N \rightarrow \infty$. So, one can assign each individual to compartments with labels s and i , respectively, such that the size of the compartments respects the conservation of population size, $S + I = N$. Compartment s initially begins with $N - 1$ members, and people transition from that compartment to compartment i following Eq. 1.1. This model is an SI model, as there are only two compartments s and i , and people may progress between them following the order of labels in the title; $s \rightarrow i$.

In Section 1.1.1, we explored how infectious diseases can be modeled in both continuous and discontinuous time frames. For simplicity, we will proceed with our epidemic modeling using a continuous-time approach. Additionally, we will address the issue of unbounded exponential growth identified in the earlier model. This will be achieved by employing the *fully mixed* or *mass-action* approximation [69]. Our method involves representing the interactions between different compartments using differential equations. Depending on our modeling perspective, the interactions between the compartments can be given through some rate equations or transition probabilities—the former leads to deterministic dynamics, and the latter leads to stochastic ones. So, given that each person, on average, interacts with β other randomly chosen people per unit time, we can rewrite the previous model with the following equations,

$$\begin{aligned} \frac{ds}{dt} &= -\beta si, \quad \text{or/and} \\ \frac{di}{dt} &= \beta si, \end{aligned} \tag{1.2}$$

where s and i are the expected numbers of susceptible and infected individuals normalized by the population size N such that $s + i = 1$. Note that as they are average values, they may not be integers, in general, while the actual numbers of susceptible and infected people are always integers. If we were to repeat the epidemic dynamics given by Eq. 1.2 multiple times under the same conditions and then take the average, these would be the values we'd arrive at.

We can eliminate s from Eq. 1.2 as $s = 1 - i$ and easily arrive at the solution that yields a “logistic growth curve” for the fraction of infected

individuals given by

$$i(t) = \frac{i_0 e^{\beta t}}{1 - i_0 + i_0 e^{\beta t}}, \quad (1.3)$$

where $i_0 = i(0) \ll 1$ is the size of the seed of infection normalized by the population size. According to this equation, as depicted in Fig. 1.1, the expected number of infected individuals initially grows exponentially with the characteristic time $\frac{1}{\beta}$, and then saturates for large t , as $t \rightarrow \infty$.

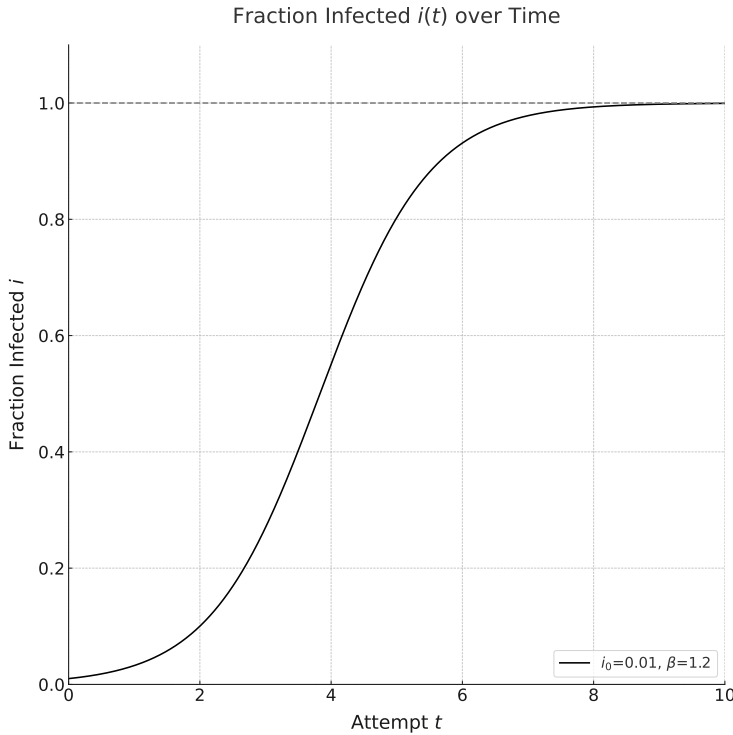


Figure 1.1. Logistic growth curve in the SI Epidemic Model as given by Eq. 1.2. The expected fraction of infected people within an SI model initially escalates exponentially. However, as the reservoir of susceptible individuals depletes over time, the growth rate reaches a saturation level, leading to a plateau in the curve as indicated by the dashed line.

As highlighted in Sec. 1.1, the SI model is overly simplistic for most practical applications. Despite its exponential growth, which aligns with many spreading phenomena in their early stages, it leads to the infection of the whole population when $i_0 > 0$, overestimating the final size of most outbreaks. The epidemic size may rapidly increase at the very early stages of an epidemic, but it slows down at higher rates due to natural immunity or facing interventions, and it almost never gets that close to the population size. Nevertheless, we can still learn from the SI model, as in the early stages of most epidemics, the number of infected people grows exponentially with the per-individual rate β similar to $i(t \approx 0) = i_0 e^{\beta t}$.

1.2.2 The SIR Model

A reasonable improvement to the SI model is to consider that people recover from the disease after some time and gain immunity against reinfection. So, we add a third compartment to our model, letting people leave the infected compartment with some rate and join the recovered compartment \mathbb{R} , giving rise to the transition pattern $\mathbb{S} \rightarrow \mathbb{I} \rightarrow \mathbb{R}$.

This three-state model is called the *susceptible–infected–recovered* or SIR model. You can find “SIR” in the literature as an acronym for different terms. Some may use *removed* instead or along with the recovered state as, in general, the person is now removed from interacting with others in the population. Regrettably, some diseases result in death rather than recovery, so the dead person is removed. For the sake of modeling, both of them can be considered in this model, and individuals in the \mathbb{R} compartment would not take part in infecting other people. In concise terms, \mathbb{R} is where people transition from the \mathbb{I} compartment. In Sec. 1.3.1, we will demonstrate how vaccination can prevent individuals from contributing to the spread of infection, and in Sec. 3.9, we will explore how isolating or quarantining people can yield similar results. \mathbb{I} can also stand for infected or infectious, as being infected does not necessarily imply being contagious. One may get infected but may never pass it on or do it after some period of time. However, from now on, everywhere we say infected, we mean the same thing as infectious, and we use them interchangeably unless otherwise noted.

To describe the dynamics of the SIR model, we use the same mass-action approximation and per-individual rate β as we used in Sec. 1.2.1, but this time, we let people leave the \mathbb{I} compartment, with the constant average rate γ so that the fraction of recovered people, r , changes as $\frac{dr}{dt} = \gamma i$. Here, the conservation of population size implies $s + i + r = 1$, and the changes in each compartment would be summarized as:

$$\begin{aligned}\frac{ds}{dt} &= -\beta si, \\ \frac{di}{dt} &= \beta si - \gamma i, \\ \frac{dr}{dt} &= \gamma i.\end{aligned}\tag{1.4}$$

There is no closed-form solution for the SIR model. However, a numerical solution is presented in Fig. 1.2.

Looking at Fig. 1.2, it is interesting to observe how the infection curve ascends, slows down, and then descends. This curve illustrates the real-time count of infected individuals, which is quite useful for a range of practical situations. For instance, in a city with limited hospital capacity, if the maximum of this curve surpasses what the hospitals can manage,

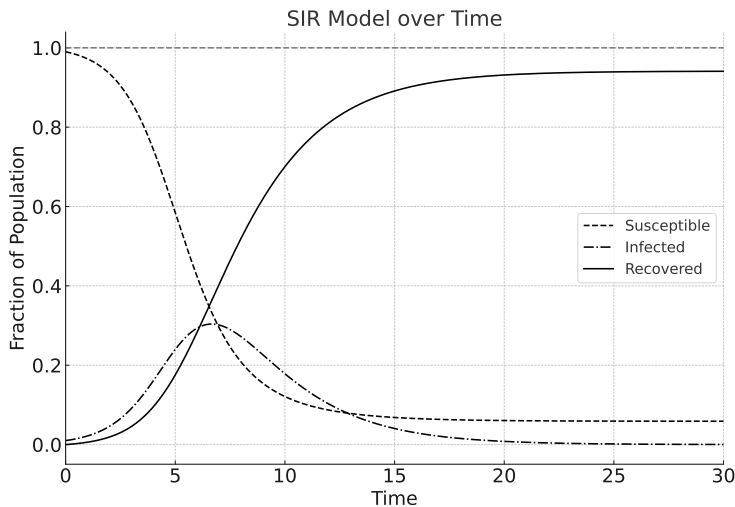


Figure 1.2. Evolution of the susceptible, infected, and recovered populations over time, based on the SIR model given. The model was integrated using parameters $\beta = 1.2$ (transmission rate) and $\gamma = 0.4$ (recovery rate). Initial conditions were set with 99% of the population as susceptible, 1% as infected, and 0% as recovered. The Infected curve is represented with a solid line for a clear distinction. The horizontal dashed line indicates the maximum value of 1 for the fraction of the population, which will always be larger than the fraction of recovered people.

things could get pretty challenging, especially with severe diseases in the mix. The “Flattening The Curve” strategy was all about promoting actions to lower this peak, aiming to ease the pressure on the healthcare system as the maximum number of individuals needing medical attention at any given time is minimized [135]. As shown in Fig. 1.3, this ensures the healthcare system is not overwhelmed. During the COVID-19 pandemic, key measures to achieve this were hand hygiene, wearing face masks, and practicing social distancing [136] to reduce the value for β .

Fig. 1.2 also shows that the value of r rises monotonically, yet it never gets to one. Similarly, the susceptible curve does not touch zero. This suggests that a portion of the population stays susceptible over time. The value of r reflects the total fraction of infected people up to time t , so the asymptotic value of r indicates the total size of the epidemic. From now on, we will always report the size of the epidemic as a fraction of the whole population.

We cannot solve the SIR model analytically, as it is not solvable by elementary functions in its standard form [89, 123]. However, we can study it at the $t \rightarrow \infty$ limit. Using equation Eq. 1.4, after some algebra, we can show the changes in r in a large population with a small seed of

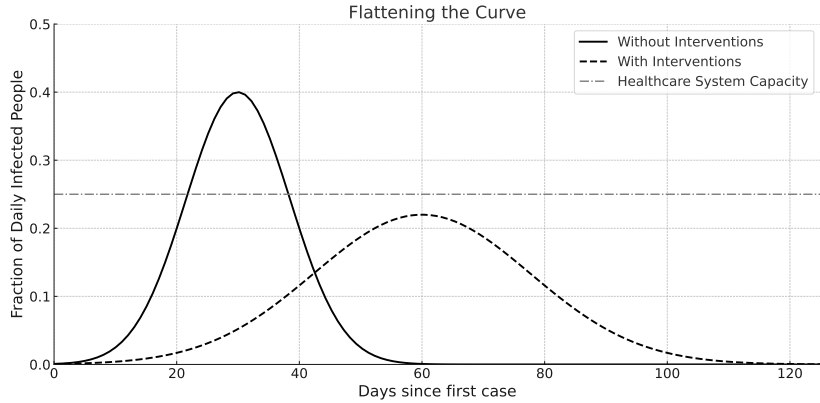


Figure 1.3. Time evolution of $i(t)$ for two different values of β . By adopting measures like hand washing, social distancing, and wearing face masks, the peak of active cases can be both lowered and postponed. This delay provides valuable time for healthcare systems to expand and handle the influx of patients more effectively. Consequently, this strategy of flattening the curve also offers an opportunity to enhance healthcare capabilities to accommodate the increased demand.

infection, can be given as [151]

$$\frac{dr}{dt} = \gamma(1 - r - e^{-\beta r/\gamma}). \quad (1.5)$$

When $t \rightarrow \infty$, $\frac{dr}{dt} = 0$ which gives

$$r_{\infty} = 1 - e^{-\beta r_{\infty}/\gamma}, \quad (1.6)$$

where r_{∞} is the final epidemic size. This equation is transcendental in r_{∞} , and one typically finds the solution graphically. They would also know that $r_{\infty} = 0$ is a trivial solution, but its stability as a fixed point of iteration depends on the value of β/γ . If $\beta \leq \gamma$, then $r_{\infty} = 0$ is a stable fixed point, which makes sense intuitively, as it suggests that if people recover from the disease faster than new infections occur, the disease will eventually die out exponentially fast. In simpler terms, in the long run, and the thermodynamic limit, the epidemic size will tend to be zero when recovery outpaces new infections. However, if $\beta > \gamma$, then $r = 0$ would be an unstable solution, and the final epidemic size would be between zero and one.

To analyze the stability of the solution $r = 0$ for Eq. 1.5, we can use linear stability analysis. This involves determining whether small perturbations around the equilibrium solution $r = 0$ grow or decay over time. The general approach is to linearize the differential equation around the equilibrium point. Let's denote a small perturbation around $r = 0$ by δ . When $r = \delta$ and δ is small, we can approximate the exponential term using the first term of its Taylor expansion, $e^{-\beta\delta/\gamma} \approx 1 - \beta\delta/\gamma$, since higher-order terms will be

negligibly small. Substituting this into the differential equation, we get:

$$\frac{d\delta}{dt} \approx \gamma(1 - \delta - (1 - \beta\delta/\gamma)) = \gamma \left(\frac{\beta\delta}{\gamma} - \delta \right) = \gamma\delta \left(\frac{\beta}{\gamma} - 1 \right).$$

So the linearized differential equation becomes:

$$\frac{d\delta}{dt} \approx \delta(\beta - \gamma).$$

From this, we can see that the sign of $\beta - \gamma$ determines the behavior of small perturbations δ : If $\beta > \gamma$, then $\beta - \gamma > 0$ and any small perturbation δ will grow exponentially, which implies that the solution $r = 0$ is unstable. If $\beta < \gamma$, then $\beta - \gamma < 0$ and any small perturbation δ will decay exponentially, suggesting that the solution $r = 0$ is stable. Therefore, when $\beta > \gamma$, the solution $r = 0$ is unstable because small deviations from this point will increase over time rather than return to equilibrium.

The transition between having an epidemic and not having one occurs at a specific point where $\beta = \gamma$, known as **the epidemic threshold**. It's important to contrast this with the simpler SI model, where there is no such threshold. In the SI model, the disease spreads because once individuals are infected, they never recover. This fundamental difference means that the number of infected individuals in the SI model can never decrease as opposed to the SIR model, where there's a critical point where the dynamics change, leading to the possibility of disease containment. In other words, the SI can be considered as the special case of the SIR model with $\gamma = 0$ so that β is larger than γ by design.

Given the value of γ , we can calculate for how long, τ , an infected person is likely to remain infected before recovery. The probability of recovering in any infinitesimal time window Δt is $\gamma\Delta t$, and the probability of not doing so is $1 - \gamma\Delta t$ [151]. This means that the person is still infected after a total time τ with probability

$$\lim_{\Delta t \rightarrow \infty} (1 - \gamma\Delta t)^{\tau/\Delta t} = e^{-\gamma\tau}. \quad (1.7)$$

So, the probability that the person stays infected for time τ and recovers dt later would be $e^{-\gamma\tau} \times \gamma dt$ leading to an exponential distribution [151]

$$p(\tau) = \gamma e^{-\gamma\tau}, \quad (1.8)$$

with mean infectious time $1/\gamma$. The artifact of this model is that the distribution of times for which an individual remains infected is not that realistic. Based on Eq. 1.8, it is most likely for an individual to recover just after infection. However, this likelihood diminishes exponentially over time. Theoretically, a person could stay infected for a duration significantly longer than the average infectious period, denoted as $1/\gamma$. As depicted in Fig. 1.4, for some diseases, people remain infected for a typical range of

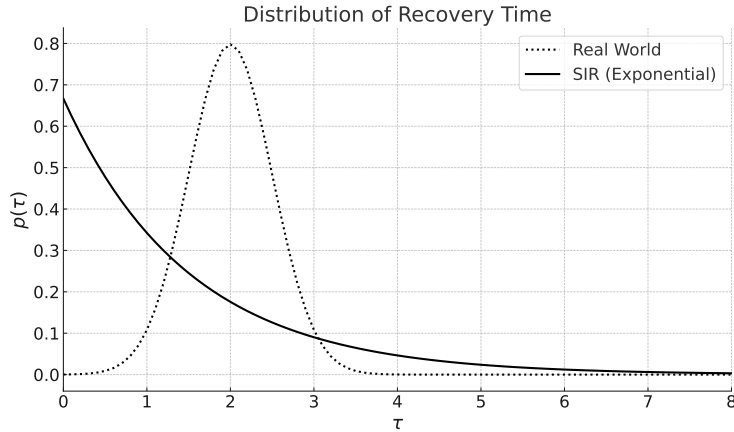


Figure 1.4. The SIR model suggests an individual has the highest likelihood of recovery immediately post-infection, with chances decreasing exponentially over time. However, there’s typically a consistent recovery timeframe for many diseases, often peaking around a specific period, such as one or two weeks, as highlighted in the depicted distribution.

time, making its distribution narrowly peak around some expected value, like one or two weeks [152].

We can employ $p(\tau)$ to determine the average number of individuals that an infected person will infect before recovery, represented as R_0 , in a naive population. Given that an individual stays infected for a duration τ , they would, on average, result in $\beta\tau$ new infections due to their contacts. By averaging over the distribution of τ , we can derive the average number R_0 [151]:

$$R_0 = \beta\gamma \int_0^{\infty} \tau e^{-\gamma\tau} d\tau = \frac{\beta}{\gamma}. \quad (1.9)$$

We call R_0 the basic reproduction number as an indicator of how many new infections can happen after a previous one [57]. Equation 1.9 offers an alternative approach to deducing the epidemic threshold for the SIR model: the threshold is at $R_0 = 1$, consistent with our earlier findings based on the long-term behavior of the I compartment mimicked with Eq. 1.6.

1.2.3 The Basic Reproduction Number

In the deterministic approach, compartmental models are often described with ordinary differential equations, which, by design, have two fixed points: disease-free equilibrium and endemic equilibrium. The stability of these fixed points will be determined by evaluating the value of the bifurcation parameter R_0 . Following Physics’ jargon, when $R_0 < 1$, we say the epidemic spreading is in the sub-critical regime. When $R_0 = 1$, we are at the critical point with many exciting phenomena [81], which I will cover later in this thesis. An outbreak happens when $R_0 > 1$, and following

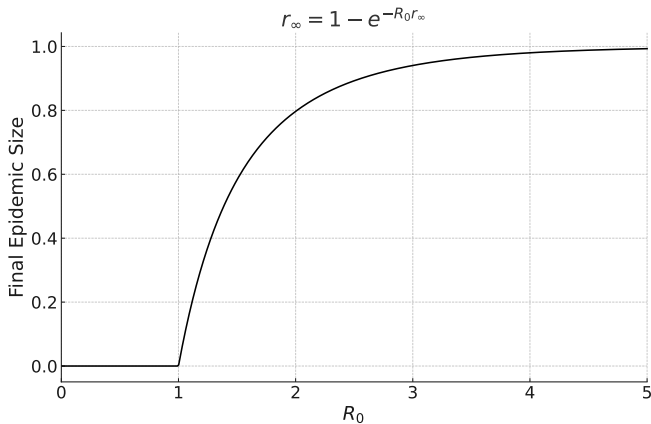


Figure 1.5. The epidemic can transition from a disease-free equilibrium state, with zero epidemic size, to an endemic equilibrium with a positive epidemic size. In the SIR model, the final epidemic size can be calculated using Eq. 1.6.

the same nomenclature, we call this regime super-critical, R_0 the control parameter and the epidemic size r_∞ the order parameter of the spreading phenomenon. In the thermodynamic limit, epidemic size vanishes in the sub-critical regime and scales with the population size in the super-critical regime.

In the SIR model, the final epidemic size can be given using Eq. 1.6 [151] such that

$$r_\infty = 1 - e^{-R_0 r_\infty}. \quad (1.10)$$

Fig. 1.5 shows the final epidemic size as a function of the basic reproduction number, and we witness a phase transition at $R_0 = 1$, commonly referred to as the epidemic threshold.

1.2.4 The SIS Model

Another extension to the SI model is to consider the possibility of not gaining immunity after infection and turning susceptible again. Making the transition between the compartments as $s \rightarrow i \rightarrow s$. So, as opposed to the SIR model, we let *reinfection* happen in this two-state model. The governing equations in this model would be

$$\begin{aligned} \frac{ds}{dt} &= -\beta si + \gamma i, \\ \frac{di}{dt} &= \beta si - \gamma i, \end{aligned} \quad (1.11)$$

with $s + i = 1$. This system of differential equations leads to:

$$i(t) = i_0 \frac{(\beta - \gamma)e^{(\beta - \gamma)t}}{\beta - \gamma + \beta i_0 e^{(\beta - \gamma)t}}, \quad (1.12)$$

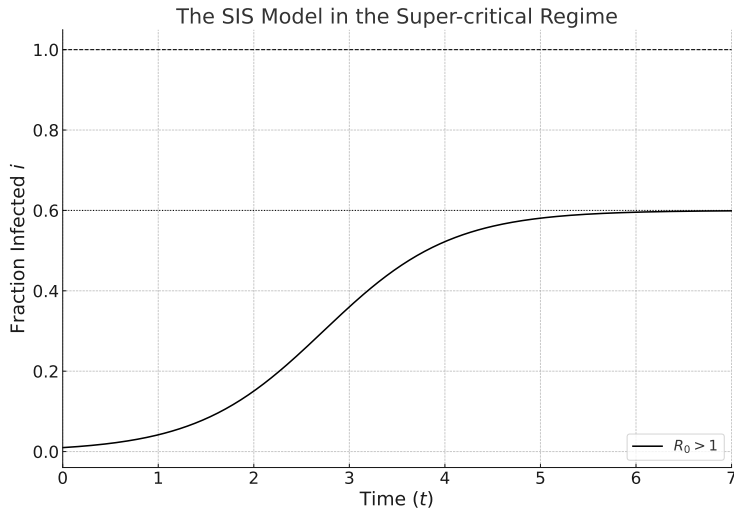


Figure 1.6. Evolution of fraction of infected people over time in the SIS model for $R_0 > 1$. i grows following a logistic curve but never saturates the whole population. Instead, it reaches a limiting value $1 - \frac{1}{R_0}$.

where i_0 is the size of the seed of infection. If $\beta < \gamma$, $i(t)$ would exponentially decay, and the disease will eventually die out. $\beta = \gamma$ will be the epidemic threshold, which can also be derived with the basic reproduction number arguments.

If $\beta > \gamma$, then this produces a logistic curve, similar to the SI model with a delicate feature that the epidemic ends up in a stable state where a steady fraction of the population, given by

$$i_\infty = \lim_{t \rightarrow \infty} i(t) = \frac{\beta - \gamma}{\beta} = 1 - \frac{1}{R_0}, \quad (1.13)$$

will be infected. Fig. 1.6 presents the time evolution of the fraction of infected people. Therefore, in the SIS model, the final size of the epidemic would always be $1/R_0$ away from saturating the whole population. This phenomenon is shown in Fig. 1.7 as it compares the dependence of the final size of the epidemic on R_0 in the SIS and SIR models, following Eq. 1.13 and Eq. 1.10, respectively.

1.2.5 The SEIR Model

In previous models, any exposed individual in the s compartment would most probably transition to the i compartment. As elaborated in Sec. 1.2.2, we often used “infected” and “infectious” interchangeably. This is because, in our model’s context, an individual becomes contagious immediately upon exposure. So, there is no distinction between being infected and being infectious. Yet, when we examine diseases like COVID-19, we notice

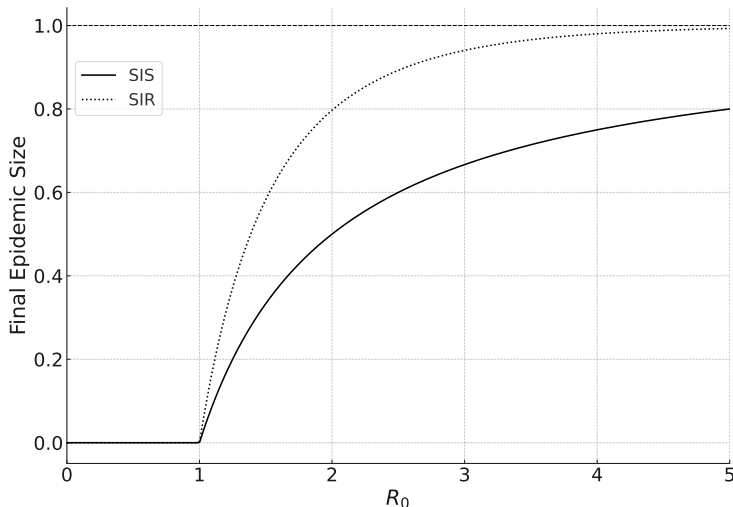


Figure 1.7. Comparison of the final epidemic size as a function of the basic reproduction number in the SIS and SIR model. In the sub-critical regime, where $R_0 < 1$, the final epidemic size is zero for both cases. In both dynamics, the entire population would never be infected; however, after the epidemic threshold, $R_0 = 1$, the SIR dynamics lead to a higher epidemic size.

that *exposed* individuals only begin to transmit the virus after a certain duration known as the incubation period, t_l , (sometimes referred to as the latent or latency period) [197]. For a more detailed understanding of infectious diseases, particularly when conceptualizing interventions, it would be instructive to contemplate a time profile similar to what is depicted in Fig. 1.8. To consider this latency, we can refine our model by introducing an intermediary E compartment between s and I . This modification results in the following transition sequence: $s \rightarrow E \rightarrow I \rightarrow R$.

Given that κ represents the average rate at which a latent individual transitions to being infectious, we can adapt the SIR model. Consequently, if the average fraction of individuals who have been exposed to the virus but are not yet infectious is e , the governing equations for the SEIR model can be expressed as:

$$\begin{aligned}
 \frac{ds}{dt} &= -\beta si, \\
 \frac{de}{dt} &= \beta si - \kappa e, \\
 \frac{di}{dt} &= \kappa e - \gamma i, \\
 \frac{dr}{dt} &= \gamma i,
 \end{aligned}
 \tag{1.14}$$

with $s + e + i + r = 1$.

The SEIR model provides a more detailed insight into the spread of infec-

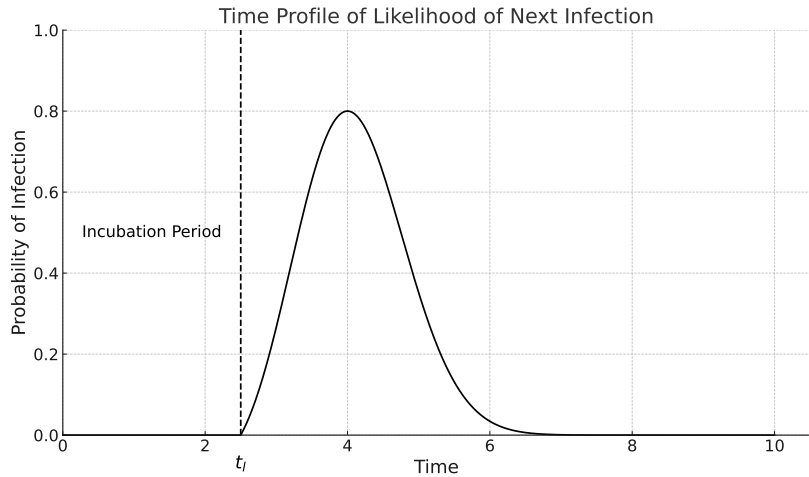


Figure 1.8. Infected individuals can start infecting their neighbors after some period known as the incubation period, t_i , denoting the interval from when an individual is first exposed to a pathogen to the onset of infectiousness or symptoms. For numerous infectious diseases, this time-frame captures the duration the pathogen needs to multiply sufficiently, eventually eliciting symptoms in the affected individual.

tious diseases, particularly when there is a clear latency period between exposure and the onset of infectiousness. However, within a reasonable range of parameter values, it does not differ fundamentally in terms of phenomenology compared to the SIR model.

1.2.6 The Next-generation Method and R_0

In structured models of epidemic spread encompassing multiple infection types, the computation of the basic reproduction number R_0 involves averaging the new infection rates across all types [56, 193, 40]. Consider a scenario like HIV transmission in a strictly heterosexual demographic, where infection types are distinctly categorized as male and female, with asymmetries in transmission rates. Here, M_{ij} represents the expected number of type i infections caused by an individual of type j in a wholly susceptible type i population. If f and m are the expected secondary infections in females and males, respectively, we can summarize the number of new infections after each type in a table \mathbf{M} , celebrated as *the next-generation matrix*, such that:

$$\mathbf{M} = \begin{pmatrix} 0 & f \\ m & 0 \end{pmatrix}. \quad (1.15)$$

As a non-negative matrix, \mathbf{M} inherently possesses a principal eigenvalue, its spectral radius $\rho(\mathbf{M})$, which epitomizes the total averaged number of

new infections. Consequently, $R_0 = \rho(\mathbf{M}) = \sqrt{mf}$ which is also the geometric mean of the expected number of female and male secondary cases, encapsulating the epidemiological virulence of the pathogen in this structured population model. If secondary infections were gender-independent, with each individual capable of infecting R_0 others, then the anti-diagonal elements of the matrix \mathbf{M} , M_{12} and M_{21} , would be identical to R_0 . As a result, the spectral radius would be $\rho(\mathbf{M}) = \sqrt{R_0^2} = R_0$.

1.2.7 The Next-generation Matrix for Compartmental Models

As we already have seen, compartmental models in epidemiology usually describe the dynamics of spreading using a set of coupled non-linear ordinary differential equations (ODE). This system of ODEs is constructed to have two fixed points: a disease-free equilibrium, an infection-free steady state where the final epidemic size is zero, and an endemic equilibrium, with a positive final epidemic size. The stability of these fixed points will be determined with the control parameter R_0 , celebrated as the basic reproduction number in epidemic modeling. For a quick reminder, look at Fig. 1.7, which shows such a phase transition in the SIS and SIR model.

For a general model, with n compartments, c_1, c_2, \dots, c_n , the time evolution of the fraction of the population in each compartment can be written as

$$\frac{dc_i}{dt} = f(c_1, c_2, \dots, c_n), \quad (1.16)$$

where $f(\cdot)$ is a non-linear combination of other compartment sizes, respectively, and conventionally, c_1 is set to be the susceptible compartment. R_0 is a threshold for the stability of the disease-free equilibrium such that its stability changes at $R_0 = 1$.

To determine R_0 , we linearize the non-linear ODEs that describe the production of new infections and transitions among the infected individuals around the disease-free equilibrium. Epidemiological interpretation of this linearization is that R_0 encapsulates the potential outbreak initiated by an infected individual in a naive population, assuming the change in the susceptible population is negligible during the initial spread. Mathematically, R_0 can be articulated as the product of the near-disease-free equilibrium infection rate and the average infectious duration. It may be helpful to revisit the derivation of the SIR model presented in Eq. 1.9.

As matrices can represent linear ODE systems, we can average the expected number of new infections over all possible infected types with the next-generation matrix \mathbf{M} [55]. This matrix is a linear positive operator that maps the current infection generation to the subsequent one. It's essential to highlight that this matrix operator primarily targets the number of infections, excluding other compartments. Iteratively applying this operator sheds light on the initial propagation of the infection across a

diverse population. Setting the spectral radius (Perron root), or the largest modulus of the eigenvalues of this operator to one, we can find the basic reproduction number [196, 57, 37].

$$R_0 = \rho(\mathbf{M}). \quad (1.17)$$

To clarify this framework, let's go through a rather complicated example. Assume a disease governed by SEIR dynamics similar to the one in Sec. 1.2.5 but with this consideration that new susceptible people arrive in that population with rate λ and any individual can leave it with rate μ . It can be a model for studying COVID-19 in a region without travel or mobility restrictions or in a closed population with a birth and death rate γ and μ , respectively. In this scenario, the disease dynamics would be updated as:

$$\begin{aligned} \frac{ds}{dt} &= -\beta si - \mu s + \lambda, \\ \frac{de}{dt} &= \beta si - (\kappa + \mu)e, \\ \frac{di}{dt} &= \kappa e - (\gamma + \mu)i, \\ \frac{dr}{dt} &= \gamma i - \mu r. \end{aligned} \quad (1.18)$$

We can represent the time evolution of this system with vector $\mathbf{x} = (s, e, i, r)$ where x_j represents the fraction of population in the j -th component corresponding to the SEIR order. Now, let $F_j(\mathbf{x})$ represent the rate of appearance of new infections in compartment j , considering only the infections that are newly emerging and excluding terms that depict the movement of infectious individuals between compartments [56, 193, 40]. If V_j^+ is the rate at which individuals move to compartment j through other means, and V_j^- is the rate of leaving the j -th compartment, then the difference $F_j(\mathbf{x}) - V_j(\mathbf{x})$ describes the rate of change, where $V_j(\mathbf{x}) = V_j^-(\mathbf{x}) - V_j^+(\mathbf{x})$.

From here, we can formulate matrices of partial derivatives of F and V such that

$$\begin{aligned} F_{jk} &= \frac{\partial F_j(\mathbf{x}_{\text{eq}})}{\partial x_k}, \quad \text{and} \\ V_{jk} &= \frac{\partial V_j(\mathbf{x}_{\text{eq}})}{\partial x_k}, \end{aligned} \quad (1.19)$$

where $\mathbf{x}_{\text{eq}} = (s_0, e_0, i_0, r_0) = (\lambda/\mu, 0, 0, 0)$ is the disease-free equilibrium. F is a non-negative matrix that represents the infection rates near the equilibrium, and V^{-1} represents the average duration of infectiousness. So, we can write the next-generation matrix as $\mathbf{M} = \mathbf{FV}^{-1}$ [57, 56, 55, 193, 40]. Every element of the next-generation matrix, M_{jk} , gives the rate at which infected individuals in the compartment j produces new infections in

compartment k , times the average period an individual spends in a single visit to compartment j . For this example, we can have:

$$\mathbf{F} = \begin{pmatrix} 0 & \beta s_0 \\ 0 & 0 \end{pmatrix}, \quad \text{and} \quad (1.20)$$

$$\mathbf{V} = \begin{pmatrix} \mu + \kappa & 0 \\ -\kappa & \gamma + \mu \end{pmatrix},$$

and therefore, the basic reproduction number is calculated as

$$R_0 = \rho(\mathbf{M}) = s_0 \frac{\beta \kappa}{(\mu + \kappa)(\mu + \gamma)}. \quad (1.21)$$

With the more challenging situations on the horizon, the next-generation matrix will come in handy. We plan to apply it to diverse situations later on.

1.2.8 Beyond the SIR Model

We can further extend the number of compartments to include more possibilities; for example, one may extend the SEIR model to account for the *waning immunity*. Waning immunity describes the gradual reduction of our body's protective response against disease over time, whether that protection was gained through natural infection or vaccination. As this immunity fades, there's a possibility of becoming susceptible to the disease again. So, the model can be extended to **SEIRS**. This phenomenon is a significant factor in the development and scheduling of vaccines. For certain diseases, periodic booster shots are administered to reinforce the body's immune response and ensure continued protection.

Compartmental models are the building blocks for epidemic modeling, allowing us to capture specific events of interest. However, this approach involves a balance between model complexity and its analytical tractability. With each additional compartment introduced, the model becomes subject to more mathematical constraints and wider implications. Consequently, the more compartments a model contains, the more challenging it becomes to rigorously follow and analyze its outcomes. This reflects the inherent complexity of translating the multifaceted nature of disease spread into a structured, mathematical framework. On the other hand, we eventually want to apply our model to the real world, and when dealing with data, we will face new challenges in inferring the model's parameters. Therefore, anyone who intends to work with more complex models should be concerned that without having enough justifiable data and reasons, it would be hard to shed light on any phenomenon. We are not the type of scientist who doesn't care about Occam's razor [181]; If we have two theories that both explain the observed facts, then we use the simplest until more evidence comes along.

SIR model shows how different factors influence the spread and eventual containment of an epidemic, making it a suitable choice for our analysis of the epidemic threshold and outbreak size, allowing for a comprehensive understanding of epidemic characteristics [207, 50, 2]. While the SEIR model and others offer more detail, especially regarding the latency period of an infection, they do not significantly alter the fundamental dynamics we aim to explore [150]. Therefore, SIR dynamics may sweep some epidemiological details under the rug, yet they can capture broader features of disease dynamics. These dynamics strike an ideal balance between realism and simplicity for epidemic problems we are interested in this work. Therefore, we will continue to use to this model and its different manifestations in the following chapters, leaving room for more complexity from the contact network structure. After all, the SIR model gets the phenomenology – macroscopic behaviors and trends – right, which is the most essential modeling point for a physicist to begin with.

With four parameters I can fit an elephant,
and with five I can make him wiggle his trunk.

John von Neumann in conversation with
Enrico Fermi [65]

1.3 Herd Immunity and Failures of Simple Models

In any population, individuals can acquire immunity to specific infections either through prior exposure to the pathogen, via prophylactic measures like vaccination, or a combination of both [122]. For instance, in Finland and other countries, an annual influenza vaccination initiative is launched at the beginning of autumn. This vaccination offers protection against influenza and shields from its secondary diseases, encompassing ear infections, bronchitis, pneumonia, myocardial infarction, and cerebral circulatory disorders [73]. The ultimate objective is to attain a population-level immunity; if a significant fraction of the population is immunized, it yields collective protection, often referred to as *herd immunity*. We should keep in mind that within each population, certain people either cannot receive the vaccine or opt not to for various reasons. Nevertheless, the principle of herd immunity ensures protection for the broader population, even when a disease has the potential to spread rapidly among the unvaccinated or those previously immune.

1.3.1 Herd Immunity after Vaccination

When vaccinating a population before the infection is introduced, we are trying to modify the basic reproduction number of the upcoming disease dynamics such that $R_0 < 1$ and, consequently, keeping the disease in its sub-critical regime. But how much of a population should we vaccinate to reach herd immunity? Assume a population with no prior immunity that we can protect π_v fraction of them with perfect vaccines. What is the critical mass we need to vaccinate? For policy-makers, it is of vital significance to always estimate how many people they need to vaccinate as they have to assign enough budget for their vaccine campaigns. Moreover, they must not only consider the number of vaccines needed but also adapt their strategies. This includes prioritizing high-incidence regions and simultaneously vaccinating different age groups to effectively mitigate the pandemic's impact. Such dynamic strategies, grounded in scientific modeling, can significantly enhance the effectiveness of vaccine campaigns, especially in diverse and changing pandemic scenarios. Ref [142] evaluates the efficiency of various heuristic strategies for allocating COVID-19 vaccines, comparing them to strategies derived from optimal control theory.

In the paradigmatic SIR model of infectious disease in a fully mixed population, herd immunity is reached when the fraction π_v of the population that is immune to the disease through vaccination or previous infection is larger than

$$\pi_v^c = 1 - \frac{1}{R_0}. \quad (1.22)$$

The argument behind this is simple. According to the SIR model, every infected person will, on average, infect R_0 more people. If we vaccinate π_v fraction of people effectively, $1 - \pi_v$ fraction of people participate in the disease dynamics. Therefore, if $(1 - \pi_v)R_0 < 1$, then we reach herd immunity, and we can find the herd immunity threshold as given by Eq.1.22. Whenever we are referring to disease dynamics in the presence of interventions or not at the early stages of the epidemic, we will use the term *effective* reproduction number R_e instead of the basic reproduction number. In this case, $R_e = (1 - \pi_v)R_0$ and hence we need to keep R_e below one to prevent large outbreaks. Now, picture a scenario with $R_0 = 3$. Then, the herd immunity threshold would be roughly calculated as $1 - 1/3 \approx 70\%$.

However, such a directive, though widespread, may oversimplify the complexities at play. First and foremost, Eq. 1.22 draws the epidemic threshold from the fully-mixed SIR model, which operates on the assumption that all individuals in a population mix uniformly, with interactions being random and uninfluenced by specific attributes, such as their vaccination status. When it comes to the real world, this generalization can be limiting as human–human interactions are far from being random. Moreover, in practice, vaccines never get distributed equally in a population. Think

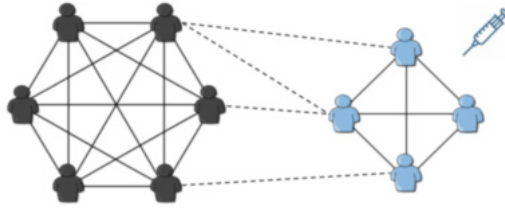


Figure 1.9. Vaccination patterns within a population reveal non-random connections between individuals. Social dynamics often lead to individuals interacting more with those who with the same vaccination status rather than vaccines being distributed uniformly at random across the population. Here, solid lines depict connections within the community, while dashed lines represent links between different communities.

of the correlation between an individual's vaccination status and that of the people they frequently interact with. For example, vaccinated people are more likely to interact with other vaccinated people in the population [31]. This propensity for like to associate with like is what we term as *homophily*. Fig. 1.9 demonstrates a situation with *vaccination homophily*. We use the term vaccination homophily to describe such patterns where interactions are more common within similar vaccination groups than between them. This phenomenon, rooted in the tendency of people with similar socio-demographic and behavioral characteristics to interact, leads to non-uniform vaccine adoption, as demonstrated in [38]. The interaction patterns between vaccinated and non-vaccinated individuals, shaped by homophily, crucially affect disease transmission dynamics. A study in British Columbia, Canada, involving 1 304 respondents, observed clear patterns of vaccine homophily, revealing its substantial role in epidemic growth and infection rates among different vaccination groups under varying conditions of vaccine efficacy [7].

We will later see that in some settings, herd immunity can be easily not achieved. As we show in [Publication I](#), the presence of homophily considerably increases the critical vaccine coverage needed for herd immunity, and strong homophily can push the threshold entirely out of reach. Another artifact of vaccination homophily in our model is that the epidemic size monotonically increases as a function of homophily strength for a perfect vaccine. We will discuss the consequence of vaccination homophily in [Sec. 3.7](#).

1.3.2 Herd Immunity through Natural Infection

As mentioned earlier, herd immunity can be gained through natural infection. For some diseases, recovered people stay immune to future infections. It is worth noting that herd immunity after natural immunity due to previous exposure varies in strength and nature compared to vaccine immunity.

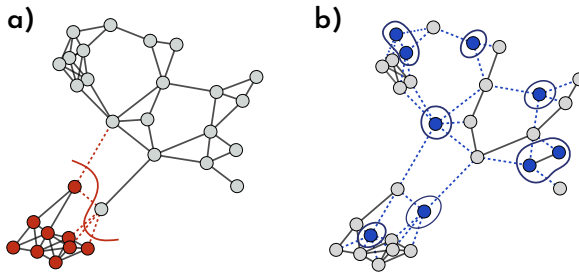


Figure 1.10. How natural immunity is localized in a population. (a) Nodes immunized due to previous exposure(s) shown with color red. The dashed lines and the red solid line indicate the interface between susceptible and immune nodes. (b) The same number of randomly immunized nodes in the same population, this time in blue, resulted in more interfaces.

Empirical observations in network science reveal that the number of connections per individual, known as *degrees*, varies considerably across a population [46, 36]. Such disparities in connectivity patterns highlight a departure from a normal distribution, underscoring the *heterogeneous* nature of real-world networks. When immunity is induced by natural infection, population heterogeneity may lead to a lower herd immunity threshold than expected under homogeneous mixing because the disease spreads among highly interactive individuals, known as *superspreaders*, at the early stage of the epidemic, resulting in more efficient immunization of these influential *hubs* [35]. On the other hand, as we show in [Publication II](#), in addition to degree heterogeneity, the spatial and structural aspects of the population play a significant role here [22]. While an epidemic preferentially infects and removes people with more connections, strengthening the herd immunity effect, it is contiguous and localized in the population, weakening herd immunity. For a visual explanation, see [Fig. 1.10](#). The implications of such localization on herd immunity are yet to be comprehensively explored.

Examining herd immunity within real-world scenarios, characterized by structural nuances like communities, core-periphery constructs, and household dynamics, can offer a deeper understanding of epidemic behavior in actual settings. Such endeavors can bridge the divide between theoretical frameworks and their real-world applications, aiding in formulating effective disease control and prevention strategies. We will delve into these complications in this work. We will see how, and in what ways, various interventions can be effective considering the networked structure of human populations. Meanwhile, you might explore [Ref. \[202\]](#) to get acquainted with the progress in epidemiological modeling, particularly how it incorporates vaccination, individual behaviors, and social structures

into understanding how diseases spread. This reference underscores the transition from simple to more sophisticated models that leverage statistical physics and digital information, shedding light on the complexities of disease transmission and the effects of vaccination. The research wraps up with suggestions for future investigations, making it crucial reading for those focused on disease modeling and public health initiatives.

After many efforts, when names, definitions, observations and other sensory data are brought into contact and compared in depth, one juxtaposed with another, in the course of a scrutiny and an even-tempered but severe examination, at the end a light suddenly comes on, for whatever problem – our understanding, and a clarity of intelligence the effects of which express the limits of human power.

Plato, *Letter VIII* [172]

2. Structured Populations and Networks

Traditional models in epidemiology often do not incorporate the complexity of social connections. As we saw, in the fully mixed populations of Chapter 1, there were no constraints on the interactions between the individuals beyond the characteristics of the disease's spread. In the compartmental models introduced in Sec. 1.2, an infected individual could infect any other susceptible individual which is not a realistic assumption for any physicist interested in modeling the propagation of a property (virus) in a physical system (society).

To better understand disease dynamics in a society, we need to develop realistic models for describing the population in which the epidemic is unfolding. First, we want to respect the *principle of locality* in the sense that people can only interact with their neighbors in some physical vicinity. For airborne diseases, the primary infectious agents are often viruses, bacteria, or fungi. These pathogens can be transmitted via activities such as breathing, talking, coughing, sneezing, and other actions that generate aerosol particles or droplets [4, 9, 127, 200, 85, 67]. Therefore, an airborne transmission can only happen through sharing some medium. Moreover, within a population of N people, the total number of connections between the individuals, L , is usually around the same number as the population size, N . In technical terms, we expect the population to be *sparse* such that the L scales with N , not N^2 , for example, $L = \mathcal{O}(N)$ [132]. From this point on, space graphs will be our primary focus for network analysis, except where explicitly stated otherwise. Another essential feature we expect is that the number of connections, k , varies from person to person, such that the majority of people have almost the same number of connections, except for a few people with very high k , known as *hubs*, or in the context of spreading, *superspreaders* as they can infect much more people than a typical individual.

2.1 Random Graph Theory: Key Concepts and Definitions

With these minimum requirements, we can approximate a human population with a random graph G such that every node v in the graph represents an individual, and a link l between two people represents a connection or a pair-wise interaction between them [194]. An *undirected* graph is a type of graph where links lack direction, indicating bidirectional relationships. Within this framework, a *simple* graph is a specific form of an undirected graph characterized by two key constraints: it contains no loops (links connecting a node to itself) and no parallel links (multiple links between the same pair of vertices). These properties of a simple graph, with its non-repeating and non-self-looping links, make it an ideal model for scenarios like social networks, where edges represent unique and mutual connections between individuals.

The number of connections a node v has is called the *degree* of that node, k_v . The degree distribution p_k and other structural aspects of a network are typically referred to as network *topology*. For a graph with N nodes, and L links, the identity below holds:

$$\sum_{v=1}^N k_v = 2L = N \langle k \rangle, \quad (2.1)$$

where $\langle k \rangle$ is average degree of the nodes,

$$\langle k \rangle = \sum_k k p_k. \quad (2.2)$$

Over the past two decades, numerous random graph models have emerged to represent human populations, primarily within the realm of *Network Science* [151, 64]. These models are largely inspired by graph theory literature [58]. Consequently, we might use the terms "networks" and "graphs" interchangeably moving forward.

Fig. 1.9 displays a network with two distinct groups of nodes, representing vaccinated and unvaccinated *communities*, along with their interconnections. This network is termed a *connected* graph since there exists a *path* between any two nodes. Within the graph, any sequence where each successive pair of nodes is connected by a link is referred to as a *walk*. When this walk avoids revisiting nodes, it's termed a *path*. The length of a walk is determined by counting the number of links in its sequence. Furthermore, the *distance* between two nodes is defined as the length of the shortest path connecting them. The longest shortest path in a network is usually referred to as the *diameter* of a graph. The diameter represents the largest distance between any two connected nodes.

Figure 2.1 shows a *disconnected* network, as you can find a pair of nodes such that there is no path between them. Whenever there is no path between two nodes, we say that they are *infinitely* far from each other. The

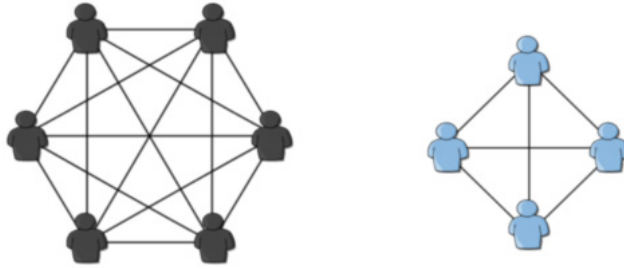


Figure 2.1. A disconnected network comprising two components: the larger left subset represents the giant component (GC) formed as a 6-clique, while the smaller right subset illustrates a 4-clique.

communities of the network in Fig. 2.1 are completely disconnected. A *subgraph* is a graph formed from a subset of the nodes and links of the original graph. A connected subgraph that is not part of any larger connected subgraph is called a *component*, and its size will be reported as the number of nodes it includes. Components can be used to partition a graph. We name the largest connected component of a graph as the *giant component*, [151, 29]. Typically, real-world networks feature a dominant giant component covering a significant portion of the entire network, wherein the majority of nodes are part of this component. A giant component's significance is underscored when its size is proportional to the overall network size. This scaling feature is integral to network infrastructure functionality. For instance, the internet's operational efficiency hinges on this network characteristic, and the rapid spread of infectious diseases can be attributed to the infection of the giant component in social networks.

In Fig. 2.1, we can see that each component has a very regular structure as every node is connected to any other node. We call such a structure a *complete graph*. Any subset of a graph that can be considered as an *induced* subgraph forming a complete graph with c nodes is called a c -clique. *Cliques* are very good candidates for representing groups in social networks. We will use them in our modeling in [Publication III](#).

In a complete graph, every pair of neighbors of a node u is connected, making the graph maximally clustered. Generally, the amount of clustering, or *transitivity*, is typically measured by counting the number of closed loops. If a path uvw forms a loop of size three, we say the path is *closed* and nodes u , v , and w form a *closed triad* or triangle, as opposed to a *triple* that misses one of the edges of the triangle [203]. To address the level of transitivity of a network, we can define the *clustering coefficient* C of a network [151] as the ratio of the number of triangles Δ to the number of connected triples Λ

$$C = \frac{3\Delta}{\Lambda}, \quad (2.3)$$

where factor 3 counts for the different ways we can count paths of length two and three. This is a global property of a network, which can also be calculated by averaging the local clustering coefficient of all the nodes. We can define [204] a local clustering coefficient for a node u , C_u , as the number of connected pairs of neighbors of u over the number of pairs of neighbors of u . C_u represents the average probability that a pair of u 's friends are friends of one another. Following Watts and Strogatz [204], we can also define the clustering coefficient for the network as the average of the local clustering coefficients for each node, $C_{\text{WS}} = \langle C_u \rangle$.

We can represent the connections in a network through the *adjacency matrix* \mathbf{A} such that $A_{uv} = 1$ when node u is connected to node v and $A_{uv} = 0$ otherwise. So, the matrix representation of the graph in Fig. 2.1 would be:

$$\mathbf{A} = \left(\begin{array}{cccccc|cccc} 0 & 1 & 1 & 1 & 1 & 1 & & & & & \\ 1 & 0 & 1 & 1 & 1 & 1 & & & & & \\ 1 & 1 & 0 & 1 & 1 & 1 & & & & & \\ 1 & 1 & 1 & 0 & 1 & 1 & & & & & \\ 1 & 1 & 1 & 1 & 0 & 1 & & & & & \\ 1 & 1 & 1 & 1 & 1 & 0 & & & & & \\ \hline & & & & & & 0 & 1 & 1 & 1 & \\ & & & & & & 1 & 0 & 1 & 1 & \\ & & & & & & 1 & 1 & 0 & 1 & \\ & & & & & & 1 & 1 & 1 & 0 & \end{array} \right) \quad (2.4)$$

where we have rearranged the rows and columns to show the block nature of the adjacency matrix for a network that has two components. \mathbf{A} is a symmetric matrix, $A_{uv} = A_{vu}$ as we are not imposing any direction on the links in the network. The diagonal elements are also zero, $A_{uu} = 0$, as the network has no self-loop and it is a *simple* graph. A simple graph is a graph with no self-loops, and it does not have more than one link between any two nodes. The degree of node u can be calculated by summing over the specific rows or columns of matrix \mathbf{A} such that $k_u = \sum_v A_{uv}$. The matrix representation of the graph serves as a gateway to the intriguing world of algebra with its fascinating machinery.

With these terms defined and agreed upon, we can now explore random graph models and what they offer.

2.2 Erdős–Rényi Networks

We begin with the simplest model that people usually refer to as *the* random graph, known as the *Erdős–Rényi* (ER) model [151], and will go through more detailed models later. Imagine we want to build a network

G with N nodes such that L distinct pairs of them are uniformly chosen at random and get connected. We will refer to this model as $G(N, L)$ [68]. We can do better and define the model as an ensemble of networks [151], such that the model $G(N, L)$ is the probability distribution $P(G)$ over all simple networks G with

$$P(G) = \frac{1}{\binom{N}{2}^L}, \quad (2.5)$$

as we are choosing L links from the $\binom{N}{2}$ possibilities. When we analyze property f of random graphs (like the number of connections each node has or how many steps it takes to get from one node to another), we are actually looking at the average of these properties across many different graphs generated by the same random model [151]. Since each graph produced by this process can be different, we focus on the average value in the ensemble of these graphs rather than on the specifics of any single graph. This approach helps us understand the general behavior of random graphs as a whole. Therefore, any property of random graphs, $f(G)$, is the average property of the ensemble [151]. The term *ensemble* comes from the community of physics. So, the ensemble average of a property f would be written as:

$$\langle f \rangle = \sum_G f(G)P(G). \quad (2.6)$$

For mathematical convenience in calculating the average values using Eq. 2.6, it would be better to use a slightly different mathematical definition than the one with a fixed number of links L given by Eq. 2.5 [188]. Instead, we connect every uniformly selected pair of nodes at random with independent probability p [151]. This will enable us to write Eq. 2.5 as

$$P(G) = p^L (1-p)^{\binom{N}{2}-L}. \quad (2.7)$$

We name this model $G(N, p)$. It is straightforward now to show [151] that the expected number of links in such an ensemble is:

$$\langle L \rangle = p \binom{N}{2} \simeq pN^2. \quad (2.8)$$

Moreover, the degree distribution, p_k , of a random graph made with $G(N, p)$ model follows a binomial distribution [151] as:

$$p_k = \binom{N-1}{2} p^k (1-p)^{N-1-k}. \quad (2.9)$$

For large enough network sizes, Eq. 2.9 can be approximated with a Poisson distribution. Therefore, in the thermodynamic limit, an ER network possesses a Poisson degree distribution with mean $\langle k \rangle$, such that

$$p_k = e^{-\langle k \rangle} \frac{\langle k \rangle^k}{k!}. \quad (2.10)$$

Due to the Poisson degree distribution, some scholars call this model *Poisson random graph* [151].

We can use this equation and find the average degree $\langle k \rangle$ in a network generated with this model as:

$$\langle k \rangle = \left\langle \frac{2L}{N} \right\rangle = \frac{2}{N} \langle L \rangle = p(N-1) \simeq pN, \quad (2.11)$$

as the mean degree in a network with L links is $2L/N$. The factor 2 is responsible for the contribution of the link in the degree of two nodes.

2.2.1 Emergence of the Giant Component

An interesting property of ER networks is how their giant component size changes as we vary p [29]. We will later in Sec. 2.8, [Publication III](#) and [IV](#) discuss how the size of the giant component will be related to evaluating the final outbreak size in an epidemic spreading on a network. Now, assume the probability that a node is not in the giant component is given by ϕ . This probability also represents the relative size of the giant component as $\Sigma = 1 - \phi$. A node u belongs to the giant component if all of its neighbors are connected to the giant component. Therefore, the probability that node u is not connected to the giant component via a neighbor v is $1 - p + p\phi$ [151]. Simply, $1 - p$ accounts for the probability of not connecting to node v , and $p\phi$ is the probability of the link between u and v existing but not leading to the giant component. Therefore, the total probability of not being connected to the giant component via any of the $N - 1$ other nodes in a large network can be written [151] as a self-consistent equation below

$$\phi = (1 - p + p\phi)^{N-1}. \quad (2.12)$$

We can rearrange the terms in this equation, use an approximation in the thermodynamic limit, and find that

$$\phi = \exp(-\langle k \rangle (1 - \phi)). \quad (2.13)$$

Eliminating ϕ in favor of the size of the giant component gives us

$$\Sigma = 1 - e^{-\langle k \rangle \Sigma}. \quad (2.14)$$

There is no closed-form solution for this equation, but we know that $\Sigma = 0$ is a stable solution when $\langle k \rangle < 1$. In cases where the *branching factor*, $\langle k \rangle$, is less than one, there is an exponential decay in this branching process [10], leading to its swift termination. When $\langle k \rangle > 1$, every node is, on average, connected to more than one other node, leading to a chain of connections. Therefore, we expect the size of the largest component to undergo a phase transition from constant size to extensive size at $\langle k \rangle = 1$. We can also show that in the thermodynamic limit, only one component spans the entire network in the super-critical regime [151].

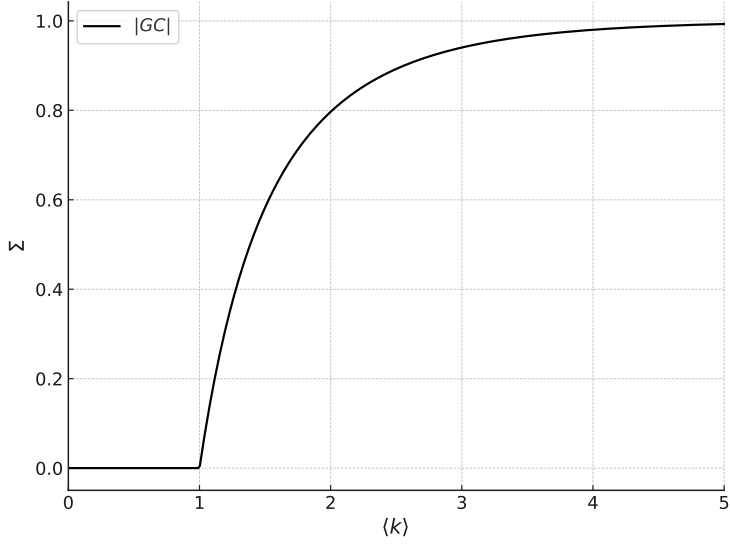


Figure 2.2. Phase transition in an ER network from disconnected to connected regime with an extensive giant component.

Figure 2.2 captures such a phase transition. Following Eq. 2.11, this transition happens at the critical writing probability $p_c = 1/N$. Interestingly, Eq. 2.14 has the same form as Eq. 1.6, and it manifests the same type of phase transitions as depicted in Fig. 1.7.

We will use similar but more detailed and complicated arguments in all our publications to find the size of the giant component of a random graph under different conditions. Alternatively, we can show that the average size of the small components, any component other than the giant, vanishes in the super-critical regime as the average degree or p increases. The average size of a small component to which a randomly chosen node in an ER network belongs can be derived [151] as:

$$\sigma = \frac{1}{1 - \langle k \rangle + \langle k \rangle \Sigma}. \quad (2.15)$$

When $\langle k \rangle < 1$ and there is no giant component, this equation leads to $(1 - \langle k \rangle)^{-1}$ which diverges at the critical point. In the super-critical regime where $\langle k \rangle > 1$, we must solve for Σ and then evaluate σ . Fig. 2.3 depicts the behavior of the average size of small components in an ER network.

From the point of view of Critical Phenomena [183], we can think about σ as the *singular* property at the phase transition point. σ 's behavior is analogous to *susceptibility* χ in the field of critical phenomena, which measures the response magnitude generated by a small external field disturbance [63]. In our case, a small external field disturbance can be adding a link uniformly at random in the network and measuring how the average size of its giant component changes. Even adding a single link

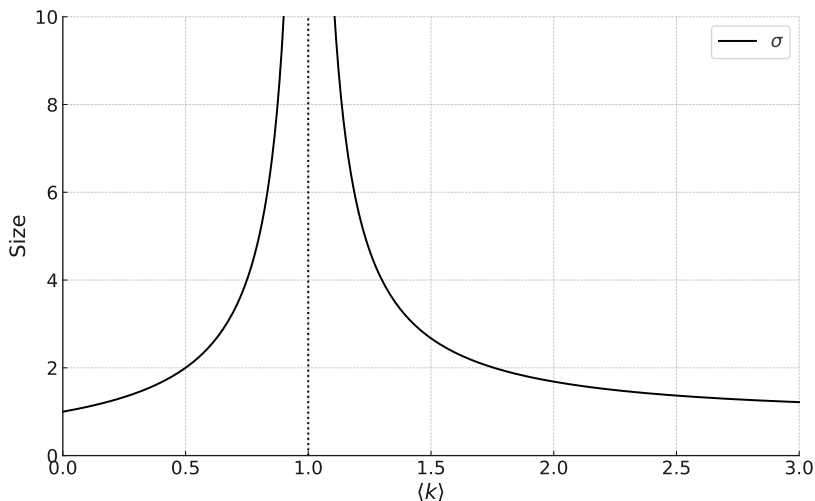


Figure 2.3. Average size of the small components in an ER network. The average size σ of the component to which a randomly chosen node in a small component belongs using Eq. 2.15.

can dramatically change the component average sizes at the critical point. Using the ER model, if we generate an ensemble of random graphs and look at the ensemble average of the giant component sizes, it will follow Eq. 2.14, and the fluctuations around this mean value would diverge at the critical point. Therefore, if we run a set of simulations and measure the coefficient of variation of the giant component sizes, the ratio of the standard deviation of giant component sizes to their ensemble average would behave the same as σ around the critical point.

2.2.2 Shortcomings of ER Networks in Modeling Contact Networks

We will examine in this section the limitations of the ER network in accurately modeling contact networks.

An ER network $G(N, p)$ comes with a single tuning parameter p . So, any property of a random graph of this ensemble depends on the *wiring probability* p . For example, the clustering coefficient of an ER network is

$$C = \frac{\langle k \rangle}{N-1} = p, \quad (2.16)$$

as the probability that any two nodes are neighbors is exactly the same across the network [151]. We can traverse the ER networks without spending much time going from one node to another. In technical words, the diameter of ER networks grows logarithmically with the network's size

[28, 151], such that

$$D = \frac{\ln N}{\ln \langle k \rangle}. \quad (2.17)$$

An intuitive way to understand the logarithmic growth of the diameter is that since the clustering of an ER network is given by p , the network can be approximated as a *tree*, a connected acyclic undirected graph that branches with $\langle k \rangle$. Therefore, in D steps, it should statistically cover all the N nodes such that $N = 1 + \langle k \rangle + \langle k \rangle^2 + \dots + \langle k \rangle^D$. In the thermodynamic limit and when $\langle k \rangle > 1$, the dominant term in this series will be the last one, so $N \simeq \langle k \rangle^D$ which leads to Eq. 2.17. This result always holds even though we used a very crude approximation here. This *tree-like assumption* is a useful trick that allows us to ignore loops when we are calculating some network property locally [139].

ER networks come with a Poisson degree distribution, short (logarithmic) diameter, and low clustering. It is an improvement upon the fully-mixed population that is far from reality. By controlling p , we can always have a sparse network with a giant component, which is a necessary condition for the functionality of many networked systems. However, the implicit low clustering of this model makes it unrealistic to model social networks that exhibit transitivity, especially in the form of *triadic closure*, a tendency for two individuals with a mutual acquaintance to become connected themselves.

Sparse network candidates with high clustering can be the d -dimensional lattices that Condensed Matter physicists have used for decades to describe crystal structures. However, these networks usually possess so many symmetries or regularities that make them over-structured for us. Moreover, the diameter of a d -dimensional lattice scales algebraically with the space dimension as $N^{1/d}$, while we prefer shortcuts and logarithmically scaled diameter networks. Despite this, if we shuffle enough links in a lattice, we can add some randomness to make some long-range connections, making the diameter shorter while preserving the local structure to a reasonable extent. A random network with high clustering in which its diameter scales as $\ln N$ is called a *small-world* network. The celebrated Watts–Strogatz model features these rewirings and produces a small-world random graph [204].

The friendship paradox, first introduced by Feld (1991) [72], highlights a common reality in social networks where your friends are likely to have more friends than you. This concept is not only limited to the number of friends; it also applies to many other characteristics where your friends, on average, rank higher than you [66]. For example, your friends have more enemies than you do on average. If we uniformly at random sample nodes and count the links connected to them, we get an estimate over the average degree of a network. Suppose we sample links uniformly at random instead, follow them to one of their ends and look at the degree of

that node excluding the link we just came from. In that case, we will get an estimate over a network's average *excess degree* $\langle q \rangle$ [151]. In mathematical terms, the friendship paradox states that social networks have a larger average excess degree than an average degree.

The Erdős–Rényi (ER) networks with Poisson degree distributions fall short in regards to the “friendship paradox” primarily because of the uniformity of their connectivity. This uniformity means that ER networks lack the necessary variance in the number of connections to model the friendship paradox effectively, which is more accurately represented in networks with skewed degree distributions, such as scale-free networks [98].

As we will see in the next section, given the degree distribution p_k of a network that locally looks like a tree, the average excess degree can be derived from Eq. 2.23 in terms of the first and the second moments of the degree distribution such that

$$\langle q \rangle = \frac{\langle k^2 \rangle}{\langle k \rangle} - 1, \quad (2.18)$$

where $\langle k^m \rangle = \sum_k k^m p_k$ is the m -th moment of the degree distribution.

ER networks have a Poisson degree distribution, and consequently, the variance and mean of degrees are equal. So, $\langle k^2 \rangle = \langle k \rangle + \langle k \rangle^2$. Substituting this into Eq. 2.18 yields

$$\langle q \rangle = \langle k \rangle. \quad (2.19)$$

Therefore, in an ER network, your friends have the same number of friends as you. Sometimes ER networks are referred to as *homogeneous* random networks as degrees are highly centered around the mean value, and there is no chance of strong degree heterogeneity.

We are interested in models with large but finite variances in their degrees to better approximate the social networks. In practice, the degree distribution of networks should allow for the possibility of having nodes with high degrees. In ER models, the tail of the distribution falls dramatically and leaves no chance for the emergence of hubs. The next section shows that the configuration model network allows us to create a network with whatever distribution we want.

2.3 The Configuration Model

In this section, we explore the configuration model, an important tool in network science for constructing random networks. Unlike the ER model, the configuration model allows for more realistic representations of social networks by using a prescribed degree sequence. Each network created through this model is uniquely tailored based on its specific degree sequence, which dictates the number of connections each node should have.

This approach allows for flexible network structures, including uneven distributions of connections, providing a more accurate reflection of social network patterns than the homogenous ER model.

For a valid degree sequence represented by k_1, k_2, \dots, k_N , when each of the N nodes has k_u stubs, a configuration model network can be constructed by connecting pairs of stubs uniformly at random [75]. In a configuration model network, the total probability of a connection between a pair of nodes u and v will be

$$p_{uv} = \frac{k_u k_v}{2L}, \quad (2.20)$$

where $2L = \sum_u k_u$ [151]. In the configuration model, while self-loops or multi-links might occur, their number becomes negligible in the thermodynamic limit where $N \rightarrow \infty$, especially when dealing with a degree sequence that ensures a finite average degree. If the variance of the degree sequence is finite, the infinitely large network that emerges from this model tends to be a simple graph without self-loops or multiple links between the same nodes. We can show the expected density of self-loops that may pop up in the network vanishes as $N \rightarrow \infty$ since

$$\frac{1}{N} \sum_u p_{uu} = \frac{1}{N} \sum_u \frac{k_u(k_u - 1)}{4L} = \frac{1}{N} \frac{\langle k^2 \rangle - \langle k \rangle}{2\langle k \rangle}. \quad (2.21)$$

The adjustment for p_{uu} is because the probability of a self-loop from node u to itself is $k_u(k_u - 1)/4L$.

The expected number of common neighbors of node u and v , as a noteworthy characteristic, can be given as

$$n_{uv} = p_{uv} \frac{\langle k^2 \rangle - \langle k \rangle}{\langle k \rangle} = p_{uv} \langle q \rangle. \quad (2.22)$$

The last identity follows Eq. 2.18 for the average excess degree. Note that the excess degree distribution plays an important role in many calculations and can be derived as

$$Q_k = \frac{1}{\langle k \rangle} (k + 1) p_k, \quad (2.23)$$

where $\langle k \rangle$ is averaged over the degree distribution p_k [151].

We can now calculate the clustering coefficient [151] in a configuration network model as

$$C = \sum_{k_u, k_v=0}^{\infty} Q_{k_u} Q_{k_v} p_{uv} = \frac{1}{N} \frac{[\langle k^2 \rangle - \langle k \rangle]^2}{\langle k \rangle^3}. \quad (2.24)$$

Configuration model networks, the same as ER networks, have vanishingly small clustering in the thermodynamic limit, making them locally tree-like networks.

There are different versions of the configuration model with fewer constraints [194]. In various contexts, the term *soft* configuration model

is used to denote variants of the configuration model with relaxed constraints [157, 195]. For example, the Chung-Lu model [44, 45] is a soft configuration model which, instead of building a graph that satisfies a specific degree sequence, generates a random graph with given expected degrees $\bar{k}_1, \bar{k}_2, \dots, \bar{k}_N$. The Chung-Lu model is prized for its ability to replicate complex network structures found in the real world, thanks to its accommodating of arbitrary degree distributions. It turns out that the link probability between node u and v in this variant will be the same as Eq. 2.20 with the expected values replaced. From now on, whenever we say a configuration model, we mean a soft version, specifically the Chung and Lu variant [44].

If we sample the expected degrees from a Poisson distribution, we will recover an ER network [61]. For more realistic modeling, specifically in modeling the contact network for disease spreading, we can use a negative binomial distribution as we can control its variance and produce a heavier tail [154]. This flexibility allows for generating random networks with more degree heterogeneity.

2.3.1 Existence of the Giant Component

The configuration model has a giant component if and only if $\langle q \rangle > 1$ [151] or in terms of moments of the degree distribution, if and only if

$$\langle k^2 \rangle - \langle k \rangle > 0. \quad (2.25)$$

This is known as the Molloy and Reed condition [143, 103]. When there is a giant component, starting from a typical node in a configuration model network, we can expect to have N_d d -order neighbors [151], given as

$$N_d = \langle q \rangle^{d-1} \langle k \rangle. \quad (2.26)$$

2.3.2 Size of Giant Component and Generating Functions

We can find the size of the giant component, if any, similar to how we argued for the ER model in Sec. 2.2.1 [151]. We begin from some node and follow one of its neighbors. Assume the probability that the neighbor is not in the giant component is ϕ . A node does not belong to the giant component when its k neighbors are not, which happens with probability ϕ^k . So, the size of the giant component would be given by

$$\Sigma = 1 - \langle \phi^k \rangle, \quad (2.27)$$

where we have averaged ϕ^k over the entire network with degree distribution p_k . It is common to name $\langle \phi^k \rangle$ as $g_0(\phi)$ where the function g_0 is called the *probability generating function* for the probability distribution

p_k [151];

$$g_0(\phi) = \sum_k p_k \phi^k = \langle \phi^k \rangle. \quad (2.28)$$

The probability ϕ was introduced for a neighbor node rather than a randomly chosen node. Therefore, its degree follows the excess degree distribution. We can write a self-consistent equation for ϕ as

$$\phi = \langle \phi^k \rangle_Q, \quad (2.29)$$

such that

$$g_1(\phi) = \sum_k Q_k \phi^k = \langle \phi^k \rangle_Q, \quad (2.30)$$

where we have averaged ϕ^k over the excess degree distribution Q_k and g_1 is the probability generating function of Q . Given the degree distribution p_k of a network, we can calculate g_0 and consequently, using Eq. 2.23, g_1 can be written as

$$g_1(\phi) = \frac{1}{\langle k \rangle} g'_0(\phi), \quad (2.31)$$

where g'_0 is the first derivative of g_0 with respect to its argument [151]. When evaluated at 1, g'_0 would give the average degree

$$g'_0(1) = \langle k \rangle, \quad (2.32)$$

leading to

$$g_1(\phi) = \frac{g'_0(\phi)}{g'_0(1)}. \quad (2.33)$$

When there is no giant component, the average size of the component a node belongs to would be specified entirely by the first and second moments of the degree distribution. With some algebra, we can show that

$$\sigma = 1 + \frac{g'_0(1)}{1 - g'_1(1)} = 1 + \frac{\langle k \rangle^2}{2\langle k \rangle + \langle k^2 \rangle} \quad (2.34)$$

where we have used Eq. 2.18 for the evaluating $g'_1(1)$. The good news is that the expected small component size, unlike the giant component size, can be evaluated without calculating any generating functions.

The diameter of a configuration model network would also scale logarithmically with the size of the network [44] such that

$$D = \frac{\ln N}{\ln \langle q \rangle} + \text{constant}. \quad (2.35)$$

2.4 Random Graph Models For Networks with Group Structure

Random graph models for networks with groups play a pivotal role in modeling epidemic diseases. These models effectively capture the complexity of

social interactions and the dynamics of disease spread within and between different groups in a population. By incorporating group structures, these models offer a more nuanced understanding of how diseases propagate through networks, accounting for variables like contact patterns, group sizes, and connectivity. This enhanced realism is crucial for predicting outbreaks, assessing the impact of interventions, and informing public health policies. In the following sections, we will delve into specific models that provide us with detailed group structures, further elucidating their significance in epidemiological modeling and disease control strategies.

2.4.1 Bipartite Network

Most social networks contain groups of densely connected subgraphs. One way to model them is to use a bipartite network model, also known as a two-mode or bi-modal network, which represents a type of graph where nodes are divided into two distinct sets, and links only exist between nodes of different sets. In other words, there are no links between nodes within the same set. This structure is useful in modeling systems where relationships occur only between distinct categories. Common examples of bipartite networks include author-paper relationships in academic databases (where authors are in one set and papers in another, and links indicate authorship) or customer-product purchase histories in market research (where customers are in one set, products in another, and links indicate a purchase). The bipartite nature of these networks offers unique analytical challenges and opportunities, distinct from traditional one-mode networks. We will utilize a refined version of the bipartite network model as outlined in [Publication III](#). This model distinctively categorizes one set of nodes as individuals and another set as the groups to which these individuals are affiliated. By projecting this network model, we aim to intricately map the complex interactions between individuals and their respective groups.

2.4.2 Random Clique Networks

In studying epidemic processes, cliques are commonly used to represent social groups within contact networks. Within social networks, c -cliques are complete subgraphs indicating a group of c people who are all interconnected and can potentially infect one another. These structures have been identified in real-world social networks, challenging the standard tree-like assumption often applied in epidemic studies [192, 166, 209]. These networks can be constructed by dividing a graph into two sections: node groups and clique groups. Since it's a bipartite structure, connections only form between these groups. In the thermodynamic limit, the unipartite projection of this graph forms a contact network with a negligible number of self-loops or multi-links. See [205, 29] for further details on these net-

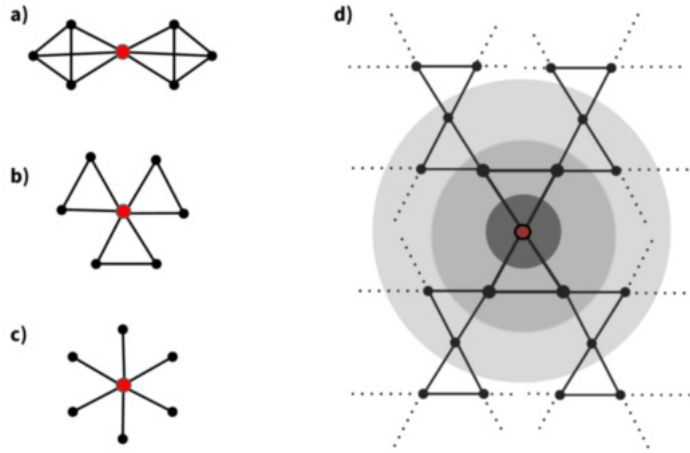


Figure 2.4. Schematic of 6-regular c -clique networks from [Publication III](#). Panels (a-c) illustrate the neighborhoods of a (highlighted) node within networks of 4, 3, and 2-cliques, respectively. These configurations recur around each node in the random network with cliques. Panel (d) depicts a segment of the broader neighborhood in a 3-clique network, highlighting an expanded area around the panel. It's notable that each node possesses a degree of 4, with only a portion of the node connections being displayed. Such a pattern is typical in a large clique network.

work structures. Consequently, every c -clique adds $c - 1$ links to a node's degree. As [Fig. 2.4](#) shows, in cases where $c = 2$, the model reduces to a *random regular graph*. A *regular graph* is a graph where each node has the same number of neighbors. We will use these types of structures in [Publication III](#).

2.4.3 Stochastic Block Models

As we transition from examining small, closely-knit groups in network models, our focus shifts to encompassing substantially larger groups that cover a significant portion of the entire network [108]. This shift in scale necessitates a more versatile modeling approach, which is where the Stochastic Block Model (SBM) [95, 125] becomes particularly valuable. Unlike smaller groups that are typically densely connected, larger blocks in a network can exhibit a broader range of connectivity patterns. The SBM's flexibility in modeling these large, complex structures makes it an ideal choice, not only for our study but also for a wide array of applications. The SBM has demonstrated its versatility in various fields, including federated learning [104, 180], graph clustering [125], social network analysis [94], and community detection [1, 160].

Now, consider [Eq. 2.4](#), which presents an adjacency matrix for a network comprising two distinct communities, as shown in [Fig. 2.1](#). A *community*

in this context refers to a group of nodes that share similar connection patterns with other groups. The structure of matrix Eq. 2.4 is meticulously arranged to accentuate the block configuration of the graph, thereby illuminating regions of high density (indicative of strong intra-community ties) and areas of sparsity (reflecting weaker or non-existent inter-community connections).

In general, when constructing a network with B communities using the SBM, nodes are allocated into blocks such that $b_u \in \{1, \dots, B\}$ signifies the community or block to which node u is assigned. This model allows for the application of probabilistic rules governing the likelihood of connections both within and across these communities. For instance, in the stark scenario depicted by Fig. 2.1, nodes within a single community are completely interconnected with a probability of $p = 1$, while there are no inter-community links. Conversely, in scenarios like the one illustrated in Fig. 1.9, there is a non-zero probability for the formation of links between different communities, demonstrating the SBM's adaptability to various network configurations.

Quantitatively, the number of links between two blocks r and s (or within a single block) can be expressed as:

$$e_{rs}(G) = \sum_{u < v} A_{uv} \delta_{b_u, r} \delta_{b_v, s}, \quad (2.36)$$

where A_{uv} represents the adjacency matrix, and $\delta_{\cdot, \cdot}$ is the Kronecker delta function ensuring that nodes u and v belong to blocks r and s respectively. The ensemble of graphs generated by the SBM is, in essence, the maximum entropy ensemble [157], where the expected values of these link numbers conform to specified values, allowing for a broad range of network structures.

2.4.4 Networks with Homophily

Figure 1.9 illustrates the phenomenon of homophily regarding vaccination status within a community. Let us now discuss a particular version of block models that emphasizes the higher probability of connections within two groups than between them. This idea is, of course, consistent with the Stochastic Block Model (SBM) framework.

Consider a population where a fraction π_v is vaccinated, and the remainder, $\pi_u = 1 - \pi_v$, is not. This scenario examines the propensity of individuals with the same vaccination status to connect. Specifically, π_{vv} denotes the probability of a vaccinated individual connecting with another vaccinated person, while π_{uu} represents the same for unvaccinated individuals. Crucially, these probabilities are not independent but are influenced by the overall vaccination rate, π_v . To model this network, we need only establish π_{vv} , as the remaining probabilities can be inferred: $\pi_{vu} = 1 - \pi_{vv}$, $\pi_{uv} = \frac{\pi_v}{1 - \pi_v}(1 - \pi_{vv})$, and $\pi_{uu} = \frac{1 - \pi_v - \pi_v(1 - \pi_{vv})}{1 - \pi_v}$. The second equation, in par-

ticular, balances the links from vaccinated to unvaccinated individuals, conforming to $\pi_v N \pi_{vu} \langle k \rangle = (1 - \pi_v) N \pi_{uv} \langle k \rangle$. For more details, see [Publication I](#) and [Publication IV](#).

Using these connection probabilities, we can use the Coleman homophily index [49], originally proposed for social network analysis and defined by

$$h = \frac{\pi_{vv} - \pi_v}{1 - \pi_v} = \frac{\pi_{uu} - \pi_u}{1 - \pi_u}, \quad (2.37)$$

to determine the level of homophily in the network. This index provides a consistent measure of homophily across varying π_v values. The index has three key properties: it increases with both π_{vv} and π_{uu} , is symmetrical for vaccinated and unvaccinated groups, and ranges from 0 (no homophily) to 1 (complete homophily). Negative values suggest heterophilic networks based on vaccination status. Note that the connection probabilities $\pi_{vv} = \pi_v + \pi_u h$ and $\pi_{uu} = \pi_u + \pi_v h$ must be positive, and therefore, the Coleman homophily index is bounded from below as $h \geq \max(-\pi_v/\pi_u, -\pi_u/\pi_v)$. We will use networks with homophily in [Publication I](#) and [Publication IV](#).

2.5 Spatial Random Graphs

Spatial networks are crucial for modeling disease spread because they incorporate the essential element of space into network structures [21, 22]. In real-world scenarios, like transportation, social contact, and mobility networks, space plays a significant role in influencing how nodes (individuals or locations) interact. The cost associated with the length of connections (links) in these networks directly impacts their topological structure. This spatial dimension is critical in understanding how diseases propagate, as it affects various dynamics like contact frequency, mobility patterns, and connectivity, all of which are key factors in the spread of diseases. Understanding the spatial constraints of networks, therefore, provides valuable insights into disease transmission and informs effective strategies for managing epidemics [87, 74]. The most basic forms of spatial networks can be exemplified by lattices or random geometric graphs. In these structures, nodes are uniformly and randomly placed across a two-dimensional area, and connections are formed between nodes if their Euclidean distance is less than a specified radius.

2.5.1 Random Geometric Graphs

Random Geometric Graphs (RGGs) represent a specific spatial graph type wherein nodes are randomly distributed within a defined space [162]. Connections between nodes are established based on spatial proximity, specifically if they fall within a predetermined distance or radius from each other. This model is particularly adept at representing networks

where spatial closeness dictates connectivity [6]. Unlike certain networks from the configuration model family, such as random regular graphs and Erdős–Rényi (ER) networks, which lack a defined spatial organization, RGGs, similar to lattices, exhibit a more systematic arrangement. These graphs are characterized by a higher degree of spatial embeddedness, reflecting the inherent spatiality in their structure. This contrast highlights the diverse ways networks can be structured, ranging from completely random to highly spatially oriented configurations.

2.6 Lattices

Lattices are a type of spatial network where nodes are arranged in a regular, repeating pattern, often resembling a grid. Unlike random geometric graphs where nodes are placed randomly, lattices have a structured and predictable layout. Each node in a lattice is typically connected to its nearest neighbors based on the lattice structure, which can vary (e.g., square, hexagonal, triangular) [5]. Lattices are used in various scientific fields, including physics, for modeling phenomena in a structured yet simplified environment [23]. They are particularly useful in studying spatial relationships and processes in a controlled, orderly framework.

2.7 Temporal Networks

So far, our discussion has centered on complex networks that do not change or evolve over time. We use temporal frameworks in [Publication V](#), [VI](#) and [Ref. \[177\]](#). In other publications, we use static complex networks. Static network models struggle to encapsulate time-dependent properties observed in many systems [97, 144, 110, 71, 33, 131, 170, 11, 178]. In models like the ER network, a node’s number of neighbors might differ from other nodes, but it stays constant over time. To accurately represent the dynamics of/on social networks, we should take into account not just topological heterogeneities but also those that occur over time. Empirical observations challenge the common assumption that entities in static network models interact consistently. Many real-world systems, ranging from human behavior to natural phenomena, display bursts of high activity followed by inactivity periods [109, 18, 43, 82, 52, 25, 16, 51]. To address these limitations, time-dependent systems have been depicted as layers of static networks, sometimes termed snapshot graph sequences, each capturing behavior within a specific time window [117, 100, 77, 32, 186, 15, 210]. The core concept of temporal networks enhances static models by retaining temporal information about network interactions. In these models, an event signifies a single interaction instance between two nodes. These

interactions can be instantaneous or can span a duration. Figure 2.5(a) illustrates the temporal network using a time-line visualization. In this representation, individual nodes are depicted as horizontal dashed lines and events as vertical line segments joining two interacting nodes.

A temporal network is mathematically represented as $G = (\mathcal{V}, \mathcal{E}, \mathcal{T})$, where \mathcal{V} denotes the set of nodes, \mathcal{E} the set of events, and \mathcal{T} the time window. Each event e in \mathcal{E} is defined as $e = (\mathbf{u}, \mathbf{v}, t_{\text{start}}, t_{\text{end}})$, with t_{start} and t_{end} indicating the start and end times of an interaction. The network encapsulates dynamic interactions between entities over time. Temporal networks can be further conceptualized as an event graph $D = (\mathcal{E}, E_D, \Delta t(e, e'))$, where nodes are events and edges represent time differences between events. Adjacent events share a common node and are sequenced in time. Therefore, the event graph [137, 138, 118, 179, 101] encapsulates the full set of paths in the network, making it easier to study reachability and other properties.

In temporal networks, unlike static ones, connections are not inherently transitive. For instance, if node i connects to j , and j to k , this doesn't automatically ensure an effect from i can reach k unless the timings of these connections align sequentially. *Temporal adjacency* is defined where events e and e' are adjacent if $\mathbf{v} \cap \mathbf{u}' \neq \emptyset$ and $t'_{\text{start}} > t_{\text{end}}$, allowing the formation of *time-respecting paths*. This dependency on time and node specifics leads to the concept of temporal clusters or components distinct from those in static networks. Temporal network *reachability* requires nuanced analytical approaches. The concept of limited waiting-time reachability, or restless reachability, adds temporal constraints to paths, defining δt -adjacency based on a maximum time δt between events. This approach models various processes, including the SIS process, in a temporal network framework. For more details, see Publication V, VI, and Ref. [177].

The event graph representation encapsulates all time-respecting paths [121]. This approach facilitates the application of static network analysis methods to the structural study of temporal networks. Every path in the event graph, aligning with a time-respecting path in the temporal network, reveals the range of vertices and times they are accessible from a starting event, considering temporal adjacency. Therefore, the out-components in the event graph represent the spread or reachability from an initial event. Conversely, the in-components illustrate which events can reach a particular vertex, essentially mapping the influence or reachability to that event. This approach allows for a detailed understanding of how effects propagate and interact within a temporal network.

It is worth noting that to determine the out-component of a single event node, a straightforward breadth-first search (BFS) suffices. However, the task becomes more computationally expensive if we aim to grasp broader reachability patterns in temporal networks, such as how the reachability cluster evolves on average across multiple start points. One could sample

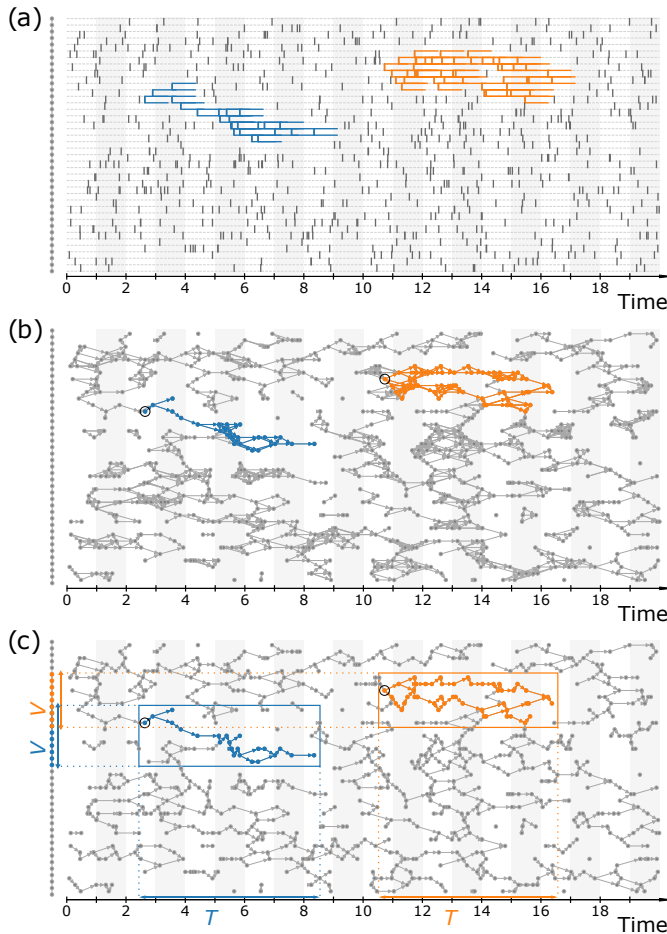


Figure 2.5. Representation of a temporal network and two limited-waiting-time spreading processes on that network, from Publication VI. The network is built using a static path graph, which is shown vertically to the left, and each link has activation times determined by the Poisson process. In part (a), the temporal network is depicted through a time-line chart. Here, every horizontal dashed line stands for an individual node, while vertical solid line segments indicate immediate interactions or events between two nodes at a given moment. Two specific spreading processes with limited waiting times, initiated from two separate events, are highlighted using different colors. These colored horizontal segments indicate the duration of infectivity for each node, and the highlighted events mark potential paths of transmission. (b) The event graph of the temporal network is illustrated as a directed acyclic graph. In this representation, every event from the original network becomes a node in the event graph. Two nodes are linked if their corresponding events are next to each other. (c) This event graph can be simplified by removing unnecessary feed-forward loops, all the while preserving the characteristics of the spreading process. The **Cluster volume**, which refers to the distinct count of infected nodes in the temporal network, and the **Cluster lifetime**, representing the duration from the beginning to the end of the process, are determinable from the properties of the event graph. Meanwhile, the **Cluster mass** — the cumulative node-hours of infectivity, equivalent to the total of colored horizontal lines seen in panel (a) — can be gauged in the event graph by counting the distinct events in the infected cluster.

a selection of starting events and execute a BFS for each, but this method grows costly in terms of computational resources. This is mainly because each BFS demands operations on the order of $O(|\mathcal{E}_D|)$, where \mathcal{E}_D represents the set of links or adjacency relationships within the event graph. Ref. [14] introduces a method that efficiently computes estimates of sizes of in- or out-components in temporal networks. This method has far-reaching implications, as we show in [Publication V](#) and [VI](#).

A stone is a prototypical “thing”: we can ask ourselves where it will be tomorrow. Conversely, a kiss is an “event.” It makes no sense to ask where the kiss will be tomorrow. **The world is made up of networks of kisses, not of stones.**

Carlo Rovelli, *The Order of Time*

2.8 Percolation Theory

Percolation theory is a mathematical framework used in statistical physics, materials science, and network theory to study the behavior of connected components in a random graph [173]. It provides a way to analyze how various properties of a system change as the number of connections or occupied sites increases. The theory is particularly famous for describing phase transitions, which are sudden changes in the system’s properties.

Percolation theory is also useful in understanding disease propagation in social networks, offering analytical tools that will be specifically utilized in [Publication III](#) and [IV](#). This theory emphasizes the need to consider both the structural aspects of networks and the nuances of individual disease transmission behaviors. Our development of this framework, as detailed in [Publication V](#), [VI](#), and Ref. [177], extends its application to temporal networks. We map spreading phenomena onto directed percolation problems, thereby enhancing our understanding of how diseases proliferate over time in complex network structures.

2.8.1 Bond Percolation

In [Sec. 2.2](#), we introduced the ER network $G(N, p)$ where each pair of nodes were connected with probability p . That model results in a network that undergoes a phase transition, as illustrated by [Fig. 2.2](#), from a disconnected to a connected system such that if $p > p_c$, the giant component of the network spans a non-zero fraction of all nodes. The wiring probability p stochastically connects any pair of nodes and acts as the *control parameter* here and adjusts the network’s giant component size, the *order parameter*

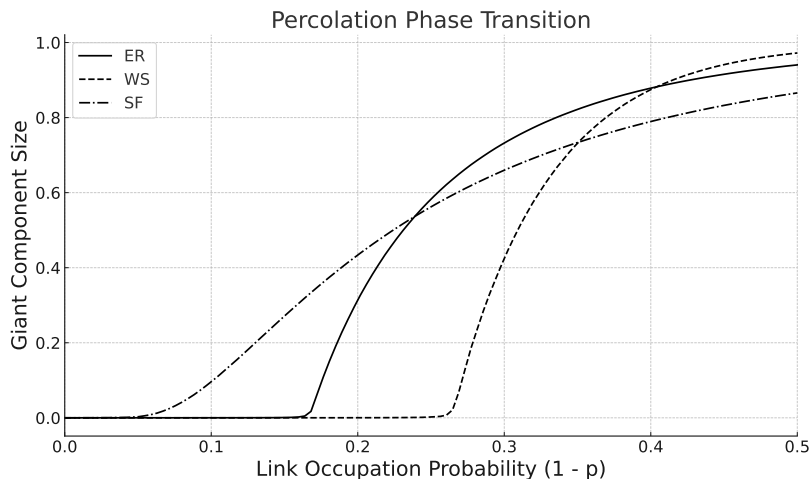


Figure 2.6. Simulation results for the percolation phase transition in three networks (each of size 6×10^5 and average degree 6). The solid line represents the Erdős-Rényi (ER) network, with a critical probability ($p_c = 1/6$), as discussed in Sec. 2.2.1. The dash-dotted line illustrates a configuration model network with a heavy-tail degree distribution ($p_k \sim k^{-3.01}$, see Sec. 2.3), which is more robust against link removal. The critical probability for this network can be derived using Eq. 2.38. This network exhibits more degree heterogeneity compared to an ER network and demonstrates lower critical p . The dashed line shows a Watts–Strogatz small-world network with a rewiring probability of 0.1 (see Sec. 2.2.2), which has a higher percolation threshold than the ER network. Due to its high clustering coefficient, the standard approach for calculating the epidemic threshold (Eq. 2.38) is not applicable for this network.

of the problem. We can do the opposite: Begin with any graph G , remove any link uniformly at random with probability p (or leave the link occupied with probability $1 - p$), and check how the giant component size varies as a consequence of link removal. Fig. 2.6 shows what happens to the size of the giant component of three different networks as we remove their links uniform at random with p . As we can see, different networks undergo different changes depending on their topology. When the giant component emerges by including a non-zero fraction of the nodes in the network, we say the network has percolated.

In the realm of physics, this approach is known as bond-percolation, where only a subset of the system’s original bonds (or links) remain active [47, 128]. Most connected graphs experience a phase transition at a particular probability, p_c , which is referred to as the bond percolation threshold. In the case of tree-like networks, this threshold is determined by observing how the percolation probability p affects the average excess degree, given that the transition occurs when $\langle q \rangle = 1$. It’s worth noting that various properties, such as the size of the giant component, small component size distribution, network percolation characteristics, and more, are all intrinsically linked to this tree-like property.

For configuration model networks, we can find the size of the giant component or the percolation threshold using the same arguments we followed in Sec. 2.3.2 such that

$$p_c = \frac{1}{g_1'(1)} = \frac{\langle k \rangle}{\langle k^2 \rangle - \langle k \rangle}, \quad (2.38)$$

where g_1 is the generating function of the excess degree distribution of the configuration model network.

2.8.2 Site Percolation

If instead of removing or keeping the links, we remove each node and its connecting links from the network, a process known as *site-percolation* [168], we will again go through a phase transition but this time through a different mechanism such that the threshold happens at different values. Vaccination can be modeled as a site-percolation process since by vaccinating people, we remove them from the transmission network [202, 129].

2.8.3 Percolation as a Critical Phenomenon

Percolation phase transitions are a fascinating area of study in statistical physics, characterized by the emergence of a giant component that connects a significant portion of a system [128, 148]. This transition is governed by *scaling laws* and *critical exponents* [81], which offer a quantitative framework for understanding these phenomena. These laws describe the behavior of various physical quantities as the system approaches the critical threshold of percolation, denoted as p_c . Near the critical point, properties of the system exhibit power-law scaling, indicating that they can be expressed as a power of the distance from p_c . Critical exponents are key to understanding these scaling laws [81]. They describe how certain properties of the system change as the percolation threshold is approached [62]. Accordingly, the size of the giant component and the average size of small components scale with their specific critical exponents at the critical point [63]. This can be expressed as:

$$\sigma \sim |p - p_c|^{-\gamma}$$

The symbol \sim denotes that the left-hand side scales as a power of the right-hand side, and γ is the critical exponent that describes how the average size of components diverges as the percolation threshold p_c is approached. Another singular property at the critical point is the *correlation length*. The correlation length ξ indicates the scale of spatial correlations in a system, say, the typical size of components, and its divergence signifies the onset of long-range order. The scaling of the correlation length can also be expressed as follows:

$$\xi \sim |p - p_c|^{-\nu}$$

where ν is the critical exponent associated with the correlation length.

These scaling laws and critical exponents are not just mathematical curiosities; they reveal the underlying *universality* of phase transitions [81]. A *universality class* in the context of statistical physics and critical phenomena is a classification that groups various physical systems and models based on their similar critical behavior, particularly as they approach a phase transition. A fridge magnet and boiling water exhibit similar behaviors near their critical temperature, despite their differences [81]. This concept suggests that different systems, even with diverse microscopic structures or dynamics, can exhibit identical large-scale statistical behavior near their critical points. Besides, it highlights the profound interconnectedness of physical and mathematical worlds, where the same fundamental rules can govern both material states and abstract structures.

Taking percolation as an example, systems within the same universality class will share critical exponents that dictate the scaling behavior of key properties like component sizes or correlation lengths near the percolation threshold. This remarkable similarity means that by studying the critical behavior of one system in a given universality class, we can infer the behavior of other systems in the same class despite their microscopic differences. This principle of universality is crucial in simplifying and unifying our understanding of complex phenomena across a wide range of disciplines, from condensed matter physics to network theory. Ref. [39, 86, 187, 63] provide comprehensive insights into the mathematical foundations and physical interpretations of scaling laws and critical exponents in percolation theory.

2.8.4 Directed Percolation

Following the exploration of percolation in various network topologies, as discussed in the context of the ER network and configuration model networks, we now turn our attention to a specific type of percolation process known as *directed* percolation. This process is a cornerstone example of continuous, non-equilibrium phase transitions, distinct from *isotropic* phase transitions due to its imposition of a preferred direction in one of the system's dimensions [90, 91].

Consider the process of brewing espresso as an illustrative example of a percolation process. In this scenario, the network is the finely ground coffee held within a portafilter, a porous medium. The percolation occurs when hot or steamed water is forced through the coffee grounds, extracting the coffee from the bottom. Unlike isotropic percolation processes, the liquid in espresso-making travels predominantly in a downward direction, guided by the combined forces of the espresso machine's pressure and gravity. This directional flow of water through the coffee grounds exemplifies a directed percolation process, where the flow is not random or isotropic but instead

follows a specific, predetermined path. This directional bias in the percolation process significantly alters the dynamics of the system, disrupting the usual symmetry between the horizontal and other spatial dimensions. This phenomenon, where the percolation process is guided in a specific direction, can be likened to the concept of directed percolation in physics [90], as opposed to isotropic percolation, where the fluid or the agents would move uniformly in all directions. This directed percolation process, as seen in espresso brewing, is a metaphoric analogy to the theoretical models of directed percolation discussed in non-equilibrium physics. It provides a tangible example of how directional constraints in a percolation process can fundamentally change the behavior and outcome of the system.

Directed percolation can also be conceptualized as a $d + 1$ -dimensional system with one dimension having a preferred direction, time evolution, given the unidirectional nature of time [91, 90]. In this framework, the evolution of the system in discrete-time directed bond percolation is governed by two simple rules: 1) each occupied node leads to the occupation of neighboring nodes, and 2) any occupation not reinforced in a turn results in the node becoming unoccupied. This dynamic leads to three distinct phenomena: death (or extinction at dead-ends), multiplication (where an occupied node infects a neighboring one), and coalescence (where two occupied nodes interact, leaving only one occupied).

Similar to the isotropic percolation discussed earlier, the evolution of directed percolation systems is characterized by changes in order parameters and characteristic quantities in response to variations in the control parameter p , the probability of link existence. At a critical threshold $p = p_c$, the system undergoes a phase transition. Below this threshold, percolating clusters starting from a single node are finite in both lifetime and size. As the threshold is approached, these clusters grow, and beyond it, they remain indefinitely active in an infinite system [90, 91]. This behavior is quantified through various parameters such as the probability of survival $P(t)$, mean cluster mass M , volume V , and lifetime T , each scaling with different critical exponents.

In [Publication V](#) and [VI](#), we will discuss in more detail that in scenarios where the spreading process begins from all nodes at $t = 0$, the system remains active for a finite duration at $\tau < 0$ but indefinitely for $\tau > 0$. This leads to the definition of occupation density $\rho(t)$ and stationary density ρ_{stat} , which scale differently based on the system's state relative to the critical threshold. The influence of an external field on ρ_{stat} is particularly noteworthy near the critical threshold, where even minor changes can significantly affect the system, as indicated by the susceptibility χ .

While these quantities have distinct critical exponents, not all are independent. For example, the static occupation density ρ_{stat} and the ultimate probability of survival P_∞ are closely related under a time-reversal transformation, leading to the equality of certain critical exponents [90].

Despite its theoretical elegance and extensive study, practical observations of directed percolation systems in real-world scenarios were elusive until recently. This gap is partly due to the difficulty in replicating certain features of classical directed percolation systems, such as a non-fluctuating absorbing phase, in natural settings [90]. However, recent experimental breakthroughs have begun to bridge this gap, demonstrating the applicability of directed percolation concepts in various fields ranging from star formation to biological evolution [190, 175, 126]. Ref. [177] revolves around analyzing the temporal evolution of spreading dynamics on networks. We contribute to forming a concrete connection between temporal network reachability and percolation theory in [Publication V](#) and [VI](#). We show that limited-waiting-time reachability, a feature of constrained connectivity in temporal networks, undergoes a directed percolation phase transition. This suggests that spreading behaviors on these networks can be analyzed using directed percolation universality class, a finding consistent across various models and actual temporal networks. Building on this, we aim to connect the reachability in temporal networks to epidemic spreading similarly as connectivity in static networks is related to late-stage disease-spreading results [150, 114].

3. Epidemics on Networks

The COVID-19 pandemic has made us come to grips with the epidemic problems, as they offer not only a set of practical problems to solve but also interesting theoretical puzzles. The interconnectedness of individuals in society plays a pivotal role in determining the scale and likelihood of an outbreak [158, 115]. Integrating more realistic assumptions into our models while employing advanced mathematical and computational tools to study these complex systems is imperative. In this chapter, we discuss how different diseases unfold in social networks and how, and in what ways, various interventions can be effective considering the networked structure of human populations.

3.1 Identifying Key Nodes in Networks

As discussed in Section 2.2.2, the friendship paradox is a key concept in understanding the dynamics on social networks, particularly in the context of disease spread [115]. In social networks, certain individuals, known as *hubs*, are characterized by their high number of connections [158]. These hubs play a crucial role in the propagation of diseases. Due to their extensive network of connections, hubs are more susceptible to contracting illnesses. The significance of hubs in accelerating the spread of diseases within networks is twofold. Firstly, due to their higher-than-average number of connections, these hubs have a greater probability of encountering and contracting infections. Secondly, once infected, their extensive connections facilitate them to transmit the disease to a larger number of individuals compared to a typical node.

In the case of Severe Acute Respiratory Syndrome (SARS), a viral respiratory disease caused by a SARS-associated coronavirus, data from Singapore revealed that the index patient, who had a large number of contacts, transmitted the disease to many people [102]. Not all of these contacts further spread the disease, but a few acted as hubs and were responsible for its widespread transmission. This highlights the critical role of these hubs

in propagating the disease. Therefore, an interesting strategy would be to focus vaccination efforts specifically on these *super-spreaders*. The idea of *targeted vaccination* [159, 76], suggests that immunizing these key individuals could disrupt the transmission chain, effectively curbing the disease spread with fewer vaccine doses. The complexities and strategies of vaccination campaigns, including this targeted method, are explored in detail in [Publication I](#) and [Chapter II](#).

However, identifying these hubs poses a challenge. Traditional vaccination methods often rely on random selection, which may not be optimal. This is because the majority of the population tends to have average or below-average connections, whereas the few true hubs have a disproportionate impact on spreading the disease [158]. To address this, an innovative approach called *acquaintance immunization* was proposed [48]. Rather than vaccinating individuals chosen at random, this method involves asking the selected person to nominate a friend or acquaintance for vaccination. By doing so, the likelihood of vaccinating a hub increases, making the process more efficient and targeted in curtailing the spread of diseases like SARS.

The logic behind the effectiveness of acquaintance immunization is similar to the way that the friendship paradox works. At first, this might seem counter-intuitive, but there's a logical reasoning behind it. If a person has a high number of connections (a hub), they have a higher chance of being nominated by any one of their numerous acquaintances. On the other hand, a person with fewer connections has fewer chances of being nominated. Therefore, this method naturally leads to the identification and vaccination of hubs more frequently than a random approach would. This method has been tested through simulations and works well there. However, implementing the acquaintance immunization strategy in real-world scenarios presents distinct challenges. First, there is a technical hurdle: acquiring accurate network data can be complex and demanding. This data is crucial for identifying key individuals within the network and ensuring the strategy's effectiveness. Second, a moral or legal challenge arises when asking individuals to nominate friends. This request may encounter resistance due to privacy concerns, as people might be hesitant to share personal connections, or due to logistical issues in gathering and managing such sensitive information. Despite these challenges, the potential effectiveness of this strategy, as demonstrated in simulations, highlights its promise as a valuable tool in combating infectious diseases.

3.2 Modeling Epidemics on Networks

To delve into epidemics within structured populations, it's essential to weave together the compartmental models presented in [Chapter 1](#) with

the network system methodologies discussed in Chapter 2. Achieving analytical arguments necessitates analyzing the interplay between the structure of contact patterns and the dynamics of disease propagation. The primary hurdle is that compartment models are typically characterized by coupled non-linear differential equations. Directly solving these complicated equations on a graph is a daunting task, both numerically and analytically.

Considering the inherently high-dimensional nature of dynamical systems on networks, we need to find a more manageable, lower-dimensional representation that retains the essence of the original system. Such representations should ideally be more intuitive and potentially amenable to analytical approaches, like deriving approximate closed-form expressions for quantities of interest [167]. *Mean-field* theories stand out as a promising strategy to achieve this [115]. When it comes to dynamical systems on networks, these theories and similar methods of approximation are of special importance [19].

3.3 Mean-field Approximations

In Physics, a mean-field approximation is a technique where the state of a specific particle (for us, a node or a link, depending on the context, in a network) is viewed in interaction with the collective average state of the rest or, extending the idea, the distribution of states among all particles. This approach is a valuable starting point for deciphering complex systems. The approximation becomes even more accurate when interactions are broadly of the same magnitude, reminiscent of those in a densely populated random graph [167].

Mean-field approximation and heterogeneous mean-field theory are commonly used in the study of epidemic spread on networks [158]. Generally, the mean-field approximation assumes that each node in the network interacts with every other node in an identical manner, which simplifies the model but may not capture network heterogeneity. On the other hand, heterogeneous mean-field theory takes into account the different characteristics and behaviors of nodes within a network, providing a more nuanced and accurate representation of epidemic spread [201].

3.4 From the Contact Networks to Transmission Networks

If we model the contact network of a human population with network G , the actual disease transmission might occur on a different network G' , depending on the dynamics of the disease. The initial network, G , is termed the *contact network*, while G' is referred to as the *transmission network*

[41]. In practice, accurately describing contact networks is challenging due to difficulties in measuring them [20]. Furthermore, there's still much to learn about contact networks' topological characteristics and temporal evolution. Gathering sufficient observations and data for a comprehensive analysis remains a hurdle [155]. It is worth noting that transitioning to the transmission network that dictates disease dynamics is not straightforward, even with a clear understanding of a contact network.

Consider a rather simple scenario where a disease spreads across a contact network G . The disease's dynamics manifest on this network such that every link in the contact network has a probability p of actively transmitting the disease [83]. To transition from the contact network to the transmission network, one would replicate the original nodes, retaining each link based on probability p . The resulting graph represents the transmission network. Each node in this network represents an individual infected at some point, and the number of nodes in the giant component of this new network can serve as an indication of the epidemic size [150, 114, 113]. This mapping process is called the *bond-percolation* method. We discussed percolation in depth in Sec. 2.8.

To execute a bond-percolation mapping, it's essential to understand the structure of the original contact network. In many real-world scenarios, our knowledge about the contact network's structure is limited. Yet, we might possess a reliable estimate of the transmission network. Knowing the transmission network simplifies many analytical calculations. For instance, given a transmission network from the configuration model family, with degree distribution p_k , we can identify the basic reproduction number as the mean excess degree of the transmission network [143, 149, 191] as

$$R_0 = \langle q \rangle. \quad (3.1)$$

This is because the average excess degree of a transmission network yields the expected number of secondary cases produced by a typical infectious individual over the course of their infectious period in a fully susceptible population. For locally tree-like networks with no correlations in their connections, the basic reproduction number can be written as a function of the first and the second moments of the degree distribution of the transmission network, given by Eq. 2.19.

This understanding significantly aids in the application of our mean-field approximations. Depending on the quantity of interest, we can write different equations regarding the network structure. In the subsequent sections, we will delve into the practical applications of transmission networks.

3.5 Mapping Epidemics to Percolation

Disease spread in network models, similar to fully mixed ones in Chapter 1, operates on the contact network and is defined by a transmission rate, β , indicating the infection probability per unit time between two connected individuals. However, β in network models differs from fully mixed models as it refers to contacts between an individual and their direct connections, not the entire population. The transmission rate is influenced both by the disease's nature and social behaviors, affecting how often and closely people interact within their communities.

Network models can simulate how diseases like the SI model spread over time, with β determining the infection spread to connected susceptible individuals. While calculating the disease's spread over a general network is complex, the eventual size of an outbreak is predictable: it will include all individuals reachable from the initial infection through network paths. This behavior, where an outbreak's size depends on the network's structure and the initial infection's position, introduces stochastic elements into the model, leading to different outcomes even with identical parameters.

These network and percolation models capture more realistic dynamics of disease spread than fully mixed models, acknowledging that not all exposures lead to an epidemic. Realistically, diseases can fizzle out if initial cases do not transmit to others. The models recognize the randomness in transmission and the variability in outbreak patterns, yielding probabilities or averages rather than precise predictions.

3.5.1 SIR Model and the Configuration Model

The SIR model of Sec. 1.2.2 adds the parameter of recovery time to the network model, where the disease may not always spread to a susceptible individual before the infected one recovers. The transmission probability p is based on the transmission rate β and recovery time τ , simplifying to [150]

$$p = 1 - e^{-\beta\tau}. \quad (3.2)$$

Therefore, using the percolation threshold, the critical probability p_c , we can rearrange Eq. 2.38 to give [150]

$$\beta\tau = -\ln(1 - p_c) = \ln \frac{\langle k^2 \rangle - \langle k \rangle}{\langle k^2 \rangle - 2\langle k \rangle}. \quad (3.3)$$

Using a technique akin to bond percolation, where links are active or occupied with a probability p , we can predict that an outbreak will spread across connected occupied links, corresponding to potential disease transmission [150, 114]. The bond percolation model also indicates that the giant component size corresponds to the final epidemic size, resembling how diseases spread through populations. Similar to Sec. 2.3.2, given the

transmission probability p , the total probability ϕ that a node does not belong to the giant component can be written as [151]

$$\phi = \langle 1 - p + p\phi^k \rangle_Q = 1 - p + pg_1(\phi), \quad (3.4)$$

and the size of the giant component can be calculated as

$$\Sigma = 1 - \langle \phi \rangle = 1 - g_0(\phi), \quad (3.5)$$

where g_0 and g_1 are the probability generating functions for the degree and excess degree distributions of the contact network, respectively.

When the product of the transmission rate and the infectious period surpasses a certain threshold, an epidemic becomes a feasible event. However, this does not guarantee an outbreak will occur, as the disease's initial host might not be part of the giant component of the transmission graph where the epidemic could take hold. Conversely, if the product of β and τ does not reach the critical threshold, an epidemic will not unfold, irrespective of the seed of infection within the population. The likelihood and potential extent of an epidemic provided that it is feasible, are quantified by Eq. 3.5.

The progression towards an epidemic within this model is influenced by the value of $\beta\tau$. An increase in either the time an individual remains infectious τ or the rate at which the disease is transmitted β can propel the system toward an epidemic state. The specific value at which this transition occurs, along with the chances and magnitude of an outbreak, is intricately linked to the network's configuration, particularly the average number of connections $\langle k \rangle$ and connections squared $\langle k^2 \rangle$. This consideration of network structure marks a stark contrast from the fully mixed model, which does not take into account the effects of a network's configuration [140, 113].

In [Publication I](#), we utilize this technique to calculate the number of individuals infected after a vaccination campaign. Building on this approach, in [Publication IV](#), we further apply the same percolation trick to accurately determine the final outbreak size, incorporating the impact of contact tracing. This demonstrates the adaptability and robustness of our methodology in various public health scenarios.

3.6 Spreading on Temporal Networks

So far, our investigations have focused exclusively on static networks, which remain unchanged over time. While this approach offers a reasonable approximation for modeling social networks, it is both theoretically and practically beneficial to integrate temporal heterogeneities. as we discussed in [Sec.2.7](#), into these networks [100]. By doing so, we can more accurately assess the impact of the temporal characteristics of contact networks on disease transmission.

Temporal networks differ from static ones in that they inherently include interaction timings, capturing real-world correlations and inhomogeneities like diurnal patterns and burstiness of activity, which significantly influence spreading scenarios [134, 99, 97]. These networks also reflect structural changes over time, crucial in studies like sexually transmitted diseases, where relationship dynamics or geographical moves can alter contact networks [134, 24]. The results from simulating spreading processes on temporal networks often differ significantly from those on static networks due to factors like linger time distribution and inter-event time distribution [97, 144, 110, 71, 33, 131, 170].

3.6.1 Directed Percolation and Spreading Phenomena

Expanding upon our previous discussions, there is a well-established connection between reachability and disease spread in static networks, underpinned by percolation theory as highlighted in Sec. 2.8. However, this interplay is less examined in temporal networks. Our research, detailed in [Publication V](#) and [VI](#), is dedicated to analyzing the temporal evolution of spreading dynamics on networks and forging a solid link between reachability in temporal networks and percolation theory. We have uncovered that in these networks, limited-waiting-time reachability, a kind of constrained connectivity discussed in Sec. 2.7, exhibits a directed percolation phase transition as described in Sec. 2.8.4. This discovery implies that spreading behaviors in temporal networks can be insightfully studied using the directed percolation universality class, a finding consistent across a variety of models and actual temporal networks.

Transferring analytical tools from static to temporal networks is a complex task. We aim to bridge this gap by correlating reachability in temporal networks with epidemic spreading, akin to how connectivity in static networks is associated with late-stage disease transmission, as extensively researched in [150, 114]. Adapting some methodologies, we can interpret reachability in temporal networks through event graph representation, as cited in [118, 179, 101]. In these networks, 'reachability'—similar to connectivity in static contexts—encompasses the capability to trace a chronological path from one node to another amidst the fluctuating nature of network connections over time, as described in [96]. The event graph method outlined in Sec. 2.7 effectively translates time-sensitive reachability data into a higher-order static directed acyclic graph (DAG), elaborated further in Ref. [177]. This graph's out-component provides insights on nodes and periods that are reachable, whereas its in-component sheds light on feasible origins and timings to reach certain destinations.

The directed percolation phase transition and its universality class, introduced in Sec. 2.8.4, provide a valuable framework for converting these mathematical concepts into a tangible physical model. This framework

greatly improves our comprehension of the dynamics within temporal networks, especially concerning the spread of diseases and the flow of information. In [Publication V](#), [VI](#), and [Ref. \[177\]](#), we have developed an extensive framework that maps specific disease dynamics to a directed percolation problem. This significant development enriches our understanding of how temporal changes in network structures can influence both reachability and, ultimately, the spread of diseases in temporal environments.

3.7 Homophily and Herd Immunity Threshold

A good example to see the power of a mean-field approach is to consider a locally tree-like homophilic transmission network similar to the one in [Sec. 2.4.4](#). Let's say we are interested in the epidemic threshold as a function of network structure and spreading parameters. Assume a naive population that we can vaccinate π_v fraction of the individuals given this condition that vaccinated and unvaccinated nodes are connected to each other with different probabilities as depicted in [Fig. 1.9](#) and the network degree distribution follows p_k . We will go through more details and calculations in [Publication II](#).

Our focus is on a group of epidemic models in which infection induces complete and permanent immunity, whereas the immunity induced by vaccines is generally incomplete. We represent the number of infections among vaccinated and unvaccinated groups at generation m (stemming from the initial infected case) as $I_v^{(m)}$ and $I_u^{(m)}$, respectively. Assuming ideal vaccine efficacy, the vaccinated group would experience no infections. Hence, under a mean-field approximation, we can express the situation using the following recurrence formulas:

$$I_v^{(m+1)} = 0, \quad (3.6)$$

$$I_u^{(m+1)} = R_0 \pi_{uu} I_u^{(m)}, \quad (3.7)$$

which is a typical branching process, with branching factor $R_0 \pi_{uu}$. Remember that π_{uu} is the probability that an unvaccinated individual is connected to another unvaccinated in our homophilic network ([Fig. 1.9](#)) model of [Sec. 2.4.4](#).

It's important to recognize that vaccines might not be flawless. Two particular effects of vaccine protection are crucial when thinking about herd immunity [[88](#), [70](#)]. One, the vaccine might lower the chance that someone gets infected when exposed. This decrease is known as the efficacy against susceptibility, labeled as f_S [[130](#), [106](#)]. In our discussion, we're suggesting that the vaccine provides complete immunity to a portion f_S of those vaccinated, while the rest remain entirely vulnerable. Our model views the vaccine as being *all-or-nothing*, unlike *leaky* vaccines that slightly reduce everyone's susceptibility. These models are equivalent under the

assumption that the network is locally tree-like, on which our study is based [88, 70]. Secondly, those who get infected even after vaccination might be less likely to pass on the infection. We capture this using the efficacy against infectiousness, f_I , which indicates how much the rate of secondary infection is reduced. Given these two new parameters, the previous mean-field equations can be written as:

$$I_v^{(m+1)} = (1 - f_S)R_0[(1 - f_I)\pi_{vv}I_v^{(m)} + \pi_{uv}I_u^{(m)}], \quad (3.8)$$

$$I_u^{(m+1)} = R_0[(1 - f_I)\pi_{vu}I_v^{(m)} + \pi_{uu}I_u^{(m)}], \quad (3.9)$$

where $\pi_{uv} = 1 - \pi_{uu}$ and $\pi_{vu} = 1 - \pi_{vv}$ are the conditional probabilities that a link from one group points to the other. We can rewrite these equations in a matrix form such that

$$\mathbf{I}^{(m+1)} = \mathbf{M}\mathbf{I}^{(m)}, \quad (3.10)$$

where $\mathbf{I}^{(m)} = (I_v^{(m)}, I_u^{(m)})^\top$ and

$$\mathbf{M} = R_0 \begin{pmatrix} (1 - f_S)(1 - f_I)\pi_{vv} & (1 - f_S)\pi_{uv} \\ (1 - f_I)\pi_{vu} & \pi_{uu} \end{pmatrix},$$

we see that the infection eventually dies out after a finite number of generations if all the eigenvalues of the next-generation matrix \mathbf{M} have an absolute value of less than one. That is, at the critical point, the spectral radius $\rho(\mathbf{M}) = 1$.

In [Publication I](#), we show that by adjusting the connection probabilities using π_v and Coleman homophily index h from [Eq. 2.37](#), the critical vaccine coverage for achieving herd immunity so that $R_0 = 1$ can be expressed as:

$$\pi_v^c = \frac{1 - \epsilon R_0 h}{(1 - \epsilon)(1 - h)} \left(1 - \frac{1}{R_0}\right), \quad (3.11)$$

Here, ϵ is defined as $(1 - f_S)(1 - f_I)$ and it's necessary that $\epsilon \leq 1/R_0$. If $\epsilon > 1/R_0$, the threshold for vaccination becomes obsolete, making herd immunity unreachable.

In cases of a perfect vaccine, where either $f_S = 1$ or $f_I = 1$ or both:

$$\pi_v^c = \frac{1}{1 - h} \left(1 - \frac{1}{R_0}\right), \quad (3.12)$$

This equation narrows down to the commonly referenced threshold in [Eq. \(1.22\)](#) when there's homogeneous mixing and $h = 0$. The equation suggests that as the intensity of homophily h grows, the critical vaccine coverage π_v^c for achieving herd immunity also increases (as illustrated in [Fig. 3.1](#)). Simply put, having more homophily makes it more challenging to achieve herd immunity. It's key to highlight that when

$$h \geq \frac{1}{R_0}, \quad (3.13)$$

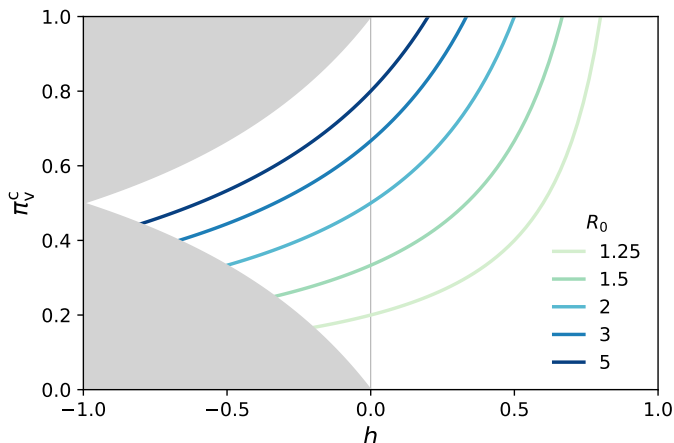


Figure 3.1. Critical coverage π_v^c of a perfect vaccine required for herd immunity as a function of homophily strength h for different values of basic reproduction number R_0 . Positive values of h indicate homophily, while negative values point to heterophily. The gray-shaded area in the figure denotes the parameter space where the network cannot be realized. This figure is from [Publication I](#)

herd immunity can't be achieved unless everyone is vaccinated. In other words, regardless of how tiny the group of unvaccinated individuals might be, there's always a risk of a significant outbreak within that group.

We built a network-based framework to accommodate homophily related to interventions. Our results show that a small level of homophily in vaccination status can considerably increase the threshold required for herd immunity and even make herd immunity impossible to reach. To truly understand and predict the dynamics of spreading processes in the presence of vaccination homophily, it is essential to incorporate these factors into our models and analyses. For more details, see [Publication I](#).

3.8 Disease-induced Herd Immunity

When immunity arises from a natural infection, the inherent heterogeneity in human interactions can significantly alter the dynamics of disease spread. In contrast to vaccine-induced immunity, natural immunity exhibits variations in its strength and nature. In particular, diseases often target highly connected individuals in the early stages, leading to the efficient immunization of these influential nodes [35]. However, while epidemics tend to target and remove high-degree nodes, enhancing herd immunity, the localized nature of these infections within the network can simultaneously weaken it.

We will investigate the strengths and weaknesses of disease-induced

herd immunity in [Publication II](#). Our analysis is anchored in understanding various network structures, with particular emphasis on two primary aspects: degree heterogeneity (which looks at the variations in how nodes connect) and spatial embeddedness (which focuses on the placement of these networks within a defined space). For a clearer picture, see [Figure 3.2](#).

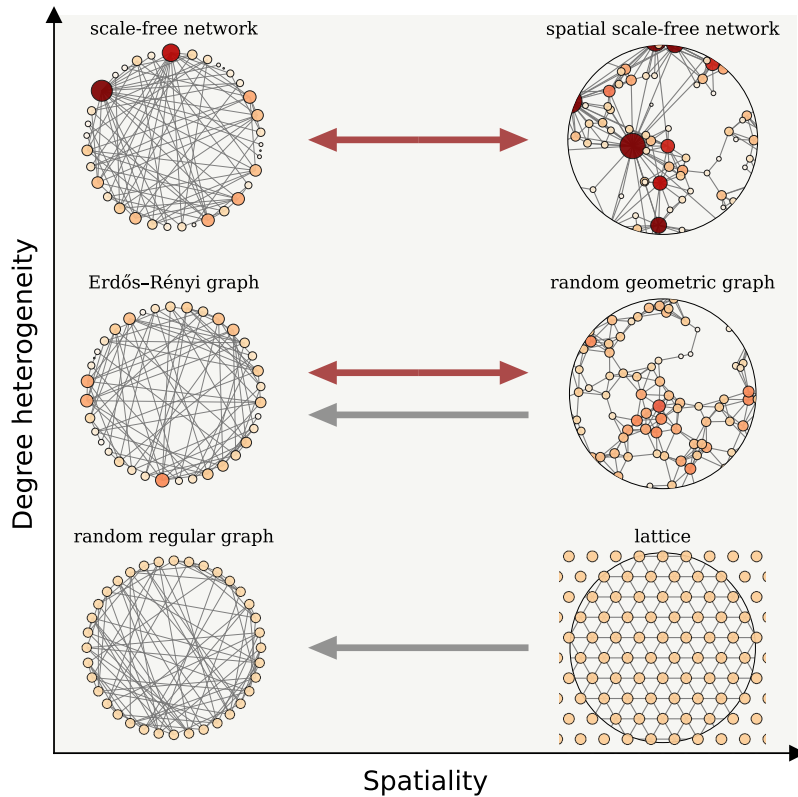


Figure 3.2. Network models according to their level of degree heterogeneity and spatiality from [Publication II](#). The three arrows indicate directions of sweeps conducted through rewiring randomization. Spatial embeddedness describes how a network is geometrically arranged in a set space. At one end, networks like RRGs and Erdős-Rényi networks show minimal spatiality, representing the most randomness. On the opposite end, lattices and RGGs have the most spatial structure

We use link randomization techniques [204] to bridge the gap between networks with high and low spatiality. Starting with a highly spatial network, like a lattice or a random geometric graph, we modify a fraction of its links. This modification can be done in two ways: double link swap (which keeps the node’s degree constant) and random rewiring (which maintains the total link count but not individual node degrees). Fully randomized links transform a lattice into a random regular graph and

a random geometric graph into an ER network. However, any network becomes an ER network with complete random rewiring, regardless of its starting point.

During these modifications, the network starts to show small-world traits [204], thanks to the formation of long-range connections. This characteristic persists until the network's local structures dissolve, but the average node degree remains unchanged. Refer to [Publication II](#) for more details. Our results reveal that when there's no degree heterogeneity, disease-induced immunity has a milder impact compared to random immunization. However, for Erdős-Rényi networks, both methods offer similar herd immunity levels. This outcome stems from two opposing forces at play in disease-induced herd immunity. On one hand, epidemics tend to target and remove nodes with many connections, bolstering the herd immunity effect. On the other hand, the spread is concentrated and localized within the contact network, which weakens herd immunity. See [Fig. 1.10](#) for a visualization. These competing forces are reflected in the number of connections between susceptible and removed nodes and the average connections of removed nodes. In networks with slight heterogeneity, the localization's influence is more pronounced than the targeted removal of well-connected nodes.

3.9 Epidemic Spreading and Contact Tracing

Ibn Sina (Avicenna, 980–1037 CE), a Persian polymath, suspected that some diseases were spread by microorganisms. He highlighted the concept of quarantine in his influential work, *The Canon of Medicine* [17]. Contrary to Galen but in line with Aristotle, he identified tuberculosis as contagious [185]. It is clear that since the old times, quarantine as a restriction on the movement and interactions between people has been around as an effective non-pharmaceutical intervention for infectious diseases.

Contact tracing involves identifying and isolating individuals who have been exposed to infected persons [34]. This method is not only effective in containing the spread of diseases but also practical [208]. In this section, we explore models that integrate epidemic spread with the implementation of contact tracing. Contact tracing as a targeted approach proves cost-effective and allows for the possibility of relaxing certain social distancing measures, striking a balance between public health and economic considerations [3, 199, 116]. Additionally, contact tracing is instrumental in predicting future outbreaks, identifying new disease clusters, and tracing the origin of infections [26, 79, 119, 120]. For a detailed analysis of contact tracing, refer to [Publication III](#) and [IV](#).

Note that in our study, we treat the concepts of isolation and quarantine as being equivalent and thus use these terms interchangeably to reflect

their similar roles in our model. However, it's important to note that in the context of public health, isolation and quarantine are considered distinct approaches to controlling the spread of infectious diseases [153]. Isolation involves separating individuals diagnosed with a contagious disease from those who are healthy to prevent the transmission of the infection. On the other hand, quarantine refers to the separation and limitation of movement of people exposed to a contagious disease to monitor if they develop symptoms. It focuses on individuals who might be infected but are not yet confirmed to be sick. Therefore, in public health, isolation is applied to ill and contagious people. In contrast, quarantine is used for individuals at risk of falling ill due to their exposure to the disease [153].

3.9.1 Digital Contact Tracing

With the rise of affordable wearable health devices and mobile apps, digital contact tracing has become more precise and efficient, addressing the challenges of traditional manual tracing, such as slowness and reluctance to share contacts due to various concerns [174, 147, 182, 156, 146, 169, 141, 189]. These modern tools not only facilitate contact tracing but also provide real-time health data that can be used for other health strategies [8]. In this section, following [Publication IV](#), we focus on digital contact tracing. It is the use of digital tools, often smartphone apps, to identify and notify individuals who have been in close proximity to someone diagnosed with a contagious disease, such as COVID-19. This technology aims to quickly and efficiently track potential disease exposure and prevent further spread.

We aim to understand how the size and threshold of the epidemic vary when apps are installed based on specific criteria like homophily (Sec. 2.4.4). In a manner akin to the homophily observed in people's vaccination status, as mentioned in Sec. 3.7, individuals using the app tend to have connections with other app users. In our representation, if one app user infects another, the infected person is likely to self-isolate, thereby halting further transmission. By adopting this method, we offer a cautious assessment of the influence of app-based contact tracing, especially when a significant portion of the population is infected at once.

Consider a network analogous to the one in the vaccination scenario. However, instead of individuals being vaccinated or not, they either use contact tracing apps or don't. These apps function effectively with a probability of f_{app} . Assuming that π_a proportion of individuals utilize the apps, we can derive a mean-field approximation for the epidemic size. This approximation is based on the branching process, similar to how it's done in Eq. 3.8 and 3.9;

$$I_n^{(t+1)} = R_0[\pi_{\text{nn}}I_n^{(t)} + \pi_{\text{an}}I_a^{(t)}], \quad (3.14)$$

$$I_a^{(t+1)} = R_0[\pi_{na}I_n^{(t)} + \pi_{aa}(1 - f_{app})I_a^{(t)}]. \quad (3.15)$$

The probabilities $\pi_{..}$ indicate the likelihood of interactions within and across groups of app-users and non-app-users. Specifically, π_{aa} represents the probability of a connection between two app-users, π_{an} denotes the probability of a connection from an app-user to a non-app-user, π_{na} signifies the probability of a connection from a non-app-user to an app-user, and π_{nn} corresponds to the probability of a connection between two non-app-users.

We can again write these equations in a matrix form and find the spectral radius of the next-generation matrix to find the critical app coverage to curb the epidemic, similar to what we did for the herd immunity threshold. We skip this as the calculations would be very similar to what we did in the previous section. However, it is worth noting that when apps are working perfectly, $f_{app} = 1$, for each value of $0 < \pi_a < 1$, there is a non-trivial optimum value for homophily h^* that leads to the largest epidemic threshold such that:

$$h^* = \frac{2 - 2\pi_a}{3\pi_a^2 - 7\pi_a + 4}. \quad (3.16)$$

This formula suggests that as the number of app users in a population increases, the optimal level of homophily also increases steadily. In practical terms, this means that to maximize the benefit of a digital contact tracing initiative, it's essential to distribute the apps so that the user group's homophily matches $h^*(\pi_a)$. So, a population with fewer app users will require a lower level of homophily to achieve the best results in terms of increasing the epidemic threshold. Moreover, for any π_a , the optimal homophily is larger than the homogenous mixing condition where $h = 0$.

In our [Publication IV](#), we explore how effective contact tracing is by modifying the conventional approach to analyzing percolation and connectivity in contact networks. This involves applying our modified methodology to networks with different characteristics like degree distributions, user numbers of the application, and chances of quarantine breaches. Additionally, we consider populations with distinct social structures characterized by homophily and heterophily and the potential for targeting specific degrees in application distribution. Our findings are derived from a mix of direct simulations and mean-field analysis. They reveal significant variations in the size and probability of epidemics compared to standard SIR processes. Notably, the variation in connections within the network (degree heterogeneity) plays a crucial role in determining the epidemic threshold, though it has less impact on the size of the epidemic. The likelihood of tracing leading to quarantine is not as critical as the rate of application adoption. Moreover, we found that a strong preference for or against (homophily and heterophily, respectively) adopting the application can be harmful. In conclusion, the dynamics of epidemics are highly sensitive to all the tested parameters, highlighting the complex, multidimensional nature of

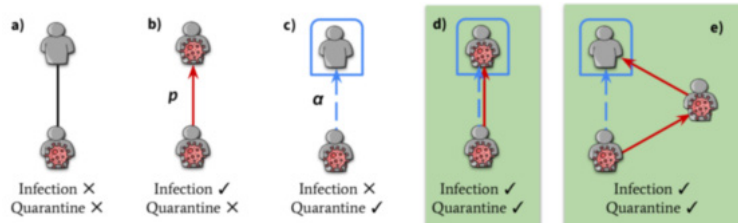


Figure 3.3. Illustration of contact tracing and transmission dynamics. The diagram shows scenarios without loops (a-d) and with local loops (e). Successful infections are indicated by solid red connections, while effective contact tracing is represented by dashed blue links. Following each exposure event, a susceptible node (S) either isolates itself with a probability of α or becomes infected with a probability of p , with these outcomes being independent. In scenarios without loops, the interplay of infections and contact tracing can be simplified to a single link, leading to four distinct outcomes: (a) no event occurs, (b) the infection is transmitted to the adjacent node, but contact tracing is unsuccessful, (c) the infection does not transmit, yet contact tracing is effective, or (d) both the transmission of the infection and the success of contact tracing occur. The final scenario, marked with a green background, demonstrates the advantage of contact tracing in interrupting indirect transmission routes, especially in clustered networks. In scenario (e), which involves local loops, the situation depicted in panel (c) becomes advantageous. This is because the quarantine, implemented near the site of infection, can hinder the spread of the infection to the neighboring node via a local loop. Essentially, timely quarantine in the vicinity of an infection source can prevent the disease from reaching the neighbor through these looped pathways.

estimating the impact of digital contact tracing.

3.9.2 Contact Tracing and Social Groups

In our previous examples, we assumed that the transmission networks locally look like trees. That is the main reason why we could use simple branching process arguments when we were interested in the phenomena around the epidemic threshold. In [Publication IV](#) Real-world social networks deviate from simple tree-like structures [133, 107], especially regarding disease spread, as we discussed in [Sec. 2.2.2](#). This can be seen in densely connected groups like families or workplaces. Clique structures play a crucial role in the spread of behaviors in complex contagion processes where prior exposures increase adoption chances. This is different from disease spread, where infections are independent of past exposures.

As we see in [Publication III](#), disease spread combined with contact tracing acts similarly to behavior spread, a.k.a complex contagion in networks, with prior exposures reducing subsequent infections. This highlights the significance of group structures in contact tracing.

To explore the dynamics of contact tracing on outbreaks based on a model that emphasizes group interactions, we use [Sec. 2.4.2](#) networks with equal connections per node but varying group sizes. When someone in a social group gets infected, they infect some members, and contact tracing isolates others. Effective contact tracing targets those both infected and

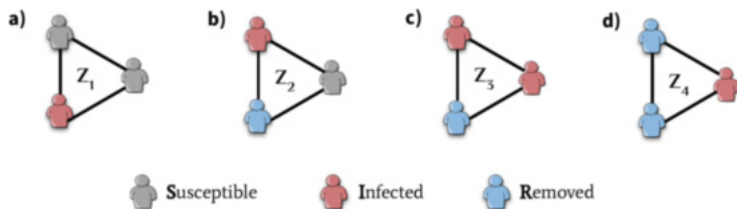


Figure 3.4. Every 3-clique is capable of exhibiting one of four distinct life stages or diffusion patterns, each including at least a single infected node. In our model, nodes that are either recovered or quarantined are grouped into the R compartment. Within a 6-regular 3-clique network, a node designated as Z_1 has the potential to form a Z_2 motif alongside two other Z_1 nodes, as well as a Z_3 motif when combined with four Z_1 nodes. Furthermore, a node identified as Z_2 is capable of creating a Z_4 motif in conjunction with two Z_1 nodes. It's important to note that nodes within the Z_1 , Z_2 , and Z_4 motifs have the possibility of transitioning to infection-eliminated states, such as R,S,S, which are not depicted here. This figure is from [Publication III](#).

isolated, breaking transmission chains. However, even isolating uninfected individuals can help control the spread. If contact tracing isn't perfect, isolating members can stop further infections. We will see that group structures boost contact tracing effectiveness in [Publication III](#). Specifically, contact tracing in networks with cliques impacts the spread more than in tree-like structures.

Let us continue with a basic mathematical model that uses a discrete-time SIR approach to represent disease dynamics. In this model, infected individuals spread the disease to nearby susceptible ones based on a **transmission probability** p . These infected individuals then move to a recovered state.

Contact tracing methods vary, such as using phone apps or manual tracing, and their effectiveness depends on factors like recall of contacts, delays in tracing, app adoption, and adherence to isolation guidelines [208]. In [Publication III](#), these complexities are represented by an **isolation probability** α , which indicates the chance a nearby node successfully isolates to prevent further infections. Infected nodes can move susceptible neighboring nodes to a quarantine compartment based on this probability. This compartment can contain both infected and susceptible individuals, as depicted in Fig. 3.3 when $\alpha = 0$ the model reduces to a simple SIR process.

The infection and contact tracing processes are considered independent in our model. The order of these processes in the model slightly affects the epidemic size but not the epidemic threshold. We compute the epidemic size by evaluating each infected-susceptible link, considering both the disease spread and contact tracing. The total size of an epidemic is determined by adding the number of infected individuals, both in and out of quarantine.

Using a multi-type branching process [111] to represent our SIR+Q model, we can derive the relationship between p , α , and clique size, c , concerning the epidemic threshold. In this model, we identify different

clique motifs that represent potential states of susceptibles, infected, or recovered nodes in any clique. These motifs are denoted by Z_i , as seen in Fig. 3.4 for a 3-node clique example.

i, j	m_{ij}
1, 1	$4p(1 - \alpha)$
1, 2	$2p(1 - \alpha)$
2, 1	$2p(1 - \alpha)^2(1 - p)$
3, 1	$p^2(1 - \alpha)^2$
4, 1	$2\alpha p(1 - \alpha)$
4, 2	$p(1 - \alpha)$

Table 3.1. Non-zero elements of the next-generation matrix $\mathbf{M}_{4 \times 4}$ for a 3-clique network. m_{ij} gives the expected number of Z_i cliques from a Z_j clique, as shown in Fig. 3.4. This table is from [Publication III](#).

Fig. 3.4 illustrates the four stages of a 3-clique's life, where isolated and recovered nodes are combined into one compartment (R) and Table 3.1 provides non-zero elements of \mathbf{M} , detailing how motifs transition. The matrix \mathbf{M} represents the transitions between these motifs. For example, the infected node in Z_1 can infect one or two neighbors, corresponding to motifs Z_2 and Z_3 . Further, $n_c - 1$ new Z_1 motifs are produced every time such an infection takes place. That is, when Z_1 turns into Z_2 there are also $n_c - 1$ new Z_1 motifs, and when it turns into Z_2 there are $2(n_c - 1)$ new Z_1 motifs created.

It is always feasible to compute the average expected number of new infections across all potential types of infection, utilizing our multi-type branching process. This calculation is based on the next-generation matrix, denoted as \mathbf{M} , which is also known as the mean or population projection matrix. The epidemic threshold in any clique network can be identified by finding values for p and α where $\rho(\mathbf{M}) = 1$.

Fig. 3.5a presents an epidemic phase diagram for networks with cliques. The curves within this diagram separate it into sub- and super-critical regions, determining the potential of an outbreak. Networks with larger cliques have a more significant sub-critical region and a smaller super-critical one. As the efficacy of contact tracing grows, the distinction between critical p values widens.

This model demonstrates the enhanced efficiency of contact tracing in clustered networks compared to tree-like structures or fully mixed populations. Specifically, when contact tracing is less reliable (for lower α values), increasing clique sizes notably reduces the outbreak size. This suggests that standard epidemic models might undervalue the efficacy of contact tracing in networks with more clustering.

Our study, along with [Publication III](#), simplifies disease transmission

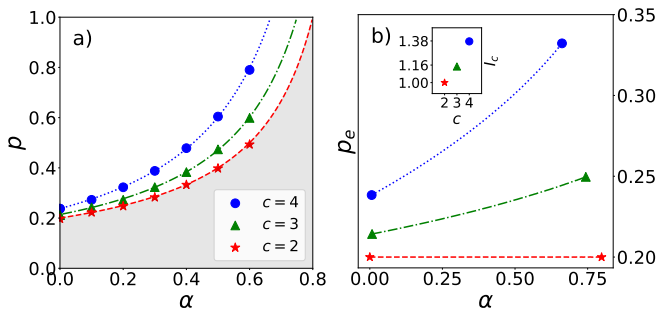


Figure 3.5. Phase diagram showing that increasing the clique size increases the epidemic threshold and effectiveness of contact tracing. (a) The critical curves where $R_e = 1$ in the αp -plane for $c \in \{2, 3, 4\}$. The shaded area is the sub-critical region for $c = 2$ where the infection eventually dies out after a finite number of generations for any clique size. (b) The same phase diagram in αp_e -plane, where $p_e = p(1 - \alpha)$ is the effective transmission probability. The inset in panel b shows the relative maximum increase in the effective epidemic threshold for different networks with cliques. Each point in the inset is the ratio of the p_e values at the endpoints of each curve outside the inset, such that $I_c = p_e(\alpha_{\max})/p_e(\alpha_{\min})$. This figure is from [Publication III](#).

and contact tracing modeling but highlights the importance of realistic social structures. Key findings include the efficiency of contact tracing in clustered networks and the impact of group sizes and contact tracing efficiency on outbreak control. Our model, which contrasts with traditional fully mixed or tree-like network assumptions, shows greater effectiveness in networks with clustering. It also reveals the importance of considering group structures in contact tracing, akin to complex contagion models where previous exposures affect adoption/infection chances. This is particularly beneficial in early disease spread stages, helping to limit infection paths. Our model also indicates that ignoring group structures in contact tracing can lead to an oversimplified understanding of infection risk and thresholds. We used a simplified dynamical model, integrating various factors into a single parameter, which may not fully capture the nuances of real-world contact tracing and disease spread.

Future research could incorporate more sophisticated SEIR models, but our focus was on the critical transition from disease-free to endemic states. The SIR model was chosen for its broad insights into epidemic outcomes, allowing us to examine the impact of clique structures and contact tracing on simple disease spread. In essence, our findings emphasize the need to consider realistic social network structures in epidemic modeling, showing that contact tracing is more efficient in clustered networks and that group size and tracing efficacy significantly influence epidemic control.

4. Conclusion

The COVID-19 pandemic has underscored the critical importance of comprehending epidemic dynamics, particularly in anticipation of future pandemics. As we discussed earlier and will explore in upcoming publications, the structure of social networks plays a pivotal role in the spread and intensity of epidemics, necessitating a deeper understanding of how various diseases propagate in society and the effectiveness of interventions within these networked structures. My research has focused on developing theoretical and computational approaches to gain insights into epidemic spreading in the presence of realistic social network structures, particularly in the context of vaccination and contact tracing, and how these interventions can be optimized given the networked nature of human populations.

The topology of contact networks significantly influences the dynamics of spreading phenomena. Group structures within these networks can either contain or facilitate the spread of information or diseases. A key element in these structures is homophily, the tendency of similar individuals to connect, which can create areas of increased vulnerability or resistance within the network. This phenomenon is particularly relevant in health behaviors like adopting digital contact tracing apps or taking vaccines. Traditional infectious disease models fall short of capturing the complexities of human interactions. Per contra, network-based frameworks give us a more detailed understanding.

The heterogeneity in human interactions also plays a crucial role when immunity arises from natural infection. Diseases initially target highly connected individuals, which can lead to efficient immunization of these nodes but also create localized weaknesses within the network. The interaction between network structure and epidemic dynamics, particularly the effects of network communities and higher-order interactions, remains a vital area of research. The impact of contact network structural and spatial properties on the threshold and robustness of herd immunity remains an area of exploration. In this thesis, I began to address these challenges by examining the effects of spatial structure on herd immunity

in various network models. Future research should extend these findings to networks with greater heterogeneity, such as scale-free networks. Non-pharmaceutical interventions like contact tracing are essential in controlling outbreaks, especially before vaccines become widely available. My research has delved into the dynamics of contact tracing within social groups and its influence on outbreak size and epidemic thresholds. Integrating real-world complexities, such as tracing delays and adherence to isolation protocols into models, remains a significant challenge.

This thesis delved into the temporal dynamics of spreading processes in networks, establishing a crucial link between temporal network reachability and percolation theory. It reveals that when constrained by limited waiting times, reachability exhibits a phase transition characteristic of directed percolation, suggesting a new approach to analyzing spreading behaviors. The research aims to uncover universal dynamics in spreading processes and reachability in complex systems, enhancing our understanding and aiding decision-making in policy and engineering. By integrating temporal network analysis with non-equilibrium statistical mechanics, the work identifies key measurable aspects of reachability, establishes their connection to directed percolation parameters, and demonstrates their alignment with directed percolation scaling behaviors. However, this is just the beginning, as further research is needed to refine methods for studying temporal network spreading and to observe these phenomena in empirical networks, thereby deepening our understanding of complex systems. A deeper understanding of reachability and spreading processes will be instrumental in navigating and comprehending complex systems and challenges.

As I draw to a close, I want to impart two profound insights that have guided me.

Modeling an epidemic is not rocket science, it's harder!

Nigel Goldenfeld, *Pritzker's COVID-19 press conference*

The most terrifying fact about the universe is not that it is hostile but that it is indifferent; but if we can come to terms with this indifference and accept the challenges of life within the boundaries of death—however mutable man may be able to make them—our existence as a species can have genuine meaning and fulfillment. However vast the darkness, we must supply our own light.

Stanley Kubrick, *Interviews (2001)*

References

- [1] Emmanuel Abbe. Community detection and stochastic block models: recent developments. *The Journal of Machine Learning Research*, 18(1):6446–6531, 2017.
- [2] Mohammed N Alenezi, Fawaz S Al-Anzi, Haneen Alabdulrazzaq, Ammar Al-husaini, and Abdullah F Al-Anzi. A study on the efficiency of the estimation models of covid-19. *Results in Physics*, 26:104370, 2021.
- [3] Alberto Aleta, David Martin-Corral, Ana Pastore y Piontti, Marco Ajelli, Maria Litvinova, Matteo Chinazzi, Natalie E Dean, M Elizabeth Halloran, Ira M Longini Jr, Stefano Merler, et al. Modelling the impact of testing, contact tracing and household quarantine on second waves of covid-19. *Nature Human Behaviour*, 4(9):964–971, 2020.
- [4] Amir A Aliabadi, Steven N Rogak, Karen H Bartlett, Sheldon I Green, et al. Preventing airborne disease transmission: review of methods for ventilation design in health care facilities. *Advances in preventive medicine*, 2011, 2011.
- [5] Philip W Anderson. *Basic notions of condensed matter physics*. CRC Press, 2018.
- [6] Alberto Antonioni and Marco Tomassini. Degree correlations in random geometric graphs. *Physical Review E*, 86(3):037101, 2012.
- [7] Elisha B Are, Kiffer G Card, and Caroline Colijn. The role of vaccine status homophily in the covid-19 pandemic: A cross-sectional survey with modeling. *medRxiv*, pages 2023–06, 2023.
- [8] H Ceren Ates, Ali K Yetisen, Firat Güder, and Can Dincer. Wearable devices for the detection of covid-19. *Nature Electronics*, 4(1):13–14, 2021.
- [9] Binish Ather, Taaha M Mirza, and Peter F Edemekong. Airborne precautions. 2018.
- [10] Krishna B. Athreya and Peter E. Ney. *Branching Processes*. Springer-Verlag, New York, 1972.
- [11] Arash Badie-Modiri. Error and attack tolerance of public transportation networks: A temporal networks approach. Master’s thesis, Aalto University School of Science, 2018. URL: <http://urn.fi/URN:NBN:fi:aalto-201806293772>.
- [12] Arash Badie-Modiri, Abbas K. Rizi, Márton Karsai, and Mikko Kivelä. Directed percolation in random temporal network models with heterogeneities. *Physical Review E*, 105(5):054313, 2022.

References

- [13] Arash Badie-Modiri, Abbas K. Rizi, Márton Karsai, and Mikko Kivelä. Directed percolation in temporal networks. *Physical Review Research*, 4(2):L022047, 2022.
- [14] Arash Badie-Modiri, Márton Karsai, and Mikko Kivelä. Efficient limited-time reachability estimation in temporal networks. *Physical Review E*, 101(5):052303, 2020.
- [15] Paolo Bajardi, Alain Barrat, Fabrizio Natale, Lara Savini, and Vittoria Colizza. Dynamical patterns of cattle trade movements. *PloS one*, 6(5):e19869, 2011. doi:[10.1371/journal.pone.0019869](https://doi.org/10.1371/journal.pone.0019869).
- [16] Per Bak, Kim Christensen, Leon Danon, and Tim Scanlon. Unified scaling law for earthquakes. *Physical Review Letters*, 88(17):178501, 2002. doi:[10.1103/PhysRevLett.88.178501](https://doi.org/10.1103/PhysRevLett.88.178501).
- [17] Laleh Bakhtiar et al. *The canon of medicine*, volume 1. Kazi Publications, 1999.
- [18] Albert-Laszlo Barabasi. The origin of bursts and heavy tails in human dynamics. *Nature*, 435(7039):207–211, 2005. doi:[10.1038/nature03459](https://doi.org/10.1038/nature03459).
- [19] Alain Barrat, Marc Barthelemy, and Alessandro Vespignani. *Dynamical processes on complex networks*. Cambridge university press, 2008.
- [20] Alain Barrat, Ciro Cattuto, Mikko Kivelä, Sune Lehmann, and Jari Saramäki. Effect of manual and digital contact tracing on covid-19 outbreaks: A study on empirical contact data. *Journal of the Royal Society Interface*, 18(178):20201000, 2021.
- [21] Marc Barthélemy. Spatial networks. *Physics reports*, 499(1-3):1–101, 2011.
- [22] Marc Barthelemy. *Spatial Networks: A Complete Introduction: From Graph Theory and Statistical Physics to Real-World Applications*. Springer Nature, 2022.
- [23] Rodney J Baxter. *Exactly solved models in statistical mechanics*. Elsevier, 2016.
- [24] Peter S Bearman, James Moody, and Katherine Stovel. Chains of affection: The structure of adolescent romantic and sexual networks. *American journal of sociology*, 110(1):44–91, 2004. doi:[10.1086/386272](https://doi.org/10.1086/386272).
- [25] John M Beggs and Dietmar Plenz. Neuronal avalanches in neocortical circuits. *Journal of neuroscience*, 23(35):11167–11177, 2003. doi:[10.1523/JNEUROSCI.23-35-11167.2003](https://doi.org/10.1523/JNEUROSCI.23-35-11167.2003).
- [26] James Bell, Ginestra Bianconi, David Butler, Jon Crowcroft, Paul CW Davies, Chris Hicks, Hyunju Kim, Istvan Z Kiss, Francesco Di Lauro, Carsten Maple, et al. Beyond covid-19: network science and sustainable exit strategies. *Journal of Physics: Complexity*, 2(2):021001, 2021.
- [27] Md Arif Billah, Md Mamun Miah, and Md Nuruzzaman Khan. Reproductive number of coronavirus: A systematic review and meta-analysis based on global level evidence. *PloS one*, 15(11):e0242128, 2020.
- [28] Béla Bollobás. The diameter of random graphs. *Transactions of the American Mathematical Society*, 267(1):41–52, 1981.
- [29] Béla Bollobás. Random graphs. In *Modern graph theory*, pages 215–252. Springer, 1998. doi:[10.1007/978-1-4612-0619-4_7](https://doi.org/10.1007/978-1-4612-0619-4_7).
- [30] Lera Boroditsky and Michael Ramscar. First, we assume a spherical cow... *Behavioral and Brain Sciences*, 24(4):656–657, 2001.

- [31] Pierre-Yves Boëlle and Eugenio Valdano. The importance of increasing primary vaccinations against covid-19 in europe. *Infectious Disease Modelling*, 9(1):1–9, 2024. URL: <https://www.sciencedirect.com/science/article/pii/S2468042723000982>, doi:<https://doi.org/10.1016/j.idm.2023.11.008>.
- [32] Dan Braha and Yaneer Bar-Yam. Time-dependent complex networks: Dynamic centrality, dynamic motifs, and cycles of social interactions. In *Adaptive Networks*, pages 39–50. Springer, 2009. doi:[10.1007/978-3-642-01284-6_3](https://doi.org/10.1007/978-3-642-01284-6_3).
- [33] Aaron Bramson and Benjamin Vandermarliere. Dynamical properties of interaction data. *Journal of Complex Networks*, 4(1):87–114, 2016. doi:[10.1093/comnet/cnv009](https://doi.org/10.1093/comnet/cnv009).
- [34] Allan M Brandt. The history of contact tracing and the future of public health, 2022.
- [35] Tom Britton, Frank Ball, and Pieter Trapman. A mathematical model reveals the influence of population heterogeneity on herd immunity to SARS-CoV-2. *Science*, 369(6505):846–849, August 2020.
- [36] Anna D Broido and Aaron Clauset. Scale-free networks are rare. *Nature communications*, 10(1):1017, 2019.
- [37] Andrew F Brouwer. Why the spectral radius? an intuition-building introduction to the basic reproduction number. *Bulletin of Mathematical Biology*, 84(9):96, 2022.
- [38] Giulio Burgio, Benjamin Steinegger, and Alex Arenas. Homophily impacts the success of vaccine roll-outs. *Communications Physics*, 5(1):70, 2022.
- [39] John Cardy. *Scaling and renormalization in statistical physics*, volume 5. Cambridge university press, 1996.
- [40] Carlos W Castillo-Garsow and Carlos Castillo-Chavez. A tour of the basic reproductive number and the next generation of researchers. *An Introduction to Undergraduate Research in Computational and Mathematical Biology: From Birdsongs to Viscosities*, pages 87–124, 2020.
- [41] Shi Chen and Cristina Lanzas. Distinction and connection between contact network, social network, and disease transmission network. *Preventive veterinary medicine*, 131:8–11, 2016.
- [42] Zesheng Chen. Discrete-time vs. continuous-time epidemic models in networks. *IEEE Access*, 7:127669–127677, 2019.
- [43] Jonathan R Chubb, Tatjana Trcek, Shailesh M Shenoy, and Robert H Singer. Transcriptional pulsing of a developmental gene. *Current biology*, 16(10):1018–1025, 2006. doi:[10.1016/j.cub.2006.03.092](https://doi.org/10.1016/j.cub.2006.03.092).
- [44] Fan Chung and Linyuan Lu. The average distances in random graphs with given expected degrees. *Proceedings of the National Academy of Sciences*, 99(25):15879–15882, 2002.
- [45] Fan Chung and Linyuan Lu. Connected components in random graphs with given expected degree sequences. *Annals of combinatorics*, 6(2):125–145, 2002. doi:[10.1007/PL00012580](https://doi.org/10.1007/PL00012580).
- [46] Giulio Cimini, Tiziano Squartini, Fabio Saracco, Diego Garlaschelli, Andrea Gabrielli, and Guido Caldarelli. The statistical physics of real-world networks. *Nature Reviews Physics*, 1(1):58–71, 2019.
- [47] Reuven Cohen and Shlomo Havlin. Percolation in complex networks. *Complex Media and Percolation Theory*, pages 419–431, 2021.

References

- [48] Reuven Cohen, Shlomo Havlin, and Daniel Ben-Avraham. Efficient immunization strategies for computer networks and populations. *Physical review letters*, 91(24):247901, 2003.
- [49] James S Coleman. Relational Analysis: The Study of Social Organizations with Survey Methods. *Human Organization*, 17:28–36, 1958. doi:10.17730/humo.17.4.q5604m676260q8n7.
- [50] Ian Cooper, Argha Mondal, and Chris G Antonopoulos. A sir model assumption for the spread of covid-19 in different communities. *Chaos, Solitons & Fractals*, 139:110057, 2020.
- [51] Alvaro Corral. Local distributions and rate fluctuations in a unified scaling law for earthquakes. *Physical Review E*, 68(3):035102, 2003. doi:10.1103/PhysRevE.68.035102.
- [52] Leonardo Dalla Porta and Mauro Copelli. Modeling neuronal avalanches and long-range temporal correlations at the emergence of collective oscillations: Continuously varying exponents mimic m/eeg results. *PLoS computational biology*, 15(4):e1006924, 2019. doi:10.1371/journal.pcbi.1006924.
- [53] Leon Danon, Ashley P Ford, Thomas House, Chris P Jewell, Matt J Keeling, Gareth O Roberts, Joshua V Ross, Matthew C Vernon, et al. Networks and the epidemiology of infectious disease. *Interdisciplinary perspectives on infectious diseases*, 2011, 2011.
- [54] Paul L Delamater, Erica J Street, Timothy F Leslie, Y Tony Yang, and Kathryn H Jacobsen. Complexity of the basic reproduction number (r_0). *Emerging infectious diseases*, 25(1):1, 2019.
- [55] Odo Diekmann, Hans Heesterbeek, and Tom Britton. *Mathematical tools for understanding infectious disease dynamics*, volume 7. Princeton University Press, 2013.
- [56] Odo Diekmann, JAP Heesterbeek, and Michael G Roberts. The construction of next-generation matrices for compartmental epidemic models. *Journal of the royal society interface*, 7(47):873–885, 2010.
- [57] Odo Diekmann, Johan Andre Peter Heesterbeek, and Johan AJ Metz. On the definition and the computation of the basic reproduction ratio r_0 in models for infectious diseases in heterogeneous populations. *Journal of mathematical biology*, 28:365–382, 1990.
- [58] Reinhard Diestel. Graduate texts in mathematics: Graph theory. 2018.
- [59] Klaus Dietz. The estimation of the basic reproduction number for infectious diseases. *Statistical methods in medical research*, 2(1):23–41, 1993.
- [60] Klaus Dietz and JAP Heesterbeek. Daniel bernoulli’s epidemiological model revisited. *Mathematical biosciences*, 180(1-2):1–21, 2002.
- [61] Aolan Ding and Rick Durrett. The phase transition in chung-lu graphs. *arXiv:2305.08203*, 2023.
- [62] Cyril Domb. *Phase transitions and critical phenomena*. Elsevier, 2000.
- [63] Sergey N Dorogovtsev, Alexander V Goltsev, and José FF Mendes. Critical phenomena in complex networks. *Reviews of Modern Physics*, 80(4):1275, 2008.
- [64] Sergey N Dorogovtsev and José FF Mendes. *The nature of complex networks*. Oxford University Press, 2022.

- [65] Freeman Dyson et al. A meeting with enrico fermi. *Nature*, 427(6972):297–297, 2004.
- [66] Young-Ho Eom and Hang-Hyun Jo. Generalized friendship paradox in complex networks: The case of scientific collaboration. *Scientific reports*, 4(1):1–6, 2014.
- [67] Byron D Erath and Andrea R Ferro. Infectious disease transmission from bioaerosols. *Journal of Exposure Science & Environmental Epidemiology*, 32(5):645–646, 2022.
- [68] P ERDdS and A R&wi. On random graphs i. *Publ. math. debrecen*, 6(290-297):18, 1959.
- [69] Péter Érdi and János Tóth. *Mathematical models of chemical reactions: theory and applications of deterministic and stochastic models*. Manchester University Press, 1989.
- [70] C. P. Farrington. On vaccine efficacy and reproduction numbers. *Mathematical Biosciences*, 185:89–109, 2003. URL: <https://www.sciencedirect.com/science/article/pii/S0025556403000610>, doi:[https://doi.org/10.1016/S0025-5564\(03\)00061-0](https://doi.org/10.1016/S0025-5564(03)00061-0).
- [71] NH Fefferman and KL2365573 Ng. How disease models in static networks can fail to approximate disease in dynamic networks. *Physical Review E*, 76(3):031919, 2007. doi:10.1103/PhysRevE.76.031919.
- [72] Scott L Feld. Why your friends have more friends than you do. *American journal of sociology*, 96(6):1464–1477, 1991. doi:10.1086/229693.
- [73] Finnish Institute for Health and Welfare. Influenza vaccine, 2023. Accessed on [Insert Access Date Here]. URL: <https://thl.fi/en/web/infectious-diseases-and-vaccinations/vaccines-a-to-z/influenza-vaccine>.
- [74] Matthias Flückiger and Markus Ludwig. Spatial networks and the spread of covid-19: results and policy implications from germany. *Review of Regional Research*, pages 1–27, 2023.
- [75] B Fosdick, D Larremore, J Nishumura, and J Ugander. Configuring random graph models with fixed degree sequences. preprint, 2016.
- [76] Sylvain Gandon and Sébastien Lion. Targeted vaccination and the speed of sars-cov-2 adaptation. *Proceedings of the National Academy of Sciences*, 119(3):e2110666119, 2022.
- [77] Laetitia Gauvin, Mathieu Génois, Márton Karsai, Mikko Kivelä, Taro Takaguchi, Eugenio Valdano, and Christian L. Vestergaard. Randomized reference models for temporal networks. *SIAM Review*, 64(4):763–830, 2022. doi:10.1137/19M1242252.
- [78] Mohammad Ghaderi. Public health interventions in the face of pandemics: Network structure, social distancing, and heterogeneity. *European Journal of Operational Research*, 298(3):1016–1031, 2022.
- [79] Marius Gilbert, Mathias Dewatripont, Eric Muraille, Jean-Philippe Platteau, and Michel Goldman. Preparing for a responsible lockdown exit strategy. *Nature medicine*, 26(5):643–644, 2020.
- [80] Julia R Gog and T Déirdre Hollingsworth. Epidemic interventions: insights from classic results. *Philosophical Transactions of the Royal Society B*, 376(1829):20200263, 2021.

- [81] Nigel Goldenfeld. *Lectures on phase transitions and the renormalization group*. CRC Press, 2018.
- [82] Ido Golding, Johan Paulsson, Scott M Zawilski, and Edward C Cox. Real-time kinetics of gene activity in individual bacteria. *Cell*, 123(6):1025–1036, 2005. doi:10.1016/j.cell.2005.09.031.
- [83] Peter Grassberger. On the critical behavior of the general epidemic process and dynamical percolation. *Mathematical Biosciences*, 63(2):157–172, 1983.
- [84] John Graunt and Walter Francis Willcox. Natural and political observations made upon the bills of mortality. (*No Title*), 1939.
- [85] Trisha Greenhalgh, Jose L Jimenez, Kimberly A Prather, Zeynep Tufekci, David Fisman, and Robert Schooley. Ten scientific reasons in support of airborne transmission of sars-cov-2. *The lancet*, 397(10285):1603–1605, 2021.
- [86] Geoffrey Grimmett and Geoffrey Grimmett. Near the critical point: Scaling theory. *Percolation*, pages 232–253, 1999.
- [87] Bnaya Gross and Shlomo Havlin. Epidemic spreading and control strategies in spatial modular network. *Applied network science*, 5(1):1–14, 2020.
- [88] M. Elizabeth Halloran, Ira M. Longini, Jr., and Claudio J. Struchiner. Design and Interpretation of Vaccine Field Studies. *Epidemiologic Reviews*, 21:73–88, 03 1999. doi:10.1093/oxfordjournals.epirev.a017990.
- [89] Tiberiu Harko, Francisco SN Lobo, and MK3197716 Mak. Exact analytical solutions of the susceptible-infected-recovered (sir) epidemic model and of the sir model with equal death and birth rates. *Applied Mathematics and Computation*, 236:184–194, 2014.
- [90] Malte Henkel, Haye Hinrichsen, Sven Lübeck, and Michel Pleimling. *Non-equilibrium phase transitions*, volume 1. Springer, 2008. doi:10.1007/978-1-4020-8765-3.
- [91] Haye Hinrichsen. Non-equilibrium critical phenomena and phase transitions into absorbing states. *Advances in physics*, 49(7):815–958, 2000. doi:10.1080/00018730050198152.
- [92] Takayuki Hiraoka, Abbas K. Rizi, Zahra Ghadiri, Mikko Kivelä, and Jari Saramäki. The strength and weakness of disease-induced herd immunity. *arXiv:2307.04700*.
- [93] Takayuki Hiraoka, Abbas K. Rizi, Mikko Kivelä, and Jari Saramäki. Herd immunity and epidemic size in networks with vaccination homophily. *Physical Review E*, 105(5):L052301, 2022. doi:10.1103/PhysRevE.105.L052301.
- [94] Elizabeth A Hobson, Matthew J Silk, Nina H Fefferman, Daniel B Larremore, Puck Rombach, Saray Shai, and Noa Pinter-Wollman. A guide to choosing and implementing reference models for social network analysis. *Biological Reviews*, 96(6):2716–2734, 2021.
- [95] Paul W Holland, Kathryn Blackmond Laskey, and Samuel Leinhardt. Stochastic blockmodels: First steps. *Social networks*, 5(2):109–137, 1983.
- [96] Petter Holme. Network reachability of real-world contact sequences. *Physical Review E*, 71(4):046119, 2005. doi:10.1103/PhysRevE.71.046119.
- [97] Petter Holme. Modern temporal network theory: a colloquium. *The European Physical Journal B*, 88(9):1–30, 2015. doi:10.1140/epjb/e2015-60657-4.

- [98] Petter Holme. Rare and everywhere: Perspectives on scale-free networks. *Nature communications*, 10(1):1016, 2019.
- [99] Petter Holme. Fast and principled simulations of the sir model on temporal networks. *Plos one*, 16(2):e0246961, 2021. doi:10.1371/journal.pone.0246961.
- [100] Petter Holme and Jari Saramäki. Temporal networks. *Physics reports*, 519(3):97–125, 2012. doi:10.1016/j.physrep.2012.03.001.
- [101] Petter Holme and Jari Saramäki. A map of approaches to temporal networks. In *Temporal Network Theory*, pages 1–24. Springer, 2019. doi:10.1007/978-3-030-23495-9_1.
- [102] Li-Yang Hsu, Cheng-Chuan Lee, Justin A Green, Brenda Ang, Nicholas I Paton, Lawrence Lee, Jorge S Villacian, Poh-Lian Lim, Arul Earnest, and Yee-Sin Leo. Severe acute respiratory syndrome (sars) in singapore: clinical features of index patient and initial contacts. *Emerging infectious diseases*, 9(6):713, 2003.
- [103] Felix Joos, Guillem Perarnau, Dieter Rautenbach, and Bruce Reed. How to determine if a random graph with a fixed degree sequence has a giant component. *Probability Theory and Related Fields*, 170(1-2):263–310, 2018.
- [104] Alexander Jung and Yasmin SarcheshmehPour. Local graph clustering with network lasso. *IEEE Signal Processing Letters*, 28:106–110, 2020.
- [105] Abbas K. Rizi, Ali Fageeh, Arash Badie-Modiri, and Mikko Kivelä. Epidemic spreading and digital contact tracing: Effects of heterogeneous mixing and quarantine failures. *Physical Review E*, 105(4):044313, 2022.
- [106] Rebecca Kahn, Stephanie J Schrag, Jennifer R Verani, and Marc Lipsitch. Identifying and alleviating bias due to differential depletion of susceptible people in postmarketing evaluations of covid-19 vaccines. *American journal of epidemiology*, 191(5):800–811, 2022.
- [107] Brian Karrer and Mark EJ Newman. Random graphs containing arbitrary distributions of subgraphs. *Physical Review E*, 82(6):066118, 2010.
- [108] Brian Karrer and Mark EJ Newman. Stochastic blockmodels and community structure in networks. *Physical review E*, 83(1):016107, 2011.
- [109] Márton Karsai, Hang-Hyun Jo, Kimmo Kaski, et al. *Bursty human dynamics*. Springer, 2018.
- [110] Márton Karsai, Mikko Kivelä, Raj Kumar Pan, Kimmo Kaski, János Kertész, Albert-László Barabási, and Jari Saramäki. Small but slow world: How network topology and burstiness slow down spreading. *Physical Review E*, 83(2):025102, 2011. doi:10.1103/PhysRevE.83.025102.
- [111] Leah A Keating, James P Gleeson, and David JP O’Sullivan. Multitype branching process method for modeling complex contagion on clustered networks. *Physical Review E*, 105(3):034306, 2022.
- [112] Matt J Keeling and Ken TD Eames. Networks and epidemic models. *Journal of the royal society interface*, 2(4):295–307, 2005.
- [113] Eben Kenah, Joel C Miller, et al. Epidemic percolation networks, epidemic outcomes, and interventions. *Interdisciplinary perspectives on infectious diseases*, 2011, 2011.
- [114] Eben Kenah and James M Robins. Second look at the spread of epidemics on networks. *Physical Review E*, 76(3):036113, 2007. doi:10.1103/PhysRevE.76.036113.

- [115] István Z Kiss, Joel C Miller, Péter L Simon, et al. Mathematics of epidemics on networks. *Cham: Springer*, 598:31, 2017.
- [116] Stephen M Kissler, Christine Tedijanto, Edward Goldstein, Yonatan H Grad, and Marc Lipsitch. Projecting the transmission dynamics of sars-cov-2 through the postpandemic period. *Science*, 368(6493):860–868, 2020.
- [117] Mikko Kivelä, Alex Arenas, Marc Barthelemy, James P Gleeson, Yamir Moreno, and Mason A Porter. Multilayer networks. *Journal of complex networks*, 2(3):203–271, 2014. doi:[10.1093/comnet/cnu016](https://doi.org/10.1093/comnet/cnu016).
- [118] Mikko Kivelä, Jordan Cambe, Jari Saramäki, and Márton Karsai. Mapping temporal-network percolation to weighted, static event graphs. *Scientific reports*, 8(1):1–9, 2018. doi:[10.1038/s41598-018-29577-2](https://doi.org/10.1038/s41598-018-29577-2).
- [119] Nicole E. Kogan, Leonardo Clemente, Parker Liautaud, Justin Kaashoek, Nicholas B. Link, Andre T. Nguyen, Fred S. Lu, Peter Huybers, Bernd Resch, Clemens Havas, Andreas Petutschnig, Jessica Davis, Matteo Chinazzi, Backtosch Mustafa, William P. Hanage, Alessandro Vespignani, and Mauricio Santillana. An early warning approach to monitor covid-19 activity with multiple digital traces in near real time. *Science Advances*, 7(10), 2021. URL: <https://advances.sciencemag.org/content/7/10/eabd6989>, doi:[10.1126/sciadv.abd6989](https://doi.org/10.1126/sciadv.abd6989).
- [120] Sadamori Kojaku, Laurent Hébert-Dufresne, Enys Mones, Sune Lehmann, and Yong-Yeol Ahn. The effectiveness of backward contact tracing in networks. *Nature Physics*, pages 1–7, 2021.
- [121] Gautier Krings, Márton Karsai, Sebastian Bernhardsson, Vincent D Blondel, and Jari Saramäki. Effects of time window size and placement on the structure of an aggregated communication network. *EPJ Data Science*, 1(1):1–16, 2012. doi:[10.1140/epjds4](https://doi.org/10.1140/epjds4).
- [122] Ninaad Lasrado and Dan H Barouch. Sars-cov-2 hybrid immunity: The best of both worlds, 2023.
- [123] Ignazio Lazzizzera. An analytic approximate solution of the sir model. *arXiv preprint arXiv:2011.07494*, 2020.
- [124] Melissa Leach, Hayley MacGregor, Ian Scoones, and Annie Wilkinson. Post-pandemic transformations: How and why covid-19 requires us to rethink development. *World development*, 138:105233, 2021.
- [125] Clement Lee and Darren J Wilkinson. A review of stochastic block models and extensions for graph clustering. *Applied Network Science*, 4(1):1–50, 2019.
- [126] Grégoire Lemoult, Liang Shi, Kerstin Avila, Shreyas V Jalikop, Marc Avila, and Björn Hof. Directed percolation phase transition to sustained turbulence in couette flow. *Nature Physics*, 12(3):254–258, 2016. doi:[10.1038/nphys3675](https://doi.org/10.1038/nphys3675).
- [127] Nancy HL Leung. Transmissibility and transmission of respiratory viruses. *Nature Reviews Microbiology*, 19(8):528–545, 2021.
- [128] Ming Li, Run-Ran Liu, Linyuan Lü, Mao-Bin Hu, Shuqi Xu, and Yi-Cheng Zhang. Percolation on complex networks: Theory and application. *Physics Reports*, 907:1–68, 2021.
- [129] Shuping Li, Xiaorong Zhao, and Ruixia Zhang. Site-bond percolation model of epidemic spreading with vaccination in complex networks. *Journal of Mathematical Biology*, 85(5):49, 2022.

- [130] Marc Lipsitch and Rebecca Kahn. Interpreting vaccine efficacy trial results for infection and transmission. *Vaccine*, 39(30):4082–4088, 2021.
- [131] Su-Yu Liu, Andrea Baronchelli, and Nicola Perra. Contagion dynamics in time-varying metapopulation networks. *Physical Review E*, 87(3):032805, 2013. doi:10.1103/PhysRevE.87.032805.
- [132] László Lovász. *Large networks and graph limits*, volume 60. American Mathematical Soc., 2012.
- [133] R Duncan Luce and Albert D Perry. A method of matrix analysis of group structure. *Psychometrika*, 14(2):95–116, 1949.
- [134] Naoki Masuda and Petter Holme. Predicting and controlling infectious disease epidemics using temporal networks. *F1000prime reports*, 5, 2013. doi:10.12703/P5-6.
- [135] Auni Aslah Mat Daud. Five common misconceptions regarding flattening-the-curve of covid-19. *History and Philosophy of the Life Sciences*, 44(3):41, 2022.
- [136] Laura Matrajt and Tiffany Leung. Evaluating the effectiveness of social distancing interventions to delay or flatten the epidemic curve of coronavirus disease. *Emerging infectious diseases*, 26(8):1740, 2020.
- [137] Andrew Mellor. The temporal event graph. *Journal of Complex Networks*, 6(4):639–659, 2018. doi:10.1093/comnet/cnx048.
- [138] Andrew Mellor. Event graphs: Advances and applications of second-order time-unfolded temporal network models. *Advances in Complex Systems*, 22(03):1950006, 2019. doi:10.1142/S0219525919500061.
- [139] Sergey Melnik, Adam Hackett, Mason A Porter, Peter J Mucha, and James P Gleeson. The unreasonable effectiveness of tree-based theory for networks with clustering. *Physical Review E*, 83(3):036112, 2011.
- [140] Joel C Miller. Epidemic size and probability in populations with heterogeneous infectivity and susceptibility. *Physical Review E*, 76(1):010101, 2007. doi:10.1103/PhysRevE.76.010101.
- [141] Tejaswini Mishra, Meng Wang, Ahmed A Metwally, Gireesh K Bogu, Andrew W Brooks, Amir Bahmani, Arash Alavi, Alessandra Celli, Emily Higgs, Orit Dagan-Rosenfeld, et al. Pre-symptomatic detection of covid-19 from smartwatch data. *Nature Biomedical Engineering*, 4(12):1208–1220, 2020.
- [142] Jeta Molla, Alejandro Ponce de León Chávez, Takayuki Hiraoka, Tapio Ala-Nissila, Mikko Kivelä, and Lasse Leskelä. Adaptive and optimized covid-19 vaccination strategies across geographical regions and age groups. *PLoS computational biology*, 18(4):e1009974, 2022.
- [143] Michael Molloy and Bruce Reed. A critical point for random graphs with a given degree sequence. *Random structures & algorithms*, 6(2-3):161–180, 1995.
- [144] James Moody. The importance of relationship timing for diffusion. *Social forces*, 81(1):25–56, 2002. doi:10.1353/sof.2002.0056.
- [145] Alfredo Morabia. Epidemiology’s 350th anniversary: 1662–2012. *Epidemiology (Cambridge, Mass.)*, 24(2):179, 2013.
- [146] Eden Morales-Narváez and Can Dincer. The impact of biosensing in a pandemic outbreak: Covid-19. *Biosensors and Bioelectronics*, 163:112274, 2020.

- [147] Aravind Natarajan, Hao-Wei Su, and Conor Heneghan. Assessment of physiological signs associated with covid-19 measured using wearable devices. *NPJ digital medicine*, 3(1):1–8, 2020.
- [148] Alexander Nesterov and Pablo Héctor Mata Villafuerte. Critical phenomena in complex networks: from scale-free to random networks. *The European Physical Journal B*, 96(11):1–14, 2023.
- [149] M. E. J. Newman, S. H. Strogatz, and D. J. Watts. Random graphs with arbitrary degree distributions and their applications. *Phys. Rev. E*, 64:026118, Jul 2001. URL: <https://link.aps.org/doi/10.1103/PhysRevE.64.026118>, doi: [10.1103/PhysRevE.64.026118](https://doi.org/10.1103/PhysRevE.64.026118).
- [150] Mark EJ Newman. Spread of epidemic disease on networks. *Physical review E*, 66(1):016128, 2002. doi:[10.1103/PhysRevE.66.016128](https://doi.org/10.1103/PhysRevE.66.016128).
- [151] Mark EJ Newman. *Networks*. Oxford university press, 2018.
- [152] Michael Nikolaou. Revisiting the standard for modeling the spread of infectious diseases. *Scientific Reports*, 12(1):7077, 2022.
- [153] US Department of Health, Human Services, et al. What is the difference between isolation and quarantine?, 2020.
- [154] Augustine Okolie, Johannes Müller, and Mirjam Kretzschmar. Parameter estimation for contact tracing in graph-based models. *Journal of the Royal Society Interface*, 20(208):20230409, 2023.
- [155] Nuria Oliver, Bruno Lepri, Harald Sterly, Renaud Lambiotte, Sébastien Deletaille, Marco De Nadai, Emmanuel Letouzé, Albert Ali Salah, Richard Benjamins, Ciro Cattuto, et al. Mobile phone data for informing public health actions across the covid-19 pandemic life cycle, 2020.
- [156] Daniel P Oran and Eric J Topol. Prevalence of asymptomatic sars-cov-2 infection: a narrative review. *Annals of internal medicine*, 173(5):362–367, 2020.
- [157] Juyong Park and Mark EJ Newman. Statistical mechanics of networks. *Physical Review E*, 70(6):066117, 2004.
- [158] Romualdo Pastor-Satorras, Claudio Castellano, Piet Van Mieghem, and Alessandro Vespignani. Epidemic processes in complex networks. *Reviews of modern physics*, 87(3):925, 2015. doi:[10.1016/j.physrep.2020.12.003](https://doi.org/10.1016/j.physrep.2020.12.003).
- [159] Romualdo Pastor-Satorras and Alessandro Vespignani. Immunization of complex networks. *Physical review E*, 65(3):036104, 2002.
- [160] Leto Peel, Daniel B Larremore, and Aaron Clauset. The ground truth about metadata and community detection in networks. *Science advances*, 3(5):e1602548, 2017.
- [161] Lorenzo Pellis, Neil M Ferguson, and Christophe Fraser. The relationship between real-time and discrete-generation models of epidemic spread. *Mathematical biosciences*, 216(1):63–70, 2008.
- [162] Mathew Penrose. *Random geometric graphs*, volume 5. OUP Oxford, 2003.
- [163] Nicola Perra. Non-pharmaceutical interventions during the covid-19 pandemic: A review. *Physics Reports*, 913:1–52, 2021.
- [164] Nicola Perra, Duygu Balcan, Bruno Gonçalves, and Alessandro Vespignani. Towards a characterization of behavior-disease models. *PloS one*, 6(8):e23084, 2011.

- [165] Nicola Perra, Bruno Gonçalves, Romualdo Pastor-Satorras, and Alessandro Vespignani. Activity driven modeling of time varying networks. *Scientific reports*, 2(1):469, 2012.
- [166] Carlo Piccardi. Social networks and the spread of epidemics. *Lettera Matematica*, 1:119–126, 2013.
- [167] Mason A Porter and James P Gleeson. Dynamical systems on networks.
- [168] MJ Powell. Site percolation in random networks. *Physical Review B*, 21(8):3725, 1980.
- [169] Giorgio Quer, Jennifer M Radin, Matteo Gadaleta, Katie Baca-Motes, Lauren Ariniello, Edward Ramos, Vik Kheterpal, Eric J Topol, and Steven R Steinhubl. Wearable sensor data and self-reported symptoms for covid-19 detection. *Nature Medicine*, 27(1):73–77, 2021.
- [170] Luis EC Rocha, Fredrik Liljeros, and Petter Holme. Simulated epidemics in an empirical spatiotemporal network of 50,185 sexual contacts. *PLoS computational biology*, 7(3):e1001109, 2011. doi:[10.1371/journal.pcbi.1001109](https://doi.org/10.1371/journal.pcbi.1001109).
- [171] Kenneth J Rothman. The rise and fall of epidemiology, 1950–2000 ad. *International journal of epidemiology*, 36(4):708–710, 2007.
- [172] Carlo Rovelli. *There Are Places in the World Where Rules Are Less Important Than Kindness: And Other Thoughts on Physics, Philosophy and the World*. Penguin, 2023.
- [173] Abbas Ali Saberi. Recent advances in percolation theory and its applications. *Physics Reports*, 578:1–32, 2015.
- [174] Marcel Salathe, Linus Bengtsson, Todd J Bodnar, Devon D Brewer, John S Brownstein, Caroline Buckee, Ellsworth M Campbell, Ciro Cattuto, Shashank Khandelwal, Patricia L Mabry, et al. Digital epidemiology. *PLoS Comput Biol*, 8(7):e1002616, 2012.
- [175] Masaki Sano and Keiichi Tamai. A universal transition to turbulence in channel flow. *Nature Physics*, 12(3):249–253, 2016. doi:[10.1038/nphys3659](https://doi.org/10.1038/nphys3659).
- [176] Clodomir Santana, Federico Botta, Hugo Barbosa, Filippo Privitera, Ronaldo Menezes, and Riccardo Di Clemente. Covid-19 is linked to changes in the time–space dimension of human mobility. *Nature Human Behaviour*, pages 1–11, 2023.
- [177] Jari Saramäki, Arash Badie-Modiri, Abbas K. Rizi, Mikko Kivelä, and Márton Karsai. Weighted temporal event graphs and temporal-network connectivity. In *Temporal Network Theory*, pages 107–130. Springer, 2023.
- [178] Jari Saramäki and Petter Holme. *Temporal Network Theory*. Springer International Publishing, Cham, 2023. doi:[10.1007/978-3-031-30399-9](https://doi.org/10.1007/978-3-031-30399-9).
- [179] Jari Saramäki, Mikko Kivelä, and Márton Karsai. Weighted temporal event graphs. In *Temporal Network Theory*, pages 107–128. Springer, 2019. doi:[10.1007/978-3-030-23495-9_6](https://doi.org/10.1007/978-3-030-23495-9_6).
- [180] Yasmin SarcheshmehPour, Yu Tian, Linli Zhang, and Alexander Jung. Clustered federated learning via generalized total variation minimization. *IEEE Transactions on Signal Processing*, 2023.
- [181] Jonathan Schaffer. What not to multiply without necessity. *Australasian Journal of Philosophy*, 93(4):644–664, 2015.

References

- [182] Dhruv R Seshadri, Evan V Davies, Ethan R Harlow, Jeffrey J Hsu, Shanina C Knighton, Timothy A Walker, James E Voos, and Colin K Drummond. Wearable sensors for covid-19: a call to action to harness our digital infrastructure for remote patient monitoring and virtual assessments. *Frontiers in Digital Health*, 2:8, 2020.
- [183] James Sethna. *Statistical mechanics: entropy, order parameters, and complexity*, volume 14. Oxford University Press, USA, 2021.
- [184] Emily Seto, Priyanka Challa, and Patrick Ware. Adoption of covid-19 contact tracing apps: A balance between privacy and effectiveness. *Journal of medical Internet research*, 23(3):e25726, 2021.
- [185] Roy J Shephard. *An illustrated history of health and fitness, from pre-history to our post-modern world*. Springer, 2015.
- [186] Amir H Shirazi, Arash Badie-Modiri, Sara Heydari, Jennifer L Rohn, Gholam R Jafari, and Ali R Mani. Evolution of communities in the medical sciences: evidence from the medical words network. *Plos one*, 11(12):e0167546, 2016. doi:10.1371/journal.pone.0167546.
- [187] Didier Sornette. *Critical phenomena in natural sciences: chaos, fractals, selforganization and disorder: concepts and tools*. Springer Science & Business Media, 2006.
- [188] Tiziano Squartini, Joey de Mol, Frank den Hollander, and Diego Garlaschelli. Breaking of ensemble equivalence in networks. *Physical review letters*, 115(26):268701, 2015.
- [189] Juliette Stehlé, Nicolas Voirin, Alain Barrat, Ciro Cattuto, Lorenzo Isella, Jean-François Pinton, Marco Quaggiotto, Wouter Van den Broeck, Corinne Régis, Bruno Lina, et al. High-resolution measurements of face-to-face contact patterns in a primary school. *PloS one*, 6(8):e23176, 2011.
- [190] Kazumasa A Takeuchi, Masafumi Kuroda, Hugues Chaté, and Masaki Sano. Experimental realization of directed percolation criticality in turbulent liquid crystals. *Physical Review E*, 80(5):051116, 2009. doi:10.1103/PhysRevE.80.051116.
- [191] Pieter Trapman, Frank Ball, Jean-Stéphane Dhersin, Viet Chi Tran, Jacco Wallinga, and Tom Britton. Inferring R_0 in emerging epidemics—the effect of common population structure is small. *Journal of The Royal Society Interface*, 13:20160288, 2016. URL: <https://royalsocietypublishing.org/doi/abs/10.1098/rsif.2016.0288>, doi:10.1098/rsif.2016.0288.
- [192] Lucas Daniel Valdez, Lautaro Vassallo, and Lidia Adriana Braunstein. Epidemic control in networks with cliques. *Physical Review E*, 107(5):054304, 2023.
- [193] Pauline Van den Driessche. Reproduction numbers of infectious disease models. *Infectious disease modelling*, 2(3):288–303, 2017.
- [194] Remco Van Der Hofstad. *Random graphs and complex networks*, volume 43. Cambridge university press, 2016.
- [195] Pim van der Hoorn, Gabor Lippner, and Dmitri Krioukov. Sparse maximum-entropy random graphs with a given power-law degree distribution. *Journal of Statistical Physics*, 173:806–844, 2018.
- [196] Richard S Varga. Iterative analysis. *New Jersey*, 322, 1962.
- [197] Emilia Vynnycky and Richard White. *An introduction to infectious disease modelling*. OUP oxford, 2010.

- [198] Benjamin Wacker and Jan Schlüter. Time-continuous and time-discrete sir models revisited: theory and applications. *Advances in Difference Equations*, 2020(1):556, 2020.
- [199] Patrick GT Walker, Charles Whittaker, Oliver J Watson, Marc Baguelin, Peter Winskill, Arran Hamlet, Bimandra A Djafaara, Zulma Cucunubá, Daniela Olivera Mesa, Will Green, et al. The impact of covid-19 and strategies for mitigation and suppression in low-and middle-income countries. *Science*, 369(6502):413–422, 2020.
- [200] Chia C Wang, Kimberly A Prather, Josué Sznitman, Jose L Jimenez, Seema S Lakdawala, Zeynep Tufekci, and Linsey C Marr. Airborne transmission of respiratory viruses. *Science*, 373(6558):eabd9149, 2021.
- [201] Wei Wang, Ming Tang, H Eugene Stanley, and Lidia A Braunstein. Unification of theoretical approaches for epidemic spreading on complex networks. *Reports on progress in physics*, 80(3):036603, 2017.
- [202] Zhen Wang, Chris T Bauch, Samit Bhattacharyya, Alberto d’Onofrio, Piero Manfredi, Matjaž Perc, Nicola Perra, Marcel Salathé, and Dawei Zhao. Statistical physics of vaccination. *Physics Reports*, 664:1–113, 2016.
- [203] Stanley Wasserman, Katherine Faust, et al. *Social network analysis: Methods and applications*. Cambridge university press, 1994.
- [204] Duncan J Watts and Steven H Strogatz. Collective dynamics of ‘small-world’ networks. *nature*, 393(6684):440–442, 1998. doi:[10.1038/30918](https://doi.org/10.1038/30918).
- [205] Nicholas C Wormald et al. Models of random regular graphs. *London Mathematical Society Lecture Note Series*, pages 239–298, 1999.
- [206] Ana Pastore y Piontti, Nicola Perra, Luca Rossi, Nicole Samay, and Alessandro Vespignani. *Charting the next pandemic: modeling infectious disease spreading in the data science age*. Springer, 2019.
- [207] W Yang, D Zhang, L Peng, C Zhuge, and L Hong. Rational evaluation of various epidemic models based on the covid-19 data of china [internet]. *Nueva York: ArXiv*, 2020.
- [208] Dongni Zhang and Tom Britton. Epidemic models with digital and manual contact tracing. *arXiv preprint arXiv:2211.12869*, 2022.
- [209] Zhaoyang Zhang, Honggang Wang, Chonggang Wang, and Hua Fang. Modeling epidemics spreading on social contact networks. *IEEE transactions on emerging topics in computing*, 3(3):410–419, 2015.
- [210] Qiankun Zhao, Yuan Tian, Qi He, Nuria Oliver, Ruoming Jin, and Wang-Chien Lee. Communication motifs: a tool to characterize social communications. In *Proceedings of the 19th ACM international conference on Information and knowledge management*, pages 1645–1648, 2010. doi:[10.1145/1871437.1871694](https://doi.org/10.1145/1871437.1871694).

Publication I

T. Hiraoka, A. K. Rizi, J. Saramäki and M. Kivelä. Herd immunity and epidemic size in networks with vaccination homophily . *Physical Review E*, 105(5) L052301, May 2020.

© 2020 Hiraoka et al.

Reprinted with permission.

Herd immunity and epidemic size in networks with vaccination homophily

Takayuki Hiraoka ^{*}, Abbas K. Rizi , Mikko Kivelä , and Jari Saramäki
Department of Computer Science, Aalto University, 00076 Espoo, Finland

 (Received 21 December 2021; accepted 26 April 2022; published 12 May 2022)

We study how the herd immunity threshold and the expected epidemic size depend on homophily with respect to vaccine adoption. We find that the presence of homophily considerably increases the critical vaccine coverage needed for herd immunity and that strong homophily can push the threshold entirely out of reach. The epidemic size monotonically increases as a function of homophily strength for a perfect vaccine, while it is maximized at a nontrivial level of homophily when the vaccine efficacy is limited. Our results highlight the importance of vaccination homophily in epidemic modeling.

DOI: [10.1103/PhysRevE.105.L052301](https://doi.org/10.1103/PhysRevE.105.L052301)

I. INTRODUCTION

In the paradigmatic susceptible-infectious-recovered model of infectious disease in a fully mixed population [1,2], so-called herd immunity is reached when the fraction π_v of the population that is immune to the disease through vaccination or previous infection is larger than

$$\pi_v^c = 1 - \frac{1}{R_0}, \quad (1)$$

where R_0 denotes the basic reproduction number, i.e., the expected number of secondary cases produced by a typical infectious individual in a fully susceptible population. Here, herd immunity means that the disease cannot spread in the population because each infected individual can only transmit the infection to less than one other individual on average; that is, the effective reproduction number $R_{\text{eff}} = (1 - \pi_v)R_0 < 1$. Consequently, not only those who are vaccinated but also the unvaccinated individuals are collectively protected from the disease.

This model assumes homogeneous mixing where individuals interact with each other randomly and independently of their properties, such as their vaccination status. However, this is a premise that may be too simplistic for modeling real-world populations, which often exhibit inhomogeneous mixing patterns that can lead to nontrivial epidemic outcomes [3–6]. One of the inhomogeneities that would be particularly relevant to vaccine-induced herd immunity is the correlation between the vaccination status of interacting individuals [7–12]. When this correlation exists, the vaccinated and unvaccinated individuals have different compositions of vaccinated and unvaccinated neighbors. Let us introduce the term *vaccination homophily* to represent mixing patterns that are assortative with respect to vaccination status, so that connections are more probable within the vaccinated and unvaccinated populations than between them. In this Letter, we

investigate the effect of vaccination homophily on the herd immunity threshold and the expected epidemic size.

II. MODEL

To this end, we formulate a random network theory of epidemic spreading under homophily with respect to the adoption of an immunity-inducing vaccine. The links in the network represent transmissible contacts between individuals, i.e., a susceptible individual will get infected if connected to an infected individual. We refer to this network as the *transmission network* to avoid confusion with the *contact network*. Each link in the contact network will let the disease be transmitted through it with a certain probability; the links on which transmission actually takes place constitute the transmission network [13,14]. Here, we do not explicitly consider this probabilistic transmission process but rather take the transmission network as a given.

Within the population, a fraction π_v of the population adopts the vaccine, while the remaining fraction $\pi_u = 1 - \pi_v$ is not vaccinated. Vaccination homophily can be expressed in terms of the bias in the probabilities of connections within the two groups. Let us denote the conditional probability that a random neighbor of an individual is vaccinated given that the individual is vaccinated by π_{vv} and, similarly, the conditional probability that a random neighbor of an unvaccinated individual is not vaccinated by π_{uu} . Assuming that the average degrees (numbers of connections) of the vaccinated and unvaccinated populations are equal, the two probabilities are related as $\pi_{uu} = 1 - (1 - \pi_{vv})\pi_v/\pi_u$.

The problem of using the connection probabilities π_{vv} and π_{uu} as measures of homophily is that they are not orthogonal to π_v , so even if we fix the value of π_{vv} , the strength of homophily varies with different values of π_v . Moreover, the two connection probabilities are coupled in a nonlinear manner, making it difficult to justify using either of them as a representative measure of the homophily of the entire network structure. To address these issues, we adopt the Coleman homophily index, originally proposed for social network analysis [15] and

^{*}takayuki.hiraoka@aalto.fi

defined by

$$h = \frac{\pi_{vv} - \pi_v}{1 - \pi_v} = \frac{\pi_{uu} - \pi_u}{1 - \pi_u}. \quad (2)$$

This measure has desirable axiomatic properties: (i) it is an increasing function of both π_{vv} and π_{uu} , (ii) it is symmetric for the vaccinated and unvaccinated populations, and (iii) it takes a value of zero when the mixing is homogeneous (no homophily) and a value of one when all links are inside the two groups, that is, $\pi_{vv} = \pi_{uu} = 1$. A negative value implies that the network is heterophilic in terms of vaccination status. Note that the connection probabilities $\pi_{vv} = \pi_v + \pi_u h$ and $\pi_{uu} = \pi_u + \pi_v h$ must be positive and therefore the Coleman homophily index is bounded from below as $h \geq \max(-\pi_v/\pi_u, -\pi_u/\pi_v)$.

We consider the transmission network structure where π_v , h , and the degree distribution $P(k)$ are specified but otherwise maximally randomized. By letting $\langle \cdot \rangle$ denote an average with respect to $P(k)$, the distribution of the excess degree \tilde{k} , i.e., the number of other neighbors that a randomly chosen neighbor of a randomly chosen node has, is given by $(\tilde{k} + 1)P(\tilde{k} + 1)/\langle k \rangle$. Neglecting the rare cycles, we can identify the basic reproduction number as the mean excess degree of the transmission network as $R_0 = \langle k^2 \rangle / \langle k \rangle - 1$ [16–18].

We consider a class of epidemic models where infection induces complete and permanent immunity, whereas the immunity induced by vaccines is generally incomplete. There are two effects of vaccine protection that are of interest for modeling herd immunity [19,20]. First, the vaccine can reduce the probability that the recipient becomes infected upon exposure. This reduction is referred to as the efficacy against susceptibility and denoted by f_s [21]. Second, individuals who are infected despite being vaccinated may have a lower probability of transmitting the infection to others. We represent this with the efficacy against infectiousness, f_i , defined as the reduction in the secondary infection rate.

Under this setup, the herd immunity threshold and the expected final size of a large epidemic can be derived from the structure of the transmission network alone, without explicitly considering the epidemic dynamics. In the following, we leverage the theory of branching processes and percolation theory to investigate these quantities of interest.

III. HERD IMMUNITY THRESHOLD

For a heterogeneous population consisting of multiple subpopulations, we can use the next-generation matrix (NGM) method [22,23] to identify the vaccination threshold π_v^c above which the disease cannot spread. While the NGM method was originally developed for epidemic dynamics described by ordinary differential equations, it can be naturally interpreted as a description of the local structure of the transmission network by a multitype branching process where the branching factor is the excess degree of the network. Let us denote by $I_v^{(m)}$ and $I_u^{(m)}$ the number of infections in the vaccinated and unvaccinated populations, respectively, at generation m from an index case (the first infected individual). Assuming a locally treelike network, we can

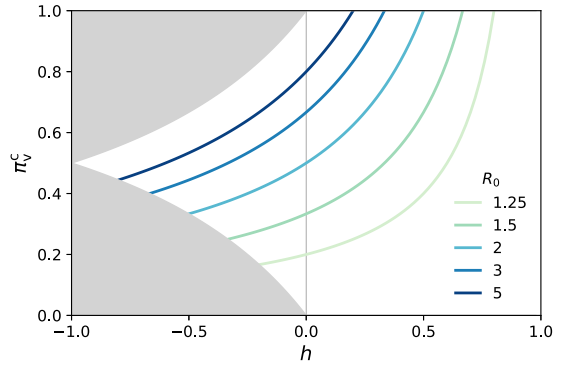


FIG. 1. Critical coverage π_v^c of a perfect vaccine required for herd immunity as a function of homophily strength h for different values of basic reproduction number R_0 . Positive and negative values of h imply homophily and heterophily, respectively. The area shaded in gray represents the parameter region where the network is unrealizable.

write the following recurrence equations under a mean-field approximation:

$$I_v^{(m+1)} = (1 - f_s)R_0[(1 - f_i)\pi_{vv}I_v^{(m)} + \pi_{uv}I_u^{(m)}], \quad (3)$$

$$I_u^{(m+1)} = R_0[(1 - f_i)\pi_{vu}I_v^{(m)} + \pi_{uu}I_u^{(m)}], \quad (4)$$

where $\pi_{uv} = 1 - \pi_{uu}$ and $\pi_{vu} = 1 - \pi_{vv}$ are the conditional probabilities that a link from one group points to the other. By writing $\mathbf{I}^{(m+1)} = \mathbf{A}\mathbf{I}^{(m)}$, where $\mathbf{I}^{(m)} = (I_v^{(m)}, I_u^{(m)})^\top$ and

$$\mathbf{A} = R_0 \begin{pmatrix} (1 - f_s)(1 - f_i)\pi_{vv} & (1 - f_s)\pi_{uv} \\ (1 - f_i)\pi_{vu} & \pi_{uu} \end{pmatrix},$$

we see that the infection eventually dies out after a finite number of generations if all the eigenvalues of the NGM \mathbf{A} have an absolute value of less than one. That is, at the critical point, the spectral radius $\rho(\mathbf{A}) = 1$.

By reparameterizing the connection probabilities with π_v and h , the critical vaccine coverage needed for herd immunity is given by

$$\pi_v^c = \frac{1 - \epsilon R_0 h}{(1 - \epsilon)(1 - h)} \left(1 - \frac{1}{R_0}\right), \quad (5)$$

where we define $\epsilon = (1 - f_s)(1 - f_i)$ and require $\epsilon \leq 1/R_0$. For $\epsilon > 1/R_0$, the vaccination threshold disappears and herd immunity becomes unattainable. For a perfect vaccine with $f_s = 1$ and/or $f_i = 1$, we have

$$\pi_v^c = \frac{1}{1 - h} \left(1 - \frac{1}{R_0}\right), \quad (6)$$

which reduces to the well-known threshold of Eq. (1) for homogeneous mixing with $h = 0$.

Equation (6) indicates that if the homophily strength h increases, so does the vaccine coverage π_v^c required for herd immunity (see Fig. 1). In other words, the presence of homophily makes herd immunity harder to reach. Notably, the

threshold occurs at $\pi_v^c = 1$ for

$$h \geq \frac{1}{R_0}, \tag{7}$$

implying that above this critical strength of homophily, one cannot attain herd immunity at all unless the entire population is vaccinated. That is, no matter how small the unvaccinated population is, there will always be a nonzero probability of a large epidemic within this population.

Finally, we note that the above discussion applies to any degree distribution $P(k)$ with mean excess degree R_0 .

IV. EPIDEMIC SIZE

When the vaccine coverage is below the threshold, an outbreak can result in an epidemic that infects a substantial fraction of the population. The size of such an epidemic coincides with the size of the giant component of the transmission network because all the individuals in a connected component will be infected if the index case belongs to the same component [13,17]. Let us denote the probability that a link pointing to a vaccinated node does not lead to the giant component by ϕ_v and the equivalent probability for an unvaccinated node by ϕ_u . These probabilities are subject to the following consistency equations:

$$\phi_v = f_S + (1 - f_S)g_1(f_I + (1 - f_I)(\pi_{vv}\phi_v + \pi_{vu}\phi_u)), \tag{8}$$

$$\phi_u = g_1(\pi_{uv}\phi_v + \pi_{uu}\phi_u), \tag{9}$$

where $g_1(x) = \sum_{k=1}^{\infty} kP(k)x^{k-1}/\langle k \rangle$ denotes the probability generating function of excess degree. Having solved the above consistency equations for ϕ_v and ϕ_u , we can compute the size of the vaccinated and unvaccinated populations contained in the giant component as

$$s_v = (1 - f_S)\pi_v[1 - g_0(f_I + (1 - f_I)(\pi_{vv}\phi_v + \pi_{vu}\phi_u))], \tag{10}$$

$$s_u = \pi_u[1 - g_0(\pi_{uv}\phi_v + \pi_{uu}\phi_u)], \tag{11}$$

respectively, where $g_0(x) = \sum_{k=0}^{\infty} P(k)x^k$ is the probability generating function of the degree distribution $P(k)$. The total size of the giant component is the sum of these two fractions $s = s_u + s_v$.

As an illustration, let us solve the above equations for a random network with a Poisson degree distribution $P(k) = \langle k \rangle^k e^{-\langle k \rangle} / k!$. For this network, the excess degree distribution is identical to the degree distribution and hence $\langle k \rangle = R_0$. Given this degree distribution, we get $g_0(x) = g_1(x) = \exp[-R_0(1 - x)]$. In the thermodynamic limit and in the absence of homophily ($h = 0$), this random network model with the Poisson degree distribution reduces to the Erdős-Rényi (ER) random graph ensemble, which is equivalent to homogeneous mixing. In other words, our model represents the simplest deviation from the ER model through the addition of homophily that biases the randomness of links.

First, let us consider the case of a perfect vaccine, for which $\phi_v = 1$. Equation (9) now becomes

$$\phi_u = \exp[-R_0\pi_{uu}(1 - \phi_u)], \tag{12}$$

which has an analytical solution:

$$\phi_u = -\frac{W(-R_0\pi_{uu} \exp(-R_0\pi_{uu}))}{R_0\pi_{uu}}. \tag{13}$$

Here, $W(\cdot)$ denotes the Lambert W function, which is the inverse function of $f(w) = we^w$. The giant component size is then calculated from Eq. (11) as

$$s = s_u = \pi_u\{1 - \exp[-R_0\pi_{uu}(1 - \phi_u)]\}, \tag{14}$$

where all infections are restricted to the unvaccinated population.

Figures 2(a)–2(d) show the solution of Eq. (14). The main observation is that the expected epidemic size always increases with homophily strength h . The difference in epidemic size under strong and weak homophily is especially significant when the vaccine coverage π_v is not small. As an example, for a disease with $R_0 = 1.5$, the homogeneous mixing assumption leads to the prediction that the vaccination threshold is 33%. However, even if the vaccine coverage is well above this threshold, strong homophily can still let the disease spread in the unvaccinated population and infect up to 58% of it [see Fig. 2(b)].

In the case of imperfect vaccines, the coupled consistency equations are not analytically tractable. The solution of Eq. (9) is given by

$$\phi_u = -\frac{W(-R_0\pi_{uu} \exp[-R_0[1 - (1 - \pi_{uu})\phi_v]])}{R_0\pi_{uu}}, \tag{15}$$

whereas for $f_S < 1$ and $f_I < 1$, Eq. (8) leads to

$$\phi_v = \frac{1}{1 - \pi_{vv}} \left(1 - \pi_{vv}\phi_v + \frac{1}{(1 - f_I)R_0} \log \frac{\phi_v - f_S}{1 - f_S} \right). \tag{16}$$

We can numerically solve for ϕ_v by equating the right hand sides of Eqs. (15) and (16). Plugging the results into Eqs. (10) and (11) yields the giant component size.

In what follows, we present the results for $f_I = 0$ and only vary the efficacy against susceptibility, f_S , for the sake of simplicity. Figures 2(e) and 2(f) show the epidemic size under the coverage of an imperfect vaccine. As expected, a smaller efficacy leads to a larger epidemic and a higher vaccination threshold. Unexpectedly, contrary to the case of perfect immunization, the epidemic size first grows and then shrinks with increasing homophily. This can be attributed to the following competing mechanisms affected by increased levels of homophily: (1) Similarly to the case of a perfect vaccine, more unvaccinated individuals will be infected as they are connected to fewer immune individuals and more densely within themselves, making them less protected by the herd immunity effect. (2) An imperfect vaccine leaves a part of the vaccinated population susceptible to breakthrough infections. In the weak homophily regime, more vaccinated individuals may contract the disease due to the larger epidemic in the unvaccinated population. The risk of breakthrough infection

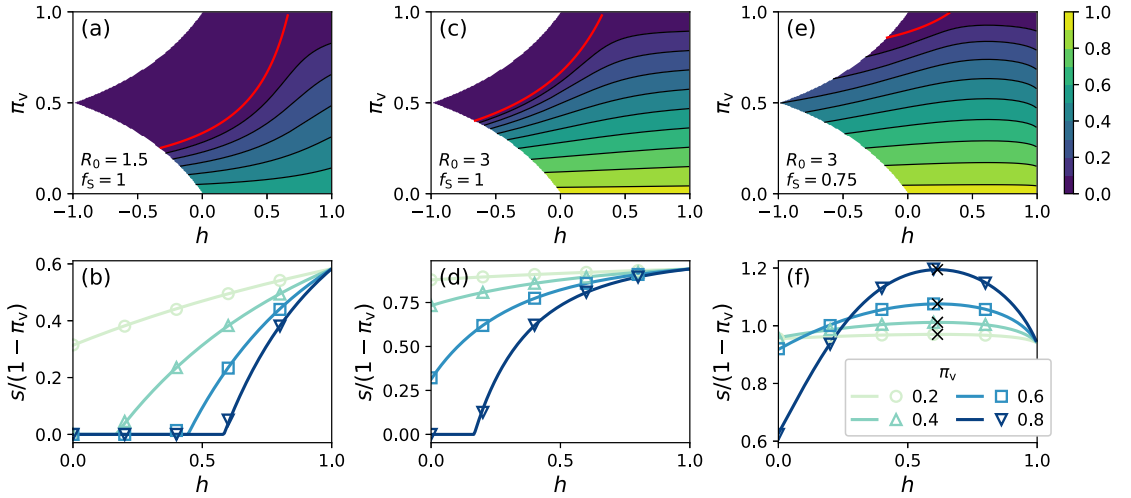


FIG. 2. Epidemic size in Poisson networks as a function of homophily strength h and vaccine coverage π_v . Top row: Two-dimensional heat maps representing the epidemic size. The solid red line in each panel denotes the vaccination threshold. We represent contours of the epidemic size at 0.1 intervals by different colors and solid black lines. Bottom row: Epidemic size divided by the size of the unvaccinated population. Theoretical predictions (in lines) are compared with the giant component sizes obtained by simulating networks of size $N = 10^5$ (in symbols). The details of the network simulation can be found in the Supplemental Material [24]. (a) and (b) show the results for $R_0 = 1.5$ and a perfect vaccine, (c) and (d) are for $R_0 = 3$ and a perfect vaccine, and (e) and (f) are for $R_0 = 3$ and an imperfect vaccine with $f_S = 0.75$. If the vaccine is perfect, only the unvaccinated individuals contract the disease; thus, the vertical axis in (b) and (d) corresponds to the fraction of the unvaccinated population that will be infected. The cross symbols in (f) indicate the maximum of each curve. Note that the homophily strength at which the epidemic size takes the maximum is independent of π_v .

decreases as they become less connected with the unvaccinated population in the strong homophily regime. Figure 3(a) gives an example of the two competing processes, where given $\pi_v = 0.8$, $R_0 = 3$, and vaccine efficacy $f_S = 0.75$, the final epidemic size varies between 13% and 24%, reaching its peak around $h = 0.62$.

As a consequence of the competition, the total number of infected individuals is maximized, in general, at a non-trivial level of homophily h^* , which depends on f_S and R_0 but not on the vaccine coverage π_v . The smaller the R_0 and higher the value of f_S , the higher the strength of homophily h^* that leads to the worst overall outcome [see Fig. 3(b)]. In other words, a highly infectious disease

countered by a vaccine with low efficacy spreads maximally in a population with a medium level of vaccination homophily, while less infectious diseases generally benefit from higher levels of homophily, especially if the vaccine efficacy is high. The maximum impact of homophily on epidemic size is further discussed in the Supplemental Material [24].

In the above discussion, we presented the results for the case where the transmission network has a Poisson degree distribution and the efficacy against infectiousness $f_I = 0$. These conditions can be altered. In the Supplemental Material [24], we calculate the epidemic size for transmission networks with more realistically heterogeneous excess degrees that follow the negative binomial distribution. We also discuss the case where both f_S and f_I are varied. In both cases, the epidemic outcomes are qualitatively similar to those obtained for Poisson networks and vaccines that purely affect susceptibility, except for the fact that the homophily level at which the epidemic size is maximized is no longer independent of vaccine coverage.

V. CONCLUSIONS AND DISCUSSION

We have studied the effect of vaccination homophily, i.e., assortative mixing by vaccination status, on the herd immunity threshold and the expected epidemic size. In human society, vaccination homophily can emerge due to the presence of confounding factors, such as age [5], geography [25,26], socioeconomic status [27], and personal and religious beliefs [28], that influence both the likelihood of interaction between

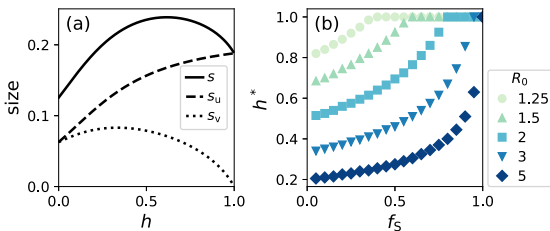


FIG. 3. Effects of vaccination homophily for imperfect vaccines. (a) The sizes of vaccinated population s_v and unvaccinated population s_u in the epidemic of size s . The parameters are $R_0 = 3$, $\pi_v = 0.8$, $f_S = 0.75$. (b) The homophily strength h^* maximising s as a function of f_S and R_0 .

individuals and the likelihood of them being in a common vaccination status. It can also occur as a consequence of behavioral contagion [29,30] or inequality in the access to the vaccine. Our analysis is built on a model that embodies a minimalistic departure from the traditional assumption of homogeneous mixing and shows that the vaccination threshold for herd immunity is higher for stronger vaccination homophily. This suggests that herd immunity is more difficult, if not impossible, to achieve in the presence of vaccination homophily. It also implies that the well-known formula of Eq. (1) underestimates the vaccination threshold by not taking homophily into account.

We also show that the behavior of epidemic size as a function of homophily varies depending on the vaccine efficacy against susceptibility; when the efficacy is high, homophily monotonically amplifies the epidemic, while the epidemic size peaks at a nontrivial level of homophily when the efficacy is low. This is due to the competition between the herd immunity effect by homogeneous mixing and the epidemic containment by segregation. We can identify the parameter values for which homophily has a large impact on the epidemic size, which will have direct implications for the design of intervention strategies.

Apart from vaccination homophily, another important type of inhomogeneity in networked epidemics is degree heterogeneity; namely, real-world epidemics often exhibit a large variance in the number of secondary infections, whose distribution can be modeled by a negative binomial distribution [4,6]. The herd immunity threshold given by Eq. (5) is not affected by the overdispersion of the distribution, but the

epidemic size depends on the full shape of the distribution and therefore differs from the one for a Poisson network, as shown in the Supplemental Material [24].

Recently, we became aware of two other research works [31,32] that report results in line with what we have described here. They found qualitatively similar effects of homophily on epidemic size for scale-free networks [31] and empirical contact networks [32]. This further corroborates the generalizability of our theoretical findings to networks with heterogeneous degree distributions [33].

As a final remark, we note that our approach has a broader scope. In this Letter, we focused on homophily by vaccination status; however, our framework is general enough to account for homophily by adherence to other epidemic interventions that reduce the susceptibility or infectiousness of individuals, such as the practice of social distancing [34], use of protective equipment [31], and adoption of digital contact tracing [35,36]. It can also be applied to the analysis of herd immunity in the case where the past infection (and consequent disease-induced immunity) is localized to a subpopulation [37] and in the case where the mixing pattern is assortative by risk factors of the disease [38].

ACKNOWLEDGMENTS

M.K. acknowledges support from Project No. 105572 NordicMathCovid as part of the Nordic Programme on Health and Welfare funded by NordForsk. The authors wish to acknowledge Aalto University Science-IT project for generous computational resources.

-
- [1] R. M. Anderson and R. M. May, *Infectious Diseases of Humans: Dynamics and Control* (Oxford University Press, Oxford, 1992).
- [2] H. W. Hethcote, The mathematics of infectious diseases, *SIAM Rev.* **42**, 599 (2000).
- [3] M. E. J. Newman, Mixing patterns in networks, *Phys. Rev. E* **67**, 026126 (2003).
- [4] J. O. Lloyd-Smith, S. J. Schreiber, P. E. Kopp, and W. M. Getz, Superspreading and the effect of individual variation on disease emergence, *Nature (London)* **438**, 355 (2005).
- [5] J. Mossong, N. Hens, M. Jit, P. Beutels, K. Auranen, R. Mikolajczyk, M. Massari, S. Salmaso, G. S. Tomba, J. Wallinga, J. Heijne, M. Sadkowska-Todys, M. Rosinska, and W. J. Edmunds, Social contacts and mixing patterns relevant to the spread of infectious diseases, *PLoS Medicine* **5**, e74 (2008).
- [6] L. Hébert-Dufresne, B. M. Althouse, S. V. Scarpino, and A. Allard, Beyond R_0 : Heterogeneity in secondary infections and probabilistic epidemic forecasting, *J. R. Soc. Interface* **17**, 20200393 (2020).
- [7] M. Salathé and S. Bonhoeffer, The effect of opinion clustering on disease outbreaks, *J. R. Soc. Interface* **5**, 1505 (2008).
- [8] M. L. Ndeffo Mbah, J. Liu, C. T. Bauch, Y. I. Tekel, J. Medlock, L. A. Meyers, and A. P. Galvani, The impact of imitation on vaccination behavior in social contact networks, *PLoS Comput. Biol.* **8**, e1002469 (2012).
- [9] V. C. Barclay, T. Smieszek, J. He, G. Cao, J. J. Rainey, H. Gao, A. Uzicanin, and M. Salathé, positive network assortativity of influenza vaccination at a high school: Implications for outbreak risk and herd immunity, *PLoS ONE* **9**, e87042 (2014).
- [10] R. Edge, J. Heath, B. Rowlingson, T. J. Keegan, and R. Isba, Seasonal influenza vaccination amongst medical students: A social network analysis based on a cross-sectional study, *PLoS ONE* **10**, e0140085 (2015).
- [11] S. A. Truelove, M. Graham, W. J. Moss, C. J. E. Metcalf, M. J. Ferrari, and J. Lessler, Characterizing the impact of spatial clustering of susceptibility for measles elimination, *Vaccine* **37**, 732 (2019).
- [12] C. Kadelka and A. McCombs, Effect of homophily and correlation of beliefs on COVID-19 and general infectious disease outbreaks, *PLoS ONE* **16**, e0260973 (2021).
- [13] M. E. J. Newman, Spread of epidemic disease on networks, *Phys. Rev. E* **66**, 016128 (2002).
- [14] R. Pastor-Satorras, C. Castellano, P. Van Mieghem, and A. Vespignani, Epidemic processes in complex networks, *Rev. Mod. Phys.* **87**, 925 (2015).
- [15] J. S. Coleman, Relational analysis: The study of social organizations with survey methods, *Human Organization* **17**, 28 (1958).
- [16] M. Molloy and B. Reed, A critical point for random graphs with a given degree sequence, *Random Struct. Alg.* **6**, 161 (1995).
- [17] M. E. J. Newman, S. H. Strogatz, and D. J. Watts, Random graphs with arbitrary degree distributions and their applications, *Phys. Rev. E* **64**, 026118 (2001).
- [18] P. Trapman, F. Ball, J.-S. Dhersin, V. C. Tran, J. Wallinga, and T. Britton, Inferring R_0 in emerging epidemics—the effect of

- common population structure is small, *J. R. Soc. Interface* **13**, 20160288 (2016).
- [19] M. E. Halloran, I. M. Longini, Jr., and C. J. Struchiner, Design and interpretation of vaccine field studies, *Epidemiologic Reviews* **21**, 73 (1999).
- [20] C. P. Farrington, On vaccine efficacy and reproduction numbers, *Math. Biosci.* **185**, 89 (2003).
- [21] Here we assume that the vaccine induces full immunity to a fraction f_S of the vaccinated individuals but leaves the remainder fully susceptible. In this model, the vaccine is *all or nothing*, in contrast to *leaky* vaccines which reduce the susceptibility of every recipient by an equal degree. The two models are equivalent under the assumption that the network is locally treelike, on which our study is based.
- [22] O. Diekmann, J. A. P. Heesterbeek, and J. A. J. Metz, On the definition and the computation of the basic reproduction ratio R_0 in models for infectious diseases in heterogeneous populations, *J. Math. Biol.* **28**, 365 (1990).
- [23] O. Diekmann, H. Heesterbeek, and T. Britton, *Mathematical Tools for Understanding Infectious Disease Dynamics* (Princeton University Press, Princeton, 2012).
- [24] See Supplemental Material at <http://link.aps.org/supplemental/10.1103/PhysRevE.105.L052301> for the details of network simulation and additional analysis on epidemic size.
- [25] S. B. Omer, K. S. Enger, L. H. Moulton, N. A. Halsey, S. Stokley, and D. A. Salmon, Geographic clustering of non-medical exemptions to school immunization requirements and associations with geographic clustering of pertussis, *Am. J. Epidemiol.* **168**, 1389 (2008).
- [26] S. Takahashi, C. J. E. Metcalf, M. J. Ferrari, A. J. Tatem, and J. Lessler, The geography of measles vaccination in the African Great Lakes region, *Nat. Commun.* **8**, 15585 (2017).
- [27] K. Danis, T. Georgakopoulou, T. Stavrou, D. Laggas, and T. Panagiotopoulos, Socioeconomic factors play a more important role in childhood vaccination coverage than parental perceptions: A cross-sectional study in Greece, *Vaccine* **28**, 1861 (2010).
- [28] P. A. Gastañaduy, J. Budd, N. Fisher, S. B. Redd, J. Fletcher, J. Miller, D. J. McFadden, J. Rota, P. A. Rota, C. Hickman, B. Fowler, L. Tatham, G. S. Wallace, S. de Fijter, A. Parker Fiebelkorn, and M. DiOrio, A measles outbreak in an underimmunized Amish community in Ohio, *N. Engl. J. Med.* **375**, 1343 (2016).
- [29] E. Campbell and M. Salathé, Complex social contagion makes networks more vulnerable to disease outbreaks, *Sci. Rep.* **3**, 1905 (2013).
- [30] P. Konstantinou, K. Georgiou, N. Kumar, M. Kyprianidou, C. Nicolaides, M. Karekla, and A. P. Kassianos, Transmission of vaccination attitudes and uptake based on social contagion theory: A scoping review, *Vaccines* **9**, 607 (2021).
- [31] H. Watanabe and T. Hasegawa, Impact of assortative mixing by mask-wearing on the propagation of epidemics in networks, [arXiv:2112.06589](https://arxiv.org/abs/2112.06589).
- [32] G. Burgio, B. Steinegger, and A. Arenas, Homophily impacts the success of vaccine roll-outs, *Commun. Phys.* **5**, 70 (2022).
- [33] Some readers may be curious about the herd immunity threshold for scale-free networks for which R_0 diverges. In a nonassortative scale-free network, $\pi_c^c = 1$, but Eq. (6) seems to imply that negative values of h could lower the threshold. However, the lowered threshold $\pi_c^c = 1/(1-h)$ agrees with the boundary of the parameter region in which a network is realizable. This means that the realizable scale-free networks will always be in the epidemic phase regardless of the vaccine coverage and strength of homophily (except for the trivial case where everyone is vaccinated).
- [34] S. Sajjadi, A. Hashemi, and F. Ghanbarnejad, Social distancing in pedestrian dynamics and its effect on disease spreading, *Phys. Rev. E* **104**, 014313 (2021).
- [35] G. Burgio, B. Steinegger, G. Rapisardi, and A. Arenas, Homophily in the adoption of digital proximity tracing apps shapes the evolution of epidemics, *Phys. Rev. Research* **3**, 033128 (2021).
- [36] A. K. Rizi, A. Faqeeh, A. Badie-Modiri, and M. Kivelä, Epidemic spreading and digital contact tracing: Effects of heterogeneous mixing and quarantine failures, *Phys. Rev. E* **105**, 044313 (2022).
- [37] T. Britton, F. Ball, and P. Trapman, A mathematical model reveals the influence of population heterogeneity on herd immunity to SARS-CoV-2, *Science* **369**, 846 (2020).
- [38] P. Lemieux-Mellouki, M. Drolet, J. Brisson, E. L. Franco, M.-C. Boily, I. Baussano, and M. Brisson, Assortative mixing as a source of bias in epidemiological studies of sexually transmitted infections: The case of smoking and human papillomavirus, *Epidemiol. Infect.* **144**, 1490 (2016).

Publication II

T. Hiraoka, A. K. Rizzi, Z. Ghadiri, J. Saramäki and M. Kivelä. The strength and weakness of disease-induced herd immunity. *Presented at [NetSci 2023 Conference](#)*, pre-print: arXiv:2307.04700, Jul 2023.

© 2023 Hiraoka et al.

Reprinted with permission.

The strength and weakness of disease-induced herd immunity

Takayuki Hiraoka,* Abbas K. Rizi, Zahra Ghadiri, Mikko Kivelä, and Jari Saramäki
Department of Computer Science, Aalto University, 00076, Finland

When a fraction of a population becomes immune to an infectious disease, the risk of widespread outbreaks decreases non-linearly as a result of the collective protection known as herd immunity. Typically, immunity to a disease can be acquired through natural infection or vaccination. It has been argued that natural infection in a heterogeneous population may induce a stronger herd immunity effect than homogeneous vaccination, because the early stages of transmission would primarily affect highly interactive individuals, leading to more efficient suppression of subsequent infections. In this study, we provide a comprehensive assessment of the herd immunity effect by analyzing the behavior of the susceptible-infected-recovered (SIR) model on static contact networks. We find that the effectiveness of disease-induced herd immunity is shaped by two competing mechanisms: While it exploits degree heterogeneity in the contact network to efficiently target highly connected individuals for immunity, it also introduces mixing heterogeneity between immune and susceptible individuals, weakening herd immunity. By controlling the degree of spatial embeddedness of the contact network structure, we find that spatial structure generally makes herd immunity stronger and also enhances the advantage of the herd immunity effect induced by random immunization over the disease-induced one in networks with low degree heterogeneity. These findings provide valuable insights into the complexity of herd immunity and have implications for designing effective disease control strategies.

INTRODUCTION

When an infectious disease is transmitted directly through contact between individuals, conferring immunity on individuals has a non-linear impact on the level of protection of the population as a whole. Even if the disease is transmissible enough to spread through an immunologically naive population, it may stop circulating when a fraction of the population is immune due to either previous infection or vaccination. This phenomenon is called “herd immunity”, as it represents a collective effect where the immune individuals convey protection to the entire population. There are parallels between herd immunity and percolation phenomena, where a continuous phase transition separates the two phases in which the disease dies out and in which it spreads through a finite fraction of the population [1–5].

Historically, the threshold for herd immunity has been calculated assuming a population that is homogeneous in terms of mixing and consequently in terms of the number of contacts per individual (degree): everyone can randomly interact with everyone else, giving rise to Poisson degree distribution. Importantly, it has also been assumed that there is no structure in how immunity is distributed in the population. However, these assumptions are overly simplistic when applied to real-world populations—in reality, contact patterns are not uniform and random, mixing within the population is typically heterogeneous [6–9], and immunity may not be uniformly distributed [10, 11].

Many of such heterogeneities are readily captured by the complex networks of contacts through which the disease spreads. Network epidemiology has revealed the significant impact of heterogeneity on epidemic spread, chal-

lenging simplistic assumptions of homogeneity [2, 12–14]. For instance, in scale-free networks, the threshold can be as low as one, implying that containment is impossible unless the entire population acquires immunity. On the other hand, population heterogeneity can be leveraged to design targeted and efficient immunization strategies. Furthermore, a recent study by Britton *et al.* [15] demonstrated that, when immunity is induced by natural infection, population heterogeneity may lead to a lower herd immunity threshold than expected under homogeneous mixing because the disease spreads among highly interactive individuals at the early stage of the epidemic, resulting in more efficient immunization of these influential hubs.

However, in addition to degree heterogeneity, the structural aspects of the contact network need to be addressed. Random immunization through vaccination that is agnostic to individual attributes distributes immunity uniformly throughout the population; in contrast, natural immunity is inherently localized in the contact network. This is because those who get infected in an outbreak that originates from a single source are connected to each other in a chain of transmission, necessarily forming a connected subgraph in the contact network. This gives rise to mixing heterogeneities between immune and susceptible individuals, akin to those discussed in the context of vaccination and other interventions [10, 11, 16–18]. The consequences of such localization for herd immunity have not yet been explored in a systematic way [19–21].

Our aim in this paper is to conduct a comprehensive analysis of herd immunity induced by natural infection on contact networks by comparing it to the benchmark of herd immunity induced by random immunization. Building on the framework introduced by Newman [22], we

MODEL

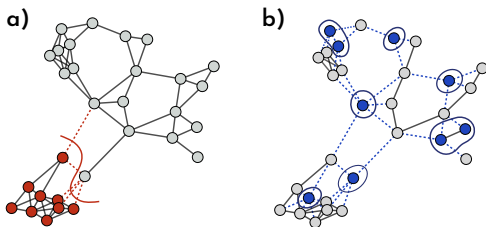


FIG. 1. (a) Nodes immunized by an epidemic outbreak (red) on a random geometric graph. The dashed edges and the red solid line indicate the interface between susceptible and immune nodes. (b) The same number of randomly immunized nodes (blue) on the same graph, resulting in a larger number of interface edges.

employ the susceptible-infected-recovered (SIR) dynamics as the epidemic model and measure the largest possible epidemic size after removing the recovered nodes. We show that the net effectiveness of disease-induced herd immunity is determined by the interplay of two competing mechanisms: the preferential immunization of highly connected nodes by the epidemic and the localization of immune nodes within the contact network. The former makes the herd immunity effect stronger, while the latter makes it weaker. Refer to Fig. 1 for visualization.

We illustrate the presence of the two mechanisms by inspecting the mean degree in the residual subgraph and the cut size between the removed and residual subgraphs. We analytically show that within the configuration model family of networks, the natural infection and random immunization yield herd immunity of equal effectiveness, specifically in Erdős-Rényi (ER) contact networks, even though they result in different mean residual degrees and cut sizes. Natural infection has an advantage over random immunization in networks with higher degree heterogeneity, while the opposite is true for networks with a more homogeneous degree distribution.

We further extend the comparison between natural infection and random immunization across various network geometries. Namely, we explore a wide spectrum of networks by systematically varying the levels of degree heterogeneity and spatial embeddedness of the network. Interestingly, when the spatially constrained network structure is gradually perturbed through random rewiring of edges, we find a non-monotonous behavior in both the strength of disease-induced herd immunity and its relative advantage over random immunization.

Epidemic dynamics and immunity

The susceptible-infected-recovered (SIR) model is a canonical compartmental model for non-recurrent epidemics. The individuals and the contacts between them are represented as nodes and edges in a static, undirected contact network of size N . Each node can be in one of three states: susceptible, infected, or recovered. The dynamics run in continuous time. Transmission occurs between each connected pair of an infected node and a susceptible node independently at rate β , after which the susceptible node becomes infected. An infected node recovers at rate γ , losing the ability to infect its neighbors. After recovery, nodes gain immunity and never become infected again, meaning that they are effectively removed from the system. The probability T that transmission occurs on an edge between an infected node and a susceptible node is given by $T = \beta/(\beta + \gamma)$ [2]. In the following, we set $\gamma = 1$ without loss of generality.

We consider two scenarios for introducing immunity into a fully susceptible population. In the first scenario, individuals gain immunity through infection and subsequent recovery. We randomly select a seed node to be initially infected. After the disease spreads from this primary source of infection and eventually dies out, we remove the recovered nodes (i.e., those who experienced infection) from the contact network. The second scenario is random immunization, where we randomly select individuals to be immunized and removed from the contact network.

Regardless of how immunity is induced, its effectiveness at the population level is defined by its ability to prevent future occurrences of diseases from invading the population and to reduce the size of epidemics. Specifically, consider a disease that spreads among susceptible individuals with a transmission rate that is potentially larger than β but cannot infect the immune (and removed) individuals. If immunity is conferred on a fraction C of the population, either by natural infection or immunization, the subsequent epidemic cannot be larger than $1 - C$ as a result of individual protection. In fact, $1 - C$ is the size of the subgraph induced by the nodes that remained susceptible, which we call *residual subgraph*. The actual size of the epidemic depends on the contagiousness of the disease, but it is further upper bounded by the size C' of the giant component of the residual subgraph, or *residual giant component* for short. Since the removed nodes, which account for a fraction C , are protected by individual immunity, the difference $\Delta = 1 - C - C'$ between the sizes of the residual subgraph and its giant component quantifies the herd immunity effect in the case where the transmission rate is infinitely large. See Fig. 2 for a schematic illustration.

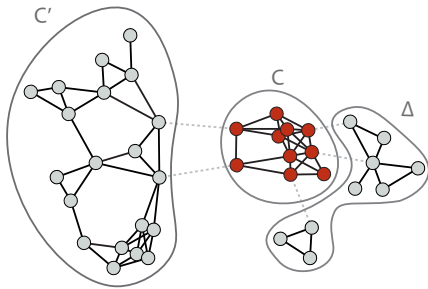


FIG. 2. A schematic figure of individual immunity, herd immunity, and residual giant component in a contact network. The immune population of size (fraction) C , indicated by red, is directly protected by individual immunity. The residual graph, indicated by grey nodes, may consist of multiple connected components and there is at most one giant component that single-handedly occupy a finite fraction of the graph. Its size C' defines the upper bound for the size of a subsequent epidemic. The sum of the sizes of the other components, denoted by Δ , quantifies the herd immunity effect because they are not directly protected by individual immunity, yet protected from a major post-immunity epidemic.

Network structure

For analytical tractability, networks are often assumed to be locally tree-like, meaning that the likelihood of a node being part of a finite-length cycle diminishes as the network size increases. This simplifies analysis, especially for configuration model networks where the network structure is solely determined by the distribution of node degrees.

However, the real-world contact networks through which infectious diseases spread are hardly tree-like. Rather, they are characterized by the abundance of short cycles, which stems from the fact that contacts are heavily influenced by physical space; transmission only occurs when individuals are in physical proximity to each other, resulting in network structures that deviate from the locally tree-like assumption and exhibit a higher prevalence of triangles and other short cycles.

In this study, we aim to explore a wide range of network geometries, focusing on two key characteristics: degree heterogeneity (variations in node connectivity) and spatial embeddedness. Figure 3 illustrates these features. Spatial embeddedness refers to the geometric arrangement of the network within a specific metric space. The least spatial networks belong to the configuration model family, representing maximum randomness under the given degree distribution. This includes random regular graphs (RRGs) and Erdős-Rényi (ER) networks. On the other end of the spectrum, lattices and random geometric graphs (RGGs) exhibit the highest spatiality.

To continuously connect the two extremes of the spa-

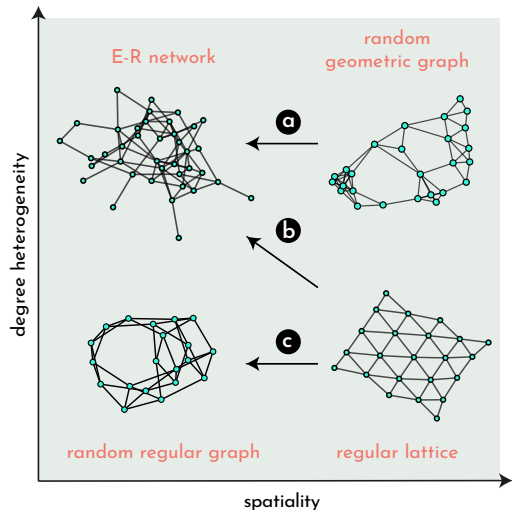


FIG. 3. Network models used in this paper, positioned according to their level of degree heterogeneity and spatiality. The three arrows indicate directions of sweeps conducted through rewiring randomization.

tiality spectrum, we employ edge randomization procedures. We start with an instance of a network model with the highest spatiality, namely a lattice or an RGG, and rewire fraction ϕ of the edges. The rewiring process is carried out either by exchanging the endpoints of two randomly selected edges (double edge swap) [23], or by removing a random edge and adding an edge between a randomly selected unconnected pair of nodes (random rewiring). The former preserves the degree of each node, while the latter only preserves the total number of edges in the network but not the individual node degrees. By completely shuffling edges (i.e., $\phi = 1$), the double edge swap operation transforms a lattice into an RRG and an RGG into an ER network. On the other hand, random rewiring effectively generates an ER network at $\phi = 1$, irrespective of the initial structure.

PREFERENTIAL BUT LOCALIZED IMMUNITY

Let us first focus on the herd immunity effect in configuration model networks, where the degree distribution is the only determinant of the network structure. Because of the locally tree-like property of configuration model networks, we can use the analytical framework to map epidemic spreading to bond percolation process and solve self-consistent equations to derive and calculate relevant quantities, such as the expected sizes of an outbreak and the giant component in the residual subgraph [2, 22]. We begin with defining the probability generating functions

(PGFs) of the degree distribution p_k and the excess degree distribution q_k :

$$F_0(x) = \sum_{k=0}^{\infty} p_k x^k, \quad F_1(x) = \sum_{k=0}^{\infty} q_k x^k = \frac{F_0'(x)}{F_0'(1)}.$$

When the immunity of nodes is induced by natural infection with transmission probability T , probability u that a random edge does *not* transmit the disease during the first outbreak satisfies a self-consistency equation [2]: $u = 1 - T + TF_1(u)$. A node is susceptible after the first outbreak (and thus in the residual subgraph) if each of its neighbors either (i) does not become infected (in which case the edge between them remains S-S), which happens with probability $F_1(u)$, or (ii) becomes infected but fails to infect the node (in which case the edge between them is S-R), which happens with probability $(1 - F_1(u))(1 - T) = u - F_1(u)$. Since the probability of being in the residual subgraph is $F_0(u)$, the degree distribution $P(m)$ of the residual graph is given by [22]

$$P(m) = \frac{1}{F_0(u)} \sum_{k=m}^{\infty} p_k \binom{k}{m} [F_1(u)]^m [u - F_1(u)]^{k-m}.$$

The PGFs of the degree and excess degree of the residual graph are given by

$$G_0(x) = \frac{F_0(u + (x-1)F_1(u))}{F_0(u)},$$

$$G_1(x) = \frac{F_1(u + (x-1)F_1(u))}{F_1(u)},$$

respectively. We obtain the size C' of the giant component in the residual graph as $C' = (1 - C)(1 - G_0(v))$, where v is the solution of self-consistent equation $v = G_1(v)$.

This framework allows us to calculate not only the fraction of nodes in each state but also the fraction of edges between nodes in each state. For instance, a random edge will have a removed node on one end and a susceptible node on the other end with probability $F_1(u)(1 - F_1(u))(1 - T)$. Therefore, the fraction of edges between susceptible and removed nodes is

$$\rho_{\text{SR}} = 2F_1(u)(u - F_1(u)), \quad (1)$$

where factor 2 accounts for the arbitrariness in choosing the ends of the edge.

If the immunity is instead induced by random immunization of coverage C , the immunity of neighbors are independent, so the residual degree m is distributed as

$$P(m) = \sum_{k=m}^{\infty} p_k \binom{k}{m} (1 - C)^m C^{k-m}.$$

Following the same recipe, the PGFs of the degree and excess degree of the residual graph are given by

$$H_0(x) = F_0(x(1 - C) + C),$$

$$H_1(x) = F_1(x(1 - C) + C).$$

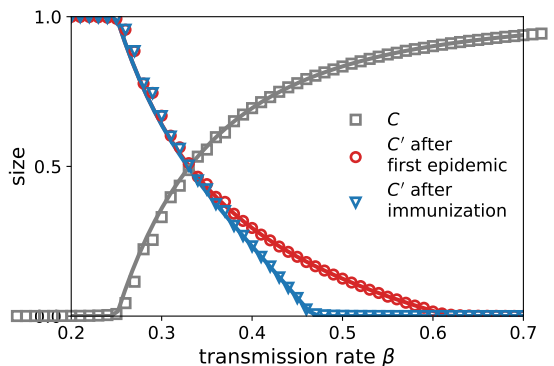


FIG. 4. The outbreak size C of the first epidemic (gray), the largest possible epidemic size C' after the first epidemic (red), and after randomly immunizing the same number of nodes as in the first epidemic (blue), plotted as a function of transmission rate β of the first epidemic. The contact network is modeled by the regular random graph with $N = 10^5$ nodes and degree $k = 6$. The symbols represent numerical results, and the lines indicate theoretical predictions.

The size C of the giant component in the residual graph is given by $C' = (1 - C)(1 - H_0(v))$, $v = H_1(v)$. The fraction of edges between susceptible and removed edges is simply

$$\rho_{\text{SR}} = 2C(1 - C). \quad (2)$$

To see the impact of localization of the disease-induced immunity on herd immunity, we first look at regular random graphs in which every node has the same degree d . The PGFs of the contact network are given by

$$F_0(x) = x^d, \quad F_1(x) = x^{d-1}.$$

By numerically solving the self-consistent equations, we obtain a theoretical prediction for C' , which is corroborated by numerical results as shown in Fig. 4. The numerical results are obtained by averaging over 50 different realizations. Our results clearly show that the giant component of the residual graph is smaller after random immunization compared to the case where immunity is induced by natural infection. This means that, in the absence of degree heterogeneity, random immunization provides a significant advantage in building herd immunity compared to relying on natural infection.

Next, let us discuss the case where the contact network is an instance of the Erdős-Rényi (ER) network. In a large ER network, the degree distribution is a Poisson distribution, i.e., the degree and excess degree are generated by the same PGF:

$$F_0(x) = F_1(x) = \exp(m(x - 1)),$$

where m is the mean degree. In this case, the PGF of the residual degree is the same for disease-induced immunity

and random immunization:

$$G_0(x) = H_0(x) = \exp[me^{m(u-1)}(x-1)].$$

In other words, the residual graphs in the two scenarios have the same degree distribution, and therefore, the effect of herd immunity is equal. This is again supported by the results from numerical simulation (see Fig. 5(b)). Interestingly, even in this case, the fraction of edges between susceptible and removed nodes, ρ_{SR} , is smaller in the case of disease-induced immunity, indicating localization of the first epidemic (Fig. 5(f)). However, the impact of localization is canceled out by the effect of preferential infection and immunization of high-degree nodes, which is represented by the larger average degree of removed nodes (Fig. 5(j)).

EFFECT OF SPATIALITY ON HERD IMMUNITY

In the previous section, we limited ourselves to the family of configuration model networks, which are characterized by the locally tree-like property and thus provide analytical insights into the impact of the degree distribution on the strength of herd immunity. In this section, we explore a wider range of network structures by introducing spatiality. In particular, we investigate the effect of spatial structure on herd immunity by studying canonical spatial graphs, namely lattices and random geometric graphs, and by systematically interpolating the spatial-to-tree-like spectrum of network structures via random rewiring of edges.

First, we consider contact networks modeled by triangular lattices and random geometric graphs (RGGs) with an average degree of $\langle k \rangle = 6$. Figure. 5(c) compares the size C' of the giant component in the residual graph in lattices. We see mixed results when comparing the two strategies: Natural infection results in smaller C' than random immunization when the fraction C of removed nodes is small, while the trend is reversed as C becomes closer to the transition point, although the difference between the two strategies is small over the entire range of C . The strong localization of the removed nodes for the disease-induced immunity is manifested in the fraction of boundary edges, shown in Fig. 5(g). For RGGs, we find that random immunization is much more effective in dismantling the residual giant component compared to disease-induced immunity, as shown in Fig. 5(d). Although the disease-induced immunity can exploit the degree heterogeneity of RGGs, the localization of disease-induced immunity is even more emphasized (Fig. 5(h)), overtaking the effect of preferential removal of high-degree nodes (Fig. 5(l)).

Next, we investigate how different levels of spatiality affect the herd immunity effect. To this end, we use the edge rewiring method described in the Model section.

Specifically, we apply the degree-preserving process (double edge swaps) to transform the contact network structure from a lattice to an RRG and from an RGG to an ER network; in addition, we use the non-degree-preserving process (random rewiring) for transformation from a lattice to an ER network. To summarize the effectiveness of herd immunity for each value of ϕ , we introduce C^* , the minimum fraction of nodes that need to be removed to dismantle the residual giant component, i.e., $C' = 0$. In other words, even a disease with an infinitely large transmission rate cannot invade the population if $C \geq C^*$; thus, C^* represents the herd immunity threshold in the worst case. Here, we numerically identify C^* by observing the value of C when Δ is the largest.

Figure 6 shows C^* as a function of rewiring probability ϕ for each rewiring path. Each data point represents 50 independent realizations of the contact network structure at a given ϕ . We see that for each path, random immunization leads to smaller C^* than disease-induced immunity over the entire range of ϕ except for the case of the ER network, for which C^* is equal in both scenarios. This confirms our previous findings for the configuration networks that random immunization provides a greater benefit to herd immunity when the degree distribution is more homogeneous than the Poisson distribution. We also find that the C^* is generally smaller for spatial networks (on the left end) compared to configuration networks (on the right end). The difference between $\phi = 0$ and $\phi = 1$ is most pronounced for the case of random immunization in the RGG and ER network, but the same trend is seen for all of the scenarios and rewiring paths.

By inspecting threshold C^* as a function of rewiring probability ϕ , we find that it is not linear and, in many cases, not even monotonic. This is especially true for random immunization, where C^* is minimized at the intermediate values of ϕ . Compared to random immunization, C^* changes more modestly in the case of disease-induced immunity. As a result, the difference in the transition points under the two scenarios is greatest in the region where ϕ takes intermediate values. This can be explained as follows: When a small number of edges are rewired ($0 < \phi \ll 1$), the network is locally full of short cycles, and these local neighborhoods are bridged by a few long-range edges. When natural infection induces immunity in such a network, large pockets of susceptibles will remain in the network after the first outbreak if the infection fails to spread across the bridging edges. On the other hand, random immunization will have an equal ability to block infection in every local neighborhood, so the effect of low-dimensionality that makes percolation more difficult becomes predominant, leading to smaller values of C^* .

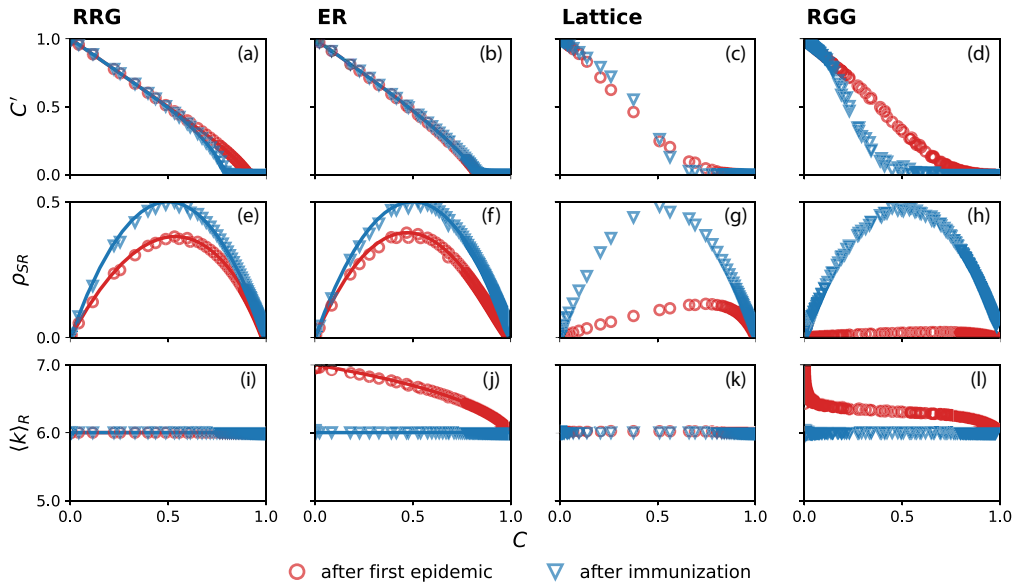


FIG. 5. Comparison of disease-induced immunity and random immunization as a function of the fraction C of removed nodes in four different networks: regular random graphs (RRG), Erdős-Rényi graphs (ER), triangular lattices (Lattice), and random geometric graphs (RGG). The size $N = 10^5$ and the average degree $\langle k \rangle = 6$ in all networks. The top row shows the residual giant component size C' after the first epidemic (red) and after random immunization (blue). The center and the bottom rows show the fraction ρ_{SR} of edges between susceptible and removed nodes and the average degree $\langle k \rangle_R$ of the removed nodes, respectively. The symbols represent numerical results and the lines denote theoretical predictions.

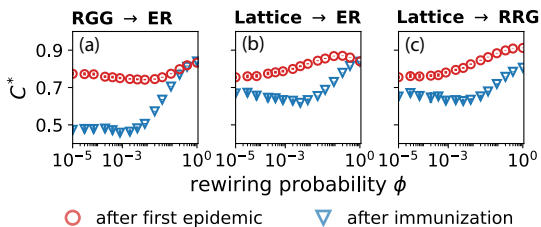


FIG. 6. Threshold C^* as a function of edge rewiring probability ϕ for disease-induced immunity (red) and random immunization (blue). Edge rewiring is performed on three different rewiring paths, correspondingly labeled in Fig. 3: (a) from random geometric graph (RGG) to Erdős-Rényi network (ER) by double edge swaps; (b) from lattice to ER by double edge swaps; (c) from lattice to regular random graph (RRG) by random rewiring. The size $N = 10^5$ and the average degree $\langle k \rangle = 6$ in all networks.

CONCLUSION

In this paper, we investigated the effectiveness of disease-induced immunity as compared to random immunization. First, we analytically compared the herd immunity effect, quantified by the size of the giant component

in the residual graph, under the two scenarios in configuration model networks. We found that disease-induced immunity leads to a weaker effect than random immunization in the absence of degree heterogeneity, while both of them lead to an equivalent amount of herd immunity for Erdős-Rényi networks. This is a consequence of the competition between the two mechanisms that shape disease-induced herd immunity: while an epidemic preferentially infects and removes high-degree nodes, making the herd immunity effect stronger, it is contiguous and localized in the contact network, making herd immunity weaker. The presence of these two mechanisms is captured by the fraction of edges between susceptible and removed nodes and the average degree of removed nodes, respectively. Our results show that the impact of localization outweighs that of preferential removal of high-degree nodes in weakly heterogeneous networks.

We further examined the role of the spatiality of the contact network structure on herd immunity. By scanning through the spectrum of spatiality by rewiring edges of lattices and random geometric graphs, we find that spatial network structure generally makes herd immunity stronger. The influence of space is particularly pronounced in the case of random immunization, giving it an additional advantage over disease-induced immu-

nity. Furthermore, we found a non-monotonic behavior in the effectiveness of herd immunity as a function of edge rewiring probability. Throughout the rewiring process, the small-world property emerges as long-range connections form within the network [24, 25]. The connection between the small-world property and herd immunity would be an interesting direction for further investigation.

We note that a similar line of research has been explored in the pioneering work by Ferrari *et al.* [19]. However, their work is based on observation of numerical simulations and rather ad hoc quantification. Furthermore, the network structures considered are limited to a few representative ones corresponding to discrete points in the space of network geometries we study here. Our contribution in this work is to elucidate the origins of the variation in herd immunity strength, to provide theoretical support for evaluating the effectiveness of disease-induced herd immunity, and to cover the full range of network geometries in order to provide a fuller picture of the strength and weakness of disease-induced herd immunity.

In order to further advance our understanding of disease-induced herd immunity, future research should explore the implications of our findings for networks with stronger degree heterogeneity, such as scale-free networks. Although this line of research is particularly relevant for real-world applications since most empirical contact networks are known to be degree heterogeneous, the challenge would be to develop a network model that allows for both tunable degrees of degree heterogeneity and spatiality. In addition, investigating the herd immunity effect in real-world social networks, which often exhibit various structural features, such as communities, core-periphery structures, and households, would provide valuable insights into the epidemic dynamics in a more realistic setting. Such studies would help bridge the gap between theoretical models and practical applications, contributing to the development of effective strategies for disease control and prevention.

ACKNOWLEDGMENTS

MK acknowledges support from the project 105572 NordicMathCovid as part of the Nordic Programme on Health and Welfare funded by NordForsk. The authors wish to acknowledge Aalto University “Science-IT” project for generous computational resources.

* takayuki.hiraoka@aalto.fi

[1] H. W. Hethcote, The mathematics of infectious diseases, *SIAM Review* **42**, 599 (2000).

- [2] M. E. J. Newman, Spread of epidemic disease on networks, *Physical Review E* **66**, 016128 (2002).
- [3] R. Pastor-Satorras, C. Castellano, P. Van Mieghem, and A. Vespignani, Epidemic processes in complex networks, *Reviews of Modern Physics* **87**, 925 (2015).
- [4] A. Badie-Modiri, A. K. Rizi, M. Karsai, and M. Kivela, Directed percolation in temporal networks, *Physical Review Research* **4**, L022047 (2022).
- [5] A. Badie-Modiri, A. K. Rizi, M. Karsai, and M. Kivela, Directed percolation in random temporal network models with heterogeneities, *Physical Review E* **105**, 054313 (2022).
- [6] M. E. J. Newman, Mixing patterns in networks, *Physical Review E* **67**, 026126 (2003).
- [7] J. O. Lloyd-Smith, S. J. Schreiber, P. E. Kopp, and W. M. Getz, Superspreading and the effect of individual variation on disease emergence, *Nature* **438**, 355 (2005).
- [8] J. Mossong, N. Hens, M. Jit, P. Beutels, K. Auranen, R. Mikolajczyk, M. Massari, S. Salmaso, G. S. Tomba, J. Wallinga, J. Heijne, M. Sadkowska-Todys, M. Rosinska, and W. J. Edmunds, Social Contacts and Mixing Patterns Relevant to the Spread of Infectious Diseases, *PLoS Medicine* **5**, e74 (2008).
- [9] L. Hébert-Dufresne, B. M. Althouse, S. V. Scarpino, and A. Allard, Beyond R_0 : heterogeneity in secondary infections and probabilistic epidemic forecasting, *Journal of The Royal Society Interface* **17**, 20200393 (2020).
- [10] G. Burgio, B. Steinegger, and A. Arenas, Homophily impacts the success of vaccine roll-outs, *Communications Physics* **5**, 70 (2022).
- [11] T. Hiraoka, A. K. Rizi, M. Kivela, and J. Saramäki, Herd immunity and epidemic size in networks with vaccination homophily, *Physical Review E* **105**, L052301 (2022).
- [12] R. Pastor-Satorras and A. Vespignani, Epidemic Spreading in Scale-Free Networks, *Physical Review Letters* **86**, 3200 (2001).
- [13] R. Pastor-Satorras and A. Vespignani, Immunization of complex networks, *Physical Review E* **65**, 036104 (2002).
- [14] M. J. Keeling and K. T. Eames, Networks and epidemic models, *Journal of The Royal Society Interface* **2**, 295 (2005).
- [15] T. Britton, F. Ball, and P. Trapman, A mathematical model reveals the influence of population heterogeneity on herd immunity to SARS-CoV-2, *Science* **369**, 846 (2020).
- [16] G. Burgio, B. Steinegger, G. Rapisardi, and A. Arenas, Homophily in the adoption of digital proximity tracing apps shapes the evolution of epidemics, *Physical Review Research* **3**, 033128 (2021).
- [17] A. K. Rizi, A. Faqeeh, A. Badie-Modiri, and M. Kivela, Epidemic spreading and digital contact tracing: Effects of heterogeneous mixing and quarantine failures, *Physical Review E* **105**, 044313 (2022).
- [18] H. Watanabe and T. Hasegawa, Impact of assortative mixing by mask-wearing on the propagation of epidemics in networks, *Physica A: Statistical Mechanics and its Applications* **603**, 127760 (2022).
- [19] M. J. Ferrari, S. Bansal, L. A. Meyers, and O. N. Bjornstad, Network frailty and the geometry of herd immunity, *Proceedings of the Royal Society B: Biological Sciences* **273**, 2743 (2006).
- [20] T. Hasegawa and N. Masuda, Robustness of networks against propagating attacks under vaccination strategies, *Journal of Statistical Mechanics: Theory and Experi-*

- ment **2011**, P09014 (2011).
- [21] S. Bansal and L. A. Meyers, The impact of past epidemics on future disease dynamics, *Journal of Theoretical Biology* **309**, 176 (2012).
- [22] M. E. J. Newman, Threshold Effects for Two Pathogens Spreading on a Network, *Physical Review Letters* **95**, 108701 (2005).
- [23] B. K. Fosdick, D. B. Larremore, J. Nishimura, and J. Ugander, Configuring Random Graph Models with Fixed Degree Sequences, *SIAM Review* **60**, 315 (2018).
- [24] D. J. Watts and S. H. Strogatz, Collective dynamics of ‘small-world’ networks, *Nature* **393**, 440 (1998).
- [25] M. E. J. Newman, I. Jensen, and R. M. Ziff, Percolation and epidemics in a two-dimensional small world, *Physical Review E* **65**, 021904 (2002).

Publication III

A. K. Rizi, L. A. Keating, J. P. Gleeson, David J.P. O'Sullivan and M. Kivelä.
Effectiveness of Contact Tracing on Networks with Cliques. *Physical Review E*, 109, 024303, Feb 2024.

© 2024 K. Rizi et al.

Reprinted with permission.

Effectiveness of contact tracing on networks with cliquesAbbas K. Rizi ¹, Leah A. Keating ^{2,3}, James P. Gleeson,² David J. P. O'Sullivan,² and Mikko Kivela¹¹*Department of Computer Science, School of Science, Aalto University, FI-00076 Aalto, Finland*²*MACSI, Department of Mathematics and Statistics, University of Limerick, Limerick V94 T9PX, Ireland*³*Department of Mathematics, University of California, Los Angeles, California 90095, USA*

(Received 8 June 2023; accepted 8 January 2024; published 9 February 2024)

Contact tracing, the practice of isolating individuals who have been in contact with infected individuals, is an effective and practical way of containing disease spread. Here we show that this strategy is particularly effective in the presence of social groups: Once the disease enters a group, contact tracing not only cuts direct infection paths but can also pre-emptively quarantine group members such that it will cut indirect spreading routes. We show these results by using a deliberately stylized model that allows us to isolate the effect of contact tracing within the clique structure of the network where the contagion is spreading. This will enable us to derive mean-field approximations and epidemic thresholds to demonstrate the efficiency of contact tracing in social networks with small groups. This analysis shows that contact tracing in networks with groups is more efficient the larger the groups are. We show how these results can be understood by approximating the combination of disease spreading and contact tracing with a complex contagion process where every failed infection attempt will lead to a lower infection probability in the following attempts. Our results illustrate how contact tracing in real-world settings can be more efficient than predicted by models that treat the system as fully mixed or the network structure as locally treelike.

DOI: [10.1103/PhysRevE.109.024303](https://doi.org/10.1103/PhysRevE.109.024303)**I. INTRODUCTION**

Contact tracing identifies, assesses, and manages people exposed to the disease through an infected individual [1]. This approach, inclusive of testing [2,3] and isolating, has been a cornerstone in controlling disease spread and preventing outbreaks. The COVID-19 pandemic saw this methodology employed globally with mixed results [4]. Countries like China, South Korea, and Singapore have been lauded for their effective contact-tracing efforts [5], while countries such as the United Kingdom and the United States faced challenges in executing successful programs [5–7]. Despite the targeted nature of contact tracing, which avoids the broad societal and economic impacts of more blanket measures like school closures and travel bans, it is not without significant costs [8]. Implementing these programs can be resource-intensive and may lead to unintended consequences, particularly regarding privacy when digital tracking systems are involved [5]. Such concerns emphasize the need for a reasonable evaluation of the trade-offs associated with contact tracing initiatives.

The effectiveness of any public health intervention cannot be divorced from the societal context in which it is applied. To evaluate the success of both pharmaceutical and nonpharmaceutical interventions, we must take into account the network structure of social interactions and health behaviors within the

population [9–12]. Given the complexity of social structures, a strategy effective in one setting may fail in another. It is, therefore, imperative to rigorously evaluate the factors affecting the efficacy of contact tracing and other interventions, considering the diverse ways social structures can influence disease transmission.

The effectiveness of contact tracing is typically evaluated based on the number of infected individuals preemptively quarantined and its influence on halting transmission chains [7,13]. This process is often assessed with the assumption that contact networks are treelike. However, social networks consist of overlapping groups such as families and workplaces. Within these networks, an infected individual transmits the infection to specific group members, while contact tracing preemptively isolates others. Its success is most notable in the intersection of these groups—those who are both infected and isolated—as this effectively disrupts direct transmission chains. However, preemptively isolating uninfected members of these groups can also be crucial in controlling the spread of the disease. If contact tracing is not entirely effective, omitting some infectious individuals, then the isolation of others becomes vital in stopping further infections. Accordingly, even isolations that might seem unnecessary due to contact tracing can significantly positively impact controlling the disease.

Social networks exhibit diverse and dense substructures which significantly impact contagion dynamics [14,15]. These networks often feature clustering, crucial in complex contagion models for behavior spreading, where repeated exposure increases behavior adoption likelihood [16,17]. This approach contrasts with traditional disease-spreading models that treat each infection event as independent. Gatherings can

Published by the American Physical Society under the terms of the Creative Commons Attribution 4.0 International license. Further distribution of this work must maintain attribution to the author(s) and the published article's title, journal citation, and DOI.

be modeled to show a nonlinear relationship between infected contacts and infection risk [18]. Empirical studies have also highlighted that the effectiveness of contact tracing varies with the size of gatherings and can exhibit nonmonotonic patterns [19]. Theoretical works in this area include the development of a *prompt* quarantine model in clique-based networks, where infected individuals and their contacts are quarantined with a fixed probability. As detailed in Ref. [20], this model results in continuous and discontinuous phase transitions and even backward bifurcations, offering new insights into epidemic control. It has also been shown that contact tracing is more effective for large-scale epidemics with low tracing rates in degree-assortative networks [21]. In contrast, in disassortative networks, higher contact rates make it more effective. Disassortative networks are also more conducive to contact tracing for more minor epidemics due to the robustness of assortative networks against link removal [21]. This underscores the complex interplay between network structures and epidemic control strategies, highlighting the need for tailored approaches in different network settings.

In this work, we demonstrate the group dynamics of contact tracing and their effect on outbreak sizes and the epidemic threshold by developing a stylized contact tracing model and a random network model with social groups manifested as cliques. This allows us to build on methods developed for spreading processes in networks with cliques [22–24]. Our findings indicate that group structure enhances the effectiveness of contact tracing. Specifically, contact tracing in a network with cliques has a nonlinear impact on the efficiency of halting the spread of chains that occur over a single link. This contrasts with models that assume a locally treelike contact structure. We show that the combination of disease spreading and contact tracing can be approximated as a complex contagion process, where repeated exposures reduce the probability of infection because they can lead to isolation and thus can make subsequent infections impossible. This interpretation of contact tracing as a complex contagion explains our results on the importance of group structure.

The structure of this paper is organized as follows: In Sec. II, we introduce (a) the random network models employed and (b) detail the epidemic model, along with the contact tracing procedures. Section III is divided into two main parts: (a) The first part focuses on identifying the epidemic threshold and observing the phase transition in epidemic size in networks with cliques. This is achieved using multitype branching processes, which provide mean-field solutions for the reproduction number. (b) The second part examines how the subcritical epidemic size grows with disease parameters and the sizes of cliques. Section IV discusses how contact tracing in networks with cliques can be interpreted as a complex contagion process. Finally, in Sec. V, we highlight the implications of our findings for understanding and mitigating disease spread in social networks.

II. MODEL

We first introduce a random network model featuring cliques as social groups in Sec. II A. After this, in Sec. II B, we present the stylized dynamics we use for modeling disease spreading and contact tracing.

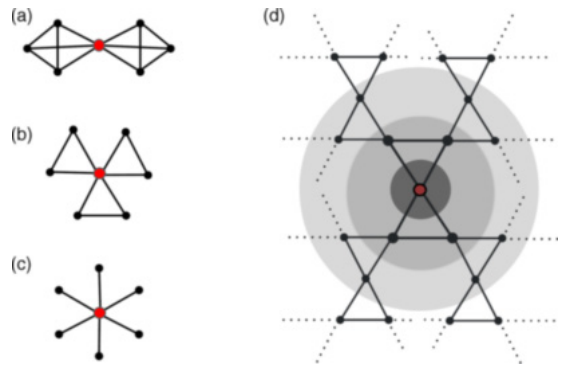


FIG. 1. Illustration of r -regular c -clique network structures. Panels [(a)–(c)] highlight the immediate network vicinity of a focal (red) node within networks formed by 4-, 3-, and 2-cliques, respectively, where each node consistently has a degree of 6. These configurations are representative of the local topology repeated throughout the entire network. Panel (d) provides an example of a 4-regular 3-clique network, with each node having a degree of 4 and being part of two 3-cliques. Displayed are link stubs indicating connections to other nodes, demonstrating the typical local structure one would encounter in an extensive clique-based network. The shaded circular regions signify the proximity to a central node, which is marked in red. This shows the connectivity structure we examine using our r -regular clique-type networks.

A. Random networks with cliques

Social networks, known for their complex, dense local structures, significantly differ from treelike topologies, especially in disease-spreading scenarios [25]. This complexity is due to high clustering in social units like families and workplaces [14,15,23,26], leading to the need for novel tools to understand cliques’ effects on spreading processes [16,26]. We aim to investigate the sole effect of social groups on contact tracing, ignoring other salient social network features such as degree heterogeneity or homophily [9,10].

In studying epidemic processes on networks, cliques are idealized representations of social groups within contact networks. Each social group is represented as a complete graph, where every member is connected to every other member, illustrating the all-to-all connection pattern within these groups. Figures 1(a) and 1(b) depict a focal node that belongs to two 4-cliques and three 3-cliques, respectively. In social networks, c -cliques are complete subgraphs representing a group of c people who are all connected and, thus, can potentially infect each other [22,23].

To investigate the sole impact of group structure, we compare network results in which nodes possess an equal number of connections but belong to groups of different sizes. In our model, we analyze homogeneous networks where all nodes have the same number of links and the same level of network clustering. We then compare different homogeneous networks, where only the amount of clustering varies between networks. This will allow us to isolate the impact of contact tracing on spreading disease in the presence of cliques. In

practice, this is made possible using clique-based network generation methods [16,25,27–30].

The algorithm for generating networks with prescribed clique structures generates an auxiliary bipartite graph with one part for individuals and the other for groups, where links are only between individuals and groups. This network is then projected into a unipartite network of individuals, where the groups become cliques, i.e., all the individuals in each group are connected. We construct the bipartite graph by giving each group c stubs and each individual n_c stubs. As we have a total of N individuals, each with degree n_c , the total number of stubs leading out of individuals should be $N \times n_c$. The total number of stubs leading out of groups must be the same. Therefore, the bipartite network must have $(N \times n_c)/c$ groups. We connect, uniformly at random, stubs leading out of individuals to stubs leading out of groups. This provides a bipartite network that defines which individuals belong to which groups. Finally, we take an unipartite projection of the bipartite network where individuals are the only nodes we keep, and we connect two individuals if they belong to the same group, i.e., if they are connected to the same group in the bipartite network. The groups become the cliques in the contact network, connecting individuals who are the nodes.

In the thermodynamic limit, such contact networks have a vanishingly small number of self-loops or multilinks. See Refs. [31,32] for further details on these network structures. In practice, when we build such networks for our simulations, we remove the few self-loops and multilinks, ending up with a simple graph. Note that each c -clique contributes $c - 1$ links to a node degree. Therefore, the number of cliques that a node is a part of, n_c , satisfies the condition $n_c(c - 1) = r$. When $c = 2$, the model generates a random r -regular graph, see Fig. 1(c). Figure 1(d) illustrates a 4-regular 3-clique network, where each node has a degree of 4 and is part of two 3-cliques.

B. SIRQ dynamics

Both contact tracing and disease transmission are complicated processes in reality and are affected by various details related to the particular disease, contact tracing procedure, and the underlying social system. We aim to reduce these complications into a minimal mathematically tractable model that captures stylized dynamics of contact tracing and disease spreading. We employ a discrete-time susceptible-infectious-recovered (SIR) model to model disease dynamics [33], where at each time step, each infected (I) individual independently infects each neighboring susceptible (S) node with *transmission* probability p . After this, the infected individuals are moved to the recovered (R) compartment. Importantly, this time-discretized model ignores variations in recovery times and can only implicitly consider complications such as incubation periods [34].

Contact tracing can be implemented in various ways, such as with phone applications [9], in different manual tracing settings, or with combinations of these two [35]. The success of contact tracing can be affected by the ability of individuals to recall contacts, the delay times in the tracing process, mobile phone application adoption, and the extent to which the individuals follow the isolation or quarantine

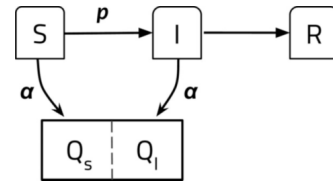


FIG. 2. Diagram of the SIRQ model showing the flow between compartments based on transition probabilities based on the stochastic dynamics introduced in Sec. II B. Susceptible individuals become infected with probability p and enter quarantine with probability α . The Q compartment includes people in quarantine, either infected or susceptible. Those who are both infected and quarantined move to the Q_I subcompartment, while those who are only quarantined go to the Q_S subcompartment of Q. Figure 3 depicts these two situations. Infected individuals who are not quarantined go to the I compartment and will recover deterministically in the subsequent time step.

recommendations [36–38]. We model all these complications with the probability α of a neighboring node successfully moving to compartment Q such that all further infections are avoided. Further, the contact tracing moving nodes to the Q compartment is done independently using the same contact network as the infections. In the model, this translates to each infected node placing each neighboring node into compartment Q with probability α . The nodes in the Q compartment can be either infected (Q_I) or susceptible (Q_S). It is important to highlight that the nodes within Q are distinctly separated from those in set R, as they are housed in separate compartments. Despite this distinction, it should be noted that neither group of nodes contributes to the propagation dynamics. Figure 2 depicts the compartmental structure and the associated

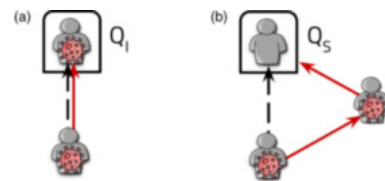


FIG. 3. Schematic of contact tracing and spreading without loops (a) and with local loops (b). Infections that would be successful are marked with solid red links, and successful contact tracing with dashed black links. After each exposure, a susceptible node isolates itself with probability α and becomes infected with probability p independently. If no loops are considered, then the combination of infections and contact tracing can be reduced to a single link. There are four possible scenarios: nothing happens; the infection spreads to the neighbor, but contact tracing fails; the infection fails to spread, but contact tracing succeeds; or (a) both infections spread, and the contact tracing succeeds so that the node will be in subcompartment Q_I . The last case is where we can benefit from contact tracing cutting indirect spreading paths thanks to the presence of clustering. (b) With local loops, an infection through a common neighbor of both nodes can be avoided. As the quarantine takes place close to the infection, it can prevent the infection from arriving at the neighbor through a local loop as the node is in subcompartment Q_S .

transition probabilities, while Fig. 3 demonstrates the benefits of contact tracing, particularly when loops are present.

Our model treats isolation and quarantine identically, encapsulating both by the probability α . Consequently, we will refer to both terms interchangeably, reflecting their similar dynamics in our model. In public health, however, isolation and quarantine are distinct strategies for preventing the spread of contagious diseases [39]. Isolation separates individuals who are sick with an infectious disease from those who are not, and it is applied to confirmed cases to prevent the spread of the infection to others. Quarantine, in contrast, involves separating and restricting the movement of people exposed to a contagious disease to see if they become sick, targeting those who may have been exposed but are not yet confirmed to be ill. Thus, in public health literature, while isolation is for those already sick and contagious, quarantine is for those who might become sick due to exposure [39]. It is worth mentioning that our model also captures the impact of ring vaccination [40], a strategy that involves vaccinating individuals around an infected person, effectively isolating them from the disease network [41]. This strategy, which successfully eradicated smallpox [42], is paralleled in our model by transitioning individuals to a quarantined compartment with probability α .

Our model assumes the infection and contact tracing processes are independent (i.e., we treat p and α as independent probabilities). See Fig. 3 for an illustration of the process. The order in which they are evaluated in the discrete-time model does not make a difference for the epidemic threshold. However, there is a slight variation in the epidemic size depending on the order, as the number of isolated infected individuals is affected by the order in which nodes are infected and placed in the quarantined compartment. For this purpose, we follow an order where we go through one infected-susceptible link at a time. First, we evaluate the spread of the epidemic and then the contact tracing for that link.

We focus on contact tracing when the disease does not reach a significant part of the population. An upsurge in the number of infections can strain the contact tracing process, leading to increased delay times that potentially weaken its overall effectiveness [35,43]. In reality, a node may be reinfected after leaving the compartment Q. However, as our contact networks are large-enough random graphs with cliques (see Sec. II A), the infection paths will not form significant long loops. This means that for our model, we can assume that the isolation times are long enough that they will stop all the incoming infections to a node. We can indefinitely keep the isolated nodes in the Q compartment. In other words, with prolonged isolation, which may vary based on clique size, postquarantine infection becomes negligible. Intuitively, this modeling choice can be understood as the re-entry of quarantined individuals into the susceptible (S) or infected (I) states being unlikely before the infection subsides locally. The impact of this assumption is explored in more detail in Appendix E.

III. RESULTS

In this section, we demonstrate the impact of contact tracing in networks with cliques. We begin by analyzing epidemic

thresholds in treelike networks (Sec. III A 1) and then assess phase transitions in epidemic sizes in networks with cliques (Sec. III A 2). We employ a multitype branching process to understand the influence of spreading parameters and clique sizes on the effective reproduction number (Sec. III A 3). The effect of contact tracing on these thresholds is examined (Sec. III A 4), followed by an analysis of outbreak sizes in subcritical regimes, highlighting the role of quarantine probability and clique size (Sec. III B).

A. Epidemic threshold and reproduction number

Given a population in a demographic steady state, with no history of a given infection or introduction of any intervention, the *basic reproduction number* R_0 determines if the introduction of the infectious agent causes an outbreak ($R_0 > 1$) or not ($R_0 < 1$) in the absence of interventions [44]. This is because R_0 yields the expected number of secondary cases produced by a typical infectious individual throughout their contagious period in a fully susceptible population. Therefore, R_0 as a threshold for the stability of a disease-free equilibrium in a compartmental model divides the phase space into super- and subcritical regions, respectively. When interventions such as contact tracing are implemented, we use the term *effective reproduction number* R_e instead of the *basic reproduction number* to differentiate between situations with no interventions in this paper. Therefore, to determine if the epidemic dies out or yields an outbreak in the presence of an intervention, we need to compute the value of R_e [10]. R_e as a bifurcation parameter in our epidemic model depends on the spreading parameters, p and α , and the network structure, which is determined by c and r .

1. Random treelike networks

For a large treelike network, like a random r -regular graph built with blocks the same as the one in Fig. 1(c), we can find the epidemic threshold in the αp plane using

$$R_e = p(1 - \alpha)\bar{d}, \quad (1)$$

and setting $R_e = 1$. Here \bar{d} represents the average excess degree of the network. This is the average count of additional connections that a node has, apart from the one used to arrive at when it is found by traversing a uniformly randomly selected link in the network. As our networks have uniform degree distributions, such that every node has degree r , the expected excess degree is just the degree minus one, $\bar{d} = r - 1$. It should be noted that even with the most severe disease with $p = 1$, it is still possible to avoid an outbreak. By setting $p = 1$ in Eq. (1) and solving for α , we can determine that if the quarantine is carried out in such a way that $\alpha > 1 - 1/\bar{d}$, then the effective reproduction number, R_e , will remain below 1.

In general, for a treelike random network with expected excess degree \bar{d} , we can rewrite the effective reproduction number as a product of spreading properties and network structure as $R_e = p_e \bar{d}$ where p_e is the *effective transmission probability* and defined as

$$p_e = p(1 - \alpha). \quad (2)$$

So every active node can, on average, infect $R_e = p_e \bar{d}$ new people who can propagate the disease, i.e., are not themselves quarantining. When contact tracing is not in place ($\alpha = 0$), the effective reproduction number reduces to the basic reproduction number, $R_0 = p \bar{d}$. Since we ignore variations in recovery time, the SIR dynamics can be mapped to a bond percolation problem, where p represents the link occupation probability and the size of the giant component corresponds to the final outbreak size [10,34,45,46]. This mapping results in the epidemic threshold being equivalent to the percolation threshold, which occurs at $p_* = 1/\bar{d} = 1/(r-1)$. Thus, a phase transition is expected from a disease-free equilibrium to an endemic state. For example, for a 6-regular graph $p_* = 0.2$, and when $\alpha = 0.5$, the epidemic threshold occurs at $p = 0.4$, according to Eq. (1). Our forthcoming explanation of simulation results of random networks with cliques shows that this equation aligns exceedingly well with $c = 2$ (no loops). When the treelike assumption does not hold, for example, when $c > 2$ in our network model, an alternative method is required to determine R_e . This is the focus of the following sections.

2. Simulating the epidemic

Equation (1) is not applicable for networks with cliques, as it assumes a locally treelike structure. However, we can simulate the epidemic dynamics to observe how the outbreak size varies with changes in disease parameters and network structure. These simulations reveal a sharp increase in the outbreak size, transitioning from a few individuals to a significant portion of the network, upon crossing certain thresholds of p and α . Additionally, at the epidemic threshold, an ensemble of simulations shows considerable variation in outbreak sizes, reflecting the critical nature of this point as noted in Refs. [46,47]. In our simulations, we build large networks (with $N \approx 10^5$ nodes) according to Sec. II A, run the SIRQ dynamics 10^4 times, and find the ensemble average of the number of nodes in the different compartments in each run as our measure of disease spread from simulations. Using this, we can calculate other quantities of interest. For example, the size of the outbreak is then given by the ensemble averages of the number of people in the R and Q_I compartments. We follow an order to go through one infected-susceptible link at a time for the epidemic size computations. First, we evaluate the spread of the epidemic and then the contact tracing for that link. This way, the number of infected people in quarantine can be computed as $N_{Q_I} = pN_Q$. We find the size of an epidemic E by summing up the number of infected people in and out of quarantine, N_{Q_I} and N_R , respectively.

Figures 4(a)–4(c) illustrates the dependence of outbreak size on the value of p under different scenarios, namely in the absence of contact tracing ($\alpha = 0$), and with contact tracing at $\alpha = 0.25$ and $\alpha = 0.5$, for networks consisting of 2-, 3-, and 4-cliques. As the clique size increases, the outbreak size decreases for any given transmission probability. Moreover, this effect is magnified by an increase in the value of α .

Furthermore, we use the fluctuations in the outbreak sizes, χ , for determining the epidemic thresholds as illustrated in Fig. 4(d). Fluctuation in outbreak sizes typically displays a peak even in finite systems. When computed as a function of

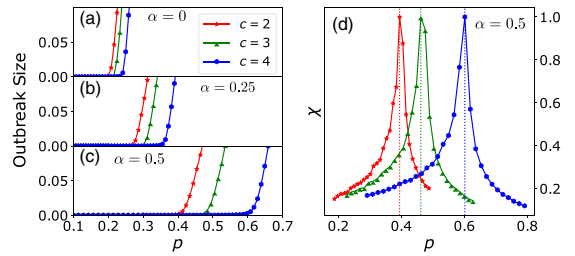


FIG. 4. Phase transitions from a disease-free equilibrium to an endemic state for 2-, 3-, and 4-clique networks with degree 6 as introduced in Sec. II A. [(a)–(c)] The outbreak size E , normalized to the network size, is shown on the vertical axis for when (a) $\alpha = 0$ (no contact tracing), (b) $\alpha = 0.25$, and (c) $\alpha = 0.5$, from top to bottom respectively. Note that the transition points are shifted slightly to the right for larger clique sizes, c , even when there is no contact tracing ($\alpha = 0$), but this difference is substantially amplified for larger α values. (d) The coefficient of variation of outbreak sizes in an ensemble, χ normalized to unity for $\alpha = 0.5$. We use χ to numerically detect the transition point as it peaks at the epidemic threshold. Results are based on Monte Carlo simulations introduced in Sec. III A 2.

infection probability p , the peaks in χ indicate the epidemic thresholds for some value of α . This measure is analogous to susceptibility in critical phenomena [48], which measures the response magnitude generated by a small external field disturbance [49]. In practice, we run a set of simulations and calculate the coefficient of variation of the outbreak sizes, which is the ratio of the standard deviation of outbreak sizes to their ensemble average, $\chi = \sigma_E / \langle E \rangle$ [33]. Figure 4(d) shows that for a fixed r , here $r = 6$, contact tracing on networks with cliques is more effective when the contact networks include larger cliques. So the larger the clique size, the larger the critical transmission probability.

3. Mean-field reproduction number

By representing our stylized SIRQ model using a multitype branching process, we can derive the relationship between p , α , and clique size, c , on the epidemic threshold. In the multitype branching process representation of our SIRQ model, we track different clique states, which we refer to as *clique motifs*. Each clique motif accounts for the possible number of susceptible, infected, or recovered nodes that any clique can inhabit at a given time. Every possible motif is denoted by Z_i (refer to Fig. 5 for listing possible clique motifs for a 3-node clique). Regardless of the network structure, we can always average the expected number of new infections over all possible infected types from our multitype branching process with the next-generation matrix [44]. To do this, we track the propagation of clique motifs in a network under the introduced dynamics and form the next-generation matrix \mathbf{M} for the number of motifs in the network. The matrix \mathbf{M} is also known as the mean matrix or the population projection matrix [50], and its element m_{ij} gives the expected number of motifs of type Z_i that are created in the next time steps from a motif of type Z_j .

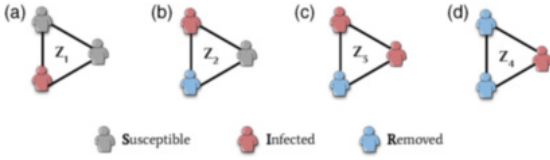


FIG. 5. Each 3-clique can have four life stages or diffusion patterns with at least one infected node. Section III A 3 considers both recovered and quarantined nodes in the R compartment. Using a 6-regular 3-clique network, we observe that a Z_1 node can form a Z_2 motif with two Z_1 nodes and a Z_3 motif with four Z_1 nodes. A Z_2 node can also create a Z_4 motif with two Z_1 nodes. Nodes in the Z_1 , Z_2 , and Z_4 motifs can transition to an infection-annihilated states such as {R, S, S} which are not shown here. In Sec. IV, we assume that both quarantined and susceptible nodes are in the S compartment, while only recovered individuals are in the R compartment.

Figure 5 shows the motifs corresponding to the four life stages of a 3-clique. In this representation, we have combined the isolated and recovered nodes into a single R compartment because these two compartments are equivalent for the epidemic threshold computations. The next-generation matrix represents the transitions between these motifs. For example, the infected node in Z_1 can infect one or two neighbors, corresponding to motifs Z_2 and Z_3 . Further, $n_c - 1$ new Z_1 motifs are produced every time such an infection occurs. That is, when Z_1 turns into Z_2 , there are also $n_c - 1$ new Z_1 motifs, and when it turns into Z_2 , there are $2(n_c - 1)$ new Z_1 motifs created.

Table I shows the nonzero elements of \mathbf{M} . For example, the transition from Z_2 to Z_4 occurs when contact tracing fails (with probability $1 - \alpha$). The infection is successful with probability p , which means that, in expectation, a single Z_2 motif produces $m_{42} = p(1 - \alpha)$ new Z_4 motifs. The motif Z_4 can also be made when the infected node in Z_1 puts one neighbor in quarantine (with probability α) and fails to do so for the neighbor and infects it instead [which happens with probability $p(1 - \alpha)$]. As there are two ways of choosing the infected and isolated neighbor, the expected number of Z_4 motifs produced by the Z_1 motif is given by $m_{41} = 2\alpha[(1 - \alpha)p]$. The rest of the transitions are produced similarly by computing the probabilities of going from one motif to another. As described in Appendix D, we write general formulas for any transition and use this to automatically generate the desired mean matrix, \mathbf{M} , for cliques of any size.

TABLE I. Nonzero elements of the next-generation matrix $\mathbf{M}_{4 \times 4}$ for a 3-clique network. m_{ij} gives the expected number of Z_i cliques from a Z_j clique, as shown in Fig. 5.

i, j	m_{ij}
1, 1	$4p(1 - \alpha)$
1, 2	$2p(1 - \alpha)$
2, 1	$2p(1 - \alpha)^2(1 - p)$
3, 1	$p^2(1 - \alpha)^2$
4, 1	$2\alpha p(1 - \alpha)$
4, 2	$p(1 - \alpha)$

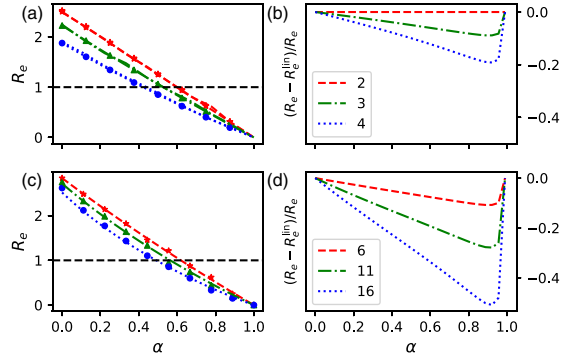


FIG. 6. The impact of contact tracing in clique networks on mitigating epidemic spread: This figure illustrates the decline in the effective reproduction number, R_e , with the contact tracing parameter, α , across networks with various clique configurations. Specifically, we examine cliques of sizes $c = 2, 3, 4$ with $r = 6$ and transmission probability $p = 0.5$ in panel (a), and cliques of sizes $c = 6, 11, 16$ when $r = 30$ and $p = 0.1$ in panel (c). Networks with larger cliques achieve the critical threshold of $R_e = 1$ with less contact tracing effort. When $c = 2$, the influence of contact tracing on R_e aligns linearly with α , according to Eq. (1). In scenarios involving larger cliques, this relationship turns concave and is further intensified as the clique size increases or the transmission probability decreases. The dotted lines are from the mean-field calculations introduced in Sec. III A 3, and the markers are from Monte Carlo simulations described in Sec. III A 2. Panels (b) and (d) show a relative difference of R_e to the linear case when $c = 2$ (R_e^{lin}). Figure 13 shows similar results to panel (a) for different p values. The larger the transmission probability, the larger the differences between the curves of other networks with cliques.

What is significant about the next-generation matrix is that its spectral radius (Perron root), or the largest modulus of the eigenvalues [51], yields the effective reproduction number [52,53] such that

$$R_e = \rho(\mathbf{M}), \tag{3}$$

and epidemic thresholds for any given clique network can be found for finding p and α such that $R_e = 1$. We give more detailed arguments about this identity in Appendix C, and show that this definition aligns with the simulation results of Fig. 6.

In Fig. 6, we present the effective reproduction number, R_e , across various clique sizes under differing transmission probabilities, integrating results from both mean-field calculations and simulations, detailed in Sec. III B. The figure reveals a nonlinear relationship between R_e and the intervention parameter α , particularly for larger cliques. This observation is crucial in practical scenarios where the basic or effective reproduction number is a key metric for monitoring and controlling epidemic situations. Public health officials often rely on this data, represented on the horizontal axis, to gauge the extent of interventions required to bring the epidemic under control, aiming to reduce R_e below the critical threshold of 1 by increasing α .

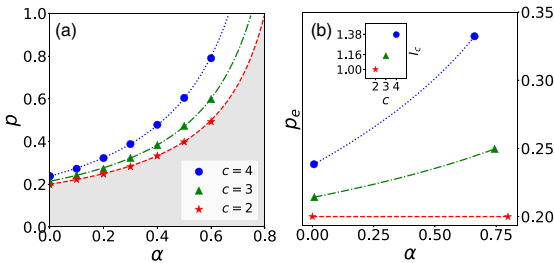


FIG. 7. Phase diagram showing that increasing the clique size increases the epidemic threshold and effectiveness of contact tracing. (a) The critical curves where $R_e = 1$ in the αp plane for $c \in \{2, 3, 4\}$. The lines indicate the results of the mean-field approximations described in Sec. III A, and the markers show results for simulations described in Sec. III A 2. The shaded area is the subcritical region for $c = 2$ where the infection eventually dies out after a finite number of generations for any clique size. (b) The same phase diagram in αp_e plane, where $p_e = p(1 - \alpha)$ is the effective transmission probability defined in Eq. (2). The larger markers in the right end in panel b indicate extreme points from Eq. (4). The inset in panel b shows the relative maximum increase in the effective epidemic threshold for different networks with cliques. Each point in the inset is the ratio of the p_e values at the endpoints of each curve outside the inset, such that $I_c = p_e(\alpha_{\max})/p_e(\alpha_{\min})$.

More successful contact tracing leads to a lower effective reproduction number, and the extent of this reduction in networks with cliques is larger than in treelike networks. As seen from Eq. (1), given the basic reproduction number, R_0 (R_e without contact tracing), the R_e decreases linearly with α , following $R_e^{\text{lin}} = (1 - \alpha)R_0$. However, as demonstrated in Figs. 6(a) and 6(c), this reduction is not linear in networks with cliques. The difference between this simplistic linear estimation and the more realistic R_e [Eq. (3)] yields the error of assuming contact networks are locally treelike. Figures 6(b) and 6(d) highlight this discrepancy by showing the relative error, $\frac{R_e - R_e^{\text{lin}}}{R_e}$, between these two approaches. These errors become more pronounced in networks with larger groups. It reaches around 20% for cliques of size 4 and around 50% for cliques of size 16.

4. Epidemic threshold

Next, we will use the mean-field framework developed above to investigate the epidemic thresholds. Figure 7(a) presents the phase diagram of the epidemic for various networks with cliques by drawing $R_e = 1$ curves in the αp plane. These curves divide the plane into sub- and supercritical regions. In the subcritical region, there is no possibility of an outbreak that scales with the network size. In contrast, in the supercritical region, there is a positive probability of such an outbreak upon infection. For networks with cliques, increasing the clique size enlarges the subcritical region and shrinks the supercritical region. Note that even without contact tracing (i.e., when $\alpha = 0$), including a clique structure in random graph models raises the epidemic threshold slightly. However, this effect is amplified by contact tracing, which can

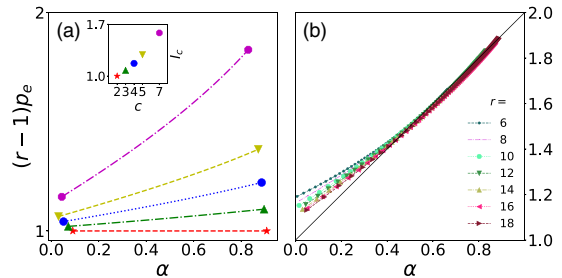


FIG. 8. Critical curves rescaled as effective branching factors for treelike networks $(r - 1)p_e$. Panel (a) is the same as panel Fig. 7(b), but on the vertical axis, the effective transmission probabilities are multiplied by the excess degree. Further, results are shown for a larger network where $r = 12$. The red curves marked with stars are for the case that there $c = 2$ and the network is treelike, therefore Eq. (1) holds such that $R_e = p_e \bar{d} = p_e(r - 1) = 1$ for any α value. For $c > 2$, this equation does not hold. The right end markers on panel a indicate extreme points from Eq. (5). The inset shows the relative maximum increase in the effective epidemic threshold for different networks with cliques. Each point in the inset is the ratio of the p_e values at the endpoints of each curve outside the inset, such that $I_c = p_e(\alpha_{\max})/p_e(\alpha_{\min})$. (b) This panel shows how $(1 - r)p_e$ changes when we have networks with different degrees, $r = 6$ to $r = 18$, and maximal connectivity-preserving clique size (i.e., when $n_c = 2$).

be observed as an increased difference between the critical p value as α increases.

We illustrate that the combined impact of contact tracing and cliques is larger than one would expect by the treelike assumption by plotting the critical effective transmission probability p_e , defined in Eq. (2), as a function of α . Figure 7(b) displays this rescaling of the critical values. For treelike networks, such as 2-clique networks, $R_e = 1$ corresponds to a constant (horizontal line) in the rescaled representation, while for networks with cliques, this value increases with α . This indicates that networks with cliques require much larger effective transmission probabilities to reach the epidemic threshold compared to what is expected by the treelike approximation, with the difference growing as the isolation probability α increases. This shows the moderating effect that clique structures can have on an epidemic in the presence of contact tracing, as it helps to cut not only onward infections but also local indirect spreading paths in the network.

The transition points strongly depend on the node degree, r , in the class of clique networks we consider here. For most of the analysis in this paper, we kept the node degree fixed to $r = 6$ (Fig. 7); here, we turn our attention to how node degree can affect disease spreading. We do this by varying r and holding other network properties constant. This is interesting because the node degree, r , rescales the transition points between sub- and supercritical regions. More precisely, if we use the excess degree to scale the critical p_e by plotting $(r - 1)p_e$ as a function of α , then the phase diagram returns to a scale that is independent of r such that the $c = 2$ line is precisely at $(r - 1)p_e = 1$. This rescaling is illustrated for

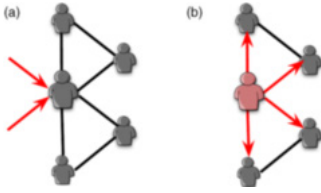


FIG. 9. Spreading process in a 6-regular 3-clique network under the extreme case of $p = 1$, where the infection propagates severely through the cliques. In this scenario, (a) an active node (infected but not in quarantine) can transmit the disease to other nodes in its adjacent cliques, (b) resulting in new infections. The number of new infections caused by an active node is not equal to the total number of members in the cliques that the node belongs to, which is $n_c(c - 1)$, but rather the number of members in the cliques attached to that node, excluding the clique that infection is coming from, which is $(n_c - 1)(c - 1) = 2 \times 2$. For further details on the network structure and spreading dynamics, refer to Secs. II A and II B.

$r = 6$ and $r = 12$ in Fig. 7 and Fig. 8(a) for valid network configurations, respectively. Recall that the networks we study still must obey $n_c(c - 1) = r$.

A more systematic exploration can be found in Fig. 8(b), where each node belongs only to two cliques, $n_c = 2$, representing the extreme nontrivial scenario where each clique is as large as possible without the network consisting solely of isolated cliques. In this case, the critical curves collapse in the rescaled plot for a range of $r = 6$ to $r = 18$ that we tested. The collapse approximately follows a straight line from $(r - 1)p_e = 1$ for $\alpha = 0$ to $(r - 1)p_e = 2$ for $\alpha = 1$, with the approximation getting better for larger values of α . Note that for $\alpha = 0$, the critical transmission probability equals the critical bond percolation probability for the SIR model [20,24,34,54].

The curve collapse can be understood by examining the extreme case $p = 1$ (where the infection always succeeds), and the critical point for contact tracing probability α_* (i.e., how large does α need to be to prevent an outbreak when $p = 1$). In this case, infected nodes always infect all of their neighbors, and during the early stages of the epidemic, each clique either has (1) exactly one infected node and $c - 1$ susceptible nodes, (2) one recovered node and $c - 1$ infected nodes (from which a fraction of α are isolated in expectation), or (3) only susceptible nodes. When an infection arrives at a clique, the infected node, which is not in quarantine, can spread the infection to $(n_c - 1)(c - 1)$ new nodes (offspring) in the next time step, as illustrated in Fig. 9. Therefore, α_* can be obtained by setting the expected number of active (infected but not in quarantine) nodes to one, which occurs when $(1 - \alpha)(n_c - 1)(c - 1) = 1$. Therefore, the critical value for α is given by

$$\alpha_* = 1 - \frac{1}{(n_c - 1)(c - 1)}. \quad (4)$$

Markers in the right end of Fig. 7(b) shows such extreme points $(\alpha_*, 1 - \alpha_*)$. Substituting α_* into $(r - 1)p_e =$

$(r - 1)(1 - \alpha)$ and recalling that $r = n_c(c - 1)$, yields

$$(r - 1)p_e = \frac{n_c(c - 1) - 1}{(n_c - 1)(c - 1)}. \quad (5)$$

Markers in the right end of Fig. 8(a) shows such extreme points $(\alpha_*, (r - 1)(1 - \alpha_*))$. When the clique size c grows to infinity, Eq. (5) leads to

$$(r - 1)p_e \xrightarrow{c \rightarrow \infty} \frac{n_c}{n_c - 1}, \quad (6)$$

which yields the value 2 when $n_c = 2$, for example. This explains why the rescaled critical infection probability curves approach 2 when α is sufficiently large, as seen in Fig. 8(b).

Using our multitype branching process description of contact tracking, not only can we unpick the interplay of clique structure on the criticality of the process, which we have explored in this section, but we can also estimate the expected outbreak size. This is the focus of the following section. But before proceeding, it is worth noting that integrating cliques into network models increases the clustering coefficient. However, it is essential to recognize that increasing clustering in networks can be done in different ways, and it may lead to changes in other network properties, such as degree heterogeneity. Therefore, since clustering alone does not solely dictate the epidemic threshold [24,26,27,55–63] or the component size distribution [64] of network, running our SIRQ dynamics on any clustered networks may not necessarily lead to the same results we obtained here.

B. Subcritical outbreak sizes

Characterizing the spreading process described above also provides access to methods for calculating quantities of interest, such as the epidemic size, via the next-generation matrix. We are interested in the outbreak size (the expected total number of infected individuals in an outbreak) for a given parameter set. We follow closely the method outlined in Ref. [16], where they derived the expected epidemic size, E , in the subcritical regime. We consider the contributions for subtrees seed of each motif type (\vec{z}) —as well as the expected number of offspring of each type from each motif type, which has already been discussed in Sec. III A 3 via the next-generation matrix. We also need to consider the number of infected nodes contributed by each type, which will be given by the vector \vec{I} . The expected epidemic size, E , can be found by solving the following two equations:

$$(\mathbb{I} - \mathbf{M}^T)\vec{z} = \vec{I} \quad (7)$$

and

$$E = 1 + (\vec{z}^0)^T \mathbf{M}^T \vec{z}, \quad (8)$$

where \vec{z}^0 is the initial seeding of each motif type at the start of the process, and \mathbb{I} is the identity matrix. For example, consider the case where we have each node as being part of three cliques, where each clique contains three nodes (see Fig. 5), the elements of \vec{z}^0 are $(3, 0, 0, 0)^T$ and \vec{I} are $(0, 1, 2, 1)^T$. The first element of \vec{z}^0 is 3, as each node is a member of three cliques, and, as this is the seed configuration, the contagion has not spread to any other nodes, leaving all the other motif types zero. We simply count the number of active nodes in

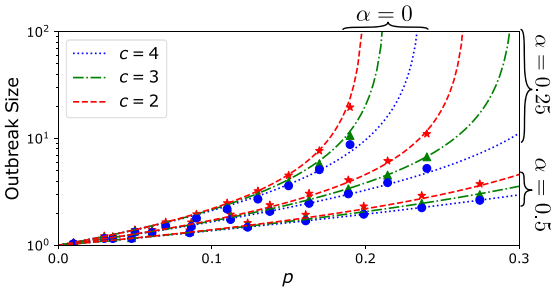


FIG. 10. Outbreak size in the subcritical regime as a function of p across the three network structures while considering the influence of isolation probability, α . Nine curves are grouped into three sets (from left to right) according to their isolation probabilities, with each set containing three curves with $\alpha = 0.0$, $\alpha = 0.25$, and $\alpha = 0.5$. These groupings demonstrate the influence of α on outbreak size in the subcritical regime. Increasing α or clique size reduces the outbreak size, as calculated by Eq. (7) and Eq. (8) using the next-generation matrix from mean-field approximation found in Sec. III B. Markers represent the results of 50 000 simulations, while dotted lines depict the results of the mean-field calculations presented in Sec. III A 2.

each motif for the elements of \vec{l} . Referring again to Fig. 5, types Z_2 and Z_4 both have one active node, and type Z_3 has two active nodes. We need to be careful not to double-count nodes, and as such, we set the first element of \vec{l} to zero. For the full derivation, please refer to Ref. [16]. Using this, we can now easily sweep through a parameter set to find the relationship between p , the initial probability of infection, and α , the probability of quarantine on the expected epidemic size under our mean-field view of the disease process.

Looking at the qualitative behavior of the curves, we see from Fig. 10 that as we increase p , naturally, the expected epidemic size rises; however, when we increase α , we see that the average size of the outbreak decreases across all three network topologies that we consider. Moreover, this effect is most pronounced for networks with larger cliques, as this network gives the quarantining behavior more opportunities to remove possible infection paths via our mean-field approximation. Note that the outbreak size in the subcritical regime does not scale with the network size and decreases dramatically by increasing α .

In the next section, we will present a complex contagion approximation to contact tracing for calculating the epidemic thresholds. The results of Fig. 10 also hold for this approximation to the model, which is discussed in the next section. Please refer to Appendix A for the complex contagion approximation calculation for the expected cascade size.

IV. COMPLEX CONTAGION FORMULATION

Next, we will show that the model described in Sec. III A 2 is closely related to a SIR model, which allows the probability of infection to change as a function of infection attempts. In this related complex contagion model, we do not keep track of isolated node states. Instead, we keep track of failed infection attempts on the susceptible nodes. Since we know that a contact tracing attempt preceded each infection attempt,

TABLE II. Nonzero elements of the next-generation matrix $\mathbf{M}_{4 \times 4}$ in the complex contagion approximation for a 3-clique network. m_{ij} gives the expected number of Z_i cliques from a Z_j clique. As shown in Fig. 5.

i, j	m_{ij}
1, 1	$4p(1 - \alpha)$
1, 2	$2p(1 - \alpha)^2$
2, 1	$2p(1 - \alpha)[1 - p(1 - \alpha)]$
3, 1	$p^2(1 - \alpha)^2$
4, 2	$p(1 - \alpha)^2$

we know there has been an equal number of infection and contact tracing attempts. In this sense, each infection attempt also carries a risk of isolation, and every attempt becomes less likely to yield an infected node. This is in contrast to the typical social complex contagion processes where each infection attempt makes it more likely for the next one to succeed.

We borrow the framework of the multitype branching processes for complex contagion as introduced in Ref. [16], where the infection state of the nodes characterizes motifs. Notably, the model is the same apart from p_k as has been previously defined in Ref. [16], where the probability of adoption after k attempts is given by

$$p_k = 1 - (1 - p)(1 - \alpha)^{k-1}. \quad (9)$$

That is, the α parameter works exactly opposite to the contact tracing here: The larger the α value, the larger the probability that infection attempts beyond the first one are likely to succeed.

In the SIR process with contact tracing each isolation fails with probability $1 - \alpha$ and a node is not isolated after k attempts with probability $(1 - \alpha)^k$. If the person is not isolated, then they have a probability of p being infected by an adjacent infected node. In total, the probability that a node gets infected by a neighbor after k attempts, given that it is not yet infected, is

$$\hat{p}_k = p(1 - \alpha)^k. \quad (10)$$

This probability describes exactly the opposite behavior to typical social complex contagion processes, where the probability of infection increases with the number of attempts. Suppose we do not track whether the susceptible node is quarantined or the infection has failed even though the node was not quarantined. In that case, we can follow the method and formulas given in Ref. [16] by simply replacing the probability p_k of Eq. (9) with \hat{p}_k from Eq. (10). In this picture, isolated and susceptible nodes are treated the same and put into the susceptible compartment. We are not explicitly tracking individuals in the Q compartment. However, we have made the probability of infection a function of the number of exposures as given by Eq. (10). In this approximation, we also retain the infected and quarantined nodes Q_1 in the susceptible compartment S, which means that a Z_1 cannot make a Z_4 directly (Fig. 5).

Table II shows the nonzero elements of the next-generation matrix for a 3-clique network, and Fig. 11 shows the result

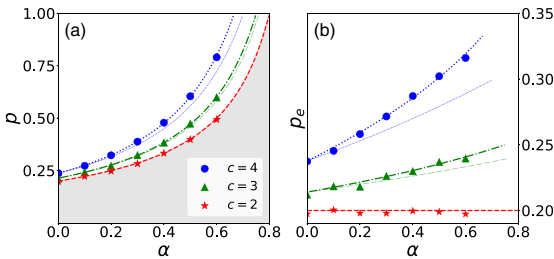


FIG. 11. Comparison of the mean-field approximation introduced in section Sec. II B with the complex contagion approximation of Sec. IV. Panels are similar to the panels of Fig. 7. Here, markers are the results of the simulations described in Sec. III A 2. Our simulation results align with the bold curves, which are the results of the mean-field approximations of Sec. III A. The thin curves result from the complex contagion approximation introduced in Sec. IV, which deviates slightly more from the other mean-field approximation when α increases. The complex contagion approximation gives the lower bound of critical transmission probability for all values of α .

of the complex contagion approximation when we set the spectral radius of the new next-generation matrix to unity. The results of this approximation are close to the simulations and the mean-field solution presented in Sec. III A when the quarantine probability α and clique size c are small. Larger α and c values will lead to underestimated epidemic threshold values for the infection probability p . As the critical curves of the complex contagion are positioned below those of the full contact tracing (see Fig. 11), it establishes the complex contagion process as the lower bound (or estimate) for the entire contact tracing process. With the complex contagion formulation, the advancement in epidemic thresholds is less pronounced. This is due to the slower upward trajectory of the curves with increasing alpha, contrasting with the original contact tracing formulation. So, the phenomenon of disease spreading under contact tracing in networks with cliques can be understood to be analogous to social complex contagion but with the opposite and more minor effect. Intuitively, analogously to social complex contagion, this explains why it is crucial to consider contact tracing in network models that contain realistic group structures.

V. CONCLUSION AND DISCUSSION

In this work, we incorporate contact tracing into disease-spread models on social networks, focusing on how local group structures, modeled with cliques, impact the epidemic thresholds and sizes. This model, contrasting with traditional assumptions of fully mixed or treelike networks, demonstrates greater efficacy of contact tracing in networks with clustering. Moreover, we show that disregarding group structure in contact tracing is analogous to ignoring group structure in complex contagion models where previous exposures increase the chance of adoption or infection. This illustrates the possible benefits of contact tracing in real-world settings, especially in the early stage of disease spread, where quarantining limits the possible paths of infection that disease can take through a network.

The dynamical model we used in this paper is an idealized representation and, therefore, oversimplifies the complexities of disease transmission and contact tracing. In actual social situations, the implementation of contact tracing may vary across different groups within the network, resulting in strong effects on infection risk and threshold size. Further, our model integrates factors related to contact tracing and isolation timing into a single parameter α . Contact tracing is always either entirely successful or unsuccessful in this simplification. In reality, contact tracing could be partially successful such that the isolated individual passes on the infection to part of the contacts that would have been infected without any intervention. Additionally, there could be additional effects in networks with cliques that are affected by the timing. Further research is needed to understand how quarantining measures impact epidemics on more realistic contact networks with contact tracing and how outbreak sizes are distributed in such settings.

The details of the epidemic model itself could also impact the effectiveness of contact tracing in networks with cliques. For example, asymptomatic individuals can be crucial in disease spread as they can unknowingly transmit the infection and therefore do not lead those people being contact traced. However, in the presence of social groups, both the asymptomatic individuals and the people infected by them can be isolated through indirect connections, potentially alleviating the problems caused by asymptomatic individuals. Similarly, one could incorporate a noncontagious *exposed* phase using the SEIR model [34,46] or various other complications that would make the models more realistic, such as temporal inhomogeneities of the contact networks [65–67].

Our model’s strength lies in its simplicity and general modeling practicality. It encapsulates identifying infected individuals, alerting their contacts, and isolating those potentially exposed within a single parameter, denoted α . This versatile model can be applied to various interventions akin to contact tracing. For instance, social distancing could theoretically fit into this model if we consider exposed individuals maintaining a large-enough physical distance with probability α from all their peers, thus mirroring the concept of self-quarantine. While social distancing may be regarded as a form of partial or complete self-isolation, the essence of both practices—and of quarantining—is fundamentally similar. Although these public health terms are often finely distinguished in specific contexts, the underlying principles governing these interventions are consistent.

In summary, our results highlight the importance of considering realistic social network structures when modeling epidemics and interventions. Our model is deliberately simplistic and is used to isolate key insights. The key conclusions we draw are as follows: (1) contact tracing is more efficient in social networks with groups than one would expect based on the treelike models, (2) the effect of groups is more prominent if the groups are larger, and if the contact tracing is more efficient, and, finally, (3) SIR spreading under contact tracing can be approximately understood as a complex contagion process where multiple exposures reduce the infection probabilities.

This study’s simulations and numerical computations are publicly available [68].

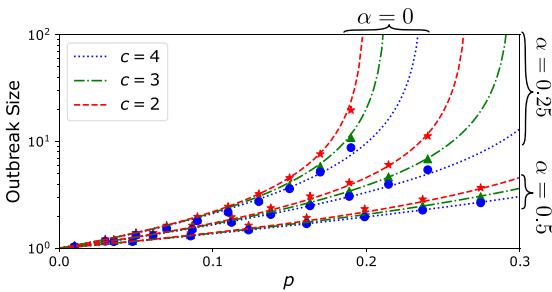


FIG. 12. Outbreak size in the subcritical regime as a function of p across the three network structures while considering the influence of isolation probability α . Nine curves are grouped into three sets (from left to right) according to their isolation probabilities, with each set containing $\alpha = 0$, $\alpha = 0.25$, and $\alpha = 0.5$. These groupings demonstrate the influence of α on outbreak size in the subcritical regime. Increasing α or clique size reduces the outbreak size, as calculated by Eq. (7) and Eq. (8) using the next-generation matrix from mean-field approximation found in Sec. IV. Markers represent the results of 50 000 simulations, while dotted lines depict the results of the mean-field calculations presented in Sec. III B.

ACKNOWLEDGMENTS

A.K.R. would like to thank Lasse Leskelä and Takayuki Hiraoka for the fruitful discussion during the preparation of this work. The simulations presented above were performed using computer resources within the Aalto University School of Science “Science-IT” project. A.K.R. and M.K. acknowledge funding from Project No. 105572 NordicMathCovid which is part of the Nordic Programme on Health and Welfare funded by NordForsk. This work was also supported by the Academy of Finland (Grants No. 349366 and No. 353799) and by Science Foundation Ireland [Grants No. 18/CRT/6049 (L.A.K.), No. 16/IA/4470 (J.P.G.), No. 16/RC/3918 (J.P.G.), and No. 12/RC/2289 P2 (J.P.G.)] with cofunding from the European Regional Development Fund. For the purpose of Open Access, the author has applied a CC BY public copyright license to any Author Accepted Manuscript version arising from this submission.

APPENDIX A: EXPECTED EPIDEMIC SIZE FOR THE COMPLEX-CONTAGION PROCESS

We can calculate the expected epidemic size for a multitype branching process in the subcritical regime, as explained in Sec. III B. Here, we examine the expected epidemic sizes for the complex contagion process. To do this, we need only to replace the next-generation matrix from the mean-field description in Sec. III A 3 with that of the complex-contagion described by Eqs. (7) and (8). As with the results from Sec. III B, we find good agreement when comparing the resulting curves for the expected epidemic (cascade) size, E , to simulation results in Fig. 12. When examining the qualitative behavior of the curves for expected epidemic size, we see from Fig. 12 that as we increase p , as expected, the average epidemic size increases. However, increasing α decreases each network’s average outbreak size. Moreover, this effect

is most pronounced for networks with larger cliques, as this network gives the quarantining behavior more opportunities to remove possible infection paths via the complex-contagion approximation to the process.

APPENDIX B: EFFECTIVE REPRODUCTION NUMBER

We investigate the role of contact tracing in networks with cliques and its effect on the effective reproduction number, R_e . Our analysis reveals that R_e reduces in response to increases in the tracing probability, α , and variations in the transmission probability, p . To find R_e in our simulations, we run our discrete-time dynamics and count, on average, how many people have been infected in each time step by a typical infected node. In different trials, we start with a single infected node, chosen uniformly randomly in the network. We follow how many susceptible nodes it infects, even counting the isolated ones, such as the case in Fig. 3(a). For finite networks, this means that we need to run the simulation long enough for the process to stabilize but short enough that the ratio of the infected nodes to the network size remains close to zero. If no new infection happens in a generation, then the disease has died out. The total number of new infections caused by the seed node would be the *individual* reproduction number of that node, and we report it as the effective reproduction number of generation $t = 1$. In the next step, we do the same for the resultant active (infected but not in quarantine) nodes generated by the seed node, one-after-another. Notice that from this step on, a neighbor of an active node may be in quarantine because of its interaction with other neighbors, not with the one it is receiving the infection from, such as the case shown in Fig. 3(b). In these cases, the active node cannot infect the node that has been in quarantine via other nodes. When we are done with all the active nodes of this generation, we report the average number of individual reproduction numbers of these nodes as the effective reproduction at generation $t = 2$. The process can be continued for more generations, depending on the network size. For large-enough networks, the ensemble average of effective reproduction number over different trials starts to stabilize from generation $t = 3$ in the parameter ranges we have explored, indicating that its value remains constant for some time, depending on the network’s size. Hence, we consider this stabilized value at $t = 3$ as the effective reproduction number R_e .

We observe that in networks with cliques of size $r = 6$ and $c = 2, 3, 4$, and transmission probabilities of $p = 1, 0.75, 0.5$, larger cliques correspond to a reduced need for quarantine measures to bring R_e down to 1. This relationship between clique size and the required intensity of quarantine efforts to control the spread is illustrated in Fig. 13, which aligns with our theoretical predictions of Sec. III A and simulations described in Sec. III A 2.

APPENDIX C: REPRODUCTION NUMBER AND THE NEXT-GENERATION MATRIX

We will next give additional details on using the leading eigenvalue of the \mathbf{M} matrix as the reproduction number R_e . Two specific issues were only briefly discussed in the main text: why does the leading eigenvalue of the reducible matrix

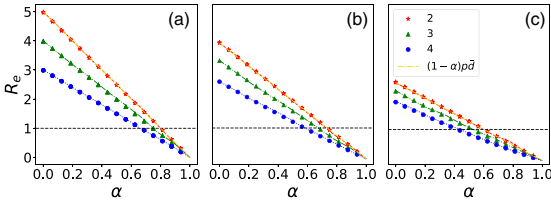


FIG. 13. How contact tracing on clique network reduces the effective reproduction number R_e by increasing α . Effective reproduction number for different networks with cliques with $r = 6$ for transmission probabilities (a) $p = 1.0$, (b) $p = 0.75$, and (c) $p = 0.5$. The dotted lines are from the mean-filed calculations introduced in Sec. III A, and the markers are from Monte Carlo simulations described in Sec. III A 2. The yellow dashed lines, which overlap with the red curves with stars, represent Eq. (1), which match the cases where $c = 2$ (treelike networks). The larger the transmission probability, the larger the differences between the curves of different networks with cliques. The larger the clique size, the less effort we need to quarantine people since networks with larger cliques reach $R_e = 1$ for lower values of α .

\mathbf{M} tell us about the critical behavior, and why can the leading eigenvalue be interpreted as R_e ?

The argument for the leading eigenvalue of the reducible matrix \mathbf{M} determining the criticality is very similar to the one made in Sec. IV A 2 of Ref. [16]. We can divide the transitions between Z states into two categories: ones that describe changes within a clique and ones that describe the infection arriving in a clique that previously only had susceptible nodes. The transitions within cliques form a directed acyclic graph (DAG), because the SIRQ process always moves in one direction, i.e., from susceptible to infected or removed or from infected to removed. DAGs can always be put into upper (or lower) triangular form. Every motif that has at least one susceptible and one infected node will have a transition to the Z_1 state, which has one infected node in an otherwise susceptible clique. We can permute the matrix \mathbf{M} by collecting these motifs to a block \mathbf{B}_1 . These motifs form a strongly connected block because Z_1 is the root of the DAG, and the block is thus irreducible. The remaining states are still triangular, where each motif forms its own block \mathbf{B}_i , so in total, we have the matrix in a normal form. Further, the motifs that do not belong to the block \mathbf{B}_1 are dead ends as they cannot produce any offspring with infected nodes.

The method described above can always be used to write the reducible matrix \mathbf{M} in its normal form such that blocks \mathbf{B}_i fill the upper triangle part of it. Since \mathbf{M} is non-negative, the spectrum of \mathbf{M} is the union of the spectra of the \mathbf{B}_i [51]. Here the B_i has zero eigenvalues for $i \neq 1$, and the largest eigenvalue of \mathbf{M} , i.e., the Perron root, is the same as the largest eigenvalue of \mathbf{B}_1 which is an irreducible matrix. Given that we initialize our spreading process sparsely such that there are only Z_1 motifs in the network in the beginning (in addition to the fully susceptible ones we do not track), the long-term dynamics will always be governed by the leading eigenvalue of \mathbf{B}_1 (and therefore \mathbf{M}) which [16].

The R_e correspondence to the leading eigenvalue might initially seem nonintuitive, considering that some transitions

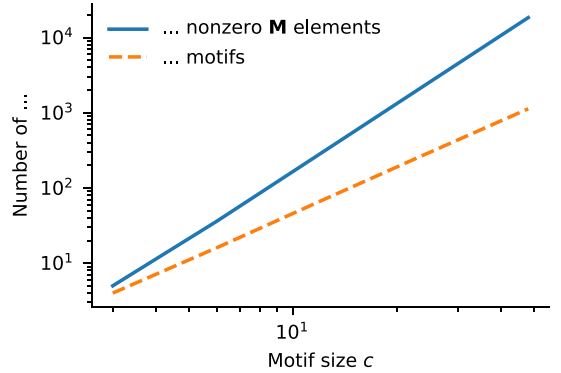


FIG. 14. Number of motifs and the number of nonzero elements of \mathbf{M} for given clique size c .

create multiple infected nodes at one step. This indicates that one needs to multiply the effects of transitions by the number of newly infected nodes in them to compute the expected number of newly infected nodes a typical infected node produces. However, this is not necessary. A key observation here is that the number of Z_1 motifs is directly proportional to the number of infected nodes in the network. Every time a node is infected, it will create $n_c - 1$ of new Z_1 motifs, where n_c is the number of cliques each node belongs to. In the next time step, those motifs transition into one of the other motif types, and the infected individuals become removed, so the number of Z_1 motifs is always updated to be $n_c - 1$ times the number of infected nodes. That is, at time step t , the number of infected nodes is $I^t = z_1^t / (n_c - 1)$, where z_1^t is the number of motifs z_1 at time t . Given that we are at the steady state, z^t is the leading eigenvector, i.e., $z^{t+1} = Mz^t = \lambda z^t$, and $z_1^{t+1} = \lambda z_1^t$, which means that $I^{t+1} = \lambda I^t$.

APPENDIX D: AUTOMATIC GENERATION OF THE NEXT-GENERATION MATRICES

We show how the next-generation matrix can be constructed for any clique size c by an algorithm described here.

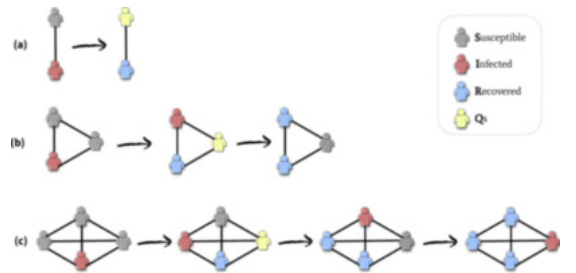


FIG. 15. Schematic of the impact of the short-time quarantine. We track the number of susceptible, infected, and recovered nodes for the three main cliques we consider. We can note that the first instance where a previously quarantined susceptible node can meet an infected node appears in the 4-clique.

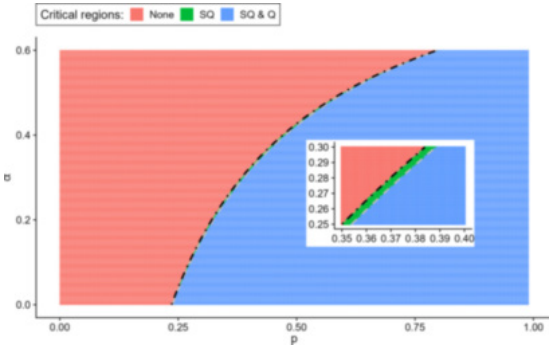


FIG. 16. Differences in the critical regions obtained from the largest eigenvalues of the mean matrix for the original quarantine time (labeled Q) and the short quarantine time (labeled SQ). Inset shows a subset of parameter values from which the difference between the two quarantine times is more apparent.

The construction is done by going through every motif and considering the transitions and expected values leading out of that motif. That is, we go one motif at a time, starting from the one with only a single infected node and the rest of the nodes susceptible, constructing the motifs one time and stepping away from that motif and the expected number of new motifs produced.

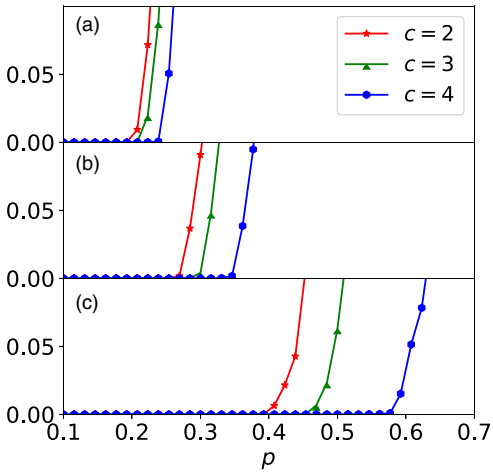


FIG. 17. Phase transitions from a disease-free equilibrium to an endemic state for 2-, 3-, and 4-clique networks with degree 6 as introduced in Sec. II A. Nodes in quarantine can leave the Q compartment at every time step with probability $\alpha' = 0.4$. [(a)–(c)] The outbreak size E , normalized to the network size, is shown on the vertical axis for when (a) $\alpha = 0$ (no contact tracing), (b) $\alpha = 0.25$, and (c) $\alpha = 0.5$, from top to bottom respectively. Note that the transition points are shifted slightly to the right for larger clique sizes, c , even when there is no contact tracing ($\alpha = 0$), but this difference is substantially amplified for larger α values. Results are based on Monte Carlo simulations introduced in Sec. III A 2 and Appendix E.

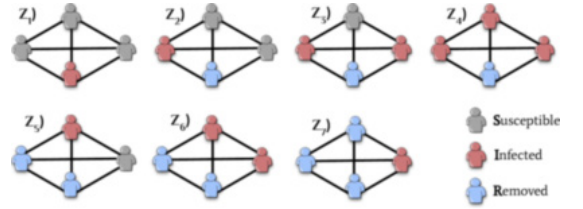


FIG. 18. Life stages or diffusion patterns of a 4-clique. Similar to Fig. 5 for a 3-clique. We can generate the next-generation matrix for any clique size with our code introduced in Appendix D.

We can note that each clique motif is uniquely defined by the number of nodes in each compartment; that is, we define each unique clique motif by $Z_i = (n_S, n_I, n_R)$ as one that has n_S susceptible nodes, n_I infected nodes, and n_R removed (either recovered or quarantined) nodes. Referring back to Fig. 5, where a 3-node clique has four possible clique motifs and, for example, $Z_1 = (2, 1, 0)$ represents two susceptible nodes, one infected, and none recovered. Initially, a general clique with c nodes will start with the clique motif $Z_1 = (c - 1, 1, 0)$. Given the probability of the susceptible nodes becoming infected, we can calculate the transition probability from Z_1 to either Z_2, Z_3 , or inactive cliques with no new infected nodes. We can calculate the possible transition probability between all clique motifs in this fashion. Once we have the transition probabilities, it is easy to calculate the expected number of newly infected nodes from each clique motif transition and, therefore, calculate the mean matrix.

All this translates into the following general pipeline for processing any clique size we might wish, where we pro-

TABLE III. Nonzero elements of the next-generation matrix \mathbf{M} for a 4-clique network as explained in Sec. III A 3. m_{ij} gives the expected number of Z_i cliques from a Z_j clique, as shown in Fig. 18. n_c is the number of cliques of size $c = 4$ which for an r -regular c -clique satisfies the identity $n_c(c - 1) = r$.

i, j	m_{ij}
1, 1	$3p(-\alpha n_c + \alpha + n_c - 1)$
1, 2	$2p(-\alpha n_c + \alpha + n_c - 1)$
1, 3	$p(1 - \alpha)(n_c - 1)[(\alpha - 1)(p - 1) + 1]$
1, 5	$-p(\alpha - 1)(n_c - 1)$
2, 1	$-3p(\alpha - 1)^3(p - 1)^2$
3, 1	$3p^2(\alpha - 1)^3(p - 1)$
4, 1	$-p^3(\alpha - 1)^3$
5, 1	$-6\alpha p(\alpha - 1)^2(p - 1)$
5, 2	$-2p(\alpha - 1)^2(p - 1)$
6, 1	$3\alpha p^2(\alpha - 1)^2$
6, 2	$p^2(\alpha - 1)^2$
7, 1	$3\alpha^2 p(1 - \alpha)$
7, 2	$2\alpha p(1 - \alpha)$
7, 3	$p(1 - \alpha)[(\alpha - 1)(p - 1) + 1]$
7, 5	$p(1 - \alpha)$

cess the clique motifs one at a time with the following rules:

(a) If the motif Z_i has no infected nodes, then we do nothing.

(b) If it has one or more infected nodes, then we then create transitions to new motifs $Z_j = (n_S + \delta n_S, n_I + \delta n_I, n_R + \delta n_R)$, for all $\delta n_I \in \{1, \dots, n_S\}$, $\delta n_R \in \{0, \dots, n_S - \delta n_I\}$, and $\delta n_S = -\delta n_I - \delta n_R$.

(c) If those new motifs have not been processed before, then they are added to a queue for being processed.

The transition probabilities m_{ji} can then be computed for $j \neq 1$ by

$$\binom{n_S}{\delta n_I} \binom{n_S - \delta n_I}{\delta n_R} p(n_I)^{\delta n_I} [1 - p(n_I)]^{n_S + \delta n_S} \cdot \alpha^{\delta n_R} (1 - \alpha)^{n_S - \delta n_R}, \quad (D1)$$

where the probability of n_I nodes causing a node to get infected is

$$p(n_I) = \sum_{k=0}^{n_I-1} (\alpha - 1)^k (1 - p)^k p. \quad (D2)$$

The element m_{1i} can be computed by

$$m_{1i} = (n_c - 1) \sum_{j \neq 1} \delta n_I(j, i) m_{ji}, \quad (D3)$$

where the value $\delta n_I(j, i)$ is the value of δn_I in the transition from Z_i to Z_j .

This procedure will yield a sparse matrix, \mathbf{M} , where the size of the matrix and the number of nonzero elements grow as shown in Fig. 14. This process allows us to automatically generate the mean matrices for any clique size we wish to examine efficiently. See Ref. [68] for the Python implementation of this process.

APPENDIX E: IMPACT OF SHORTENED QUARANTINE TIME

In the main text, we assumed that quarantine was forever, or effectively longer than the length of time a clique could have at least one infected node to propagate the infection. Here we can consider this assumption's effect on the main three network topologies that we consider, where $c = 2, 3$, and 4, where a node is only quarantined for a single time step. This means a susceptible node placed in the quarantine compartment is returned to the susceptible compartment after one time step.

For the 2-clique case, see Fig. 15(a). This will not have any effect, as the clique only represents links, and any susceptible quarantined node will not have any infected neighbors in the following time step. For the 3-clique case, see Fig. 15(b). We have the same situation as the 2-clique case. In any case, where the node is infected, and a susceptible node is in the quarantine compartment, in the following step, there will not

TABLE IV. Nonzero elements of the next-generation matrix \mathbf{M} in the complex contagion approximation for a 4-clique network. m_{ij} gives the expected number of Z_i cliques from a Z_j clique.

i, j	m_{ij}
1, 1	$3p(n_c - 1)$
1, 2	$-2(n_c - 1)[(\alpha - 1)(p - 1) - 1]$
1, 3	$(n_c - 1)[(\alpha - 1)^3(p - 1)^2 + 1]$
1, 5)	$(n_c - 1)[(\alpha - 1)^2(p - 1) + 1]$
2, 1	$3p(p - 1)^2$
3, 1	$3p^2(1 - p)$
4, 1	p^3
5, 2	$2(1 - \alpha)(p - 1)[(\alpha - 1)(p - 1) - 1]$
6, 2	$(\alpha p - \alpha - p)^2$
7, 3	$(\alpha - 1)^3(p - 1)^2 + 1$
7, 5	$(\alpha - 1)^2(p - 1) + 1$

be any active infected node to infect the returned susceptible node. The 4-clique is the only case where the shortened quarantine comes into play. This clique size has one possible infection path, illustrated in Fig. 15(c), that can result in an additional infection for this short quarantine time. If we were to readjust the mean matrix to account for this and recalculate the critical regions, see Fig. 16, then we can see that it is hard to discern any difference in the overall behavior. If we concern ourselves with the inset of Fig. 16, which concentrates on a smaller parameter region, then we can see that there is indeed a thin band of parameters for which the new quarantining behavior is super critical, but the original system is not. This difference is so small due to the presence of only a single set of low-probability events in which a returned susceptible node plays any role, and as such, our overall results are valid.

To demonstrate that the exit of nodes from the quarantine Q compartment does not significantly alter the key epidemic outcomes we focus on, we have adjusted the model described in Sec. III A 2. In this modified model, at each time step, nodes in quarantine have a probability α' of leaving the Q compartment. Consequently, nodes from the Q_S and Q_I compartments transition to the S and R compartments, respectively, with probability α' . This adjustment was made to reaffirm the results previously presented in Fig. 4(a), specifically to show that these changes do not affect the epidemic thresholds of interest. Figure 17 illustrates this scenario with $\alpha' = 0.4$.

Next-generation Matrices for 4-cliques

Figure 18 shows the life stages of a 4-clique. For this case, the next-generation matrix according to the mean-filed and complex contagion approximations are given by Table III and Table IV, respectively.

[1] A. M. Brandt, The history of contacttracing and the future of public health, *American J. Pub. Health* **112**, 1097 (2022).

[2] T. R. Mercer and M. Salit, Testing at scale during the covid-19 pandemic, *Nat. Rev. Genet.* **22**, 415 (2021).

- [3] K. Fogh, J. E. Strange, B. F. Scharff, A. R. Eriksen, R. B. Hasselbalch, H. Bundgaard, S. D. Nielsen, C. S. Jørgensen, C. Erikstrup, J. Norsk *et al.*, Testing denmark: A danish nationwide surveillance study of covid-19, *Microbiol. Spectr.* **9**, e01330-21 (2021).
- [4] D. Lewis, Why many countries failed at covid contact-tracing—but some got it right, *Nature London* **588**, 384 (2020).
- [5] Editorial, Contact tracing: Digital health on the frontline, *The Lancet Digital Health* **2**, e561 (2020).
- [6] L. E. Smith, R. Amlôt, H. Lambert, I. Oliver, C. Robin, L. Yardley, and G. J. Rubin, Factors associated with adherence to self-isolation and lockdown measures in the UK: A cross-sectional survey, *Publ. Health* **187**, 41 (2020).
- [7] X. Wang, Z. Du, E. James, S. J. Fox, M. Lachmann, L. A. Meyers, and D. Bhavnani, The effectiveness of covid-19 testing and contact tracing in a us city, *Proc. Natl. Acad. Sci. USA* **119**, e2200652119 (2022).
- [8] S. Galea, R. M. Merchant, and N. Lurie, The mental health consequences of covid-19 and physical distancing: the need for prevention and early intervention, *JAMA Intern. Med.* **180**, 817 (2020).
- [9] A. K. Rizzi, A. Faqeeh, A. Badie-Modiri, and M. Kivelä, Epidemic spreading and digital contact tracing: Effects of heterogeneous mixing and quarantine failures, *Phys. Rev. E* **105**, 044313 (2022).
- [10] T. Hiraoka, A. K. Rizzi, M. Kivelä, and J. Saramäki, Herd immunity and epidemic size in networks with vaccination homophily, *Phys. Rev. E* **105**, L052301 (2022).
- [11] S. Sajjadi, P. T. Simin, M. Shadmangohar, B. Taraktas, U. Bayram, M. V. Ruiz-Blondet, and F. Karimi, Structural inequalities exacerbate infection disparities: Acomputational approach, [arXiv:2205.04361](https://arxiv.org/abs/2205.04361).
- [12] T. Hiraoka, A. K. Rizzi, Z. Ghadiri, M. Kivelä, and J. Saramäki, The strength and weakness of disease-induced herd immunity, [arXiv:2307.04700](https://arxiv.org/abs/2307.04700).
- [13] A. J. Kucharski, P. Klepac, A. J. Conlan, S. M. Kissler, M. L. Tang, H. Fry, J. R. Gog, W. J. Edmunds, J. C. Emery, G. Medley *et al.*, Effectiveness of isolation, testing, contact tracing, and physical distancing on reducing transmission of SARS-CoV-2 in different settings: A mathematical modelling study, *Lancet Infect. Dis.* **20**, 1151 (2020).
- [14] S. L. Feld, The focused organization of social ties, *Am. J. Sociol.* **86**, 1015 (1981).
- [15] E. Bokányi, E. M. Heemskerck, and F. W. Takes, The anatomy of a population-scale social network, *Sci. Rep.* **13**, 9209 (2023).
- [16] L. A. Keating, J. P. Gleeson, and D. J. P. O’Sullivan, Multitype branching process method for modeling complex contagion on clustered networks, *Phys. Rev. E* **105**, 034306 (2022).
- [17] L. A. Keating, J. P. Gleeson, and D. J. O’Sullivan, A generating-function approach to modelling complex contagion on clustered networks with multi-type branching processes, *J. Complex Netw.* **11**, cnad042 (2023).
- [18] G. St-Onge, H. Sun, A. Allard, L. Hébert-Dufresne, and G. Bianconi, Universal nonlinear infection kernel from heterogeneous exposure on higher-order networks, *Phys. Rev. Lett.* **127**, 158301 (2021).
- [19] M. Mancastroppa, A. Guizzo, C. Castellano, A. Vezzani, and R. Burioni, Sideward contact tracing and the control of epidemics in large gatherings, *J. R. Soc. Interface* **19**, 20220048 (2022).
- [20] L. D. Valdez, L. Vassallo, and L. A. Braunstein, Epidemic control in networks with cliques, *Phys. Rev. E* **107**, 054304 (2023).
- [21] I. Z. Kiss, D. M. Green, and R. R. Kao, The effect of network mixing patterns on epidemic dynamics and the efficacy of disease contact tracing, *J. R. Soc. Interface* **5**, 791 (2008).
- [22] N. J. Salkind, *Encyclopedia of Educational Psychology* (SAGE, Los Angeles, 2008), pp. 150–152.
- [23] R. D. Luce and A. D. Perry, A method of matrix analysis of group structure, *Psychometrika* **14**, 95 (1949).
- [24] C. Stegehuis and T. Peron, Network processes on clique-networks with high average degree: The limited effect of higher-order structure, *J. Phys. Complex.* **2**, 045011 (2021).
- [25] D. J. O’Sullivan, G. O’Keefe, P. Fennell, and J. Gleeson, Mathematical modeling of complex contagion on clustered networks, *Front. Phys.* **3**, 71 (2015).
- [26] B. Karrer and M. E. J. Newman, Random graphs containing arbitrary distributions of subgraphs, *Phys. Rev. E* **82**, 066118 (2010).
- [27] J. C. Miller, Percolation and epidemics in random clustered networks, *Phys. Rev. E* **80**, 020901(R) (2009).
- [28] M. E. J. Newman, Properties of highly clustered networks, *Phys. Rev. E* **68**, 026121 (2003).
- [29] I. Z. Kiss and D. M. Green, Comment on “properties of highly clustered networks,” *Phys. Rev. E* **78**, 048101 (2008).
- [30] L. Hébert-Dufresne, P.-A. Noël, V. Marceau, A. Allard, and L. J. Dubé, Propagation dynamics on networks featuring complex topologies, *Phys. Rev. E* **82**, 036115 (2010).
- [31] N. C. Wormald *et al.*, Models of random regular graphs, *London Mathematical Society Lecture Note Series* (Cambridge University Press, 1999), pp. 239–298.
- [32] B. Bollobás, Random graphs, in *Modern Graph Theory* (Springer, Berlin, 1998), pp. 215–252.
- [33] R. Pastor-Satorras, C. Castellano, P. Van Mieghem, and A. Vespignani, Epidemic processes in complex networks, *Rev. Mod. Phys.* **87**, 925 (2015).
- [34] M. E. J. Newman, Spread of epidemic disease on networks, *Phys. Rev. E* **66**, 016128 (2002).
- [35] D. Zhang and T. Britton, Epidemic models with digital and manual contact tracing, [arXiv:2211.12869](https://arxiv.org/abs/2211.12869).
- [36] A. Anglemeyer, T. H. Moore, L. Parker, T. Chambers, A. Grady, K. Chiu, M. Parry, M. Wilczynska, E. Fleming, and L. Bero, Digital contact tracing technologies in epidemics: A rapid review, *Cochrane Database Syst Rev.* **8**, CD013699 (2020).
- [37] T. Fetzter and T. Graeber, Measuring the scientific effectiveness of contact tracing: Evidence from a natural experiment, *Proc. Natl. Acad. Sci. USA* **118**, e2100814118 (2021).
- [38] A. D. Hossain, J. Jarolimova, A. Elnaïem, C. X. Huang, A. Richterman, and L. C. Ivers, Effectiveness of contact tracing in the control of infectious diseases: A systematic review, *The Lancet Public Health* **7**, e259 (2022).
- [39] U.S. Department of Health and Human Services, What is the difference between isolation and quarantine? <https://www.hhs.gov/answers/public-health-and-safety/what-is-the-difference-between-isolation-and-quarantine/index.html> (2020).
- [40] A. J. Kucharski, R. M. Eggo, C. H. Watson, A. Camacho, S. Funk, and W. J. Edmunds, Effectiveness of ring vaccination as control strategy for ebola virus disease, *Emerg. Infect. Dis.* **22**, 105 (2016).

- [41] M. Kretzschmar, S. Van den Hof, J. Wallinga, and J. Van Wijngaarden, Ring vaccination and smallpox control, *Emerg. Infect. Dis.* **10**, 832 (2004).
- [42] M. Schleiff, A. Olateju, E. Decker, A. H. Neel, R. Oke, M. A. Peters, A. Rao, and O. Alonge, A multi-pronged scoping review approach to understanding the evolving implementation of the smallpox and polio eradication programs: what can other global health initiatives learn? *BMC Publ. Health* **20**, 1698 (2020).
- [43] L. Ferretti, C. Wymant, M. Kendall, L. Zhao, A. Nurtay, L. Abeler-Dörner, M. Parker, D. Bonsall, and C. Fraser, Quantifying SARS-CoV-2 transmission suggests epidemic control with digital contact tracing, *Science* **368**, eabb6936 (2020).
- [44] O. Diekmann, H. Heesterbeek, and T. Britton, *Mathematical Tools for Understanding Infectious Disease Dynamics* (Princeton University Press, Princeton, NJ, 2013), Vol. 7.
- [45] E. Kenah and J. M. Robins, Second look at the spread of epidemics on networks, *Phys. Rev. E* **76**, 036113 (2007).
- [46] E. Kenah and J. C. Miller, Epidemic percolation networks, epidemic outcomes, and interventions, *Interdisciplinary Perspect. Infect. Dis.* **2011**, 543520 (2011).
- [47] M. Li, R.-R. Liu, L. Lü, M.-B. Hu, S. Xu, and Y.-C. Zhang, Percolation on complex networks: Theory and application, *Phys. Rep.* **907**, 1 (2021).
- [48] N. Goldenfeld, *Lectures on Phase Transitions and the Renormalization Group* (CRC Press, Boca Raton, FL, 2018).
- [49] S. N. Dorogovtsev, A. V. Goltsev, and J. F. F. Mendes, Critical phenomena in complex networks, *Rev. Mod. Phys.* **80**, 1275 (2008).
- [50] H. Caswell, *Matrix Population Models* (Sinauer, Sunderland, MA, 2000), Vol. 1.
- [51] R. S. Varga, *Matrix Iterative Analysis* (Springer Science & Business Media, New York, 1999), Vol. 27.
- [52] O. Diekmann, J. A. P. Heesterbeek, and J. A. J. Metz, On the definition and the computation of the basic reproduction ratio R_0 in models for infectious diseases in heterogeneous populations, *J. Math. Biol.* **28**, 365 (1990).
- [53] A. F. Brouwer, Why the spectral radius? An intuition-building introduction to the basic reproduction number, *Bull. Math. Biol.* **84**, 96 (2022).
- [54] R. M. Ziff, Percolation and the pandemic, *Physica A* **568**, 125723 (2021).
- [55] M. E. J. Newman, Random graphs with clustering, *Phys. Rev. Lett.* **103**, 058701 (2009).
- [56] J. P. Gleeson, S. Melnik, and A. Hackett, How clustering affects the bond percolation threshold in complex networks, *Phys. Rev. E* **81**, 066114 (2010).
- [57] F. Ball, D. Sirl, and P. Trapman, Analysis of a stochastic sir epidemic on a random network incorporating household structure, *Math. Biosci.* **224**, 53 (2010).
- [58] J. C. Miller, Spread of infectious disease through clustered populations, *J. R. Soc. Interface* **6**, 1121 (2009).
- [59] S. Melnik, A. Hackett, M. A. Porter, P. J. Mucha, and J. P. Gleeson, The unreasonable effectiveness of tree-based theory for networks with clustering, *Phys. Rev. E* **83**, 036112 (2011).
- [60] E. Coupechoux and M. Lelarge, How clustering affects epidemics in random networks, *Adv. Appl. Probab.* **46**, 985 (2014).
- [61] R. Van der Hofstad, J. S. Van Leeuwen, and C. Stegehuis, Hierarchical configuration model, [arXiv:1512.08397](https://arxiv.org/abs/1512.08397).
- [62] C. Stegehuis, R. Van der Hofstad, and J. S. Van Leeuwen, Epidemic spreading on complex networks with community structures, *Sci. Rep.* **6**, 29748 (2016).
- [63] P. Mann, V. A. Smith, J. B. O. Mitchell, and S. Dobson, Random graphs with arbitrary clustering and their applications, *Phys. Rev. E* **103**, 012309 (2021).
- [64] M. Ritchie, L. Berthouze, and I. Z. Kiss, Beyond clustering: Mean-field dynamics on networks with arbitrary subgraph composition, *J. Math. Biol.* **72**, 255 (2016).
- [65] J. Saramäki, A. Badie-Modiri, A. K. Rizi, M. Kivelä, and M. Karsai, *Temporal Network Theory*, edited by P. Holme and J. Saramäki (Springer International Publishing, Cham, 2023), pp. 107–130.
- [66] A. Badie-Modiri, A. K. Rizi, M. Karsai, and M. Kivelä, Directed percolation in temporal networks, *Phys. Rev. Res.* **4**, L022047 (2022).
- [67] A. Badie-Modiri, A. K. Rizi, M. Karsai, and M. Kivelä, Directed percolation in random temporal network models with heterogeneities, *Phys. Rev. E* **105**, 054313 (2022).
- [68] Github repository, <https://github.com/k-rizi/Contact-Tracing-On-Clique-Networks>.

Publication IV

A. K. Rizi, A. Faqeeh, A. Badie-Modiri and M. Kivelä. Epidemic spreading and digital contact tracing: Effects of heterogeneous mixing and quarantine failures. *Physical Review E*, 105(4) 044313, April 2022.

© 2022 K. Rizi et al.

Reprinted with permission.

Epidemic spreading and digital contact tracing: Effects of heterogeneous mixing and quarantine failures

Abbas K. Rizi ¹, Ali Faqeeh,^{1,2,3} Arash Badie-Modiri ¹ and Mikko Kivelä ¹

¹*Department of Computer Science, School of Science, Aalto University, FI-00076, Finland*

²*Mathematics Applications Consortium for Science & Industry, University of Limerick, Limerick V94 T9PX, Ireland*

³*Luddy School of Informatics, Computing, and Engineering, Indiana University, Bloomington, Indiana 47408, USA*



(Received 7 July 2021; accepted 22 March 2022; published 20 April 2022)

Contact tracing via digital tracking applications installed on mobile phones is an important tool for controlling epidemic spreading. Its effectivity can be quantified by modifying the standard methodology for analyzing percolation and connectivity of contact networks. We apply this framework to networks with varying degree distributions, numbers of application users, and probabilities of quarantine failures. Further, we study structured populations with homophily and heterophily and the possibility of degree-targeted application distribution. Our results are based on a combination of explicit simulations and mean-field analysis. They indicate that there can be major differences in the epidemic size and epidemic probabilities which are equivalent in the normal susceptible-infectious-recovered (SIR) processes. Further, degree heterogeneity is seen to be especially important for the epidemic threshold but not as much for the epidemic size. The probability that tracing leads to quarantines is not as important as the application adoption rate. Finally, both strong homophily and especially heterophily with regard to application adoption can be detrimental. Overall, epidemic dynamics are very sensitive to all of the parameter values we tested out, which makes the problem of estimating the effect of digital contact tracing an inherently multidimensional problem.

DOI: [10.1103/PhysRevE.105.044313](https://doi.org/10.1103/PhysRevE.105.044313)

I. INTRODUCTION

Until effective vaccines are widely deployed in a pandemic era, carefully timed nonpharmaceutical interventions [1] such as wearing face masks [2], school closures, travel restrictions, and contact tracing [3–7] are the best tools we have for curbing the pandemic. Contact tracing is an attempt to discover and isolate asymptomatic or presymptomatic (exposed) individuals. In the absence of herd immunity, contact tracing is a potent low-cost intervention method since it puts people into quarantine where and when the disease spreads. Therefore, it can have a significant role in containing a pandemic by relaxing social-distancing interventions [8], providing an acceptable trade-off between public health and economic objectives [9,10], developing sustainable exit strategies [11,12], identifying future outbreaks [13], and reaching the “source” of infection [14].

Thanks to the emergence of low-cost wearable health devices [15–22] and mobile software applications, digital contact tracing can now be deployed with higher precision without the problems of manual contact tracing, such as the tracing being slow and labor intensive or people’s hesitation to give identifying data about their contacts due to blame, fear, confusion, or politics. On the other hand, smartphones and wearable devices also offer continuous access to real-time physiological data, which can be used to tune other nonpharmaceutical or pharmaceutical strategies. Modern apps enable us to monitor COVID-19 symptoms [23–25]; identify its hotspots [26]; track mosquito-borne diseases such as Malaria, Zika, and Dengue [27,28]; and detect microscopic pathogens.

In both forms—manual [4,5,29–37] and digital [38–44]—contact tracing has been commonly considered as an effective strategy and different empirical data sets have validated this claim in short-time population-based controlled experiments [38,40]. It has been estimated that for every percentage point increase in app-users, the number of cases can be reduced by 2.3% (in statistical analysis) [45]. However, such a linear view of the benefits of the app usage is likely too simplistic and ignores the complexities disease spreading, especially in heterogeneous populations [46–49]. For instance, degree-heterogeneity in the contact network [50] can alter epidemiological properties in the form of variance in final outbreak size [51], vanishing epidemic threshold [49,52], hierarchical spreading [53], strong finite-size effects [54], and universality classes for critical exponents [55]. Moreover, the existence of superspreaders dictates the extent to which a virus spreads in a bursty fashion [56–58], especially when there is high individual-level variation in the number of secondary transmissions [53,59,60]. Therefore, to evaluate the effectiveness of contact-tracing, degree-heterogeneity and app adoption of superspreaders [61,62] should be taken into account. Note that in some parameter settings, contact tracing may not be effective enough [8,63,64].

A potentially important factor in the effectiveness of the contact tracing apps is related to how the app-using and non-app-using populations are mixed. Several studies have shown that similar people with similar features are more likely to be in contact with each other than with people with different types of features. This phenomenon is known as homophily [65–67]. It has been reported in app adoption directly [40]

and indirectly through correlation in app adoption and other features exhibiting homophily, such as jobs, age, income, and nationality [68–70]. Therefore, the fraction of population that adopts the app is not the only important factor for reducing the peak and total size of the epidemic but also the amount of homophily in app adoption can potentially have a significant role.

Since the World Health Organization has declared the COVID-19 outbreak as a Public Health Emergency of International Concern, network scientists have developed different approaches toward analyzing epidemic tracing and mitigation with apps. Using the toolbox of network science, different groups have investigated the effectiveness of contact tracing based on the topology and directionality of contact networks [14,44,71–77]. Recently, a mathematical framework aimed at understanding how homophily in health behavior shapes the dynamics of epidemics has been introduced by Burgio *et al.* [78]. This study expanded the model of Bianconi *et al.* [71] and computed the reproduction number and attack rate in a homophilic population using mean-field equations.

Our study investigates the effect of varying app coverage on the epidemic’s threshold, probability, and expected size in homogeneous and heterogeneous contact networks with and without homophily or heterophily in app adoption. Further, we explore the effect of distributing the apps randomly and preferentially to high-degree nodes [71] in these scenarios. Our main focus is on the epidemic threshold and the final size of the epidemics. Therefore, we assume the dynamics of the epidemic to be governed by the simple SIR model [50]. This model can be easily mapped to a static bond-percolation problem [79,80] so that the epidemiological properties can be measured based on the topological structure of the underlying network [50,73,81–84]. Note that, more complex disease transmission models, such as SEIR models in which there is an infected-but-not-contagious period E, are also covered by this formalism [79,85]. The difference in the spreading framework with the app to the normal one is that the infection cannot spread further if it passes a link between two app-users (app-adopters). That is, the infection process model needs to include the memory of the type of node it is coming from. We then extend the percolation framework such that we can add memory [86,87] to it in order to keep track of the infection path. This leads to the observation that the epidemic size is not the same as the epidemic probability as it would be in this model without the app-users [88].

Our results are largely based on mean-field-type calculations of the percolation problem, which are confirmed by explicit simulations of SIR epidemic process and measurements of component sizes in finite networks. Our findings show that (1) the number of app-users has a direct effect on the epidemic size and epidemic probability and the difference between these two observables is larger in high-degree targeting strategy; (2) epidemics can be controlled to a much better degree in the high-degree targeting strategy; (3) even though degree-heterogeneity can strongly affect or even eliminate the epidemic threshold, high-degree targeting strategy can compensate this effect and increase the threshold significantly; (4) increasing heterophily from random mixing always increases the outbreak size and lowers the epidemic threshold; (5) increasing homophily does the opposite until an optimum,

that is below the maximum homophily case, is reached; and, finally, (6) the probability of contact tracing succeeding in preventing further infections is not as crucial as the fraction of app-users, but can still have significant effects on the epidemic size and epidemic threshold. The only exception is when the apps are distributed to heterogeneous networks with the high-degree targeting strategy.

II. MODELLING APPROACH

A. Disease model and connection to percolation

We employ a SIR disease model on networks with additional dynamics given by the disease interactions in the presence of the disease tracking application. In the model, without the tracking application, an infected (I) node will eventually infect a neighboring susceptible (S) node with a transmission probability p independently of other infections. The simulations are performed with a model where the infected nodes try to infect their susceptible neighbors with independent Poisson processes with rate β and go to the removed state (R) after fixed time τ . The fixed recovery time ensures that every infected individual, regardless of app adoption, can infect a susceptible neighbor independently with a transmission probability $p = 1 - e^{-\beta\tau}$ [79,89]. These assumptions allow us to study the SIR processes using component size distributions of undirected networks where parts of the links are randomly removed [79,85,88–90]: An epidemic starting from a single node can reach any other node exactly when there is a path of such transmitting links connecting them, i.e., they are in the same component in a network where the potential contact links are removed with probability p . Thus, the epidemic threshold, epidemic probability and epidemic size can be read from percolation simulations [79,85,88–90] (see Sec. II B). Note that without fixed recovery time, the presence of spreading paths through neighboring links would not be independent, and this would not be a bond percolation problem in an undirected network where edges are removed independently. However, the epidemic threshold, final epidemic size, and the expected outbreak size below the epidemic threshold would still be correctly predicted by this methodology [88,89].

We model the effect of applications to the disease spreading as follows: If an app-user infects another app-user, then that second node will get infected but will quarantine themselves with probability p_{app} . The quarantined user will have no further connections that would spread the infection they received from the other app-user. A substantial deviation from a realistic spreading case in our model is that the quarantine does not prevent the disease spreading to the quarantined node through a third node. That is, we only model the primary infection path from the other app-user causing the alarm but do not stop the possible concurrent secondary infection paths from a third node. Strictly speaking, this simplification in the modeling returns a lower bound on the effectiveness of the app-based contact tracing, but given that our contact network models are sparse random graphs (see Sec. II C) that do not contain local loops, the difference can only be observed if a large enough fraction of the population is infected at the same time. Critically, this does not affect the epidemic threshold

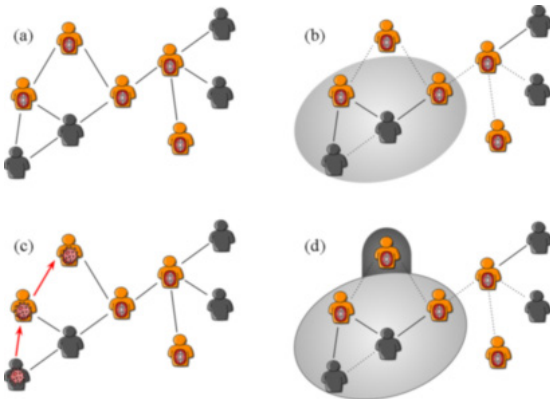


FIG. 1. (a) Original contact network with app-users marked with the oval symbol. (b) The normal largest component, after the dotted links have been removed in the percolation process at random. When apps are working perfectly, links between a pair of app-users are removed with probability $p_{app} = 1$ and other links are removed with probability p . (c) An example for a path of infection: The second app-user can be infected; therefore, it must be included in the outbreak size. (d) Extending the giant component to include the secondary app infections. The second infected app-adopter is added to the giant component with transmission probability p .

but could have implications for parameter regions where the epidemic size is large, depending on the quarantine durations.

The SIR spreading process can be mapped to a slightly more complicated percolation problem in the presence of apps [44,71]. To model app-user quarantines, one needs to delete the links between two app-users with the probability of successful quarantine due to the app, p_{app} . This ensures that we ignore the infection paths through two app-users when one of them is successfully quarantined. However, removing these links also removes the second app-user from the component, even though they are infected. To correct this, we need first to find the network components and then extend them by including all app-users outside of the component connected to another app-user (and considering the probability p that the link is kept). See Fig. 1 for an illustration of this process, which leads us to two definitions of components: normal and extended.

B. Components, epidemic size, and epidemic probability

In the SIR model without apps, the component size distribution can be used to describe the late stages of the epidemics approximately. Given an initially infected node, the size of the component it belongs to determines the size of the outbreak. In an infinitely large population, we say that an outbreak is an epidemic if it spans a nonzero fraction of the population. The relationship between percolation and the final epidemic size is straightforward if the population is large enough that it can be approximated with an infinite undirected transmission network [79,88]. In this case, the percolation threshold gives the epidemic threshold and below it, an outbreak always spans only a zero fraction of the population because all the components are of finite size. Above the percolation threshold,

there is a single giant component that spans $s_{max} = S_{max}/N$ fraction of the nodes. This is equivalent to both the size of the epidemic, given that there is one, and the probability that there is an epidemic starting from a single initially infected node [79,88]; s_{max} is the fraction of nodes that can be reached from the giant component (epidemic size) and the probability that randomly chosen node belongs to the giant component (probability of the epidemic). The expected epidemics size in a fraction of eventually infected nodes is, in this case, given as s_{max}^2 .

When we introduce apps to the spreading process, the equivalence of the epidemic size and epidemic probability breaks down. Both the normal component and the extended component become important. The component size still gives the probability that there is an epidemic, as is the case without the apps. However, the epidemic size, given that there is one, is now given by the extended component size s'_{max} . The expected epidemic size is then given by $s_{max}s'_{max}$.

Similar relationships hold for finite-size systems. For example, the expected size of the epidemics from single source becomes

$$\langle E \rangle = \sum_c \frac{S_c}{N} S'_c, \tag{1}$$

where S_c is the normal size and S'_c is the extended size of the component c and N is the total number of nodes. In this formula, S_c/N gives the probability that the initially infected node is in the component c and S'_c gives the size of the epidemic if a node in component c is chosen.

C. Network models

We aim to study how the network topology, amount, and distribution of app-users over the network affect the epidemics. We study networks with degree distribution $P(k)$ and average degree $\langle k \rangle$ such that each node is an app-user with probability π_a and not an app-user with probability $1 - \pi_a$. We distribute the app-users with one of two strategies: (1) uniformly at random or (2) by distributing the apps in the order of their degree such that the high-degree nodes get the apps first.

We use three different models to generate the network topology. We use (i) Poisson or Erdős-Rényi (ER) random graphs [91] to model homogeneous contact patterns and (ii) scale-free networks generated with the Chung-Lu model (CL) [92,93] to model heterogeneous networks. In generation of CL networks, the expected degree of each node is drawn from a continuous power-law distribution $P(k) \propto k^{-3}$ such that the minimum expected degree is set to a value that gives us the expected average degree $\langle k \rangle$ of our choice. Given a sequence of expected degrees $W = \{w_1, w_2, \dots, w_n\}$, Miller algorithm [94] assigns a link between node u and node v with probability $p_{uv} \propto w_u w_v$. This algorithm returns a network without multiple links with almost the same power-law degree distribution.

We model homophily (and heterophily) with regards to apps usage with (iii) a modular network model (MN) introduced in Refs. [95,96] with two groups of nodes: app-users and non-app-users. This model starts with a degree sequence produced either by the ER or CL models and connects the nodes depending on which groups they belong with

probabilities π_{aa} (app-user to app-user), π_{an} (app-user to non-app-user), π_{na} (non-app-user to app user), and π_{nn} (non-app-user to non-app-user). We only need to fix one of these probabilities, π_{aa} , and other types of links are formed with probabilities $\pi_{an} = 1 - \pi_{aa}$, $\pi_{na} = \frac{\pi_a}{1-\pi_a}(1 - \pi_{aa})$, and $\pi_{nn} = 1 - \pi_{na} = \frac{1-\pi_a-\pi_a(1-\pi_{aa})}{1-\pi_a}$, where π_a is the probability that a person is an app-user and the second equality comes from the balance between the number of links from app-users to non-app-users and from non-app to app-users, that is, $\pi_a N \pi_{na} \langle k \rangle = (1 - \pi_a) N \pi_{na} \langle k \rangle$. The numerical simulations of the MN work by randomly choosing a group for half edges with the given probabilities and matching them to each other uniformly randomly. This can lead to self-links and multilinks, which these are discarded after the randomization procedure.

While there is no correlation between the app adoption status in homogeneous (ER) or heterogeneous (CL) networks above, in the third model (MN), the existence of homophily or heterophily of the network structure is determined by comparing π_{aa} to its value for the neutral case with no homophily or heterophily. In the absence of homophily or heterophily, $\pi_{aa} = \eta_a$, where η_a is the ratio of the number of links that emerge from app-users to the total degree; this is because if the nodes were connected purely at random, then the probability that a link from an app-user connects it to another app-user equals the ratio of the number of stubs that app-users have to the total number of stubs, i.e., η_a . In the case of a random selection of app-users $\eta_a = \pi_a$, since both app-users and non-app-users have on average the same number of stubs and the fraction of stubs that app-users have equals the fraction of app-users in the system, i.e., π_a . In a high-degree targeting strategy, the number of stubs that app-users have on average is larger than that of non-app-users. In that case, η_a can be calculated from the degree distribution (see Sec. III A). When $\pi_{aa} > \eta_a$, app-users are more likely to be connected to each other than in a network in which a fraction of η_a of them being uniformly randomly placed. On the other hand, when $\pi_{aa} < \eta_a$ nodes are more likely to be connected to the nodes of the other type (heterophilic network). In the heterophilic regime, for some pairs of (π_{aa}, π_a) , networks are not realizable because of the constraints explained in Sec. III A. The white region in Fig. 6 shows the region of π_{aa} - π_a plane that networks cannot be created in that parameter space.

III. ANALYTIC AND SIMULATION METHODS

The epidemics are studied here with various methods of approximation. We employ analytical computations based on mean-field-type approximations to efficiently analyze our models' wide parameter space and provide explicit formulas for our main observable quantities. Here an approximation based on branching processes [97] can be used to determine the critical point. Following Ref. [44], a more detailed calculation based on percolation arguments will give us the component sizes which can be related to the final epidemic size and epidemic probability. Simulations of the network connectivity then complement these mean-field approximations. Finally, we explore the accuracy of the mean-field approximations via explicit simulations of the SIR model.

A. Giant component size from consistency equations

To study the behavior of the epidemic dynamics, we form consistency equations for the giant component size. In Ref. [44] the governing equations for the size of the epidemic and the transition point were obtained for the case of random networks in the absence of homophily. Here we derive the analytical results for the more general case of the spectrum of heterophilic to homophilic networks, a special case of which is the nonhomophilic networks of Ref. [44]. We consider that app-users and non-app-users might be connected together with a pattern different from pure random chance using the MN model.

We aim to write the self-consistent equations for the probability, u_n , that following a link to a non-app-user does not lead to the giant component and probability u_a , that following a link to an app-user does not lead to the giant component. Using these probabilities, the relative size of the giant component s and the relative size of the extended giant component s' can be obtained, where s is, in fact, the fraction of nodes infected through non-app-users, while s' also includes individuals who caught the infection through an app-user before they could quarantine themselves (see Sec. III C 1).

We need to know the probability u_n (u_a), that a randomly chosen link leading to a non-app-user (app-user) is not in the giant component. The probability that a non-app-user (app-user) is not connected to the giant component via a particular neighboring node is equal to the probability that *that* non-app-user (app-user) is not connected to the giant component via any of its other neighbors. A non-app-user is connected to another non-app-user with probability $\pi_{nn} = 1 - \pi_{na}$ and to an app-user with probability π_{na} . So, a link leading out from a non-app-user does not lead to the giant component if it leads to another non-app-user that is not in the giant component [which happens with probability $(1 - \pi_{na})u_n$] or an app-user that is not in the giant component (which happens with probability $\pi_{na}u_a$). That is, the total probability for following a link out from a non-app-user not leading to the giant component is $u_{n \rightarrow} = (1 - \pi_{na})u_n + \pi_{na}u_a$. Since the degree of neighboring nodes is disturbed according to the excess degree distribution q_k , the probability that a non-app-user that is encountered by following a link to it is not connected to the giant component via any of its k neighbors is $\sum_k q_k u_{n \rightarrow}^k$. This probability is, by definition, u_n , leading to the self-consistent equation below for u_n :

$$u_n = g_1[(1 - \pi_{na})u_n + \pi_{na}u_a], \quad (2)$$

where g_1 is the generating function for excess degree distribution [50]. To find u_a , we can use the same treatment, except that we should consider how app-app connections depend on the probability of success in contact tracing [44]. If p_{app} is the probability the apps work as expected, then $1 - p_{app}$ is the probability that the app-user does not effectively quarantine after being been in contact by an infectious app-user. Therefore, u_a can be expressed as the self-consistent equation below:

$$u_a = g_1\{(1 - \pi_{aa})u_n + \pi_{aa}[p_{app} + (1 - p_{app})u_a]\}. \quad (3)$$

Note that π_{na} is determined by the free parameters π_a and π_{aa} as we already showed that $\pi_{na} = \frac{\pi_a}{1-\pi_a}(1 - \pi_{aa})$.

Given u_n and u_a , the average probability that a node belongs to the giant component, or equivalently the fraction of the network occupied by the giant component, is now given by:

$$s = 1 - (1 - \pi_a)g_0[(1 - \pi_{na})u_n + \pi_{na}u_a] - \pi_a g_0\{(1 - \pi_{aa})u_n + \pi_{aa}[p_{app} + (1 - p_{app})u_a]\}, \quad (4)$$

where g_0 is the generating function for degree distribution. We can approximate s' by writing:

$$s' = 1 - (1 - \pi_a)g_0[(1 - \pi_{na})u_n + \pi_{na}u_a] - \pi_a g_0\{(1 - \pi_{aa})u_n + \pi_{aa}u_a\}, \quad (5)$$

where, as opposed to Eq. (4), the third term is not a function of p_{app} and the reason is that Eq. (4) assumes that if the app works (which happens with probability p_{app}) then the probability that a link connected to an app-user does not lead to the giant component is 1 (while if the app does not work it is u_a). However, whether the app works or not, the probability that an app-user does not get infected from another app-user is u_a . When apps work, if the second app-user is infected, she quarantines herself and does not infect any other node).

In the case of including a transmission probability p which is less than 1 (in the above equations it was assumed the links are transmitting with probability 1), Eqs. (2) and (3) will change to:

$$u_n = 1 - p + pg_1[(1 - \pi_{na})u_n + \pi_{na}u_a], \quad (6)$$

$$u_a = 1 - p + pg_1\{(1 - \pi_{aa})u_n + \pi_{aa}[p_{app} + (1 - p_{app})u_a]\}. \quad (7)$$

When the fraction π_a of nodes selected to adopt the app are all the highest degree nodes in the network, these nodes all have a degree higher than $k_a - 1$ such that they include some of k_a nodes and the rest are comprised of all nodes with degree larger than k_a . Then for the fraction η_a of the links protruding from the app-users (which are the top π_a fraction of nodes) we can write:

$$\eta_a = r^* k_a p_{k_a} / \langle k \rangle + \sum_{k_a+1}^{\infty} k p_k / \langle k \rangle, \quad (8)$$

$$= \sum_{k_a, \text{right}}^{\infty} k p_k / \langle k \rangle, \quad (9)$$

where r^* is the fraction of degree k_a nodes that are app-users and in Eq. (9) we absorbed r^* into p_k so that $p_{k_a, \text{right}} = r^* p_{k_a}$ represents the fraction of nodes in the network that have degree k_a and are app-users [so in Eq. (9), $k_{a, \text{right}}$ takes the value k_a].

Then for a network with homo- or heterophily:

$$u_n = 1 - p + \frac{p}{1 - \eta_a} \sum_{k=0}^{k_{a, \text{left}}} q_k [(1 - \pi_{na})u_n + \pi_{na}u_a]^k, \quad (10)$$

$$u_a = 1 - p + \frac{p}{\eta_a} \sum_{k_{a, \text{right}}}^{\infty} q_k \{(1 - \pi_{aa})u_n + \pi_{aa}[p_{app} + (1 - p_{app})u_a]\}^k, \quad (11)$$

and

$$s = 1 - \sum_{k=0}^{k_{a, \text{left}}} p_k [(1 - \pi_{na})u_n + \pi_{na}u_a]^k - \sum_{k_{a, \text{right}}}^{\infty} p_k \{(1 - \pi_{aa})u_n + \pi_{aa}[p_{app} + (1 - p_{app})u_a]\}^k. \quad (12)$$

A special case of which are networks with neutral (nonexisting) homophily, where π_{aa} is obtained to be equal to η_a and accordingly $\pi_{na} = \eta_a$, therefore,

$$u_n = 1 - p + p \frac{1}{1 - \eta_a} \sum_{k=0}^{k_{a, \text{left}}} q_k [(1 - \eta_a)u_n + \eta_a u_a]^k, \quad (13)$$

$$u_a = 1 - p + p \frac{1}{\eta_a} \sum_{k_{a, \text{right}}}^{\infty} q_k \{\eta_a [p_{app} + (1 - p_{app})u_a] + (1 - \eta_a)u_n\}^k, \quad (14)$$

and

$$s = 1 - \sum_{k=0}^{k_{a, \text{left}}} p_k [(1 - \eta_a)u_n + \eta_a u_a]^k - \sum_{k_{a, \text{right}}}^{\infty} p_k \{\eta_a [p_{app} + (1 - p_{app})u_a] + (1 - \eta_a)u_n\}^k. \quad (15)$$

These results predict the behavior of the epidemic dynamics in the thermodynamic limit. Therefore they describe the dynamics very well when the network size is large enough.

B. Mean-field approximation for the branching process

An alternative to writing the consistency equations for the giant component size is to assume that a branching process governs the epidemic dynamics. Then, a straightforward way of finding the epidemic threshold in the SIR model is to find the critical point of a branching process, where the branching factor is given by the expected excess degree q . In the epidemic setting, the branching factor $\bar{k}_e = pq$ gives the expected number of people one infected person infects during the epidemic process. Note that the branching factor has been used as the definition of the basic reproduction number R_0 [88], but is different from the basic reproduction number when it is defined in the networks as $R_0 = \beta/\gamma \langle k \rangle$ [80]. In the SIR model with the app, we need to duplicate the populations so that we separately track the ones without the app (S_n, I_n , and R_n) and with the app (S_a, I_a and R_a).

Given that the apps are uniformly distributed to π_a fraction of the nodes and \bar{k}_e is the branching factor, we can write a mean-field approximation based on the branching process as follows:

$$I_n^{(t+1)} = \bar{k}_e [\pi_{nn} I_n^{(t)} + \pi_{an} I_a^{(t)}], \quad (16)$$

$$I_a^{(t+1)} = \bar{k}_e [\pi_{na} I_n^{(t)} + \pi_{aa} (1 - p_{app}) I_a^{(t)}]. \quad (17)$$

By defining $a = \pi_{nn}\bar{k}_e$, $b = \pi_{an}\bar{k}_e$, $c = \pi_{na}\bar{k}_e$, and $d = \pi_{aa}\bar{k}_e(1 - p_{app})$, the difference equations can be written as:

$$\mathbf{X}_{t+1} = \mathbf{A}\mathbf{X}_t, \quad (18)$$

where $\mathbf{X}_t = \begin{bmatrix} I_t^{(a)} \\ I_t^{(b)} \end{bmatrix}$ and $\mathbf{A} = \begin{pmatrix} a & b \\ c & d \end{pmatrix}$.

The steady state $\mathbf{X}_{t+1} = \mathbf{X}_t$ is possible if all the eigenvalues λ of the transition matrix \mathbf{A} (whether real or complex) have an absolute value which is less than 1;

$$\lambda_{\pm} = \frac{a+d}{2} \pm \sqrt{\left(\frac{a+d}{2}\right)^2 - (ad-bc)}. \quad (19)$$

Without contact tracing, there is a chance of epidemic, given the initial reproductive number is $\bar{k}_e > 1$. In the case of app adoption, the critical value of app-users π_a^c that is needed for reducing the reproductive number can be derived by setting $\lambda = 1$ which leads to:

$$\begin{aligned} \frac{1 - \pi_a(2 - \pi_{aa})}{1 - \pi_a} [\bar{k}_e + \bar{k}_e^2 \pi_{aa}(1 - p_{app})] \\ + \bar{k}_e \pi_{aa}(1 - p_{app}) + \frac{\bar{k}_e^2 \pi_a(1 - \pi_{aa})^2}{1 - \pi_a} = 1. \end{aligned} \quad (20)$$

When apps work perfectly, the epidemic threshold is given by:

$$\begin{aligned} \bar{k}_c = \frac{\sqrt{1 + \pi_a \pi_{aa} [4(\pi_a + \pi_{aa}) - 3(\pi_a \pi_{aa} + 2)]}}{2\pi_a(\pi_{aa} - 1)^2} \\ + \frac{2\pi_a - \pi_a \pi_{aa} - 1}{2\pi_a(\pi_{aa} - 1)^2}. \end{aligned} \quad (21)$$

For each value of π_a there is a nontrivial optimum value π_{aa}^{opt} that leads to the largest epidemic threshold in terms of the branching factor, which is

$$\pi_{aa}^{\text{opt}} = \frac{\pi_a - 2}{3\pi_a - 4}. \quad (22)$$

The critical app adoption can be also calculated as:

$$\pi_a^c = \frac{1 - \bar{k}_e}{\bar{k}_e^2(\pi_{aa} - 1)^2 + \bar{k}_e(\pi_{aa} - 2) + 1}. \quad (23)$$

In the absence of homo- or heterophily, $\pi_{aa} = \pi_a$, Eq. (20), gives the same result as of Ref. [44], such that:

$$\pi_a^c = \frac{\bar{k}_e - 1 + \sqrt{(\bar{k}_e - 1)(\bar{k}_e + 3)}}{2\bar{k}_e}. \quad (24)$$

Vazquez [97] also provides a clear way of combining different intervention strategies and shows how our specific results about application homophily are affected by other interventions.

C. Component size simulations

Next, we describe how to extract the giant component in simulated networks and how these simulation results can be

used to find the critical points of the disease spreading process. The component sizes can also be used to find the epidemic size distributions as described in Sec. II B.

1. Component extension

In each simulation run, we simulate one network structure G and distribute the apps to the nodes according to one of the models described in Sec. II C. From the original network G , we keep each link with probability $p = 1 - e^{-\beta\tau}$, which is the probability of infection going through a link without apps. We also remove all the links between two app-users with probability p_{app} and call the resulting network G_a . The components of graph G_a are the normal components.

The extended components can be reached by going through every normal component and extending it. For every app-user α in the component C , we go through the neighbors $n_\alpha = \{\alpha_1, \alpha_2, \dots, \alpha_k\}$ in the original network G . If α_i is an app-user and not in the component $\alpha_i \notin C$, then we add it to the component extension C' with probability p . The total set of infected nodes, if starting from a node in C , will be $C \cup C'$. As these are disjoint sets, we can compute the size as $S'_C = |C| + |C'|$ and $S_C = |C|$.

2. Susceptibility

In numerical simulations of finite-size systems, we can use the peak of a susceptibility measure to find the critical transition point. Theoretically, susceptibility [84] is a measure of fluctuation in the component sizes, which is singular at the epidemic threshold (the critical point). In network percolation studies, it is defined as the expected growth in the size of the giant component when a random link is added to the network. Therefore, susceptibility in an ordinary percolation problem can be written as:

$$\chi = \frac{\sum_{c \neq c_{\max}} S_c^2 - S_{c_{\max}}^2}{N - S_{c_{\max}}}, \quad (25)$$

where S_c is the size of the component c , $c_{\max} = \text{argmax}_c S_c$ is the largest component.

Here, we are dealing with two types of components, and as is shown in Fig. 2(d), the fraction of the sum of component sizes and network size S_{Σ}/N can be larger than one. Susceptibility should be a monotonically decreasing function in the supercritical regime. However, plugging the extended component sizes into Eq. (25) results in a growth in the tail of susceptibility, turning it to a nonmonotonic function in the supercritical regime. Therefore, this formulation of susceptibility is not suitable in the current case since the maximum of Eq. (25) could lead to estimates of critical points that are very far from the actual one. Instead, we can use the expected growth in the extended giant component, which can be computed as:

$$\chi' = \frac{\sum_{c \neq c_{\max}} S_c S'_c \left(1 - \frac{S'_{c_{\max}}}{N}\right)}{N - S_{c_{\max}}}, \quad (26)$$

where S_c and S'_c are the size and the extended size of the component c and $c_{\max} = \text{argmax}_c S'_c$ is the largest component measured in the extended size.

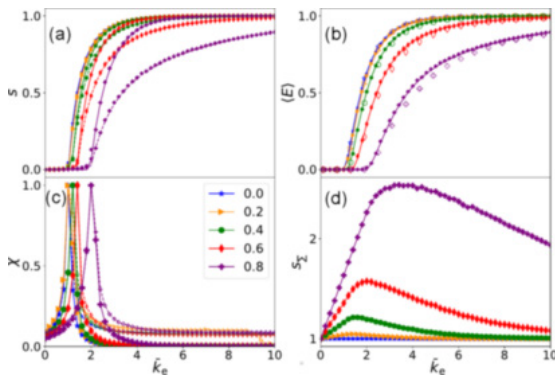


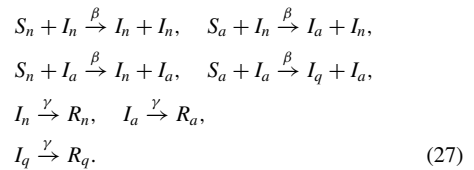
FIG. 2. Disease spreading statistics in an Erdős-Rényi network as a function of the effective connectivity \bar{k}_e when there are $\pi_a N$ perfect applications ($p_{\text{app}} = 1$) that are distributed uniformly randomly. Results are normalized to the network size N and shown for $\pi_a \in [0, 0.2, 0.4, 0.6, 0.8]$ with different markers. (a) The normal component size, i.e., the epidemic probability (dashed lines and markers following them) and the extended components, i.e., the epidemic size (solid lines and markers following them). Dashed and solid lines indicate the results from theory introduced in Sec. III A by Eq. (4) and the markers are results computed from component sizes of simulated networks as described in Sec. III C. (b) The expected epidemic size as given by Eq. (1) computed with the theoretical results introduced in Sec. III A (solid lines), simulated component sizes introduced in Sec. III C (filled markers), and explicit SIR simulations introduced in Sec. III D (empty markers). (c) Susceptibility of the normal giant component χ (dots) and the extended component χ' (solid lines) as defined in Eqs. (25) and (26). Since susceptibility is a divergent quantity at the epidemic threshold, as explained in Sec. III C 2, it is a good proxy for finding the critical point. Notice that peaks are at the same positions for both curves, normal and extended components. (d) The fraction of sum of component sizes and network size S_Σ/N .

D. Explicit compartment model simulations

Finally, we will perform explicit simulations of the spreading processes to confirm the theoretical results we arrived at via the approximations we presented above. The effect of tracking applications can be integrated into compartment model simulation by introducing separate susceptible and infected compartments for people with and without the app. The interactions between people with no app installed is similar to those of the normal SIR process, namely, susceptible individuals with no app (S_n) can become infected (I_n) by being in contact with infected people that either do not have the app installed (I_n) or have it installed (I_a). However, if a susceptible individual with the app (S_a) comes into contact with an infected individual with app (I_a), they will become infected but they will also receive infection notification from the app which means they will be quarantined (I_q). Quarantined individuals cannot infect anyone else. Eventually, all the infected individuals will move to the recovered compartment after a constant predetermined amount of time ($1/\gamma$) has passed from the beginning of their infection. The recovered compartment

is divided into three compartments R_n , R_a , and R_q to track which infected compartment the node is originating from.

The set of all reactions can be written as follows:



Note that while edge reactions are governed by Poisson processes happening at a constant rate β , unlike most common SIR models, node reactions are governed by constant cutoff time $1/\gamma$ and happen exactly $1/\gamma$ units of time after the infection of the node.

As interactions in the simulation are bound to take place over edges of a static network, with nodes belonging to each of the compartments, as shown in Sec. IV, the results are similar to a component size simulation (which are described in Sec. III C) on a network with effective connectivity of $\bar{k}_e = \langle k \rangle (1 - e^{-\beta/\gamma})$. As only the ratio between β and γ plays as a parameter in the model, we set the value of γ to 1.

In each simulation, starting from a single infected node and running the simulation in discrete time steps of 10^{-4} units until no further reaction is possible, the final number of nodes that end up in R_q , R_a , and R_n determine total size of infection corresponding to the extended component size S' of the component that the initial seed node belongs to. The final combined size of the R_n and R_a component, however, represents the size of the component S_n that the seed node (index case) would belong to, had we removed app-app links. By adding I_a and I_q compartments, as compared to normal SIR processes, and linking them to the state of the source of infection and the internal state of each node, we include information about the history of the spreading agent more than one step back in the simulation of the spreading process.

IV. NUMERICAL RESULTS

We will next illustrate using the theory and simulation introduced in Sec. III how the various parameters affect the epidemic sizes and epidemic probabilities. The simulation studies are done in networks of 10^4 nodes and averaged over 10 realizations. We use two network topologies: homogeneous networks (Erdős-Rényi networks) with expected degree $\langle k \rangle = 10$ and random networks with expected degree sequence driven from power-law degree distribution $p(k) \propto k^{-3}$, with a minimum degree cutoff adjusted such that the average degree is set to 10 [94].

A. Differences in normal and extended components

The difference between the epidemic probability (normal component size) and the epidemic size (extended component size), as given by Eqs. (4) and (5), is a phenomenon specific to epidemics in the presence of app-adaptors. Breaking the equivalence of these two measures can have practical consequences, as illustrated in Fig. 2(a). The difference between these two grows with the fraction of app-users π_a . For example, when $\pi_a = 0.8$ and the epidemic probability

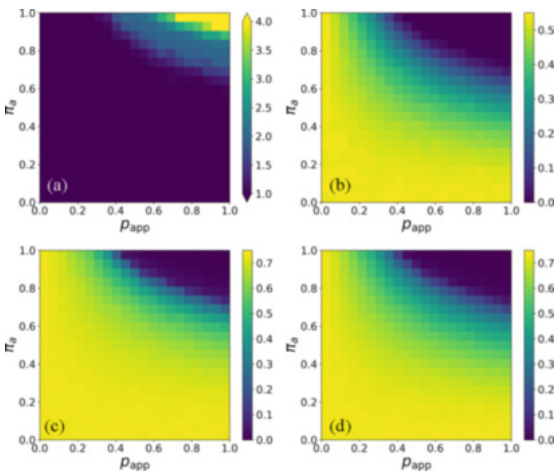


FIG. 3. The effect of quarantine failures as described in Sec. IV B in homogeneous networks when app adoption is done uniformly randomly. Results are from percolation simulations. (a) The epidemic threshold as a function of quarantine probability p_{app} and app adoption rate π_a . All threshold values larger than 4 are shown with the same color. By setting the effective connectivity of the network to $\bar{k}_e = 1.8$ (b) the expected epidemic size, (c) the extended giant component size, and (d) the normal giant component size are shown as a function of p_{app} and π_a . Note that $\bar{k}_e = 1.8$ is chosen as an illustrative example of a parameter region with interesting behavior in the various component sizes: It is large enough such that without any intervention, there is a wide epidemic spreading, but small enough such that the spread can be controlled without extreme measures.

(the normal component size) is $s_{\text{max}} \approx 0.5$, the epidemic size (the extended component size) reaches $s_{\text{max}} \approx 0.8$. This is also reflected in the expected epidemic sizes [see Fig. 2(b) and Eq. (1)]. Despite the two component definitions differing from each other, they still display the transition at the same point and this point can be measured numerically using the susceptibilities defined in Eqs. (25) and (26) [see Fig. 2(c)].

The extended component size is not a conserved quantity like the normal component size in the sense that the sum of component sizes S_{Σ} would always sum to the number of nodes N . Instead, the sum of component sizes can be significantly larger than the number of nodes [see Fig. 2(d)] and the maximum value it can reach grows with the number of application users π_a . The deviation from $S_{\Sigma}/N = 1$ reaches its maximum with disease parameters higher than the threshold values, but when the disease reaches a large enough population, the fraction S_{Σ}/N starts to decay, reaching $S_{\Sigma}/N = 1$ when everybody belongs to the normal giant component.

B. Quarantine failures

The assumption in Sec. IV A is that (i) apps work perfectly and (ii) an app-user always self-isolates before having a chance to spread the infection, meaning that there are no quarantine failures, $p_{\text{app}} = 1$. It is of practical significance to investigate the effects of quarantine failures [45] on the epidemic threshold and epidemic size. Figure 3 shows that

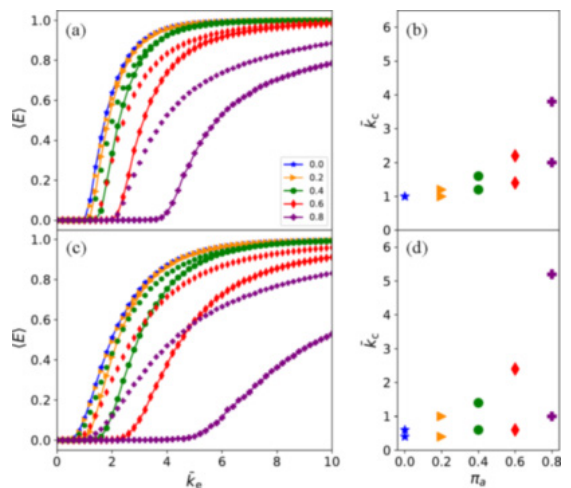


FIG. 4. Expected epidemic size $\langle E \rangle$ and epidemic threshold \bar{k}_c for two network topologies with different strategies; $\langle E \rangle$ as a function of effective connectivity \bar{k}_e for (a) homogeneous networks with Poisson degree distribution and for (c) heterogeneous networks with a power-law degree distribution $P(k) \propto k^{-3}$. Results are shown for different values of π_a using different markers: 0 (stars), 0.2 (triangles), 0.4 (disks), 0.6 (diamonds), and 0.8 (crosses). The solid lines with markers indicate the high-degree targeting strategy, while single markers indicate the random app adoption. Epidemic threshold \bar{k}_c as a function of app-adoption rate π_a (such that the upper markers represent the high-degree targeting strategy) for (b) homogeneous networks and for (d) heterogeneous networks. Differences between the threshold values in the presence of homophily are explained in Figs. 5(b) and 5(d).

in the absence of major quarantine failures, epidemic tracing and mitigation with apps can still be a valid strategy if the app adoption level in a society is high enough. The effect of app adoption rate π_a is more important than the rate at which apps function, but both need to be relatively high in order for the apps to have a significant impact.

Even if we are above the epidemic threshold, the apps can be useful. Especially when the application adoption π_a is high, the quarantines can be very unreliable and the outbreak size [Figs. 3(b) and 3(c)] and epidemic probability [Fig. 3(d)] both remain small. Again, overall, app adoption and quarantine reliability are essential, with the app adoption rate being more important.

C. Degree heterogeneity and high-degree app targeting

Real networks are degree-heterogeneous and this heterogeneity has a strong effect on the final outbreak size and the epidemic threshold. Figure 4 shows the expected epidemic sizes with two different strategies in app adoption, random, and high-degree targeting, for different fractions of app-users π_a in the network. In homogeneous networks, Fig. 4(a), contact tracing decreases the expected epidemic size and pushes the epidemic threshold forward. These effects can be further amplified by shifting to the high-degree targeting in

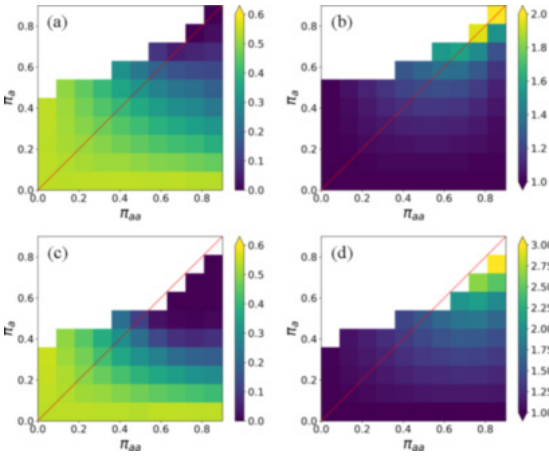


FIG. 5. The effect of homophily or heterophily in app adoption in homogeneous networks as described in Sec. IV D. Homophily (heterophily) region is below (above) the diagonal $\pi_a = \pi_{aa}$. Expected epidemic size at $\bar{k}_e = 1.8$ for (a) random app adoption and for (c) high-degree targeting strategy. The epidemic threshold for (b) random app adoption and for (d) the high-degree targeting strategy. Thresholds are from theoretical results given by Eq. (21) and expected epidemic sizes are from percolation simulations. The empty white region is the spectrum that having such a homo- or heterophilic population is impossible.

app adoption. With 80% of app-users, the epidemic threshold can move from $\bar{k}_e = 1$ to $\bar{k}_e = 4$, which means at that point expected epidemic size is zero, while without contact tracing it would be almost 1. Note that in homogeneous networks, the effective average degree of the contact network \bar{k}_e , has good correspondence to the reproduction number of the infection.

In networks with degree-heterogeneity, the epidemic threshold vanishes in normal SIR processes. This effect holds in contact-traced epidemics if we distribute the apps uniformly randomly. However, from Fig. 4(b) it is clear that contact tracing can significantly reduce the expected epidemic size even when the apps are randomly distributed and the epidemic threshold remains unchanged. With the high-degree targeting strategy, it is possible to move the epidemic threshold. Comparing the expected epidemic size at different values of $\bar{k}_e < 3$ shows that in real-world situations, app adoption of superspreaders is of significant importance. Since hubs become the app-users, this strategy has drastic effects on the size and threshold of the epidemic, such that the threshold gets pushed from somewhere near zero to a value $\bar{k}_e > 5$ with the app adoption rate $\pi_a = 0.8$. Therefore, the reproduction number can be much more controlled in the high-degree targeting strategy.

D. The effect of homophily and heterophily

In previous sections, there was an assumption that app-users are distributed with random mixing patterns; the fact that one of the connections of a node is an app-user has no effect on the probability of that node being

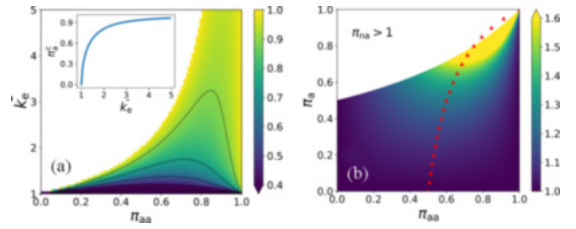


FIG. 6. Existence of optimum value for homophily based on branching process approximation as described in Sec. III B. (a) The critical value of app-users π_a^c that are needed for reducing the reproductive number as a function of effective connectivity and homophily probability π_{aa} . The value of π_a^c remains the same within each black curve. The inset is the graph of π_a^c as a function of \bar{k}_e in the absence of homophily $\pi_{aa} = \pi_a$ given by Eq. (24). (b) The epidemic threshold \bar{k}_e as a function of π_{aa} and π_a . The red symbols show the π_{aa}^{opt} for each π_a which is given by Eq. (22). The pattern here is consistent with another approximation shown in Fig. 5(b), while epidemic threshold values are slightly different due to different levels of approximations. Note that here we display the epidemic threshold for all values of π_{aa} and π_a such that $0 \leq \pi_{na} \leq 1$ so the networks with some of these parameters can be created in practice [95].

an app adopter. Next, we explore how homophily or heterophily affects epidemics based on app usage using the MN model. A Swiss experiment has reported that while a small fraction of $\pi_a = 0.2$ of people have used the app, the inside connections between them was high enough such that $\pi_{aa} = 0.7$ [40].

Figure 5 illustrates that increasing heterophily leads to a lower epidemic threshold and larger epidemic size for a fixed \bar{k}_e . Increasing homophily from random mixing is initially preferable, but the optimum lies between random mixing and full homophily. For the expected epidemic size, strong heterophily is especially detrimental [see Fig. 5(a) for the homogeneous network and with random app adoption and in Fig. 5(c) for high-degree targeting strategy]. The optimum value for heterophily or homophily is evident for the epidemic thresholds in Figs. 5(b) and 5(d), respectively, for the random and high-degree targeting strategies. Figure 6(b) gives a more clear picture of existence of an optimum value for the epidemic threshold in the case of homophily. According to Eq. (21), for each fraction of app-users π_a in the network, the epidemic threshold $\bar{k}_e(\pi_a, \pi_{aa})$ can be maximized by controlling the homophily in app adoption π_{aa} . The pattern in the Fig. 6(b) is very similar to the convex pattern in Fig. 5(b), even though they are calculated using different approximations and approaches (see Secs. III A and III B).

Another view on the effect of homophily and heterophily is given by finding the critical fraction app-users π_a^c that is needed to go beyond the epidemic threshold as a function of $(\pi_{aa}$ and $\bar{k}_e)$. Figure 6(a) depicts this relationship based on Eq. (23) and shows that π_a^c is not monotonic function of π_{aa} but there is an optimal value of π_{aa} giving the lowest fraction apps that are needed to stop the epidemic. Note that in a network without homophily or heterophily π_a^c increases monotonically as the function of the effective connectivity \bar{k}_e [see the inset of Fig. 6(a)].

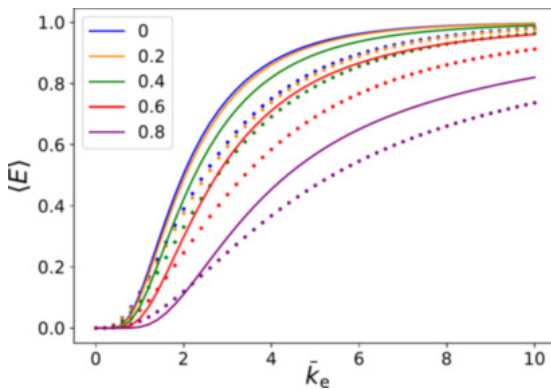


FIG. 7. The expected epidemic size computed with theoretical results introduced in Sec. III A for heterogeneous networks with degree distribution $P(k) \propto k^{-2.5}$ (solid lines) compared with ones with $P(k) \propto k^{-2.5}$ (dotted lines) as a function of the effective connectivity \bar{k}_e when apps are distributed uniformly randomly. Results are normalised to the network size N and shown for $\pi_a \in [0, 0.2, 0.4, 0.6, 0.8]$ with different colors. Note that by lowering the exponent, epidemic thresholds get closer to zero and the expected epidemic sizes decrease since there more low-degree nodes in the network. Therefore, by lowering the exponent, while we can add more degree heterogeneity in the network, the physics of the phenomena does not change.

V. DISCUSSIONS

In this article, we have developed two flexible analytic approximations to SIR epidemics in the presence of contact tracing apps. First, we use a branching process to derive explicit analytical solutions for the epidemic thresholds. Second, we expand the framework of using self-consistent equations to analyze digital contact tracing [44], which is an alternative to other approaches [71]. Contrary to the conventional SIR spreading, a full picture of the late-state epidemics in the presence of digital contact tracing is not given by a single observable (the component size), but one also needs two variables (normal and extended component sizes). These correspond to the probability of the epidemic and the epidemic size, which are equivalent in the SIR process. Here we see that the two quantities can be significantly different if the number of application users is high.

Our numerical results illustrate that the effects of digital contact tracing can be very sensitive to the network structure, how applications are distributed among the population, and how well the tracing works. Realistic estimates of the effects of digital contact tracing can only be achieved if one can choose correct parameter ranges in a high-dimensional parameter space. In this study, we had six of such parameters: the shape of the degree distribution, average degree, amount of heterophily or homophily, application prevalence, quarantine probability and targeting strategy. While we were able to establish and confirm basic laws governing individual parameters and some combinations of parameters, exploring such a parameter space fully for possible compound effects is out of the reach in simulations. However, these effects can be largely revealed by inspecting the analytic equations we derived.

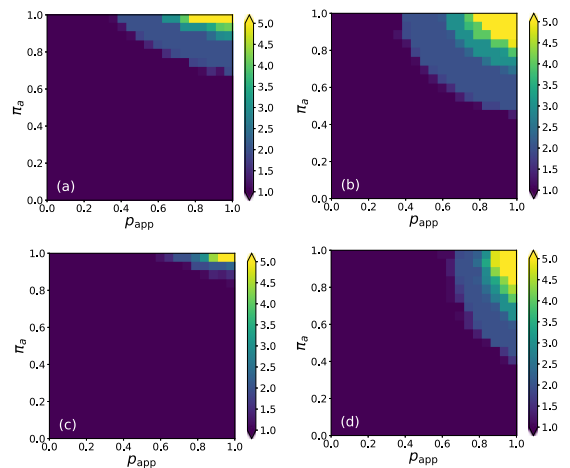


FIG. 8. The epidemic threshold as a function of quarantine probability p_{app} and app adoption rate π_a . The effect of quarantine failures in homogeneous networks with (a) random app adoption (b) and high-degree targeting strategy. Also, for heterogeneous networks with a power-law degree distribution with (c) random app adoption (d) and high-degree targeting strategy. All threshold values larger than 5 are shown with the same color.

There are several open questions for which this study and other studies only hint at the results. There are types of network structures we ignore here. For example, the heterophily

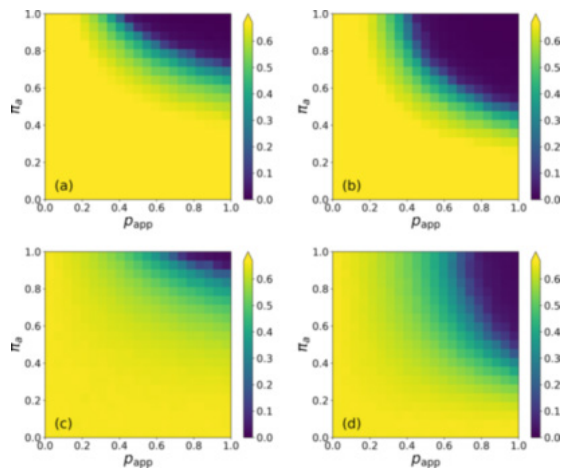


FIG. 9. Expected epidemic size in the case of quarantine failures. Expected epidemic size at $\bar{k}_e = 1.8$ for homogeneous networks with (a) random app adoption (b) and high-degree targeting strategy. Also, for heterogeneous networks with a power-law degree distribution with (c) random app adoption (d) and high-degree targeting strategy. In (b) and (d) the pattern is different due to the effects of hubs. When doing a high-degree targeting strategy, quarantine failures are more significant since the infected ones are highly influential on the spreading dynamics.

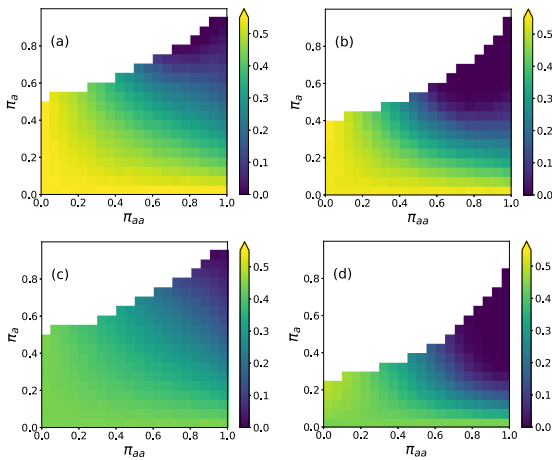


FIG. 10. The effect of homophily or heterophily in app adoption on the expected epidemic size. Expected epidemic size at $\bar{k}_c = 1.8$ from percolation simulations for homogeneous networks with (a) random app adoption (b) and high-degree targeting strategy. Also, for heterogeneous networks with a power-law degree distribution with (c) random app adoption and (d) high-degree targeting strategy. The empty white region is the spectrum that having such a homo- or heterophilic population is impossible.

and homophily could be constructed in the network in slightly different ways. For example, a case study using a realistic agent-based model [69] has recently considered, among many other modeling choices aimed at precise calibration on the French population, the contributions of individuals of different ages. One could also develop a more realistic version of our stylized model to systematically analyze the effects of homophily caused by an age-based contact structure and different scenarios of app adoption within that structure. The age-based approach would also allow one to estimate the benefits of applications relative to the risk groups in this model.

Overall the problem of digital contact tracing offers not only a practical problem to solve but also an interesting theoretical puzzle because it introduces memory to the epidemic process. This memory is limited to one step within the tracing model we use here, but one could also use multistep tracing, where also the second neighbors of infected nodes are quarantined in the case that the first neighbors have already passed on the infection. Further, here we ignore effects such as quarantines that do not directly stop the infection from one application user to another from spreading further. However, in the case of a strong group structure in the network, there could be situations where a nonapplication user A infects application user B, who alerts another application user C, who actually gets infected by A and stops the spreading because of the quarantine. Analyzing such more complicated phenomena can provide challenges for network scientists for years to come.

ACKNOWLEDGMENTS

The simulations presented above were performed using computer resources within the Aalto University School of

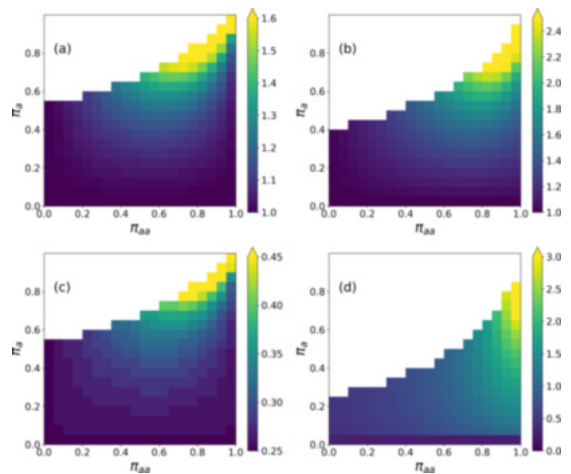


FIG. 11. The effect of homophily or heterophily in app adoption on the epidemic threshold and optimum pattern for homophily. Epidemic thresholds for homogeneous networks with (a) random app adoption (b) and high-degree targeting strategy. Also, for heterogeneous networks with a power-law degree distribution with (c) random app adoption (d) and high-degree targeting strategy. The empty white region is the spectrum that having such a homo- or heterophilic population is impossible.

Science “Science-IT” project. A.F. acknowledges funding by Science Foundation Ireland Grant No. 16/IA/4470.

APPENDIX

The heterogeneity in the number of contacts could also be modeled with other distributions, for example, the negative binomial distribution. This would have the advantage of having a nodivergent second moment supported by empirical evidence. However, we aimed to illustrate the effects of degree heterogeneity and not perform a systematic analysis. We already have many different random network models and combinations of parameters related to the app distribution, how well it works, and disease parameters. The equations we give make it possible for one to do such analysis if needed. Therefore we limited our main discussion to the differences observed in a power-law network with exponent -3 compared to the results for homogeneous networks. However, to satisfy the curiosity of the reader interested in extreme heterogeneity, we have now added Fig. 7 showing the expected epidemic size for exponent -2.5 .

About quarantine failures, as it was shown in Figs. 3, 8 and 9 also show that contact tracing can yield very good results in terms of reducing the epidemic threshold and expected epidemic size if everything goes right at least for 50% and half of the people use the apps. This effect is more prominent if we go for the high-degree targeting strategy, especially in heterogeneous networks, as shown in Figs. 8(d) and 9(d). Figures 10 and 11 show that there is an optimum value for homophily in app adoption as it was shown in Fig. 5 and Fig. 6. The only exception is when we follow a high-degree targeting strategy in heterogeneous networks. In this case, we can see the hub effect on the epidemic threshold and size.

- [1] N. Perra, Non-pharmaceutical interventions during the covid-19 pandemic: A review, *Phys. Rep.* **913**, 1 (2021).
- [2] Y. Cheng, N. Ma, C. Witt, S. Rapp, P. S. Wild, M. O. Andreae, U. Pöschl, and H. Su, Face masks effectively limit the probability of sars-cov-2 transmission, *Science* **372**, 1439 (2021).
- [3] M. J. Keeling and P. Rohani, *Modeling Infectious Diseases in Humans and Animals* (Princeton University Press, Princeton, NJ, 2011).
- [4] W. H. Foege, J. D. Millar, and J. M. Lane, Selective epidemiologic control in smallpox eradication, *Am. J. Epidemiol.* **94**, 311 (1971).
- [5] K. C. Swanson, C. Altare, C. S. Wesseh, T. Nyenswah, T. Ahmed, N. Eyal, E. L. Hamblion, J. Lessler, D. H. Peters, and M. Altmann, Contact tracing performance during the ebola epidemic in liberia, 2014-2015, *PLoS Negl. Trop. Dis.* **12**, e0006762 (2018).
- [6] G. W. Rutherford and J. M. Woo, Contact tracing and the control of human immunodeficiency virus infection, *J. Am. Med. Assoc.* **259**, 3609 (1988).
- [7] G. J. Fox, S. E. Barry, W. J. Britton, and G. B. Marks, Contact investigation for tuberculosis: a systematic review and meta-analysis, *Eur. Respir. J.* **41**, 140 (2013).
- [8] A. Aleta, D. Martin-Corral, A. P. y Piontti, M. Ajelli, M. Litvinova, M. Chinazzi, N. E. Dean, M. E. Halloran, I. M. Longini Jr, S. Merler *et al.*, Modelling the impact of testing, contact tracing and household quarantine on second waves of covid-19, *Nat. Hum. Behav.* **4**, 964 (2020).
- [9] P. G. Walker, C. Whittaker, O. J. Watson, M. Baguelin, P. Winskill, A. Hamlet, B. A. Djafaara, Z. Cucunubá, D. O. Mesa, W. Green *et al.*, The impact of covid-19 and strategies for mitigation and suppression in low-and middle-income countries, *Science* **369**, 413 (2020).
- [10] S. M. Kissler, C. Tedijanto, E. Goldstein, Y. H. Grad, and M. Lipsitch, Projecting the transmission dynamics of sars-cov-2 through the postpandemic period, *Science* **368**, 860 (2020).
- [11] J. Bell, G. Bianconi, D. Butler, J. Crowcroft, P. C. Davies, C. Hicks, H. Kim, I. Z. Kiss, F. Di Lauro, C. Maple *et al.*, Beyond covid-19: Network science and sustainable exit strategies, *J. Phys. Complex.* **2**, 021001 (2021).
- [12] M. Gilbert, M. Dewatripont, E. Muraille, J.-P. Platteau, and M. Goldman, Preparing for a responsible lockdown exit strategy, *Nat. Med.* **26**, 643 (2020).
- [13] N. E. Kogan, L. Clemente, P. Liautaud, J. Kaashoek, N. B. Link, A. T. Nguyen, F. S. Lu, P. Huybers, B. Resch, C. Havas, A. Petutschnig, J. Davis, M. Chinazzi, B. Mustafa, W. P. Hanage, A. Vespignani, and M. Santillana, An early warning approach to monitor covid-19 activity with multiple digital traces in near real time, *Sci. Adv.* **7**, eabd6989 (2021).
- [14] S. Kojaku, L. Hébert-Dufresne, E. Mones, S. Lehmann, and Y.-Y. Ahn, The effectiveness of backward contact tracing in networks, *Nat. Phys.* **17**, 652 (2021).
- [15] M. Salathe, L. Bengtsson, T. J. Bodnar, D. D. Brewer, J. S. Brownstein, C. Buckee, E. M. Campbell, C. Cattuto, S. Khandelwal, P. L. Mabry *et al.*, Digital epidemiology, *PLoS Comput. Biol.* **8**, e1002616 (2012).
- [16] A. Natarajan, H.-W. Su, and C. Heneghan, Assessment of physiological signs associated with covid-19 measured using wearable devices, *npj Digit. Med.* **3**, 156 (2020).
- [17] D. R. Seshadri, E. V. Davies, E. R. Harlow, J. J. Hsu, S. C. Knighton, T. A. Walker, J. E. Voos, and C. K. Drummond, Wearable sensors for covid-19: A call to action to harness our digital infrastructure for remote patient monitoring and virtual assessments, *Front. Digit. Health* **2**, 8 (2020).
- [18] D. P. Oran and E. J. Topol, Prevalence of asymptomatic sars-cov-2 infection: A narrative review, *Ann. Intern. Med.* **173**, 362 (2020).
- [19] E. Morales-Narváez and C. Dincer, The impact of biosensing in a pandemic outbreak: Covid-19, *Biosens. Bioelectron.* **163**, 112274 (2020).
- [20] G. Quer, J. M. Radin, M. Gadaleta, K. Baca-Motes, L. Ariniello, E. Ramos, V. Kheterpal, E. J. Topol, and S. R. Steinhubl, Wearable sensor data and self-reported symptoms for covid-19 detection, *Nat. Med.* **27**, 73 (2021).
- [21] T. Mishra, M. Wang, A. A. Metwally, G. K. Bogu, A. W. Brooks, A. Bahmani, A. Alavi, A. Celli, E. Higgs, O. Dagan-Rosenfeld *et al.*, Pre-symptomatic detection of covid-19 from smartwatch data, *Nat. Biomed. Eng.* **4**, 1208 (2020).
- [22] J. Stehlé, N. Voirin, A. Barrat, C. Cattuto, L. Isella, J.-F. Pinton, M. Quaghiotto, W. Van den Broeck, C. Régis, B. Lina *et al.*, High-resolution measurements of face-to-face contact patterns in a primary school, *PLoS ONE* **6**, e23176 (2011).
- [23] A. Ganguli, A. Mostafa, J. Berger, M. Y. Aydin, F. Sun, S. A. S. de Ramirez, E. Valera, B. T. Cunningham, W. P. King, and R. Bashir, Rapid isothermal amplification and portable detection system for sars-cov-2, *Proc. Natl. Acad. Sci. USA* **117**, 22727 (2020).
- [24] P. Fozouni *et al.*, Amplification-free detection of SARS-CoV-2 with CRISPR-Cas13a and mobile phone microscopy, *Cell* **184**, 323 (2021).
- [25] C. Menni *et al.*, Real-time tracking of self-reported symptoms to predict potential COVID-19, *Nat. Med.* **26**, 1037 (2020).
- [26] T. Varsavsky, M. S. Graham, L. S. Canas, S. Ganesh, J. C. Pujol, C. H. Sudre, B. Murray, M. Modat, M. J. Cardoso, C. M. Astley *et al.*, Detecting covid-19 infection hotspots in england using large-scale self-reported data from a mobile application: A prospective, observational study, *Lancet Publ. Health* **6**, e21 (2021).
- [27] A. Ganguli, A. Ornob, H. Yu, G. Damhorst, W. Chen, F. Sun, A. Bhuiya, B. Cunningham, and R. Bashir, Hands-free smartphone-based diagnostics for simultaneous detection of zika, chikungunya, and dengue at point-of-care, *Biomed Microdev.* **19**, 73 (2017).
- [28] L. B. Sousa, S. R. Fricker, S. S. Doherty, C. E. Webb, K. L. Baldock, and C. R. Williams, Citizen science and smartphone e-entomology enables low-cost upscaling of mosquito surveillance, *Sci. Total Environ.* **704**, 135349 (2020).
- [29] N. G. Becker, K. Glass, Z. Li, and G. K. Aldis, Controlling emerging infectious diseases like sars, *Math. Biosci.* **193**, 205 (2005).
- [30] M. Eichner, Case isolation and contact tracing can prevent the spread of smallpox, *Am. J. Epidemiol.* **158**, 118 (2003).
- [31] K. T. Eames and M. J. Keeling, Contact tracing and disease control, *Proc. R. Soc. Lond. B* **270**, 2565 (2003).
- [32] I. Z. Kiss, D. M. Green, and R. R. Kao, Infectious disease control using contact tracing in random and scale-free networks, *J. R. Soc. Interface* **3**, 55 (2006).

- [33] R. M. HOWELL, W. J. Kessler, and A. Haddix, Partner notification to prevent pelvic inflammatory disease in women: Cost-effectiveness of two strategies, *Sex. Transm. Dis.* **24**, 287 (1997).
- [34] C. Fraser, S. Riley, R. M. Anderson, and N. M. Ferguson, Factors that make an infectious disease outbreak controllable, *Proc. Natl. Acad. Sci. USA* **101**, 6146 (2004).
- [35] M. Kretzschmar, Y. T. van Duynhoven, and A. J. Severijnen, Modeling prevention strategies for gonorrhea and chlamydia using stochastic network simulations, *Am. J. Epidemiol.* **144**, 306 (1996).
- [36] D. Klinkenberg, C. Fraser, and H. Heesterbeek, The effectiveness of contact tracing in emerging epidemics, *PLoS ONE* **1**, e12 (2006).
- [37] R. Huerta and L. S. Tsimring, Contact tracing and epidemics control in social networks, *Phys. Rev. E* **66**, 056115 (2002).
- [38] P. Rodríguez, S. Graña, E. E. Alvarez-León, M. Battaglini, F. J. Darias, M. A. Hernán, R. López, P. Llana, M. C. Martín, O. Ramirez-Rubio *et al.*, A population-based controlled experiment assessing the epidemiological impact of digital contact tracing, *Nat. Commun.* **12**, 587 (2021).
- [39] I. Braithwaite, T. Callender, M. Bullock, and R. W. Aldridge, Automated and partly automated contact tracing: A systematic review to inform the control of covid-19, *Lancet Digit. Health* (2020).
- [40] M. Salathé, C. L. Althaus, N. Anderegg, D. Antonioli, T. Ballouz, E. Bugnion, S. Capkun, D. Jackson, S.-I. Kim, J. Larus *et al.*, Early evidence of effectiveness of digital contact tracing for SARS-CoV-2 in Switzerland, *Swiss Med. Weekly* **150**, w20457 (2020).
- [41] J. O’Connell and D. T. O’Keeffe, Contact tracing for covid-19—A digital inoculation against future pandemics, *New Engl. J. Med.* (2021).
- [42] G. Cencetti, G. Santin, A. Longa, E. Pigani, A. Barrat, C. Cattuto, S. Lehmann, M. Salathe, and B. Lepri, Digital proximity tracing on empirical contact networks for pandemic control, *Nat. Commun.* **12**, 1655 (2021).
- [43] H. L. Hambridge, R. Kahn, and J.-P. Onnela, Examining sars-cov-2 interventions in residential colleges using an empirical network, medRxiv [10.1101/2021.03.09.21253198](https://doi.org/10.1101/2021.03.09.21253198) (2021).
- [44] A. Barrat, C. Cattuto, M. Kivela, S. Lehmann, and J. Saramaki, Effect of manual and digital contact tracing on covid-19 outbreaks: A study on empirical contact data, *J. R. Soc. Interface* **18**, rsif.2020.1000 (2021).
- [45] C. Wymant, L. Ferretti, D. Tsallis, M. Charalambides, L. Abeler-Dörner, D. Bonsall, R. Hinch, M. Kendall, L. Milsom, M. Ayres *et al.*, The epidemiological impact of the nhs covid-19 app, Alan Turing Institute: London, UK (2021).
- [46] R. Pastor-Satorras and A. Vespignani, *Evolution and Structure of the Internet: A Statistical Physics Approach* (Cambridge University Press, Cambridge, UK, 2007).
- [47] S. N. Dorogovtsev and J. F. Mendes, *Evolution of Networks: From Biological Nets to the Internet and WWW* (Oxford University Press, Oxford, 2013).
- [48] R. Albert and A.-L. Barabási, Statistical mechanics of complex networks, *Rev. Mod. Phys.* **74**, 47 (2002).
- [49] R. Pastor-Satorras and A. Vespignani, Epidemic Spreading in Scale-Free Networks, *Phys. Rev. Lett.* **86**, 3200 (2001).
- [50] M. Newman, *Networks* (Oxford University Press, Oxford, 2018).
- [51] L. Hébert-Dufresne, B. M. Althouse, S. V. Scarpino, and A. Allard, Beyond $r < 0$: Heterogeneity in secondary infections and probabilistic epidemic forecasting, *J. R. Soc. Interface* **17**, 20200393 (2020).
- [52] M. Boguná, R. Pastor-Satorras, and A. Vespignani, Absence of Epidemic Threshold in Scale-Free Networks with Degree Correlations, *Phys. Rev. Lett.* **90**, 028701 (2003).
- [53] M. Barthélemy, A. Barrat, R. Pastor-Satorras, and A. Vespignani, Velocity and Hierarchical Spread of Epidemic Outbreaks in Scale-Free Networks, *Phys. Rev. Lett.* **92**, 178701 (2004).
- [54] R. Pastor-Satorras and A. Vespignani, Epidemic dynamics in finite size scale-free networks, *Phys. Rev. E* **65**, 035108(R) (2002).
- [55] S. Dhara, R. van der Hofstad, and J. S. van Leeuwen, Critical percolation on scale-free random graphs: New universality class for the configuration model, *Commun. Math. Phys.* **382**, 123 (2021).
- [56] S. Cléménçon, H. De Arazoza, F. Rossi, and V. C. Tran, A statistical network analysis of the hiv/aids epidemics in cuba, *Soc. Netw. Anal. Min.* **5**, 1 (2015).
- [57] J. O. Lloyd-Smith, S. J. Schreiber, P. E. Kopp, and W. M. Getz, Superspreading and the effect of individual variation on disease emergence, *Nature (Lond.)* **438**, 355 (2005).
- [58] K. Kupferschmidt, Why do some covid-19 patients infect many others, whereas most don’t spread the virus at all, *Science* **10**, 1464 (2020).
- [59] S. L. Feld, Why your friends have more friends than you do, *Am. J. Sociol.* **96**, 1464 (1991).
- [60] M. E. J. Newman, Threshold Effects for Two Pathogens Spreading on a Network, *Phys. Rev. Lett.* **95**, 108701 (2005).
- [61] Y. Liu, R. M. Eggo, and A. J. Kucharski, Secondary attack rate and superspreading events for sars-cov-2, *The Lancet* **395**, e47 (2020).
- [62] Z. Shen, F. Ning, W. Zhou, X. He, C. Lin, D. P. Chin, Z. Zhu, and A. Schuchat, Superspreading sars events, beijing, 2003, *Emerg. Infect. Dis.* **10**, 256 (2004).
- [63] L. Ferretti, C. Wymant, M. Kendall, L. Zhao, A. Nurtay, L. Abeler-Dörner, M. Parker, D. Bonsall, and C. Fraser, Quantifying sars-cov-2 transmission suggests epidemic control with digital contact tracing, *Science* **368**, eabb6936 (2020).
- [64] P. Sapiezynski, J. Pruessing, and V. Sekara, The fallibility of contact-tracing apps, [arXiv:2005.11297](https://arxiv.org/abs/2005.11297) (2020).
- [65] M. McPherson, L. Smith-Lovin, and J. M. Cook, Birds of a feather: Homophily in social networks, *Annu. Rev. Sociol.* **27**, 415 (2001).
- [66] S. Funk, M. Salathé, and V. A. Jansen, Modelling the influence of human behaviour on the spread of infectious diseases: a review, *J. R. Soc. Interface* **7**, 1247 (2010).
- [67] D. Centola, An experimental study of homophily in the adoption of health behavior, *Science* **334**, 1269 (2011).
- [68] V. von Wyl, M. Höglinger, C. Sieber, M. Kaufmann, A. Moser, M. Serra-Burriel, T. Ballouz, D. Menges, A. Frei, and M. A. Puhán, Drivers of acceptance of covid-19 proximity tracing apps in switzerland: Panel survey analysis, *JMIR Publ. Health Surveill.* **7**, e25701 (2021).
- [69] J. A. M. López, B. A. García, P. Bentkowski, L. Bioglio, F. Pinotti, P.-Y. Boëlle, A. Barrat, V. Colizza, and C. Poletto, Anatomy of digital contact tracing: Role of age,

- transmission setting, adoption and case detection, *Sci. Adv.* **7**, eabd8750 (2021).
- [70] S. Munzert, P. Selb, A. Gohdes, L. F. Stoetzer, and W. Lowe, Tracking and promoting the usage of a covid-19 contact tracing app, *Nat. Hum. Behav.* **5**, 247 (2021).
- [71] G. Bianconi, H. Sun, G. Rapisardi, and A. Arenas, Message-passing approach to epidemic tracing and mitigation with apps, *Phys. Rev. Res.* **3**, L012014 (2021).
- [72] I. Kryven and C. Stegehuis, Contact tracing in configuration models, *J. Phys. Complex.* **2**, 025004 (2021).
- [73] A. Allard, C. Moore, S. V. Scarpino, B. M. Althouse, and L. Hébert-Dufresne, The role of directionality, heterogeneity and correlations in epidemic risk and spread, [arXiv:2005.11283](https://arxiv.org/abs/2005.11283) (2020).
- [74] R. B. Simões, I. Amaral, and S. Santos, Tracking the outbreak and far beyond: How are public authorities using mobile apps to control covid-19 pandemic, *Multidisc. Perspect. Commun. Pand. Context* **1**, 166 (2021).
- [75] M. Abueg, R. Hinch, N. Wu, L. Liu, W. J. Probert, A. Wu, P. Eastham, Y. Shafi, M. Rosencrantz, M. Dikovskiy *et al.*, Modeling the effect of exposure notification and non-pharmaceutical interventions on COVID-19 transmission in Washington state, *NPJ Digital Med.* **4**, 1 (2021).
- [76] A. Bassolas, A. Santoro, S. Sousa, S. Rognone, and V. Nicosia, Optimising the mitigation of epidemic spreading through targeted adoption of contact tracing apps, [arXiv:2102.13013](https://arxiv.org/abs/2102.13013) (2021).
- [77] M. Kendall, L. Milsom, L. Abeler-Dörner, C. Wymant, L. Ferretti, M. Briers, C. Holmes, D. Bonsall, J. Abeler, and C. Fraser, Epidemiological changes on the isle of wight after the launch of the nhs test and trace programme: A preliminary analysis, *The Lancet Digit. Health* **2**, e658 (2020).
- [78] G. Burgio, B. Steinegger, G. Rapisardi, and A. Arenas, Homophily in the adoption of digital proximity tracing apps shapes the evolution of epidemics, *Phys. Rev. Res.* **3**, 033128 (2021).
- [79] M. E. J. Newman, Spread of epidemic disease on networks, *Phys. Rev. E* **66**, 016128 (2002).
- [80] R. Pastor-Satorras, C. Castellano, P. Van Mieghem, and A. Vespignani, Epidemic processes in complex networks, *Rev. Mod. Phys.* **87**, 925 (2015).
- [81] R. Albert, H. Jeong, and A.-L. Barabási, Error and attack tolerance of complex networks, *Nature (Lond.)* **406**, 378 (2000).
- [82] R. Cohen, K. Erez, D. ben-Avraham, and S. Havlin, Resilience of the Internet to Random Breakdowns, *Phys. Rev. Lett.* **85**, 4626 (2000).
- [83] A. Barrat, M. Barthelemy, and A. Vespignani, *Dynamical Processes on Complex Networks* (Cambridge University Press, Cambridge, UK, 2008).
- [84] S. N. Dorogovtsev, A. V. Goltsev, and J. F. F. Mendes, Critical phenomena in complex networks, *Rev. Mod. Phys.* **80**, 1275 (2008).
- [85] E. Kenah and J. C. Miller, Epidemic percolation networks, epidemic outcomes, and interventions, *Interdisc. Perspect. Infect. Dis.* **2011**, 1 (2011).
- [86] L. Basnarkov, M. Mirchev, and L. Kocarev, Random walk with memory on complex networks, *Phys. Rev. E* **102**, 042315 (2020).
- [87] P. Shu, Effects of memory on information spreading in complex networks, in *Proceedings of the IEEE 17th International Conference on Computational Science and Engineering* (IEEE, Los Alamitos, CA, 2014), pp. 554–556.
- [88] J. C. Miller, Epidemic size and probability in populations with heterogeneous infectivity and susceptibility, *Phys. Rev. E* **76**, 010101(R) (2007).
- [89] E. Kenah and J. M. Robins, Second look at the spread of epidemics on networks, *Phys. Rev. E* **76**, 036113 (2007).
- [90] P. Grassberger, On the critical behavior of the general epidemic process and dynamical percolation, *Math. Biosci.* **63**, 157 (1983).
- [91] B. Bollobás and B. Béla, *Random Graphs*, 73 (Cambridge University Press, Cambridge, UK, 2001).
- [92] F. Chung and L. Lu, The average distances in random graphs with given expected degrees, *Proc. Natl. Acad. Sci. USA* **99**, 15879 (2002).
- [93] F. Chung and L. Lu, Connected components in random graphs with given expected degree sequences, *Ann. Combinator.* **6**, 125 (2002).
- [94] J. C. Miller and A. Hagberg, Efficient generation of networks with given expected degrees, in *Proceedings of the International Workshop on Algorithms and Models for the Web-Graph* (Springer, Berlin, 2011), pp. 115–126.
- [95] J. P. Gleeson, Cascades on correlated and modular random networks, *Phys. Rev. E* **77**, 046117 (2008).
- [96] S. Melnik, M. A. Porter, P. J. Mucha, and J. P. Gleeson, Dynamics on modular networks with heterogeneous correlations, *Chaos* **24**, 023106 (2014).
- [97] A. Vazquez, Multitype branching and graph product theory of infectious disease outbreaks, *Phys. Rev. E* **103**, L030301 (2021).

Publication V

A. Badie-Modiri, A. K. Rizi, M. Karsai and M. Kivelä. Directed percolation in random temporal network. *Physical Review Research*, 4(7) L022047, May 2022.

© 2022 Badie-Modiri et al.

Reprinted with permission.

Directed percolation in temporal networks

Arash Badie-Modiri ¹, Abbas K. Rizi ¹, Márton Karsai ^{2,3} and Mikko Kivelä ¹¹*Department of Computer Science, School of Science, Aalto University, FI-0007 Espoo, Finland*²*Department of Network and Data Science Central European University, 1100 Vienna, Austria*³*Alfréd Rényi Institute of Mathematics, 1053 Budapest, Hungary*

(Received 18 October 2021; accepted 6 April 2022; published 25 May 2022)

Connectivity and reachability on temporal networks, which can describe the spreading of a disease, the dissemination of information, or the accessibility of a public transport system over time, have been among the main contemporary areas of study in complex systems for the last decade. However, while isotropic percolation theory successfully describes connectivity in static networks, a similar description has not yet been developed for temporal networks. Here, we address this problem and formalize a mapping of the concept of temporal network reachability to percolation theory. We show that the limited-waiting-time reachability, a generic notion of constrained connectivity in temporal networks, displays a directed percolation phase transition in connectivity. Consequently, the critical percolation properties of spreading processes on temporal networks can be estimated by a set of known exponents characterizing the directed percolation universality class. This result is robust across a diverse set of temporal network models with different temporal and topological heterogeneities, while by using our methodology we uncover similar reachability phase transitions in real temporal networks too. These findings open up an avenue to apply theory, concepts, and methodology from the well-developed directed percolation literature to temporal networks.

DOI: [10.1103/PhysRevResearch.4.L022047](https://doi.org/10.1103/PhysRevResearch.4.L022047)

Many dynamical processes evolving on networks are related to the problem of reachability. Reachability describes the existence of a possible path of connections between two nodes, denoting the possibility and the extent that one node can affect, cause a change in, or communicate with the others based on interactions represented in the network. The conception and formalism of reachability, however, change dramatically if one considers the time-varying nature of connections between nodes [1] as opposed to the classic static network modeling of systems where connections are considered constant. Time induces an inherent direction of connectivity, as it restricts the direction of influence or information flow. This in turn has an impact on many dynamical processes evolving on such networks, such as spreading [2–4], social contagion [5,6], *ad hoc* message passing by mobile agents [7], or routing dynamics [8]. In these processes, interacting entities may have limited memory, thereby only building up paths constrained by limited waiting times, further restricting the eligible temporal structure for their global emergence.

Directed percolation (DP) is a paradigmatic example to characterize connectivity in temporal systems. This process exhibits dynamical phase transitions into absorbing states with a well-defined set of universal critical exponents [9–12]. Since

its introduction [13] and during its further development [14], directed percolation has attracted considerable attention in the literature. It has applications in reaction-diffusion systems [15], star formation in galaxies [16], conduction in strong electric fields in semiconductors [17], and biological evolution [18]. While it is straightforward to define idealized models governed by directed percolation, such as lattice models [19–25], its features are more difficult to realize in nature [12,26], allowing only a few recent experimental realizations of directed percolation [27–29]. Nevertheless, this description is advantageous in providing an understanding of the connectivity of temporal structures to describe ongoing dynamical processes [30–40].

There is a thorough theoretical understanding of static network connectivity with several concepts borrowed from percolation theory, such as phase transitions, giant components, and susceptibility. These concepts, originally developed for lattices and random networks, are routinely used to analyze real-world networks and processes, e.g., disease spreading [41–45]. Connectivity is also a central property of temporal networks, with several recent techniques to characterize it, e.g., using limited-waiting-time reachability [46–50].

A mapping between the temporal reachability phase transition and directed percolation has been anticipated before. This is a straightforward intuition as directed percolation accounts for the time-induced inherent directionality that characterizes temporal networks. For the special cases of contact susceptible \rightarrow infected \rightarrow susceptible (SIS) and susceptible \rightarrow infected \rightarrow recovered \rightarrow susceptible (SIRS) processes, this mapping has been shown over a regular lattice structure with the assumption that the contact between nodes follows a

Published by the American Physical Society under the terms of the Creative Commons Attribution 4.0 International license. Further distribution of this work must maintain attribution to the author(s) and the published article's title, journal citation, and DOI.

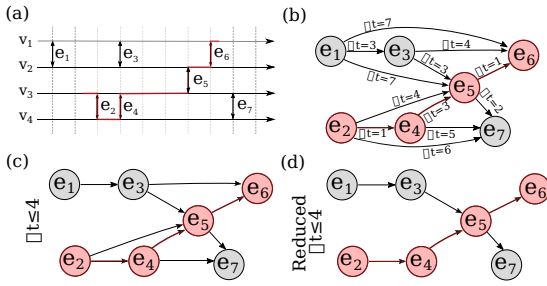


FIG. 1. Different representations of an instantaneous, undirected temporal network. (a) Vertices v_i are connected by dyadic instantaneous events e_j . (b) In a weighted temporal event graph, adjacent events are connected via links directed by time and weighted with the time difference Δt between them. Paths in an event graph are equivalent to time-respecting paths [56]. (c) Waiting-time constrained event graphs with links of weights $\Delta t \leq \delta t$ removed contain all δt -limited paths. (d) Reduced event graph in which locally redundant links are removed (see main text). The highlighted line represents a time respecting path (a) and its equivalent path over event graphs (b) and (c) and reduced event graph (d).

Poisson point process [9,12,51]. This mapping has been shown for a particular class of temporal dynamical systems, involving deterministic walks and discrete temporal layers [40]. For a more general class of temporal networks, Ref. [52] conjectured the mapping with directed percolation based on semantic similarities between the two systems and some empirical evidence. However, these studies could not provide conclusive evidence for this mapping for a broader set of temporal networks. In this Research Letter, we aim to show analytically that limited-waiting-time reachability on temporal networks, under a mean-field assumption of connectivity, has a phase transition in the directed percolation universality class. Combined with the experimental results of Ref. [53], we conclude that the same is true for a diverse subset of temporal networks, with a wider range of temporal and spatial connectivity compared with the mean-field assumption. Lastly, we illustrate how the directed percolation methodology, the formalism, and the introduced characteristic quantities can be used to analyze real-world temporal networks, for example, in detecting the onset of reachability phase transitions.

Modeling approach. A temporal network $G = (\mathcal{V}, \mathcal{E}, \mathcal{T})$ is defined as a set of nodes \mathcal{V} connected through events $e = (u, v, t_{\text{start}}, t_{\text{end}}) \in \mathcal{E}$, each of which represents an interaction of two nodes $u, v \in \mathcal{V}$ starting at time t_{start} and ending at time t_{end} observed during an observation period \mathcal{T} (i.e., $t_{\text{start}}, t_{\text{end}} \in \mathcal{T} \forall e \in \mathcal{E}$ and $t_{\text{start}} < t_{\text{end}}$). The connectivity of events is characterized by time-respecting paths [34,54], defined as sequences of adjacent events. Here, we call two distinct events $e, e' \in \mathcal{E}$ adjacent and denote this by $e \rightarrow e'$, if they follow each other in time ($t'_{\text{start}} > t_{\text{end}}$) and share at least one node in common ($\{v, u\} \cap \{v', u'\} \neq \emptyset$) as demonstrated in Fig. 1(a). For simplicity, we assume that temporal network events are instantaneous ($t_{\text{start}} = t_{\text{end}}$), but all of our notations can be easily extended to directed events and to temporal hypergraphs [47,55].

While time-respecting paths encode the possible routes of information, some dynamical processes have further restrictions on the duration they can propagate further after reaching a node. For example, in disease spreading, infected nodes may recover after some time, becoming unable to infect other nodes unless reinfected. In our definition, we define limited waiting times in temporal paths by allowing adjacent events $e = (u, v, t_{\text{start}}, t_{\text{end}})$ and $e' = (u', v', t'_{\text{start}}, t'_{\text{end}})$ to be connected (δt adjacent) only if there is less than δt time between them (i.e., $t'_{\text{start}} - t_{\text{end}} < \delta t$). In contrast to the control parameters based on node or event occupation probabilities, which could be used to adjust the overall activity level of the network, changing δt modifies the behavior of the spreading itself. Additionally, processes unconstrained by waiting time can be modeled as a special case of the limited-waiting-time process, with an infinitely large value of δt .

A compact way of describing the problem of reachability on temporal networks is provided by the weighted event graph representation $D = (\mathcal{E}, E_D, \Delta t(e, e'))$, a static directed acyclic representation of temporal networks [52]. In this description, events act as nodes, and two events e and e' are connected through a directed, weighted link if they are adjacent with weights defined as $\Delta t(e, e') = t'_{\text{start}} - t_{\text{end}}$, i.e., $E_D = \{(e, e') \in \mathcal{E} \times \mathcal{E} \mid e \rightarrow e'\}$. The event graph contains a superposition of all temporal paths [56] and retains the arrow of time even after turning the temporal structure into a static one [Fig. 1(b)]. Event graph representation of temporal networks has proven to be suitable for studying properties of temporal networks such as occurrences of motifs [57], decomposition of the temporal network into smaller components [58], and providing a lower-dimensional embedding of the temporal network that can be consumed by many machine-learning methods [59]. For our use case, a superposition of all δt -limited-time temporal paths ($D_{\delta t}$) of the temporal network can be achieved by constructing the event graph of the temporal network and removing all the event graph links with weights larger than δt ; in other words, $D_{\delta t}$ is a directed graph with the same set of vertices and the same weight function as D and set of edges $\{(e, e') \in E_D \mid \Delta t(e, e') \leq \delta t\}$ [see Fig. 1(c)].

Furthermore, we define the reduced temporal event graph \hat{D} and its waiting-time constrained variation $\hat{D}_{\delta t}$, where only the first adjacency relationships per temporal network node for each event are retained. \hat{D} and $\hat{D}_{\delta t}$ nodes have a maximum in- and out-degree of 2, yet they contain all the reachability relationships of the original event graph [60]. That is, the reduced event graph exactly retains the reachability of the original event graph by removing redundant connections (feed-forward loops) between events. The reduction allows interpretation of the three possible out-degrees using the terminology of directed percolation as annihilation (0), diffusion (1), and decoagulation (2) in the case that the out-neighbors are not already reachable through some longer loop. Note that this upper bound on in- and out-degrees is valid if the probability of simultaneous occurrence of adjacent events is negligible. See Supplemental Material (SM) for more details [61].

Order parameters and other characteristics. Compared with static structures, temporal networks incorporate time as an additional degree of freedom, which introduces an extra dimension to the characterization of their structural phase

transition of connectivity around a critical point. This is similar to directed percolation, where dimensions are related to space and time with associated independent critical exponents [62,63]. We measure the expected δt -limited-waiting-time reachability starting from a random event e . Of interest is the number of unique reachable nodes $\mathcal{V}_{e \rightarrow} \subseteq \mathcal{V}$, the time duration of the longest path (i.e., its lifetime [52]) $\mathcal{T}_{e \rightarrow} \subseteq \mathcal{T}$, and the total number of reachable events $\mathcal{M}_{e \rightarrow} \subseteq \mathcal{E}$. The expected values of these are analogous to the mean spatial volume $V = \langle |\mathcal{V}_{e \rightarrow}| \rangle$, mean survival time $T = \langle \max \mathcal{T}_{e \rightarrow} - \min \mathcal{T}_{e \rightarrow} \rangle$, and mean cluster mass $M = \langle |\mathcal{M}_{e \rightarrow}| \rangle$ in the directed percolation formalism (respectively) [9,12]. Furthermore, in parallel to directed percolation, we define the survival probability $P(t)$ as the probability that there is a path from a randomly selected initial source event at t_0 to an event after time $t_0 + t$. The ultimate survival probability $P_\infty = \lim_{t \rightarrow \infty} P(t)$ is then the survival probability at large values of t . Note that when defining these quantities, we opted for simplicity (see Supplemental Material [61] for discussion).

Using the maximum waiting time δt as a control parameter is a natural choice as it has a clear physical interpretation. However, unlike occupation probabilities that are typically used as control parameters in directed percolation, the scale of δt depends on the timescales of the system. Furthermore, although it is related to the local connectivity, this relationship is indirect and might depend on, e.g., the temporal inhomogeneities in interaction sequences. For this reason, we define another control parameter that directly measures the local connectivity of the system. We use the local effective connectivity $\hat{q}^{\text{out}}(\delta t)$, which is the average excess out-degree of the reduced event graph $\hat{D}_{\delta t}$. This is a monotonically increasing function of δt , which normalizes the changes in connectivity given by the changes in the maximum allowed waiting time δt . We then centralize this quantity by subtracting its value from its phase-transition critical point \hat{q}_c^{out} and denote the resulting control parameter as $\tau = \hat{q}^{\text{out}} - \hat{q}_c^{\text{out}}$.

In addition to the single-source scenario, where the component starts from a single node in $D_{\delta t}$, we investigated the fully occupied homogeneous initial condition, where we compute paths starting from all nodes in $D_{\delta t}$ with time $t < t_0$. Analogous to directed percolation, we define particle density $\rho(t)$ as the fraction of infected nodes in $D_{\delta t}$ at time t , while stationary density $\rho_{\text{stat}}(\tau)$, the order parameter, is defined as the particle density after the system reached a stationary state. We can incorporate the effects of an external field h into this scenario: In continuous time, this would be equivalent to the spontaneous emergence of sources of infection, i.e., occupation, of nodes in $D_{\delta t}$ (events in G) through an independent Poisson process with rate h . Susceptibility $\chi(\tau, h) = \frac{\partial}{\partial h} \rho_{\text{stat}}(\tau, h)$ can then be measured through observing the effect of changing the external field [12].

Critical behavior in random systems. Next, we derive a mean-field approximation for the above-defined measures and identify the critical point. We model temporal networks with an underlying static structure, where events are induced via links activating by independent and identical continuous-time stochastic processes. In order to do so, we need to first derive the degree distribution of the reduced event graph $\hat{D}_{\delta t}$, i.e., probabilities that one can reach zero, one, or two events from a randomly chosen event in the temporal network. Given the

excess degrees l and r of the two temporal network nodes in G incident to the link corresponding to the event $e \in \mathcal{E}$, we can compute the probability of a zero out-degree for a node in $\hat{D}_{\delta t}$ (i.e., an event in original temporal network G) as $\hat{\rho}_0^{\text{out}} = \Pi_{\delta t} \hat{\Pi}_{\delta t}^{l+r}$. Here, $\Pi_{\delta t}$ is the cumulative interevent time distribution induced by a link activation process for a given δt , and $\hat{\Pi}_{\delta t}$ is the corresponding cumulative residual interevent time distribution. Similarly, for out-degree 2, we can compute $\hat{\rho}_2^{\text{out}} = \int_0^\infty (1 - \hat{\Pi}_{\min \delta t, t}^l)(1 - \hat{\Pi}_{\min \delta t, t}^r) \pi_t dt$, where π_t is the interevent time distribution. Given that the maximum out-degree of events in the reduced event graph is 2, the $\hat{\rho}_1^{\text{out}}$ can be derived as $\hat{\rho}_1^{\text{out}} = 1 - \hat{\rho}_0^{\text{out}} - \hat{\rho}_2^{\text{out}}$. In-degree probabilities can be derived similarly.

The joint in- and out-degree distribution of the event graph can be computed from the excess degree distribution q_k of the underlying static network. If the degrees are independent, this becomes $\hat{\rho}_{i,o}^{\text{in,out}} = \sum_{l,r} \hat{\rho}_i^{\text{in}} \hat{\rho}_o^{\text{out}} q_l q_r$. We will denote the generating function of the joint degree distribution as $\mathcal{G}_0(z_{\text{in}}, z_{\text{out}})$ and the corresponding excess out-degree distribution as $\mathcal{G}_1^{\text{out}}(z_{\text{out}})$. We construct the mean-field rate equation for occupation density $\rho(t)$ in the homogeneous occupation initial condition using the excess out-degree distribution of the event graph $\hat{q}_k^{\text{out}} = \frac{d^k}{k! dz^k} \mathcal{G}_1^{\text{out}}(z)|_{z=0}$. The excess out-degree of nodes in the event graph \hat{D} gives the change in the number of further nodes we can reach from an already reached node: Nodes with out-degree 2 increase the number of reached nodes by 1, nodes with out-degree 1 do not affect the number of reached nodes, and nodes with out-degree 0 reduce by 1 the number of reached nodes. The total change therefore is $\hat{q}_2^{\text{out}} - \hat{q}_0^{\text{out}}$. In addition, some nodes we can reach are already reachable through other paths. In total we reach on expectation $\hat{q}_1^{\text{out}} + 2\hat{q}_2^{\text{out}}$ nodes where each node is already reached with probability $\rho(t)$. The rate equation becomes

$$\partial_t \rho(t) = [\hat{q}_2^{\text{out}} - \hat{q}_0^{\text{out}}] \rho(t) - [\hat{q}_1^{\text{out}} + 2\hat{q}_2^{\text{out}}] \rho^2(t). \quad (1)$$

In this equation the values of \hat{q}_k^{out} are constants in time. Noting the critical point for this equation as $\hat{q}_2^{\text{out}} - \hat{q}_0^{\text{out}} = 0$ and noting that the expected value is by definition $\hat{q}^{\text{out}} = \hat{q}_1^{\text{out}} + 2\hat{q}_2^{\text{out}}$ and that $\hat{q}_2^{\text{out}} - \hat{q}_0^{\text{out}} = \hat{q}^{\text{out}} - 1$, we can write Eq. (1) as $\partial_t \rho(t) = \tau \rho(t) - \hat{q}^{\text{out}} \rho^2(t)$.

Equation (1) follows the same form as the directed percolation mean-field equation for a $(d+1)$ -dimensional lattice [12] and can be solved explicitly (see Supplemental Material [61]). It has the critical point at $\tau = 0$, while it indicates that $\rho \rightarrow \tau / \hat{q}^{\text{out}}$ for $\tau > 0$. Asymptotically, it provides the critical exponents as $\rho(t) \sim t^{-\alpha}$ at $\tau = 0$ and $\rho_{\text{stat}}(\tau) \sim \tau^\beta$ when $\tau > 0$ and $t \rightarrow \infty$ with values $\alpha = \beta = 1$, where $\alpha = \beta / \nu_{\parallel}$ and ν_{\parallel} is the temporal correlation length exponent, in accordance with the corresponding mean-field directed percolation critical exponents [12].

The expected out-component size, i.e., mean cluster mass M , can be computed from the joint degree distribution of the event graph $\hat{D}_{\delta t}$ by assuming that it is a random directed graph with the same joint in- and out-degree distribution as $\hat{D}_{\delta t}$. The out-component size distribution probability-generating function H_0 can be derived from $H_0(z_{\text{out}}) = z_{\text{out}} \mathcal{G}_0(1, H_1(z_{\text{out}}))$, $H_1(z_{\text{out}}) = z_{\text{out}} \mathcal{G}_1^{\text{out}}(H_1(z_{\text{out}}))$, and the mean out-component size can be written as $M = \frac{\partial H_0(z_{\text{out}})}{\partial z_{\text{out}}}|_{z_{\text{out}}=1}$ [64]. These equations, when $\tau \rightarrow 0^-$, lead to $M \sim -\tau^{-\gamma}$ with $\gamma = 1$ (see

Supplemental Material [61]). Here, $\gamma = \nu_{\parallel} + d\nu_{\perp} - \beta - \beta'$, matching the mean-field exponent of mean cluster mass in directed percolation [12]. Here, ν_{\perp} indicates the spatial temporal correlation exponent.

The component survival probability $P(t)$ is measured by the out-component time span of nodes in the event graph, and the occupation density $\rho(t)$ is calculated by the in-component sizes of all possibly reachable nodes, implying that these two quantities are equal, $\rho(t) = P(t)$ (see Supplemental Material [61]). Consequently, given the control parameter τ , $\rho_{\text{stat}}(\tau) = P_{\infty}(\tau)$ as long as the time-reversed event graph has the same probability of being generated as the original one (e.g., if $\forall_{i,o} p_{i,o}^{\text{in,out}} = p_{o,i}^{\text{in,out}}$). This leads us to the rapidity-reversal symmetry for event graphs similarly characterizing directed percolation [65] where $\beta = \beta'$ and $P_{\infty}(\tau) \sim \tau^{\beta}$. Note that while the condition above holds for a variety of random temporal network models, for real-world systems intuition might suggest, e.g., a higher probability of $p_{1,2}^{\text{in,out}}$ as compared with $p_{2,1}^{\text{in,out}}$ due to over-representation of causal motifs [57]. In practice, however, we observed no deviations from the above condition in two large real-world systems (see Supplemental Material [61]).

Finite-size scaling in random systems. The critical exponents can be empirically verified through finite-size scaling of the system close to its percolation critical point, where its large-scale properties become invariant under scale transformations. We simulate random temporal networks of varying size and perform efficient reachability estimations [47] from single-source and homogeneous fully occupied initial conditions. We expect that curves of macroscopic quantities collapse when using the correct critical exponents of β , ν_{\parallel} , and ν_{\perp} corresponding to the mean-field values of directed percolation. The results confirm that the directed percolation mean-field exponents characterize the percolation phase transition of random temporal networks. This is demonstrated in Figs. 2(a)–2(f) for temporal networks induced on a 9-regular network with links activated via independent Poisson processes. These results are robust in the presence of several types of temporal and spatial heterogeneities [53].

Directed percolation measures in real-world temporal networks. We measure the same macroscopic quantities as before for four different real-world systems, concentrating on temporal networks describing air transportation, public transportation, Twitter mentions, and mobile phone calls [Figs. 3(a)–3(d)], respectively. In these networks, an event represents a flight between two airports in the United States, a public transport vehicle transiting between two consecutive stations on a typical Monday in Helsinki, a user mentioning another user in a tweet on Twitter, and a mobile phone subscriber calling another subscriber of a major European carrier, respectively. For details of the data sets, see Table S1 of the SM. In each system, there is clear evidence of an absorbing to active phase transition in terms of M , V , and ρ_{stat} . Note that the scales of these quantities are not directly comparable, highlighting the fact that distinguishing between the different notions of connectivity is important in practical terms. Furthermore, multiple peaks in susceptibility indicate multiple connectivity timescales.

The reachability phase transition can be better understood by investigating temporal connectivity profiles represented by

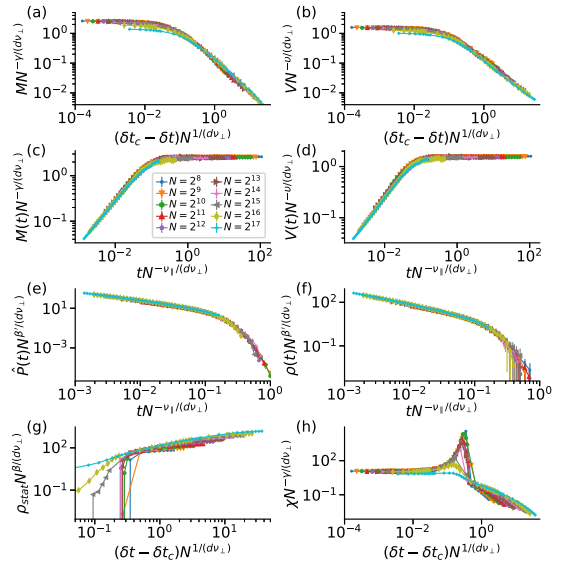


FIG. 2. Finite-size scaled (a) and (c) mean cluster mass M , (b) and (d) volume V , and (e) survival probability $\hat{P}(t)$ for single-source spreading scenarios. (f) Particle density $\rho(t)$, (g) static density ρ_{stat} , and (h) susceptibility $\chi(\delta t, 0)$ as a function of δt for the homogeneous initial condition. Measurements are averaged over at least 256 (up to 4096) realizations of temporal network constructed from random 9-regular networks ($N \in \{2^8, \dots, 2^{17}\}$) and Poisson point process activations $\lambda = 1$ of links. All functions of time are measured at $\delta t = \delta t_c = 0.08808$. d is set to directed percolation upper critical dimension $d_c = 4$.

cluster volumes of individual events. Structures similar to those of random networks (see Supplemental Material [61]) can be observed for air transport and Twitter [Figs. 3(e) and 3(g)]. However, in air transport, the structure is regular, following the diurnal pattern of flights. In Twitter, the components do not reach most nodes due to the greater separation of temporal components, and their structure reflects the rare emergence of possible macroscopic cascades. Public transport (1 day) and mobile networks display a single winglike structure [Figs. 3(f) and 3(h)]. This is induced by early components that can reach a significant fraction of nodes, which are then joined by other components reaching smaller subsets. This is also indicated by the horizontal structures under the wings.

Conclusion. The connectivity of a network is an important measure of its resilience and an underlying concept for any dynamical process running on it. It encodes the possible transportation routes or paths of information diffusion and determines how misinformation or diseases spread in real-world settings. The connectivity of static networks and related dynamical processes are routinely analyzed within the framework of (isotropic) percolation theory [30,31,41] with methods borrowed from critical phenomena [9,70]. Furthermore, many natural or synthetic networks, ranging from the brain [71,72] or artificial neural networks [73] to geological phenomena [74] and urban systems [75] tend to self-organize their medium or their parameters or be optimized by outside

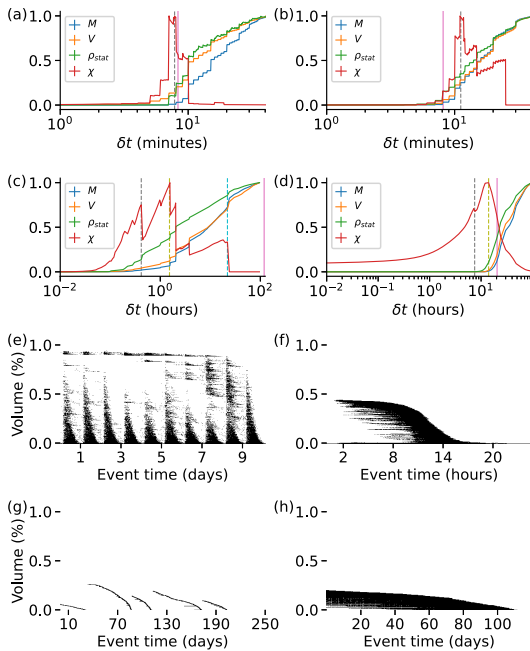


FIG. 3. Mean cluster mass M , mean cluster volume V , static density ρ_{stat} , and susceptibility $\chi(\delta t, 0)$ as a function of δt for four real-world networks: (a) Air transport [66], (b) Helsinki public transportation [67], (c) Twitter mentions [68], and (d) mobile phone calls [69] display an absorbing to active phase transition around 470 s, 670 s, 25 min, and 7.5 h, respectively, as indicated by change from very small values for M , V , and ρ_{stat} to values comparable to the size of the system and a peak in susceptibility $\chi(\delta t, 0)$. Mobile and Twitter networks show a second peak in susceptibility around 1.5 and 22 h, respectively, and Twitter data show a third peak around 14 h. The trajectories are rescaled to the range $[0, 1]$. δt_c is estimated using the analytical solution from Ref. [53] by approximating the network to a temporal network with a random regular static base and Poisson point process activation. This estimates the threshold at 500 s, 488 s, 119.1 h, and 22.5 h, respectively, displayed using solid vertical lines in (a)–(d). The temporal reachability profiles display relative cluster volumes for each event as a function of the event time for $\delta t \approx \delta t_c$ for (e) air transport, (f) Helsinki public transportation, (g) Twitter mentions, and (h) mobile phone call networks.

intervention towards criticality [76,77]. Therefore it is of great utility to locate the onset of critical phase-transition points and predict the behavior of the system in that vicinity.

While connectivity transitions and the critical behavior of the system are understood in static networks by means of isotropic percolation theory, temporal networks, by and

large, have been out of reach of a similar methodology. This has practical implications as connectivity is a limiting factor of any dynamical processes and at the same time temporal interactions have been shown to have dramatic effects on the speed and volume of any ongoing dynamical process [2–4]. For example, disease spreading in static networks can be mapped to a percolation process leading to a theoretical understanding of the epidemic threshold as a consequence of connectivity phase transition [41]. This connection has been extensively exploited to use the mathematical machinery of network percolation to derive various theoretical and practical results on static networks [31,78]. In temporal networks, such analysis is typically based on theoretical results on sequences of static networks [79] or case studies based purely on simulations [69,80]. The concise theory of temporal network connectivity provided here shows that the reachability phase transition in temporal networks belongs to the directed percolation universality class, which is a necessary step forward from the limited description provided by the theory of static networks. It also indicates that directed percolation may have many counterparts in reality with the expected scaling relations.

The mapping presented in this Research Letter allows for predicting the critical thresholds and the connectivity behaviors of a diverse set of systems that can be modeled as temporal networks. Now, similar to static network connectivity, not only do we have theoretically grounded summary statistics of the component size distribution (the order parameters and cluster mass, volume, and lifetime), but also we know ways to find their transitions even in finite-size systems. Moreover, we now possess a theory to predict the behavior of such random systems and find transition points accurately. Real networks are often approximated with random graphs, and the random models are used as reference points: Deviations from the minimal random models expose important structural features of the real systems, and conversely, agreement with these models tells us that the structures, correlations, and inhomogeneities present in the data do not have a measurable effect on the connectivity. Although introduction of heterogeneities might shift the critical threshold of connectivity in temporal networks, the directed percolation phase transition is surprisingly robust to several types of temporal and topological heterogeneities [53]. Consequently, further research is required to find the boundaries and extremities of application of this framework on theoretical and real-world networks.

Acknowledgments. We would like to thank János Kertész and Géza Ódor for their helpful comments and suggestions. The authors wish to acknowledge CSC – IT Center for Science, Finland, and the Aalto University “Science-IT” project for generous computational resources. M. Karsai acknowledges support from the DataRedux ANR project (ANR-19-CE46-0008) and the SoBigData++ H2020 project (H2020-871042).

- [1] P. Holme and J. Saramäki, *Temporal Network Theory*, Computational Social Sciences (Springer, New York, 2019).
- [2] R. Lambiotte and N. Masuda, *A Guide to Temporal Networks* (World Scientific, Singapore, 2016), Vol. 4.

- [3] P. Holme and J. Saramäki, Temporal networks, *Phys. Rep.* **519**, 97 (2012).
- [4] P. Holme, Modern temporal network theory: A colloquium, *Eur. Phys. J. B* **88**, 234 (2015).

- [5] D. J. Daley and D. G. Kendall, Epidemics and rumours, *Nature (London)* **204**, 1118 (1964).
- [6] C. Castellano, S. Fortunato, and V. Loreto, Statistical physics of social dynamics, *Rev. Mod. Phys.* **81**, 591 (2009).
- [7] C. Tripp-Barba, C. Alcaraz, and M. A. Igartua, Special issue on “Modeling and performance evaluation of wireless ad-hoc networks”, *Ad Hoc Networks* **52**, 1 (2016).
- [8] N. Nassir, M. Hickman, A. Malekzadeh, and E. Irannezhad, A utility-based travel impedance measure for public transit network accessibility, *Transp. Res. Part A: Policy Pract.* **88**, 26 (2016).
- [9] H. Hinrichsen, Non-equilibrium critical phenomena and phase transitions into absorbing states, *Adv. Phys.* **49**, 815 (2000).
- [10] G. Ódor, Universality classes in nonequilibrium lattice systems, *Rev. Mod. Phys.* **76**, 663 (2004).
- [11] H. Hinrichsen, Non-equilibrium phase transitions, *Physica A (Amsterdam)* **369**, 1 (2006).
- [12] M. Henkel, H. Hinrichsen, S. Lübeck, and M. Pleimling, *Non-equilibrium Phase Transitions* (Springer, New York, 2008), Vol. 1.
- [13] S. R. Broadbent and J. M. Hammersley, Percolation processes: I. Crystals and mazes, *Math. Proc. Cambridge Philos. Soc.* **53**, 629 (1957).
- [14] J. Blease, Directed-bond percolation on hypercubic lattices, *J. Phys. C: Solid State Phys.* **10**, 925 (1977).
- [15] F. Schlögl, Chemical reaction models for non-equilibrium phase transitions, *Z. Phys.* **253**, 147 (1972).
- [16] H. Gerola, P. Seiden, and L. Schulman, Theory of dwarf galaxies, *Astrophys. J.* **242**, 517 (1980).
- [17] N. Van Lien and B. Shklovskii, Hopping conduction in strong electric fields and directed percolation, *Solid State Commun.* **38**, 99 (1981).
- [18] P. Bak and K. Sneppen, Punctuated Equilibrium and Criticality in a Simple Model of Evolution, *Phys. Rev. Lett.* **71**, 4083 (1993).
- [19] E. Domany and W. Kinzel, Equivalence of Cellular Automata to Ising Models and Directed Percolation, *Phys. Rev. Lett.* **53**, 311 (1984).
- [20] W. Kinzel, Phase transitions of cellular automata, *Z. Phys. B: Condens. Matter* **58**, 229 (1985).
- [21] T. E. Harris, Contact interactions on a lattice, *Ann. Probab.* **2**, 969 (1974).
- [22] I. Jensen, Critical Behavior of the Pair Contact Process, *Phys. Rev. Lett.* **70**, 1465 (1993).
- [23] J. Mendes, R. Dickman, M. Henkel, and M. C. Marques, Generalized scaling for models with multiple absorbing states, *J. Phys. A: Math. Gen.* **27**, 3019 (1994).
- [24] R. M. Ziff, E. Gulari, and Y. Barshad, Kinetic Phase Transitions in an Irreversible Surface-Reaction Model, *Phys. Rev. Lett.* **56**, 2553 (1986).
- [25] D. Dhar, The collapse of directed animals, *J. Phys. A: Math. Gen.* **20**, L847 (1987).
- [26] H. Hinrichsen, On possible experimental realizations of directed percolation, *Braz. J. Phys.* **30**, 69 (2000).
- [27] K. A. Takeuchi, M. Kuroda, H. Chaté, and M. Sano, Directed Percolation Criticality in Turbulent Liquid Crystals, *Phys. Rev. Lett.* **99**, 234503 (2007).
- [28] G. Lemoult, L. Shi, K. Avila, S. V. Jalikop, M. Avila, and B. Hof, Directed percolation phase transition to sustained turbulence in Couette flow, *Nat. Phys.* **12**, 254 (2016).
- [29] M. Sano and K. Tamai, A universal transition to turbulence in channel flow, *Nat. Phys.* **12**, 249 (2016).
- [30] A. Barrat, M. Barthelemy, and A. Vespignani, *Dynamical Processes on Complex Networks* (Cambridge University Press, Cambridge, 2008).
- [31] R. Pastor-Satorras, C. Castellano, P. Van Mieghem, and A. Vespignani, Epidemic processes in complex networks, *Rev. Mod. Phys.* **87**, 925 (2015).
- [32] D. Kempe, J. Kleinberg, and A. Kumar, Connectivity and inference problems for temporal networks, *J. Comput. Syst. Sci.* **64**, 820 (2002).
- [33] J. Moody, The importance of relationship timing for diffusion, *Social Forces* **81**, 25 (2002).
- [34] P. Holme, Network reachability of real-world contact sequences, *Phys. Rev. E* **71**, 046119 (2005).
- [35] R. K. Pan and J. Saramäki, Path lengths, correlations, and centrality in temporal networks, *Phys. Rev. E* **84**, 016105 (2011).
- [36] I. Scholtes, N. Wider, R. Pfützer, A. Garas, C. J. Tessone, and F. Schweitzer, Causality-driven slow-down and speed-up of diffusion in non-Markovian temporal networks, *Nat. Commun.* **5**, 5024 (2014).
- [37] J. Stehlé, N. Voirin, A. Barrat, C. Cattuto, L. Isella, J.-F. Pinton, M. Quaggiotto, W. Van den Broeck, C. Régis, B. Lina, and P. Vanhems, High-resolution measurements of face-to-face contact patterns in a primary school, *PLoS One* **6**, e23176 (2011).
- [38] S. Dai, H. Bouchet, A. Nardy, E. Fleury, J.-P. Chevrot, and M. Karsai, Temporal social network reconstruction using wireless proximity sensors: model selection and consequences, *EPJ Data Sci.* **9**, 19 (2020).
- [39] A. Aleta, G. F. de Arruda, and Y. Moreno, Data-driven contact structures: from homogeneous mixing to multilayer networks, *PLoS Comput. Biol.* **16**, e1008035 (2020).
- [40] R. Parshani, M. Dickison, R. Cohen, H. E. Stanley, and S. Havlin, Dynamic networks and directed percolation, *Europhys. Lett.* **90**, 38004 (2010).
- [41] M. E. J. Newman, Spread of epidemic disease on networks, *Phys. Rev. E* **66**, 016128 (2002).
- [42] E. Kenah and J. M. Robins, Second look at the spread of epidemics on networks, *Phys. Rev. E* **76**, 036113 (2007).
- [43] E. Kenah and J. C. Miller, Epidemic percolation networks, epidemic outcomes, and interventions, *Interdiscip. Perspect. Infect. Dis.* **2011**, 543520 (2011).
- [44] A. K. Rizi, A. Faqeeh, A. Badie-Modiri, and M. Kivelä, Epidemic spreading and digital contact tracing: Effects of heterogeneous mixing and quarantine failures, *Phys. Rev. E* **105**, 044313 (2022).
- [45] T. Hiraoka, A. K. Rizi, M. Kivelä, and J. Saramäki, Herd immunity and epidemic size in networks with vaccination homophily, [arXiv:2112.07538](https://arxiv.org/abs/2112.07538).
- [46] P. Crescenzi, C. Magnien, and A. Marino, Approximating the temporal neighbourhood function of large temporal graphs, *Algorithms* **12**, 211 (2019).
- [47] A. Badie-Modiri, M. Karsai, and M. Kivelä, Efficient limited-time reachability estimation in temporal networks, *Phys. Rev. E* **101**, 052303 (2020).
- [48] A. Casteigts, A.-S. Himmel, H. Molter, and P. Zschoche, Finding Temporal Paths Under Waiting Time Constraints, *Algorithmica* **83**, 2754 (2021).
- [49] S. Thejaswi, J. Lauri, and A. Gionis, Restless reachability problems in temporal graphs, [arXiv:2010.08423](https://arxiv.org/abs/2010.08423).

- [50] A.-S. Himmel, M. Bentert, A. Nichterlein, and R. Niedermeier, Efficient computation of optimal temporal walks under waiting-time constraints, in *International Conference on Complex Networks and Their Applications* (Springer, New York, 2019), pp. 494–506.
- [51] D. R. De Souza and T. Tomé, Stochastic lattice gas model describing the dynamics of the SIRS epidemic process, *Physica A (Amsterdam)* **389**, 1142 (2010).
- [52] M. Kivelä, J. Cambe, J. Saramäki, and M. Karsai, Mapping temporal-network percolation to weighted, static event graphs, *Sci. Rep.* **8**, 12357 (2018).
- [53] A. Badie-Modiri, A. K. Rizi, M. Karsai, and M. Kivelä, Directed percolation in random temporal network models with heterogeneities, *Phys. Rev. E* **105**, 054313 (2022).
- [54] H. H. K. Lentz, T. Selhorst, and I. M. Sokolov, Unfolding Accessibility Provides a Macroscopic Approach to Temporal Networks, *Phys. Rev. Lett.* **110**, 118701 (2013).
- [55] A. Mellor, Event graphs: Advances and applications of second-order time-unfolded temporal network models, *Adv. Complex Syst.* **22**, 1950006 (2019).
- [56] J. Saramäki, M. Kivelä, and M. Karsai, Weighted temporal event graphs, in *Temporal Network Theory* (Springer, New York, 2019), pp. 107–128.
- [57] L. Kovanen, M. Karsai, K. Kaski, J. Kertész, and J. Saramäki, Temporal motifs in time-dependent networks, *J. Stat. Mech.* (2011) P11005.
- [58] A. Mellor, Analysing collective behaviour in temporal networks using event graphs and temporal motifs, [arXiv:1801.10527](https://arxiv.org/abs/1801.10527).
- [59] M. Torricelli, M. Karsai, and L. Gauvin, weg2vec: Event embedding for temporal networks, *Sci. Rep.* **10**, 7164 (2020).
- [60] A. Mellor, The temporal event graph, *J. Complex Networks* **6**, 639 (2018).
- [61] See Supplemental Material at <http://link.aps.org/supplemental/10.1103/PhysRevResearch.4.L022047> for details on proofs and description of datasets.
- [62] P. Grassberger, On phase transitions in Schlögl's second model, *Z. Phys. B* **47**, 365 (1982).
- [63] H. K. Janssen, On the nonequilibrium phase transition in reaction-diffusion systems with an absorbing stationary state, *Z. Phys. B* **42**, 151 (1981).
- [64] M. E. J. Newman, S. H. Strogatz, and D. J. Watts, Random graphs with arbitrary degree distributions and their applications, *Phys. Rev. E* **64**, 026118 (2001).
- [65] P. Grassberger and A. De La Torre, Reggeon field theory (Schlögl's first model) on a lattice: Monte Carlo calculations of critical behaviour, *Ann. Phys. (Amsterdam)* **122**, 373 (1979).
- [66] Bureau of Transportation Statistics, Bureau of Transportation Statistics website (2017), <https://www.bts.gov/>.
- [67] R. Kujala, C. Weckström, R. K. Darst, M. N. Mladenović, and J. Saramäki, A collection of public transport network data sets for 25 cities, *Sci. Data* **5**, 180089 (2018).
- [68] J. Yang and J. Leskovec, Patterns of temporal variation in online media, in *Proceedings of the Fourth ACM International Conference on Web Search and Data Mining* (ACM, New York, 2011), pp. 177–186.
- [69] M. Karsai, M. Kivelä, R. K. Pan, K. Kaski, J. Kertész, A.-L. Barabási, and J. Saramäki, Small but slow world: How network topology and burstiness slow down spreading, *Phys. Rev. E* **83**, 025102(R) (2011).
- [70] S. N. Dorogovtsev, A. V. Goltsev, and J. F. F. Mendes, Critical phenomena in complex networks, *Rev. Mod. Phys.* **80**, 1275 (2008).
- [71] D. R. Chialvo, Emergent complex neural dynamics, *Nat. Phys.* **6**, 744 (2010).
- [72] J. Hesse and T. Gross, Self-organized criticality as a fundamental property of neural systems, *Front. Syst. Neurosci.* **8**, 166 (2014).
- [73] C.-W. Shin and S. Kim, Self-organized criticality and scale-free properties in emergent functional neural networks, *Phys. Rev. E* **74**, 045101(R) (2006).
- [74] P. Bak and C. Tang, Earthquakes as a self-organized critical phenomenon, *J. Geophys. Res.: Solid Earth* **94**, 15635 (1989).
- [75] Y. Chen and Y. Zhou, Scaling laws and indications of self-organized criticality in urban systems, *Chaos, Solitons Fractals* **35**, 85 (2008).
- [76] P. Bak, C. Tang, and K. Wiesenfeld, Self-Organized Criticality: An Explanation of the $1/f$ Noise, *Phys. Rev. Lett.* **59**, 381 (1987).
- [77] P. Bak, C. Tang, and K. Wiesenfeld, Self-organized criticality, *Phys. Rev. A* **38**, 364 (1988).
- [78] B. Blasius, Power-law distribution in the number of confirmed COVID-19 cases, *Chaos* **30**, 093123 (2020).
- [79] J. Leitch, K. A. Alexander, and S. Sengupta, Toward epidemic thresholds on temporal networks: a review and open questions, *Appl. Network Sci.* **4**, 105 (2019).
- [80] A. Barrat, C. Cattuto, M. Kivelä, S. Lehmann, and J. Saramäki, Effect of manual and digital contact tracing on COVID-19 outbreaks: a study on empirical contact data, *J. R. Soc. Interface* **18**, 20201000 (2021).

Publication VI

A. Badie-Modiri, A. K. Rizi, M. Karsai and M. Kivelä. Directed percolation in random temporal network models with heterogeneities. *Physical Review E*, 105(17) 054313, May 2022.

© 2022 Badie-Modiri et al.

Reprinted with permission.

Directed percolation in random temporal network models with heterogeneitiesArash Badie-Modiri ¹, Abbas K. Rizi ¹, Márton Karsai ^{2,3} and Mikko Kivelä ¹¹*Department of Computer Science, School of Science, Aalto University, FI-0007, Finland*²*Department of Network and Data Science Central European University, 1100 Vienna, Austria*³*Alfréd Rényi Institute of Mathematics, 1053 Budapest, Hungary*

(Received 18 October 2021; accepted 7 April 2022; published 25 May 2022)

The event graph representation of temporal networks suggests that the connectivity of temporal structures can be mapped to a directed percolation problem. However, similarly to percolation theory on static networks, this mapping is valid under the approximation that the structure and interaction dynamics of the temporal network are determined by its local properties, and, otherwise, it is maximally random. We challenge these conditions and demonstrate the robustness of this mapping in case of more complicated systems. We systematically analyze random and regular network topologies and heterogeneous link-activation processes driven by bursty renewal or self-exciting processes using numerical simulation and finite-size scaling methods. We find that the critical percolation exponents characterizing the temporal network are not sensitive to many structural and dynamical network heterogeneities, while they recover known scaling exponents characterizing directed percolation on low-dimensional lattices. While it is not possible to demonstrate the validity of this mapping for all temporal network models, our results establish the first batch of evidence supporting the robustness of the scaling relationships in the limited-time reachability of temporal networks.

DOI: [10.1103/PhysRevE.105.054313](https://doi.org/10.1103/PhysRevE.105.054313)**I. INTRODUCTION**

Connectivity is an essential characteristic of complex networks as it determines how far information or influence can spread in a network structure. Consequently, it governs the emergence and scale of any macroscopic phenomena often modelled on networks such as disease spreading, transportation, or information diffusion, to mention a few examples. Percolation theory provides a comprehensive understanding that characterizes network connectivity with various mathematical and algorithmic tools primarily developed for complex networks. For example, percolation can be mapped to late-stage results of specific epidemic processes [1–5], such that the size of percolating components determine the final size of the epidemic. Meanwhile, the percolation transition and its related critical behavior explain the disease outcome close to the epidemic threshold.

However, these theoretical descriptions commonly assume that the network is static, with links and nodes always present, ignoring the typical character of several complex structures where links may vary in time. Since information, disease, or other effects can pass between two nodes in a network only at the time of their interactions, the temporal alternation of links may crucially influence the critical behavior and final outcome of any ongoing spreading processes [6–12]. To

characterize these processes, one needs to measure connectivity in temporal networks across time, where components are defined in terms of network nodes and links and the temporal distribution of interactions. Consequently, beyond the well-studied structural heterogeneities of static networks, like in their node degrees, the effects of temporal correlations leading to temporal heterogeneities in the interaction dynamics, like burstiness, become important [13–18]. This is especially the case for so-called limited-waiting-time processes, where an effect or information, e.g., a disease or a meme [19], arriving at a node can pass over to another node only if an interaction appears within a time window δt . Otherwise, the pathogen times out, e.g., the patient recovers or the meme becomes irrelevant, making it impossible to reach other nodes.

Similarly to static networks, the connectivity of temporal networks passes through a phase transition. However, close to this critical threshold, temporal networks exhibit different critical behavior as compared to static structures [20–22]. For limited-waiting-time connectivity, where the control parameter is δt , this phase transition can be theoretically understood under some simplifying assumptions about the homogeneous dynamics of connectivity [22]. Since there is an embedded direction (or flow) of time, the microscopic dynamics can be fundamentally irreversible with a broken detailed balance and nonequilibrium steady state. These results suggest that the dynamics of percolation on temporal networks are generically the same as any other system belonging to the directed percolation (DP) universality class, which is characterized by a one-component order parameter without additional symmetries and unconventional features such as quenched disorder [23].

The homogeneity approximations used for the derivations presented in Ref. [22], however, become less grounded when

Published by the American Physical Society under the terms of the Creative Commons Attribution 4.0 International license. Further distribution of this work must maintain attribution to the author(s) and the published article's title, journal citation, and DOI.

the underlying structure deviates from a random graph or if the interaction dynamics become inhomogeneous. In this paper, our goal is to build on the theory laid down in Ref. [22] to investigate further the relation between temporal networks and directed percolation. In other words, the primary objective of this manuscript is as follows: to show empirically that diverse classes of temporal networks, with various degrees of temporal and spatial heterogeneity, combined with the very general notion of limited-waiting-time reachability, will show an absorbing phase transition in connectivity that belongs to the directed percolation universality class.

In its epidemic interpretation, directed percolation can be one of the most basic nonequilibrium second-order phase transitions from fluctuating states into so-called absorbing states, which exhibit universal features, determined by symmetry properties and conservation laws. We demonstrate the precision of this mapping using extensive numerical simulations and provide further theoretical calculations to study synthetic temporal networks as directed percolation processes with a range of temporal and spatial inhomogeneities.

The remainder of Sec. I will be dedicated to laying the groundwork and presenting the context in which this manuscript is set: In Sec. IA we will discuss connectivity on temporal networks, the event graph representation, and modeling spreading processes and Sec. IB will introduce directed percolation and its characteristics.

Section II is dedicated to an overview of our contributions. Section IIA will describe our mapping of concepts of directed percolation and temporal networks. Section A provides an overview of the theoretical results from Ref. [22], which will be extended further in Sec. A1 by explicitly deriving some critical exponents and scaling relations. Section IIB will lay down the algorithmic techniques that make large-scale simulations of spreading processes on temporal networks possible.

Finally, in Sec. III we will describe the experimental setup and provide numerical evidence for validity of our hypothesis by application of the methods described previously, while Sec. IV provides an overview of the implications of the results and the limitations of our study.

A. Temporal networks and the event graph

A temporal network $G = (\mathcal{V}, \mathcal{E})$ provides representations of a dynamically changing complex system as a set of timed interactions known as events \mathcal{E} between a set of entities $\mathcal{V} = \{v_1, v_2, \dots, v_n\}$ known as nodes or vertices during an observation period \mathcal{T} . Each event indicates a time-dependent interaction between two nodes, e.g., physical contact or communication between two people or trade between two commercial entities [24], i.e., $e = (u, v, t_{\text{start}}, t_{\text{end}})$ such that $u, v \in \mathcal{V}$ between times of $t_{\text{start}}, t_{\text{end}} \in \mathcal{T}$ ($t_{\text{start}} < t_{\text{end}}$). Note that this definition can be easily extended to directed events and to directed or undirected temporal hypergraphs.

Two events $e, e' \in \mathcal{E}$ are *adjacent* if they share at least one endpoint node in common, $\{u, v\} \cap \{u', v'\} \neq \emptyset$, and they follow each other in time such that $\Delta t(e, e') = t'_{\text{start}} - t_{\text{end}} > 0$. Therefore, any temporal network can be represented as a higher-order static directed acyclic weighted graph known as the *event graph* $D = (\mathcal{E}, E_D, \Delta t(e, e'))$ [20,25]. Nodes of the event graph are the events of the original temporal network

and the weight of a link between two connected nodes (adjacent events) is then defined as the time difference Δt between the corresponding events.

Every path on the event graph constitutes a *causal chain* as, by definition, a path constitutes a list of events where every two consecutive events are adjacent. Paths in event graphs are, therefore, equivalent to time-respecting paths in the corresponding temporal network representation [26]. Therefore, calculating time-respecting reachability on a temporal network is equivalent to connectivity on its corresponding (static) event graph representation. The weakly connected components on an event graph determine *causal domains*, disjoint sets of events where there can be no causal connections whatsoever between events if they belong to two different weakly connected components. In addition, as compared to reachability, the size and distribution of weakly connected components are quantities, which are much easier to measure for temporal networks and they characterize a percolation transition if we assume an undirected network. Moreover, the sizes of these components put an upper bound on how much an effect can spread starting from one of the events in that component [20].

Temporal networks preserve the dynamic properties of the represented complex system, unlike aggregated static networks where this information is lost. Through the studies of time-varying networks, several new phenomena in human dynamics have been explored over the past decades, such as node and link burstiness [18,27,28], causal, temporal motifs [29], or the cyclic activation patterns of human interaction activities [30], to mention a few. As opposed to systems governed by homogeneous and independent processes, these correlations and the induced temporal dynamics may have significant effects on various dynamical processes evolving on temporal networks such as spreading [31,32], reachability [33,34], diffusion [9,35], and opinion formation [36].

The different dynamics of a temporal network are often straightforward to study through simulations. For example, in the case of spreading processes, transmission can be modeled by temporal network events [13–17]. More concretely, in a physical interaction network, where nodes represent people and events represent two people coming to close proximity, each of these contact events will have a probability of transmitting the disease. The disease then spreads to all the nodes that can be reached via such infecting events from the initially infected nodes. Similarly, in a network where events represent communication of information at a specific time, such as mobile phone calls or email exchanges, it is straightforward to model the spreading of information by keeping track of the information nodes have access to at each point in time.

Many dynamics evolving on top of networks, such as some spreading processes [37–39], social contagion [40–42] ad hoc message passing by mobile agents [43] or routing processes [44], can have a limited memory thus can only use paths constrained by limited waiting times. Limited waiting-time reachability can be modeled using the event graph, D , that contains a superposition of all temporal paths [20,26,45]. In a limited waiting-time spreading process unfolding over a temporal network, either the spreading agent (e.g., the pathogen in the disease spreading) must be transmitted onward from a node within some time δt or the infection has to be renewed before that time. In other words, the node must

participate in a possibly disease-carrying event in δt time or the process stops and the node reverts to susceptible. Therefore, all the spreading paths in the network are δt -constrained time-respecting paths. Let us call two adjacent events e and e' as δt -adjacent if $\Delta t(e, e') \leq \delta t$. A subset of the event graph D with an upper threshold of weights no greater than δt , i.e., where directed links indicate δt adjacency, enables us to calculate reachability for δt limited-time spreading process for the corresponding temporal network. Therefore, the event graph encapsulates a complete set of δt -constrained time-respecting paths for all values of δt simultaneously.

B. Directed percolation

The waiting-time limit δt can be regarded as the control parameter of a continuous phase transition, where connectivity in the event graph is determined by δt -connected paths of events. As the value of maximum waiting time decreases, more and more of the links of the event graph get removed, where each deleted link corresponding to an adjacency relationship between two events that are temporally more than δt apart. This leads to a drop in connectivity in the event graph, which is exactly equivalent to the drop in connectivity on the temporal network. In order to characterize these phase transitions, unlike characterizing the superficially similar phase transitions that take place when removing links in static (undirected) networks, we need to consider a percolation framework that can explicitly model the one-way flow of time.

Directed percolation is a paradigmatic example of dynamical phase transitions into absorbing states with a well-defined set of universal critical exponents and is often used to model phenomena with inherent directionality, such as fluids passing through porous media [23,46–48]. Originally introduced as a model for directed random connectivity [49], directed percolation attracted scrutiny in percolation theory in the late seventies [50]. Since then, a considerable body of work has been devoted to this approach of interpretation in the literature since the critical behavior of many stochastic many-particle nonequilibrium processes can be shown to belong to the directed percolation universality class. Directed percolation has applications in various domains at multiple scales ranging from galaxies to semiconductors [51–54].

As the simplest model exhibiting a transition between active and absorbing phases [46], it is straightforward to define and implement models governed by directed percolation, e.g., in the case of lattice models [55–61]. Directed percolation, however, does not appear to be an integrable model and its critical behavior is highly nontrivial. Moreover, it seems that the basic features of directed percolation, such as nonfluctuating states, are quite difficult to realize in nature [62]. Another fundamental problem is quenched disorder due to microscopic inhomogeneities of the system [23]. One of the earliest unambiguous and robust experimental realizations of a system exhibiting critical behavior in the directed percolation class was for the rather specific case of liquid crystal electrohydrodynamic convection [63]. Another experimental evidence was reported in 2016 in the case of transition to turbulence [64]. Due to the simplicity and robustness of directed percolation, it seems to be a good model for explaining ubiquitous phase transitions in many real-world phenomena, especially in the

so-called contact processes [4,33,65–72] in the realm of temporal networks [24].

Before presenting the mapping between reachability in temporal networks and the concepts in directed percolation, for the remainder of this section we will review these concepts for the case of the simple infinite lattice. Let us take the example of a spreading process across time in an infinitely large d -dimensional square lattice: Assume that each infected (or occupied) node can infect any of its neighbors independently with probability p at each tick of a discrete timer. Let us also assume that an infected node recovers (becomes unoccupied) in one tick of the clock after infection unless it is reinfected by a neighbor. This configuration is denoted in many sources as a $d + 1$ -dimensional lattice, substituting the temporal axis with another discrete spatial dimension with the only difference that, unlike the other d dimensions, this one has an inherent directionality. Throughout the rest of this section, we will continue to use the space and time analogy to facilitate a better transition to modeling phenomena on temporal networks.

The dynamics of this spreading process is defined by the topology and dimensionality of the medium of percolation and competition between two processes: the probability that an infected node infects each of its neighbors in a single tick of the clock, or “reproduction” from the perspective of the spreading agent, and the time it takes for each infected node to recover, or “self-annihilation” or “death” of the spreading agent. In the many classic representations of directed percolation, the reproduction probability is often denoted by the parameter p and the “self-annihilation” is set to happen in exactly one tick of the clock. For large-enough values of p , the system will forever stay in an “active state” where there is a nonvanishing density of nodes infected (occupied) at all times. Conversely, if the annihilation process has the upper hand, then the system eventually transitions irreversibly into an “absorbing phase” where no occupied nodes are left in the lattice and the spreading agent is extinct.

More generally, let us say the reproduction and self-annihilation process respectively happen at rates μ_p and μ_r . Let us assume that at $t = 0$, nodes are uniformly occupied with density ρ_0 . To write a mean-field rate equation for occupation density $\rho(t)$, we need to take into account how often more than one spreading agent (pathogens) simultaneously occupies (infects) the same node, in which case only one new node is occupied. Let us only consider the rate μ_c at which two other nodes simultaneously infect a single node and assume the probabilities of three or more simultaneous infections are small. In this case, the rate equation is of the form

$$\frac{\partial}{\partial t} \rho(t) = \tau \rho(t) - g \rho(t)^2, \quad (1)$$

where the *control parameter* $\tau = \mu_p - \mu_r$ is the manifestation of the competition between reproduction and death as described above and coupling constant $g = \mu_c$ describes the events of infecting a node already infected by another neighbor [23]. This equation has a steady state at $\lim_{t \rightarrow \infty} \rho(t) = \rho_{\text{stat}}(\tau) = 0$ which corresponds to the aforementioned absorbing phase. Furthermore, for $\tau > 0$ the value of $\rho(t)$ approaches a stationary occupation density of $\lim_{t \rightarrow \infty} \rho(t) = \rho_{\text{stat}}(\tau) = \tau/g$, which is identified as the order parameter of the directed percolation process. At exactly $\tau = 0$, occupation

density decays algebraically with time $\rho(t) \sim (\rho_0^{-1} + gt)^{-1}$. Naturally, for values of $\tau < 0$ the system eventually arrives at the absorbing phase $\rho(t) \rightarrow 0$ in finite time.

More generally, starting from a homogeneously occupied initial condition, order parameter $\rho_{\text{stat}}(\tau)$ of a system in the directed percolation universality scales as $\rho_{\text{stat}}(\tau) \sim \tau^\beta$, when control parameter τ is close to $\tau_c = 0$. For $\tau > 0$, density decays algebraically as $\rho(t) \sim t^{-\alpha}$ where in the mean-field regime (i.e., $d \geq 4$), $\beta = \alpha = 1$. In the case of a spreading process controlled by a percolation probability p introduced at the beginning of this section, it can be shown that $\tau \propto p - p_c$ where critical percolation probability p_c is a function of topology and dimensionality of the percolation medium [73,74].

Alternatively, we can focus on the ramifications of starting from a single seed of infection, as opposed to a homogeneous initial distribution of occupied nodes. A characteristic property of this scenario is survival probability $P(t)$: The probability that a spreading process starting from a single seed would still be in the active phase ($\rho(t) > 0$) at time t . Similarly to occupation density $\rho(t)$, at criticality $\tau = \tau_c = 0$ survival probability also decays algebraically with time $P(t) \sim t^{-\delta}$. A second alternative for order parameter is the ultimate probability of survival $P_{\text{surv}}(\tau) = \lim_{t \rightarrow \infty} P(t)$. When the control parameter is close to the critical threshold $\tau \rightarrow 0^-$, the ultimate probability of survival scales algebraically as $P_{\text{surv}}(\tau) \sim \tau^{\beta'}$.

Continuous phase transitions in models with timelike dimensions generally have the same system of two separate order parameters, controlled by two different critical exponents β and β' . For the case of directed percolation, however, ‘‘rapidity-reversal symmetry,’’ an invariance property under time reversal, ensures the two exponents have the same value $\beta = \beta'$ [75] which implies that $P(t)$ and $\rho(t)$ are at least asymptotically proportional as $t \rightarrow \infty$, and in some cases exactly equal $P(t) = \rho(t)$ [23]. Rapidity-reversal symmetry limits the number of independent critical exponents to three [76,77].

1. Characteristic quantities of the directed percolation

The single-source initial condition also allows us to define additional interesting characteristic quantities in the absorbing phase, which might lend themselves to experimental observation. Let us define *pair-connectedness function* $c(\vec{r}_1, t_1, \vec{r}_2, t_2)$ as the probability that a path exists from a node with spatial coordinates \vec{r}_1 at time t_1 and another in \vec{r}_2 at time t_2 . Note that the definition of spatial coordinates for nodes as a d -dimensional vector \vec{r}_i implies that the percolation medium and node i is embedded in a d -dimensional space, e.g., a d -dimensional lattice. Assuming that the percolation medium is invariant with respect to translations across time and space, we can simplify the pair-connectedness function by fixing the origin on the source node and denote the pair-connectedness function as $c(\vec{r}, t)$. *Mean cluster mass* M is defined as the integration of the pair-connectedness function across time and space:

$$M = \int_0^\infty dt \int d\vec{r} c(\vec{r}, t), \quad (2)$$

which, with control parameter close to the critical threshold $\tau_c = 0$ scales like $M \sim (-\tau)^{-\gamma}$ where $\gamma = \nu_{\parallel} + d\nu_{\perp} - \beta - \beta'$. Similarly, *mean spatial volume* V can be defined as the number of unique nodes that will ever get infected in a single-source spreading scenario. As with the case of the cluster mass M , spatial volume scales through a power relationship $V \sim (-\tau)^{-\nu}$ close to the critical threshold where $\nu = d\nu_{\perp} - \beta'$. It is possible to think of spatial volume V as the size of the projection of the percolation cluster over the d -dimensional spatial plane, i.e., over the original d -dimensional lattice. Projection of the same cluster on the temporal dimension will define the survival time of the cluster, which is distributed according to the probability of survival $P(t)$.

The homogeneous, fully occupied initial condition, on the other hand, allows us to study the response of a system to an *external field* h on the order parameter static density ρ_{stat} . For the case of directed percolation, an external field can be implemented as the spontaneous occupation of nodes at a rate h . A positive external field deprives the system of the possibility of ever transitioning into an absorbing phase. *Susceptibility* χ is defined as the magnitude of the response generated by a minuscule disturbance in the external field

$$\chi(\tau, h) = \frac{\partial}{\partial h} \rho_{\text{stat}}(\tau, h), \quad (3)$$

which diverges algebraically as the control parameter τ converges to the critical threshold $\tau_c = 0$, $\chi \sim |\tau|^{-\gamma}$ where γ is the same exponent as the mean cluster mass M . For the rest of this paper, when not specified, susceptibility χ is studied at minuscule values of external field ($h = 0$) as τ converges to the critical threshold $\tau_c = 0$. In practical terms, susceptibility is a useful tool for finding the transition point, as unlike the order parameters, we do not need to define an arbitrary threshold for what constitutes a small or large value for a quantity such as $M(t)$ or $V(t)$ close to the transition point in a finite system. Instead, the susceptibility will typically show a peak even in finite systems, which are discussed in more detail in Sec. IB 2.

2. Finite-size scaling properties of the system

While the dynamics described previously explain the behavior of an infinitely large system, measuring properties of infinitely large systems is a rather involved task. Verifying that the behavior of a system at criticality is explained by a specific set of critical exponents is often easier performed by studying the finite-size scaling properties of the system. This can be carried out by measuring a set of quantities for realizations at different scales and plotting the universal scaling function of each quantity as a function of scale-invariant ratios. If the exponents used are correct, then all the scaling functions of different linear system sizes for the same quantity should collapse on top of each other.

The effect of the finite size of the system manifest themselves as deviations from the scaling laws as described before and their effects are measurable after some characteristic size-dependent amount of time has elapsed since the beginning of the simulation. For example, while in an infinitely large system in active phase $\tau > 0$ the system will forever stay in an active phase, a finite system will always have a nonvanishing probability of transitioning to the absorbing state due to fluctuation of the order parameter. These finite-size effects take

place at a characteristic time t_f that scales as $t_f \sim l^z$ where $z = v_{\parallel}/v_{\perp}$ is the so-called *dynamical exponent* and l is the lateral (or linear) size of the system as opposed to system size N measured in number of nodes, where $N \propto l^d$.

In phenomenological scaling theory *simple scaling* is assumed for absorbing phase transitions. This means that large-scale properties of the system are invariant under scale transformations with the control parameter close to the critical threshold. A multiplicative transformation, or ‘‘concentration,’’ of the control parameter τ by a factor of λ , $\tau \mapsto \lambda\tau$ would result in rescaling of other quantities as

$$\begin{aligned} t &\mapsto \lambda^{-v_{\parallel}} t & l &\mapsto \lambda^{-v_{\perp}} l \\ \rho &\mapsto \lambda^{\beta} \rho & P &\mapsto \lambda^{\beta'} P \\ h &\mapsto \lambda^{\sigma} h & \chi &\mapsto \lambda^{-\gamma} \chi, \end{aligned} \quad (4)$$

where t and l denote timelike and lengthlike quantities respectively.

More specifically, scale invariance mandates very specifically how a quantity will change under multiplicative scale change. As an example, let us study changes of $\rho(t, l)$,

$$\rho = f(t, l) \mapsto \lambda^{\beta} \rho = f(\lambda^{-v_{\parallel}} t, \lambda^{-v_{\perp}} l), \quad (5)$$

where t is time from initial infection seed and l is the linear system size.

Since this relationship is valid for all values of λ , we can remove one parameter of the function by selecting a special value $\lambda = l^{1/v_{\perp}}$,

$$l^{\beta/v_{\perp}} \rho = f(l^{-v_{\parallel}/v_{\perp}} t, 1) = F(l^{-v_{\parallel}/v_{\perp}} t), \quad (6)$$

where the function $F(x)$ is referred to as the ‘‘(universal) scaling function’’ of its corresponding quantity, in this case, density ρ . The parameter to this function $l^{-v_{\parallel}/v_{\perp}} t$ is in itself invariant to scale transformations. This parameter and those similarly derived for other quantities are often known as ‘‘scale-invariant ratios.’’ The function $F(x)$ is universal, meaning that if measured to sufficient accuracy, then we obtain exactly the same type of scaling function for systems with similar boundary conditions and shape for any phenomena in the directed percolation universality class [23].

The value of each exponent is only a function of a few large-scale properties of the system, such as the number of spatial dimensions of the system. There exists an upper critical dimension d_c where systems with spacial dimensionality $d \geq d_c$ all follow the same set of values for critical exponents, which are exactly equal to those derived through mean-field estimation. For the case of the directed percolation universality class the upper critical dimension has a value of $d_c = 4$ [23].

II. METHODS

A. Directed percolation in temporal networks

Let us now take the case of δt limited-time spreading from a single source on a temporal network. Similarly to the classic directed percolation single-source spreading process, each temporal network node can participate in the spreading process by becoming infected, infecting others and recovering multiple times. Temporal networks are different from the

archetypal directed percolation systems presented in Sec. IB in that they do not present a regular lattice or metric space in the spatial dimension. Furthermore, there is typically no discrete structure in the temporal dimension, which is usually modeled as a continuous axis. Nevertheless, if the various concepts such as order parameter, control parameter, and cluster sizes are defined carefully, then temporal networks and limited waiting-time connectivity can be mapped to directed percolation [22].

To put it in the same reference frame as with other absorbing phase transitions, changing the parameter δt , in this scenario, controls the relative occurrence of ‘‘annihilation’’ and ‘‘multiplication’’ processes. A small-enough value of δt will lead to a situation where spreading scenarios will eventually die out, at which point the system enters an absorbing phase. Similarly, as δt grows, a spreading agent will be able to avoid extinction for longer time, until after some threshold $\delta t > \delta t_c$ a random spreading scenario will not die out (in an infinitely large network). As discussed in Sec. IA, such spreading scenarios are closely related to various properties of the δt thresholded limited waiting-time event graph D .

As illustrated in Fig. 1, the projection of the spreading cluster over the spatial plane amounts to a subset of temporal network nodes \mathcal{V} that has ever participated in the spreading process. This can be measured by calculating the mean number of unique temporal network nodes involved in the out-components of the event graph. The (ensemble) average number of unique nodes participating in single random source spreading processes is analogous to mean spatial volume V . The projection of the spreading cluster over the temporal axis is equal to the time window from the beginning of the spreading process to its end. The ensemble average of this time duration is analogous to mean survival time T . The sum of the duration of infectiousness for all the nodes, i.e., the integration of the pair-connectedness function, would therefore be analogous to spatial and temporal integration of the pair-connectedness function or mean component mass M . Note that the duration of the infectiousness is equal in all of the events, therefore, we use the number of reachable (i.e., possibly infection-carrying) events as a proxy for M , ignoring the overlaps. The above-defined quantities can be measured as features of the event graph. The average number of events in the out-component of a node in the event graph (equivalent to an event in the temporal network) measures the number of reachable events. The survival probability $P(t)$ can be similarly defined over an ensemble of single-source spreading instances based on the distribution of the lifetime of each spreading scenario, accounting for the finite temporal window of the simulation of the temporal network using a Kaplan-Meier estimator [78].

Another scenario is the simulation of the spreading process from homogeneous, fully occupied, initial conditions. Translating this from classic directed percolation poses a new problem; a homogeneous initial condition cannot translate to a ‘‘full row’’ of occupied nodes since we are dealing with continuous-time as opposed to the typical directed percolation case of discretized time presented in Sec. IB. Rather, a better translation of the fully occupied initial condition to continuous time is to assume all nodes to be occupied at the beginning of the observation period $t = \min(\mathcal{T})$, or more accurately by

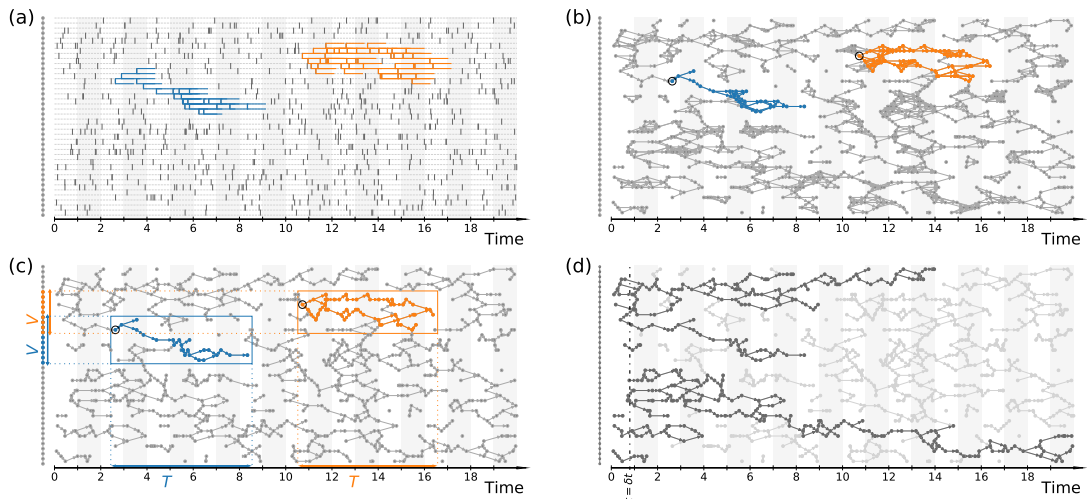


FIG. 1. Two spreading scenarios starting from random events [marked with black circles on (b) and (c)] represented over (a) temporal network, (b) δt -limited event graph, and (c) reduced event graph of a temporal network built from a one-dimensional grid of 40 nodes (displayed on the left side) with Poisson activation of events with mean interevent time 1 unit of time, simulated for 20 units of time. The adjacency relations have a maximum waiting time $\delta t = 0.8$ unit of time. Spatial volume V can be visualized as the mean size of projection of a spreading cluster on the spatial plain, i.e., the static base network on the vertical axis, whereas survival time T is equivalent to the mean size of projection of the cluster on time (horizontal) axis. While measuring a direct analog to component mass M , integrating the pair-connectedness function across time and space equivalent to the mean sum of lengths of colored horizontal lines in (a) is not straightforward with the event graph representation. It is possible to show that the mean number of uniquely counted events involved in the spreading process, corresponding to the cardinality of the out-component of the initial event here represented by the total number of colored nodes in the event graph, show the same scaling behavior. (d) Homogeneous, fully occupied initial condition with the occupied events shown in a darker shade than unoccupied events shows the decline and eventual stabilization of the occupation density as time grows. In this scenario, all nodes are considered occupied for time $-\infty < t < 0$, which translates to the occupation of all events in period $0 \leq t < \delta t$ and all events in their out-components.

assuming all nodes to be occupied for all values of t where $t \leq \min(T)$. Occupation density $\rho(t)$ is defined as the fraction of infected nodes at time t . Stationary density $\rho_{\text{stat}}(\tau)$ is therefore defined as occupation density after the system had enough time to reach a stationary state. We can also emulate the effects of an external field h in this scenario: In continuous time, this is equivalent to each node spontaneously becoming occupied through an independent Poisson point process with a rate of h . Susceptibility $\chi(\tau, h)$ can then be measured, from Eq. (3), by the rate of change in stationary density as external field changes.

B. Empirical methods for estimation of characteristic quantities

In practice, we can estimate M , V , T , and $P(t)$ on the event graph by finding all the *out-components*, i.e., every reachable event starting from every event [see Fig. 1(c)]. Calculating the exact set of out-components for every event in the event graph is time and memory intensive. However, if we are only interested number of events or number of unique nodes that participate in those events, as opposed to the full set of events in the out-components, then we can use probabilistic cardinality estimation data structures to estimate out-component sizes with arbitrary precision in $\mathcal{O}(|E| \log |E|)$ time, as opposed to $\mathcal{O}(|E|^2)$ time required for exact calculation [45]. Minimum and maximum time of all events in the out-component can be

exactly calculated in $\mathcal{O}(|E| \log |E|)$ time. Calculating properties of the *in-component* of an event is possible through a simple reversal of direction of all links in the event graph and applying the same algorithms.

Similarly, in the homogeneous fully occupied initial condition scenario, we do not need to directly estimate occupation density $\rho(t)$, stationary occupation density $\rho_{\text{stat}}(\tau)$, and susceptibility $\chi(\tau, h)$ via naive algorithms, which would explicitly compute these measures by simulating propagation. The properties of homogeneous, fully occupied, δt -constrained reachability can be estimated by marking as occupied any event that is in the out-component of at least one event with time $-\infty < t < t_0$. This can be accomplished by running the in-component size estimation algorithm [45] once over the whole network, recording minimum observed time in in-component of each event and marking those with minimum in-component time smaller than t_0 as occupied. In practice, temporal networks are only recorded or generated for a finite window of time $t_{\text{min}} < t < t_{\text{max}}$. As there are no adjacency relationship between events more than δt apart temporally, any event that has at least one event in its in-component with time $t_{\text{min}} < t < t_{\text{min}} + \delta t$ can be considered occupied. Figure 1(d) shows all occupied events (dark gray) with the initial condition that assumes all nodes are occupied from $-\infty < t < 0$. The density of occupied events, which corresponds to particle density $\rho(t)$, can be estimated from the

event graph representation by the number of occupied nodes in a band of time divided by the area covered by the band, i.e., number of nodes multiplied by the width of the band.

Normally, calculating the effects of an external field h would require simulating a fully occupied initial condition, marking some nodes randomly selected with rate h as occupied, computing their out-components, and measuring how many new events got occupied. As we are interested in the effects of a minuscule positive external field, indicated by susceptibility $\chi(\tau, 0)$, we can instead calculate the effects of spontaneously marking exactly one random event in the whole network as occupied using probabilistic counting and in-components of all events (i.e., looking back in time). If the number of events in the in-component of an event e is denoted as $|E^{\text{in}}(e)|$ and the minimum time among all events in its in-component as $t_{\min}^{\text{in}}(e) = \min_{(u,v,t) \in E^{\text{in}}(e)} t$, then the expected number of spontaneously occupied events when a minuscule external field h is applied can be estimated as $\sum_{e \in \mathcal{E}} P_{\text{occupied}}(e)$ where

$$P_{\text{occupied}}(e) = \begin{cases} 1 & \text{if } t_{\min}^{\text{in}}(e) < t_0 \\ \frac{|E^{\text{in}}(e)|}{|\mathcal{E}|} & \text{otherwise} \end{cases}. \quad (7)$$

In this scenario, the respective value for the external field that would spontaneously occupy on average one event is proportional to $h \propto 1/|\mathcal{E}|$. We approximate $\rho(t)$ by number of occupied events within a δt time window divided by spatiotemporal hypervolume of the time window $\delta t \times |\mathcal{V}|$. The estimate for $\rho(t)$ can in turn be used to approximate quantities like stationary density $\rho_{\text{stat}}(\tau)$ and susceptibility $\chi(\tau, h)$.

III. RESULTS

A. Experimental setup

In this section, we focus on validating and exploring the limits to our hypothesis that δt limited-time spreading in many forms of temporal networks belongs to the directed percolation universality class. We do this by performing single-seed and homogeneous initial-condition spreading simulations following the method defined in Sec. II A and explained in detail in Sec. II B. By measuring various observables for networks of different sizes as described in Sec. IB 2, we can verify whether for each quantity the corresponding universal scaling functions collapse for systems of different finite sizes when using the same values of critical exponents β , β' , ν_{\parallel} , and ν_{\perp} as that of DP corresponding to the dimensions of the system as a previous mean-field approximation and experimental setups for the directed percolation.

The experiments are performed on a variety of synthetic temporal networks. The generation procedure consists of generating a static *base network* corresponding to the aggregate network and generating events, i.e., activations or timestamps, for each link based on some temporal dynamic. In total, we analyzed 26 combinations of base networks and link-activation processes. In order to perform the finite-size scaling analysis, we computed all the statistics for 10 network sizes, starting from $N = 2^8$ nodes and increasing the size by a factor of two until we reached $N = 2^{17}$ nodes. For the case of d -dimensional square grids where $d \in \{2, 3, 4\}$, however, closest powers of d to the powers of two from 2^8 to 2^{17} was

used with a periodic boundary condition, to provide spatial translational invariance. Each statistic was calculated as the average of at least 256 (up to 4096) realizations and each realization of the largest configuration consists of around 3.7×10^7 events. No sampling of spreading scenarios was required for each network's realization, as the effect of starting a spreading process from any possible combinations of nodes and times could be gathered in one pass as described in Sec. II B. See the Supplemental Material [79] (which includes Refs. [80–86]) for a more detailed overview of the experimental setup.

Static base networks are either (a) one to four-dimensional square lattice grids with periodic boundary conditions, (b) random regular graphs with specified average degree [87,88], or (c) Erdős–Rényi $G(n, p)$ random networks with specified expected average degree [89]. For the random networks, we chose the average degrees 8 for the Erdős–Rényi graphs and 9 for the random regular graphs (such that both networks have the same expected excess degree). The higher degrees of random networks ensure that the probability of generating networks with large isolated components remains negligible and that, even locally, the network would be of high-enough dimensionality to be in the mean-field regime above the upper critical dimension $d_c = 4$.

Temporal dynamics of the links are either governed by (a) Poisson processes, i.e., exponential interevent times; (b) bursty processes, i.e., renewal processes with power-law interevent time distributed as $\propto \Delta t^{-\gamma}$ with exponents $\gamma \in \{2.05, 2.2, 2.8, 5.2\}$ and minimum interval cutoff set so that the expected interevent would be equal to 1; and (c) Hawkes independent self-exciting processes with different parameter sets. The Hawkes univariate exponential self-exciting process [90] is defined by the conditional intensity function

$$\lambda^*(t) = \mu + \alpha \theta \sum_{t_i < t} e^{-\theta(t-t_i)}. \quad (8)$$

The parameters of this formulation of the Hawkes process are (1) background (or exogenous) intensity of events μ indicating the random probability of events happening without being caused through self-excitation; (2) the infectivity factor α , which can be interpreted as the expected number of induced self-exciting events per each event; and (3) the rate parameter of the delay θ . Based on the properties of exponential kernel used in defining Eq. (8), $1/\theta$ is the expected interevent time between an event (e.g., a coincidental social interaction) and its corresponding induced self-exciting event (e.g., the follow-up social interactions) [91].

As the unit of time is arbitrary, temporal processes are scaled, without loss of generalization, so that they produce timestamps with a mean interevent time equal to 1. The processes are initialized in their stationary state, and in practice, the first timestamp for each event is generated through residual time distribution of each process, except for the case of Hawkes process where the process is allowed a burn-in time equal to the simulation time window before the first timestamp is recorded. The temporal processes of pairs of links are simulated independently of each other. Figure 2 shows a visualization of the different methods of generating event activations. Temporal networks were simulated for a time

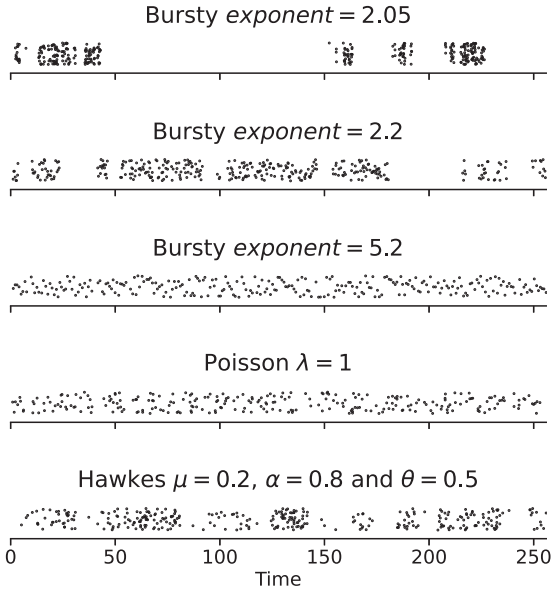


FIG. 2. Sample timestamps from a single realization (activations of a single link) with different temporal dynamics. Each point represents a single activation at a specific time. The points are scattered over the vertical axis to avoid overlaps in the visualization. All timestamps were generated for 256 units of time with parameters or minimum cutoffs that would result in an expected interevent time of 1. Equation (8) defines the parameters and the intensity function of the Hawkes univariate exponential self-exciting process.

window of at least $T = 64$ and up to $T = 8192$ units of time. See Supplemental Material [79] for the exact experimental setup for each system size. The difference in system sizes and time windows for the simulations were necessitated by the limitations and optimal utilization of the computational facilities.

B. Estimating the critical threshold δt_c and the critical exponents β , β' , ν_{\parallel} , and ν_{\perp}

Best estimate of the critical exponents β , β' , ν_{\parallel} , ν_{\perp} and critical threshold δt_c can be determined by finding the values of these exponents that would produce the best data collapse for the universal scaling functions corresponding to $\rho(t)$, $\hat{P}(t)$, $M(t)$, and $V(t)$. The quality of collapse, in turn, can be assessed by comparing the deviation of the scaling function curves for different system sizes from the average trajectory. Here, for each of the quantities $\hat{P}(t)$, $\rho(t)$, $M(t)$, and $V(t)$, we calculated one trajectory for finite-size scaling function for each system size, as defined for example for the case of $\rho(t)$ by Eq. (6). As the tested value of critical exponents and δt_c gets closer to the actual critical threshold, the curves for different sizes should more closely collapse on top of each other. Plotted with the correct values of critical exponents and critical threshold, we expect to see all trajectories collapse into one with the possible exception of very small values of t . To

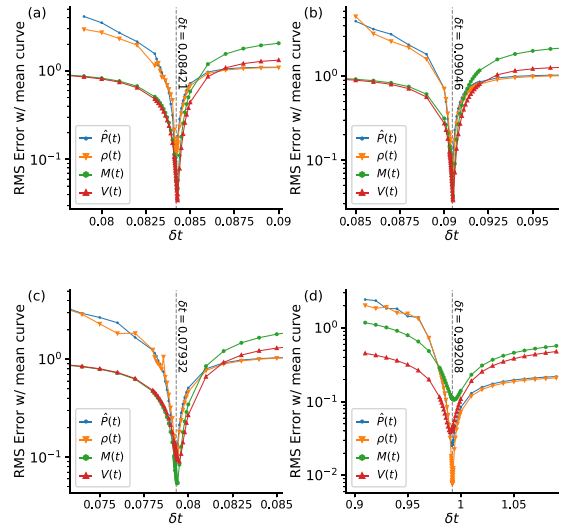


FIG. 3. Root-mean-square (logarithmic) deviation of scaling-corrected functions of probability of survival $\hat{P}(t)$, density $\rho(t)$, mass $M(t)$, and volume $V(t)$ for different system sizes from average trajectory shows a sharp drop at δt_c due to data collapse. Each instance of the network is made through realizations of (a) Erdős–Rényi static network $\langle k \rangle = 8$ and Poisson process $\lambda = 1$ activations; (b) random 9-regular networks with bursty (power law with minimum cutoff) interevent time distribution with mean 1 and exponent $\gamma = 2.8$; (c) Erdős–Rényi static network $\langle k \rangle = 8$ and Hawkes univariate exponential self-exciting process with parameters $\mu = 0.2$, $\alpha = 0.8$, and $\theta = 1.0$; and (d) one-dimensional grid with periodic boundary conditions (a circle) and Poisson process $\lambda = 1$ link activations. Refer to Sec. III A for the definitions of the parameters.

quantify the quality of a collapse, we measure the mean curve in the area where all system sizes have defined values for the scaling function and measure the root-mean-square difference of all points from all system sizes to the mean curve. The errors were measured after logarithmically scaling the values to account for the power-law nature of the scaling functions. Sum of errors for the collapse of $\hat{P}(t)$, $\rho(t)$, $M(t)$, and $V(t)$ was used in evaluating each set of parameters.

In order to assess collapse of the universal scaling functions, we first determine a value for δt_c for each network configuration. That is, the best candidate for δt_c is selected based on the least total error for collapse of $\hat{P}(t)$, $\rho(t)$, $M(t)$, and $V(t)$ assuming DP critical exponents. Figure 3 shows this total error of collapse for two network configurations. This shows a clear minimum for each configuration indicating the critical value δt_c , which is consistent across $\hat{P}(t)$, $\rho(t)$, $M(t)$, and $V(t)$ trajectories. The resulting estimates for δt_c can be used to visually verify directed percolation critical exponents and our selected optimal value of δt_c for each system by plotting the finite-size universal scaling functions of different system sizes. In total, we produce collapses for eight characteristic quantities measured in a single source or homogeneous initial conditions. Figure 5 shows these collapses measured for

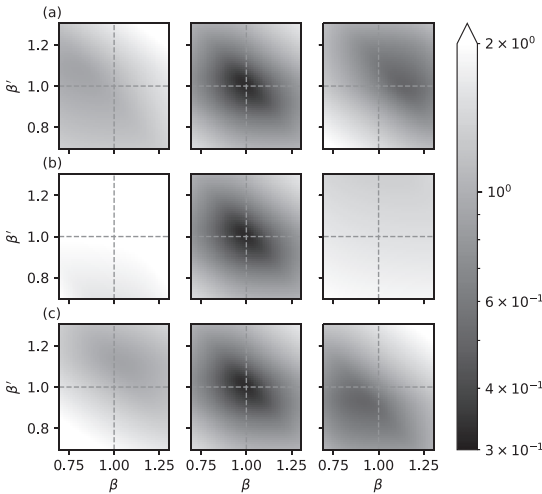


FIG. 4. Total error of collapse of universal scaling functions of $M(t)$, $V(t)$, $\hat{P}(t)$, and $\rho(t)$ for Erdős–Rényi networks $\langle k \rangle = 8$ and Poisson process activation $\lambda = 1$ as a function of β and β' . In these visualizations we set $v_{\perp} = 0.5$, $v_{\parallel} = 1$, and $\delta t_c = 0.08421$, and vary one of these parameters such that the three panels from left to right correspond to values (a) $v_{\perp} \in \{0.34, 0.5, 0.66\}$, (b) $v_{\parallel} \in \{0.84, 1, 1.16\}$, and (c) $\delta t_c \in \{0.0840, 0.08421, 0.0844\}$. Note that the center panel is repeated across the rows and always has parameter values $v_{\perp} = 0.5$, $v_{\parallel} = 1$, and $\delta t_c = 0.08421$. We see that there is a minimum in the error close to $\beta = \beta' = v_{\parallel} = 1$ and $v_{\perp} = 0.5$ within this five-dimensional space.

regular networks with bursty dynamics (renewal process with power-law interevent times) and Erdős–Rényi networks with a Hawkes self-exciting process dynamics. The full set of plots for all 26 configurations are shown in the Supplemental Material [79]. In all cases, a satisfactory collapse can be observed for at least probability of survival $\hat{P}(t)$ and density $\rho(t)$ and in most cases, other quantities show a good collapse as well. It is important to note that quantities that depend on measuring values as time approaches infinity, e.g., $\rho_{\text{stat}}(\delta t)$ and $\chi(\delta t)$ have generally lower quality of measurement and collapse since the time to reach a stable value for these increases substantially close to criticality [46].

Table I (column “Est. δt_c ”) shows our best estimate of the critical threshold δt_c for each configuration using the method described above. As the systems become rapidly more and more connected after the critical threshold, a lower value for the critical threshold δt_c indicates higher, or more robust, spatiotemporal connectivity, meaning that the same δt limited-time spreading would result in a larger number of reachable nodes, $V(\delta t)$, or larger number of reachable events, $M(\delta t)$. When modeling infectious disease spreading as directed percolation on temporal networks, larger values for $V(\delta t)$ and $M(\delta t)$ may indicate larger epidemic sizes and the total number of human hours of infection in the population, respectively.

These results indicate that within each spatial configuration, increased burstiness (as indicated by lower value for the

power-law exponent γ) generally leads to a lower value for δt_c threshold and higher connectivity. Furthermore, for the case of the self-exciting process, increasing the expected number of self-induced events, as indicated by α , generally results in a lower value for δt_c (higher connectivity). While it was previously understood that a wide range of temporal inhomogeneities slows down spreading processes over temporal networks [13], these results demonstrate that certain temporal inhomogeneities, e.g., a highly bursty or self-exciting temporal dynamic, can enable a *more limited* spreading agent (expressed in terms of a maximum waiting time) to spread to a wider set of nodes. For example, spreading processes with maximum waiting time between $0.063 < \delta t < 0.084$ over an Erdős–Rényi networks $\langle k \rangle = 8$ will spread to a much larger set of nodes and span a longer span of time if the link activations are highly bursty ($\gamma = 2.05$) compared to a Poisson process with the same mean interevent time, as the latter will be spreading in the subcritical regime compared to the supercritical regime for the former.

It is also interesting to note that while the random spatial configurations, namely random 9-regular networks and the Erdős–Rényi networks $\langle k \rangle = 8$, both result in networks with the same expected excess degree value, the Erdős–Rényi networks with higher levels of spatial inhomogeneity, which manifests as a wider spread degree distribution, can be observed to have a lower δt_c critical threshold. While testing on a wider range of spatial (structural) inhomogeneities would be required before a conclusion is reached, these results might hint at a similar behavior as with temporal inhomogeneities, namely that introducing certain spatial inhomogeneities might result in higher connectivity in the sense that the same limited-time spreading agent can eventually spread to a wider share of the network.

Additionally, we present a method to assess the quality of a collapse for a range of different values of critical exponents (β , β' , v_{\parallel} , and v_{\perp}) and δt_c . A five-dimensional grid search for optimal values for critical exponents and δt_c based on the quality of collapse for $P(t)$, $\rho(t)$, $M(t)$, and $V(t)$ shows that the total error declines around critical exponent values close to that of directed percolation, i.e., $\beta = \beta' = v_{\parallel} = 1$ and $v_{\perp} = 0.5$ for mean-field regimes and their respective DP values for lower-dimensionality square grid networks. Figure 4 shows for Erdős–Rényi static networks with $\langle k \rangle = 8$ and Poisson process link activation, the $\beta \times \beta'$ plane from the five-dimensional grid search with two sandwiching parallel planes along each of the v_{\parallel} , v_{\perp} , and δt_c dimensions. This verifies that there is a minimum close to $\beta = \beta' = v_{\parallel} = 1$, $v_{\perp} = 0.5$, and $\delta t_c = 0.08421$ for total error of collapse of $P(t)$, $\rho(t)$, $M(t)$, and $V(t)$. Similar plots for some other network configurations (along with a different two-dimensional slice, $v_{\parallel} \times v_{\perp}$) can be viewed in the Supplemental Material [79]. It is important to note that while other combinations of parameters in the grid might lead to other local optima, visual inspection of the resulting collapse show that to be mainly numerical artifacts where the total error changes rapidly close to extreme values of the parameters (i.e., critical exponents and δt_c) where only a very small fraction of the trajectories for different finite sizes actually overlap.

Furthermore, for each of the critical exponents, we can measure an estimation error based on this five-dimensional

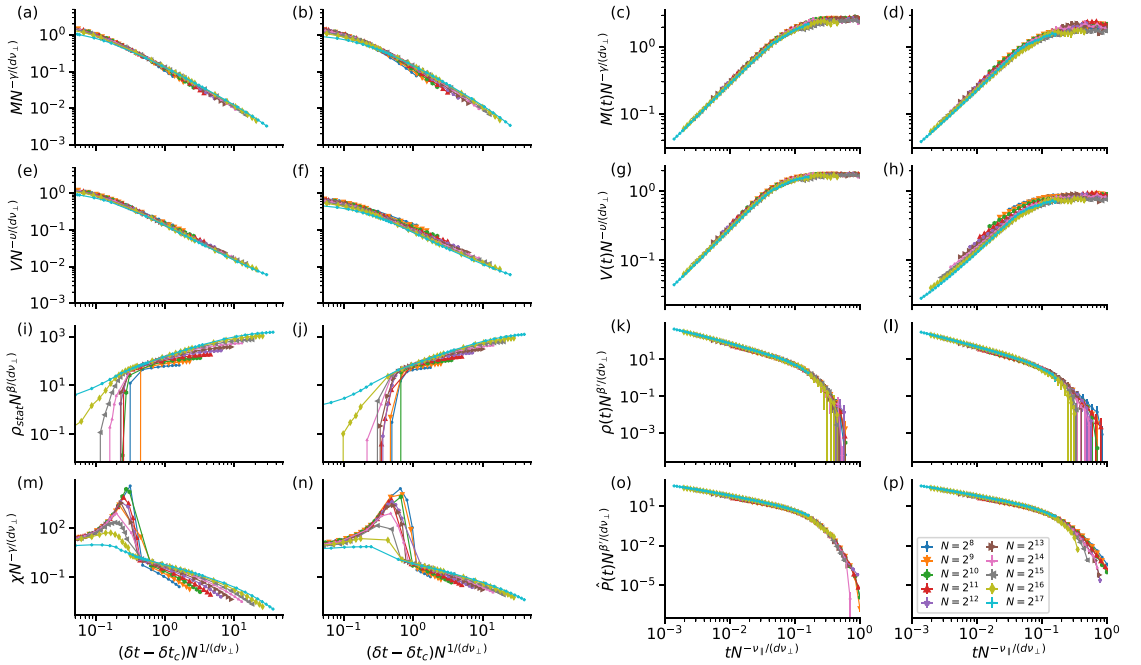


FIG. 5. Universal scaling functions for δt limited-time reachability over [(a), (c), (e), (g), (i), (k), (m), and (o)] random 9-regular network with bursty (heavy-tail with minimum value cutoff) link activation with mean interevent time of 1 and exponent $\gamma = 2.8$ and [(b), (d), (f), (h), (j), (l), (n), and (p)] random Erdős–Rényi network ($k = 8$) with Hawkes univariate exponential self-exciting process link activation with parameters $\mu = 0.2$, $\alpha = 0.8$, and $\theta = 1.0$. The finite-size scaling is performed for the following single-source scenarios: [(a) and (b)] The mean component mass M as function of δt close to critical point and [(c) and (d)] as function of time t at the critical point and [(e) and (f)] the mean component volume V as function of δt close to critical point, and [(g) and (h)] as function of time t at the critical point and [(o) and (p)], Survival probability \hat{P} as function of time t at the critical point. For fully occupied initial conditions the finite-size scaling is performed for [(k) and (l)] the occupation density ρ as function of time t at the criticality, and both [(i) and (j)] the static density ρ_{stat} and [(o) and (p)] susceptibility χ as function of δt close to the critical point. The collapse of the universal scaling functions validates the hypothesis that these systems are governed by the same critical exponents as in directed percolation in the mean-field regime. See Sec. III A for the full definitions of the parameters.

parameter grid. For each exponent, we find a range of values where, assuming that all other exponents are fixed at their DP values, would produce collapses of higher or equal quality compared to the DP value of that exponent. The sizes of these ranges, which by definition includes the DP value for all exponents, provides a confidence interval for the range of possible exponent values that are able to explain the behavior of the system with at least the same quality as that of directed percolation. As shown in Table I, these errors are in most cases only a few percentages, with a notable exception of the highly bursty renewal processes with $\gamma = 2.05$. Simulating power-law distributions becomes a much harder problem as the magnitude of the exponent approaches 2. Close to this exponent, it takes a larger and larger number of realizations for the properties of the population, e.g., average interevent time for bursty temporal dynamics, to converge. It is also possible that the large estimation error is an indicator that the system is approaching a breakdown of one of the key symmetries, with the most likely candidate being rapidity-reversal symmetry based on the fact that the estimation error for β' is much larger than that of the other exponents.

C. Estimating critical exponents by simulating very large systems

As discussed before in Sec. IB, the effects of the finite size of the system manifest at characteristic times $t_f \propto N^{\nu_{\parallel}/d\nu_{\perp}}$ in the form of fluctuations that causes the transition of the system to the absorbing phase. At times much smaller than t_f the system shows approximately the scaling behavior of an infinitely large system where at criticality, $\rho(t) \sim t^{-\alpha}$ and $\hat{P}(t) \sim t^{-\delta}$ where $\alpha = \beta/\nu_{\parallel}$ and $\delta = \beta'/\nu_{\parallel}$. On the other hand, the power-law scaling behavior becomes visible at times comparable to the mean interevent time of the dynamic process but not up to arbitrarily infinitesimal values of t . Given these properties, we fitted two power-law functions using the least-squares method to the results of experiment with the largest system size for the range of time $2 < t < 0.04 \times N^{\nu_{\parallel}/d\nu_{\perp}}$ on $\rho(t)$ and $\hat{P}(t)$ to derive exponent α and δ . Figure 6 shows one such fitting for a system made from Erdős–Rényi networks with $\langle k \rangle = 8$ and $N = 2^{17}$ nodes and bursty (power law with minimum cutoff) interevent time distribution with mean 1 and exponent $\gamma = 2.8$. Table I (columns Est. α and Est. δ) shows the best

TABLE I. Column “Est. δt_c ” shows the best candidate for critical threshold δt_c selected by minimizing the collapse error of the universal scaling functions for probability of survival $\hat{P}(t)$, density $\rho(t)$, mass $M(t)$, and volume $V(t)$ derived for different system sizes, assuming DP exponents. The collapse error is measured by the sum of root-mean-squared deviation of logarithmically scaled trajectories for all four scaling functions. For the best estimate for exponents $\alpha = \beta/v_{\parallel}$ and $\delta = \beta'/v_{\parallel}$, reported respectively in columns “Est. α ” and “Est. δ ,” a power law was fitted to the head of values of probability of survival $\hat{P}(t)$ and density $\rho(t)$, respectively, for the largest system size simulated for the time period between $2 < t < 0.04 \times N^{v_{\parallel}/d v_{\perp}}$, where both functions are expected to be still mostly behaving, similar to an infinite system, according to power relations $t^{-\alpha}$ and $t^{-\delta}$ respectively. Directed percolation mean-field values for these critical exponents are $\delta = \alpha = 1$, which is close to the value estimated for random, high-dimensional networks. Furthermore, the value of these critical exponents in a DP system are expected to be close to $\alpha = \delta = 0.15946$ for 1+1 dimensional, $\alpha = \delta = 0.450$ for 2+1 dimensional, $\alpha = \delta = 0.732$ for 3+1 dimensional and equal to the mean-field estimates systems $\alpha = \delta = 1$ for 4+1 dimensional [46], which is close to values estimated for one-dimensional lattice and two- to four-dimensional square lattices.

Configuration	Est. δt_c	β Error	β' Error	v_{\parallel} Error	v_{\perp} Error	Est. α	Est. δ
Erdős–Rényi (k) = 8							
Poisson	0.08421	0.01	0.01	0.06	0.03	1.0702	1.0338
Bursty							
$\gamma = 2.05$	0.06231	0.06	0.17	0.08	0.09	1.0110	0.9816
$\gamma = 2.2$	0.08013	0.02	0.05	0.04	0.03	1.0320	1.0285
$\gamma = 2.8$	0.08649	0.01	0.01	0.05	0.01	1.0625	1.0368
$\gamma = 5.2$	0.08655	0.01	0.01	0.06	0.02	1.0540	1.0499
Hawkes self-exciting							
$\mu = 0.2 \alpha = 0.8 \theta = 0.5$	0.0815	0.01	0.04	0.07	0.03	0.9929	1.0015
$\mu = 0.2 \alpha = 0.8 \theta = 1.0$	0.07932	0.02	0.06	0.06	0.04	1.0185	0.9747
$\mu = 0.5 \alpha = 0.5 \theta = 0.5$	0.08339	0.01	0.03	0.05	0.02	1.0791	1.0328
$\mu = 0.5 \alpha = 0.5 \theta = 1.0$	0.08281	0.01	0.04	0.07	0.03	1.0311	1.0116
$\mu = 0.8 \alpha = 0.2 \theta = 0.5$	0.08397	0.01	0.01	0.07	0.02	1.0542	1.0246
$\mu = 0.8 \alpha = 0.2 \theta = 1.0$	0.08383	0.01	0.02	0.07	0.02	1.0251	1.0087
Random 9-regular							
Poisson	0.08808	0.03	0.05	0.05	0.02	1.0096	0.9947
Bursty							
$\gamma = 2.05$	0.06484	0.08	0.17	0.11	0.08	0.9752	0.9660
$\gamma = 2.2$	0.08413	0.04	0.05	0.05	0.03	1.0044	0.9825
$\gamma = 2.8$	0.09046	0.02	0.03	0.05	0.02	1.0190	0.9874
$\gamma = 5.2$	0.09049	0.02	0.02	0.07	0.01	0.9886	0.9755
Hawkes self-exciting							
$\mu = 0.2 \alpha = 0.8 \theta = 0.5$	0.0853	0.05	0.06	0.06	0.03	0.9982	0.9686
$\mu = 0.2 \alpha = 0.8 \theta = 1.0$	0.08303	0.02	0.06	0.08	0.04	0.9680	0.9564
$\mu = 0.5 \alpha = 0.5 \theta = 0.5$	0.08728	0.02	0.03	0.06	0.02	1.0094	0.9702
$\mu = 0.5 \alpha = 0.5 \theta = 1.0$	0.08663	0.02	0.05	0.09	0.03	0.9861	0.9664
$\mu = 0.8 \alpha = 0.2 \theta = 0.5$	0.0879	0.05	0.01	0.12	0.01	0.9901	0.9563
$\mu = 0.8 \alpha = 0.2 \theta = 1.0$	0.08769	0.04	0.05	0.06	0.03	0.9936	0.9796
1D lattice							
Poisson	0.9919	0.01	0.03	0.01	0.03	0.1583	0.1456
2D square lattice							
Poisson	0.28428	0.01	0.08	0.03	0.01	0.4109	0.3922
3D square lattice							
Poisson	0.15375	0.01	0.06	0.02	0.01	0.7229	0.6899
4D square lattice							
Poisson	0.1045	0.02	0.03	0.03	0.02	1.0077	0.9870

estimates of these exponents, which as expected are very close to respective directed percolation critical exponents of 1 (for the mean-field regime $d \geq 4$) for the case of random networks and 0.159, 0.450 and 0.732 for one-, two-, and three-dimensional lattices respectively [46].

IV. DISCUSSIONS

Through combining multiple methods of empirical and theoretical verification, we are able to confidently state that limited waiting-time connectivity percolation over a wide

range of synthetic temporal networks incorporating a range of temporal and topological inhomogeneities show behavior compatible with the directed percolation universality class. It is of utmost importance to discuss the limitations of our method: chief among them, that our empirical finite-size simulation method, as described in Sec. II B, is not able to measure quantities which are defined at $t \rightarrow \infty$, such as the ultimate probability of survival P_{surv} and static density ρ_{stat} (and therefore susceptibility χ) to the same standard of accuracy as the other quantities due to the finite size of the synthetic networks used for analysis. This is exacerbated

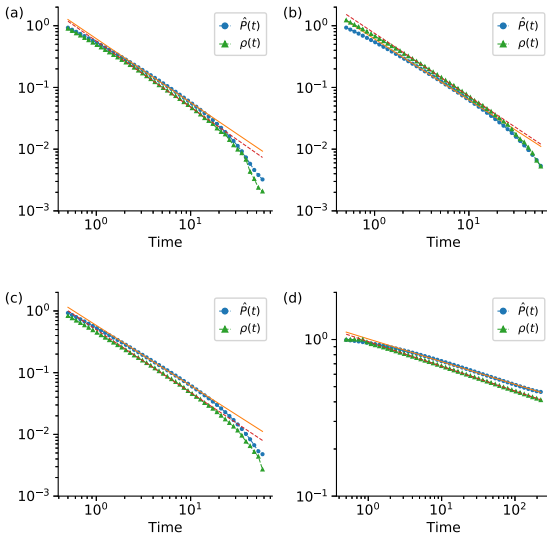


FIG. 6. An example of fitting power-law functions on empirical $\rho(t)$ and $\hat{\rho}(t)$ results on finite networks for deriving critical exponents $\alpha = \beta/v_{\parallel}$ and $\delta = \beta'/v_{\parallel}$. Power-law functions were fitted on experimental results of spreading over Erdős–Rényi networks with $\langle k \rangle = 8$ and $N = 2^{17}$ nodes and bursty (power law with minimum cutoff) interevent time distribution with mean 1 and exponent $\gamma = 2.8$. The fitting was performed on values in range $1 < t < 0.04 \times N^{v_{\parallel}/d_{v_{\perp}}}$ (i.e., $1 < t < 14.48$) to limit the interference of finite-size effects with the scaling behavior.

close to the critical threshold where the equilibration time, the time required for the network to reach a stationary state, grows rapidly while the memory and computational cost of simulating a temporally larger temporal network grow linearly and log-linearly, respectively, with the increased simulated time [46]. This is visible in Figs. 5(e), 5(f), 5(k), and 5(l) as a worse collapse as compared to other quantities.

Also, while it is computationally much more feasible to measure susceptibility χ by inducing occupation of exactly one existing event in the temporal network (described in Sec. II B) as compared to inducing occupation of nodes at random times (as described in Sec. I B), the latter method might be more robust, especially when dealing with a temporal network with a high degree of temporal inhomogeneity. Although our experiments with this alternative method were limited to smaller system sizes, we could not observe any significant difference between the two methods for the network configurations presented in this manuscript.

While a wide range of temporal dynamics and network structures with different levels of inhomogeneity are studied here, there is still a wide variety of systems that present computational and theoretical challenges. First, the effects of event-event correlations between links are not studied. It has been shown that event-event correlations, among other forms of inhomogeneity, can affect the rapidity of the spreading process on temporal networks [13]. Conceptually, local event-event correlations such as temporal motifs [29], are close to temporal event graphs, which are in practice computed using

isomorphisms on slightly modified temporal event graphs. Thus, incorporating temporal motifs to the framework at the level of analytical computations is an interesting future direction, as that corresponds to modifying the frequency of appearance of structural motifs in the event graphs. Second, the effect of static base networks with heavy-tail degree distributions and other more complicated network topologies are absent from this study. Here, of especial interest are the networks with heavy-tailed degree distribution with static network reachability percolation threshold at zero occupied links, e.g., $p(k) \propto k^{-2}$. While initial results did not support the conclusion that a δt limited waiting time over this class of synthetic temporal networks would be in the directed percolation universality class, due to limitations on computational resources, we were not able to perform the analysis on the larger system sizes comparable to the other types of networks.

Depending on the physical mechanism involved in the modeled connectivity phenomenon or spreading process, alternative methods of defining the adjacency relationship might be more suitable than the one used here. For example, for the case of disease spreading over a physical contact network, the currently used definition of event graph causes a “reinfection” of the infected party, manifested as a restart of their δt duration of disease. This can be resolved by substituting each undirected event in the temporal network with two simultaneous directed events. Similarly, for a disease spreading scenario over transportation networks, such as an airplane traffic network, the time between two events (the value that is compared to the maximum duration of disease δt to determine whether two flights are adjacent) should be calculated from the departure of one flight to departure of the possibly adjacent flight and not, as it is currently presented, from the arrival of the latter to the departure of the former. This might be an important factor when dealing with scenarios in which the reasonable values for δt are comparable to the delay or the duration of the events, e.g., the time from the departure of a flight to the arrival in a spreading process over an air transport network.

For some spreading mechanisms, it might also be more suitable to replace the hard δt limited-time cutoff of adjacency requirement used in this work with a probabilistic process by measuring quantities over an ensemble of event graphs. For example, using a Poisson process instead of a δt limited-time cutoff would produce dynamics similar to simulations of SIS processes over networks while simulating results of the simulation starting at every possible starting point in one pass. Viewed this way, normal δt limited-time cutoff can be seen as a probabilistic process where the probability of adjacency is a step function at $\Delta t = \delta t$. It is also possible to combine an occupation probability similar to classic directed percolation (see Sec. I B) with a δt limited-time cutoff (or a Poisson process cutoff or other forms of temporal locality constraint) to construct a two-dimensional phase diagram for each temporal network.

It would also be possible to define connectivity in the event graphs in a way that mimics the SIR process. In this case, one would need to prune some of the temporal paths in the event graph such that temporal network nodes are not repeated. This distinction is equivalent to paths and simple paths (or walks and paths, respectively) in static graphs. The algorithmic

techniques employed in this work are not directly applicable to this case, and in fact, it has been recently shown that algorithmic problems in such settings can be computationally difficult. For example, in the SIR interpretation of the event graph, finding if it is possible for a node infected at a specific time to infect a given node is an NP-hard problem [92]. In any case, averaging over explicit simulations of spreading scenarios is always an alternative option to the algorithms that take advantage of the redundancies in computing reachability.

Connectivity, which encapsulates several important phenomena on complex systems such as spreading processes [37–39] and routing dynamics [44], has not yet undergone the same level of development on temporal networks as the static networks. It has been previously suggested that connectivity on temporal networks, or other adjacent representations such as dynamic networks, might show the same properties as any other directed percolation system [20,21], a class of percolation models with built-in directionality which has enjoyed abundant attention in the past decades. In Ref. [22], we laid formal foundations by providing one-to-one analogues between concepts from directed percolation and temporal network connectivity and provided theoretical evidence supporting this hypothesis. In this work, we presented multiple accounts of empirical evidence showing that connectivity on many model temporal networks belongs to the directed percolation universality class and that this hypothesis is robust for a range of temporal and spatial heterogeneities.

This work focused mainly on establishing the vocabulary and developing the required tools in the hopes of rendering studies of connectivity in temporal networks ripe for future analysis, especially from a critical phenomena perspective. It is important to note that this work has only scratched the surface of the analytical study of connectivity on temporal networks and still, a vast body of analytical and phenomenological topics, some of which were eluded to in the previous paragraphs, remains open for future study.

ACKNOWLEDGMENTS

We thank János Kertész and Géza Ódor for their helpful comments and suggestions. The authors acknowledge the CSC–IT Center for Science, Finland, and Aalto University “Science-IT” project for generous computational resources. Márton Karsai acknowledges support from the DataRedux ANR project (ANR-19-CE46-0008) and the SoBigData++ H2020 project (H2020-871042).

APPENDIX: MEAN-FIELD SOLUTION FOR DIRECTED PERCOLATION IN TEMPORAL NETWORKS

The event graph representation contains many redundant adjacency relationships, e.g., triangles, or more generally feed-forward loops, that can be removed without changing reachability of nodes, producing a *reduced event graph* [22]. Assuming the probability of two or more adjacent events happening at exactly the same time is negligible, the reduced event graph, a subset of the event graph with exactly the same reachability properties, has a maximum in- and out-degree of 2 [22,25]. If we make the simplifying assumption that the reduced event graph representation of δt limited waiting-time

spreading process on a specific temporal network is indistinguishable from a random directed network with the same joint in- and out-degree distribution $P(k_{\text{in}}, k_{\text{out}})$, then a mean-field solution to order parameter occupation density ρ_{stat} for a δt limited-time spreading process over temporal networks, as defined in Sec. II A, can be derived in the form

$$\frac{\partial}{\partial t} \rho(t) = (\langle Q_{\text{out}} \rangle - 1) \rho(t) - \langle Q_{\text{out}} \rangle \rho(t)^2, \quad (\text{A1})$$

where $\langle Q_{\text{out}} \rangle$ is the mean excess out-degree of the reduced event graph [22]. This rate equation has the same form as Eq. (1). The solution to this equation shows a phase transition at $\tau_c = 0$ and other behavior consistent with $\tau = \langle Q_{\text{out}} \rangle - 1$ being the control parameter of directed percolation. As with Eq. (1) this sets two of the four critical exponents in the mean-field regime to the same values as those of mean-field DP, $\alpha = \beta = 1$.

Under the same assumption, the probability-generating function representation of the out-degree distribution is $G_0^{\text{out}}(y) = G(1, y)$ where $G(x, y)$ is the joint in- and out-degree distribution probability-generating function. Similarly, the excess out-degree distribution probability-generating function can be defined as

$$G_1^{\text{out}}(y) = \frac{1}{\langle k_{\text{EG}} \rangle} \frac{\partial}{\partial x} G(x, y)|_{x=1}, \quad (\text{A2})$$

where $\langle k_{\text{EG}} \rangle = \frac{\partial}{\partial x} G(x, y)|_{x=y=1} = \frac{\partial}{\partial y} G(x, y)|_{x=y=1}$ is the mean in- or out-degree on the event graph. This can be used to derive the out excess-degree distribution as $Q_1^{\text{out}} = \frac{\partial}{\partial y} G_1^{\text{out}}(y)|_{y=0}$.

Making the same assumption as above, namely that the event graph representation is indistinguishable from a random directed network with the same joint in- and out-degree distribution $P(k_{\text{in}}, k_{\text{out}})$, we can derive the mean cluster mass, which as discussed in Sec. II A can be calculated as the number of reachable events or mean out-component size on the event graph, as

$$M = 1 + \langle k_{\text{EG}} \rangle (-\tau)^{-1} = \frac{\langle k_{\text{EG}} \rangle - \tau}{-\tau}, \quad (\text{A3})$$

which has a power-law asymptote at $\tau_c = 0$ of the form $M \sim -\tau^{-1}$ which confirms the mean-field DP exponent $\gamma = 1$ [22].

Deriving a closed-form solution for τ becomes prohibitively complex for many types of synthetic temporal networks that involve even the slightest traces of spatial or temporal inhomogeneities and require many simplifying approximations of the structure of networks. As the nature of the assumption are similar to the ones we used while showing the critical exponents in the mean-field regime, this alone would not be productive as a mean to validate or refute the previous theoretical claims for networks with heterogeneous structure or dynamics. Therefore, we complemented these analytical derivations of τ (from Sec. A 1) and the critical exponents (from the mean-field approach of Ref. [22] and the current section) with measurements derived from simulations. While it would be possible to measure τ from the simulated event graphs, we elected to use $\delta t - \delta t_c$ as a stand-in for control parameter τ , similar to how $p - p_c$ was used in Sec. IB for lattices. Very close to the critical threshold $\tau \rightarrow \tau_c$, $\delta t - \delta t_c$ linearly approximates the control parameter τ , which would

preserve the power-law relationships mentioned before at least for some neighborhood of $\tau = \tau_c = 0$. δt is simply a parameter of the simulation and δt_c can be derived empirically for each configuration, either by trial and error or through the finite-size scaling method described in Sec. IB 2. This means that, by virtue of not relying on the methods and assumptions presented previously, we can provide a clean separation between the empirical validation and our theoretical assumptions.

It is possible to find a closed-form solution for τ for very simple systems, such as the case of random k -regular networks with Poisson process link activations. This, however, entails making simplifying assumptions about the structure of the event graph. The results of this derivation and the comparison with empirical measurements follows in Sec. A 1.

1. Solution for random k -regular static base networks with Poisson link activation

For the case of random k -regular static base networks and Poisson process activation of links with mean interevent time λ , we were able to analytically derive a closed-form solution of the control parameter τ as a function of δt , k , and λ . To this end, it is necessary to derive the joint degree distribution probability-generating function $G(x, y)$ of the event graph based on the excess degree distribution of the base random k -regular network and the Poisson process [22]. This leads to a formulation of out-degree and excess out-degree distribution probability-generating functions of the form

$$\begin{aligned} G_0^{\text{out}}(y) = G_1^{\text{out}}(y) = & -\frac{2(k-1)(y-1)y e^{\delta t(-k)\lambda}}{k} \\ & + \frac{(y-1)(2k(y-1) - 2y + 1)e^{\delta t(1-2k)\lambda}}{2k-1} \\ & + \frac{y(2(k-1)^2y + 3k-2)}{k(2k-1)}. \end{aligned} \quad (\text{A4})$$

This in turn, based on relation $\tau = \langle Q_{\text{out}} \rangle - 1 = G_1^{\text{out}}(1) - 1$, produces

$$\tau = \frac{(4k^2 - 6k + 2)e^{\delta t(-k)\lambda} + ke^{\delta t(1-2k)\lambda} - 2(k-1)^2}{(1-2k)k}. \quad (\text{A5})$$

Figure 7(a) shows the relationship between the theoretically derived value of the control parameter τ from Eq. (A5) for different random k -regular networks with a Poisson process with mean interevent time fixed to 1. As expected, a denser network has a lower onset of criticality in terms of the maximum waiting time δt . Furthermore, a linear approximation of $\tau \propto \delta t - \delta t_c$ works quite well for these systems for the neighborhood close to $\tau = 0$ given the lower curvature for at least the immediate surrounding of τ_c .

Given that, for the event graph representation of an infinite random k -regular networks with a Poisson process activation configuration the out-degree and the excess out-degree distributions are equal, as derived in Eq. (A4) [i.e., $G_0^{\text{out}}(x) = G_1^{\text{out}}(x)$], Eq. (A3) simplifies to $M = -\tau^{-1}$ for $\tau < 0$. Figure 7(b) compares this analytical solution of mean

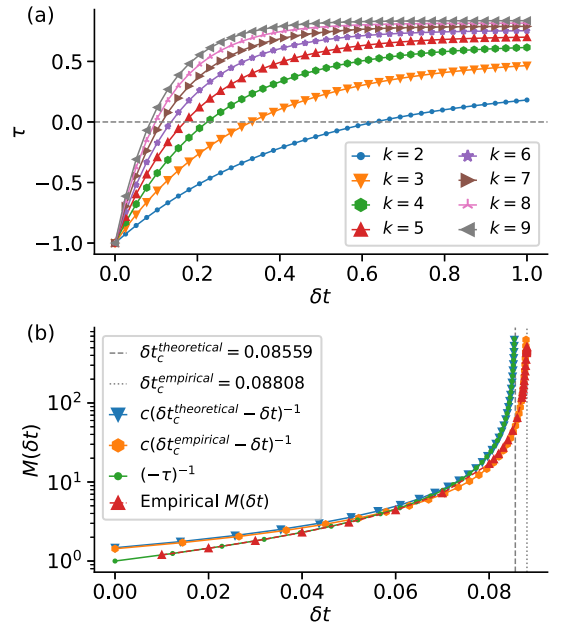


FIG. 7. (a) Theoretically derived value of control parameter τ as a function of δt as given in Eq. (A5) for random k -regular networks with Poisson processes link activation with $\lambda = 1$. The intersection with the horizontal line at $\tau = 0$ indicates the predicted critical value δt_c . (b) The analytical solutions for mean out-component size $M = (-\tau)^{-1}$ as a function of δt compared to empirical measurement of $M(\delta t)$ over 256 realizations of large ($N = 2^{17}$) finite network for random 9-regular networks in the absorbing phase $\delta t < \delta t_c$. Also visualised is the effect of using $\delta t - \delta t_c$ as an approximation of control parameter τ , which shows similar behavior close to δt_c .

out-component size (calculated with the assumption of the randomness of the event graph) with empirical measurements of a large network. Note that, for $k = 9$, our best empirical estimate for δt_c , $\delta t_c^{\text{empirical}} = 0.08808$, compared to the estimate from the analytical method, $\delta t_c^{\text{theoretical}} = 0.08559$, have a difference of around 3%. This is also visible when comparing empirical measurements of mean cluster mass $M(\delta t)$ and the theoretical estimations for the system in Fig. 7(b). This can be attributable to the fact that the rate equation Eq. (A1) is constructed for temporal networks under the assumption that the event graph is indistinguishable from a random directed network with the same joint in- and out-degree distribution. This difference seems to suggest that certain local structures in the event graph are very slightly over-represented compared to a random directed graph with the same degree distribution. Also indicated by Fig. 7(b) is the fact that the power-law behavior of the empirical trajectory with a critical exponent of $\gamma = -1$ can quite easily be validated by using an empirical estimation of δt_c .

- [1] M. E. J. Newman, Spread of epidemic disease on networks, *Phys. Rev. E* **66**, 016128 (2002).
- [2] E. Kenah and J. M. Robins, Second look at the spread of epidemics on networks, *Phys. Rev. E* **76**, 036113 (2007).
- [3] E. Kenah and J. C. Miller, Epidemic percolation networks, epidemic outcomes, and interventions, *Interdisc. Perspect. Infect. Dis.* **2011**, 543520 (2011).
- [4] R. Pastor-Satorras, C. Castellano, P. Van Mieghem, and A. Vespignani, Epidemic processes in complex networks, *Rev. Mod. Phys.* **87**, 925 (2015).
- [5] A. K. Rizi, A. Faqeeh, A. Badie-Modiri, and M. Kivelä, Epidemic spreading and digital contact tracing: Effects of heterogeneous mixing and quarantine failures, *Phys. Rev. E* **105**, 044313 (2022).
- [6] S.-Y. Liu, A. Baronchelli, and N. Perra, Contagion dynamics in time-varying metapopulation networks, *Phys. Rev. E* **87**, 032805 (2013).
- [7] F. Karimi and P. Holme, Threshold model of cascades in empirical temporal networks, *Physica A* **392**, 3476 (2013).
- [8] V.-P. Backlund, J. Saramäki, and R. K. Pan, Effects of temporal correlations on cascades: Threshold models on temporal networks, *Phys. Rev. E* **89**, 062815 (2014).
- [9] J.-C. Delvenne, R. Lambiotte, and L. E. Rocha, Diffusion on networked systems is a question of time or structure, *Nat. Commun.* **6**, 7366 (2015).
- [10] M. Bazzi, M. A. Porter, S. Williams, M. McDonald, D. J. Fenn, and S. D. Howison, Community detection in temporal multilayer networks, with an application to correlation networks, *Multiscale Model. Simul.* **14**, 1 (2016).
- [11] U. Aslak, M. Rosvall, and S. Lehmann, Constrained information flows in temporal networks reveal intermittent communities, *Phys. Rev. E* **97**, 062312 (2018).
- [12] A. Koher, J. P. Gleeson, and P. Hövel, Spreading of infection on temporal networks: An edge-centered perspective, in *Temporal Network Theory* (Springer, Berlin, 2019), pp. 235–252.
- [13] M. Karsai, M. Kivelä, R. K. Pan, K. Kaski, J. Kertész, A.-L. Barabási, and J. Saramäki, Small but slow world: How network topology and burstiness slow down spreading, *Phys. Rev. E* **83**, 025102(R) (2011).
- [14] L. E. Rocha, F. Liljeros, and P. Holme, Simulated epidemics in an empirical spatiotemporal network of 50,185 sexual contacts, *PLoS Comput. Biol.* **7**, e1001109 (2011).
- [15] D. X. Horváth and J. Kertész, Spreading dynamics on networks: The role of burstiness, topology and non-stationarity, *New J. Phys.* **16**, 073037 (2014).
- [16] E. Ubaldi, A. Vezzani, M. Karsai, N. Perra, and R. Burioni, Burstiness and tie activation strategies in time-varying social networks, *Sci. Rep.* **7**, 46225 (2017).
- [17] T. Hiraoka and H.-H. Jo, Correlated bursts in temporal networks slow down spreading, *Sci. Rep.* **8**, 15321 (2018).
- [18] M. Karsai, H.-H. Jo, K. Kaski *et al.*, *Bursty Human Dynamics* (Springer, Berlin, 2018).
- [19] T. Kuhn, M. Perc, and D. Helbing, Inheritance Patterns in Citation Networks Reveal Scientific Memes, *Phys. Rev. X* **4**, 041036 (2014).
- [20] M. Kivelä, J. Cambe, J. Saramäki, and M. Karsai, Mapping temporal-network percolation to weighted, static event graphs, *Sci. Rep.* **8**, 12357 (2018).
- [21] R. Parshani, M. Dickison, R. Cohen, H. E. Stanley, and S. Havlin, Dynamic networks and directed percolation, *Europhys. Lett.* **90**, 38004 (2010).
- [22] A. Badie-Modiri, A. K. Rizi, M. Karsai, and M. Kivelä, Directed percolation in temporal networks, *Phys. Rev. Research* **4**, L022047 (2022).
- [23] M. Henkel, H. Hinrichsen, S. Lübeck, and M. Pleimling, *Non-equilibrium Phase Transitions*, Vol. 1 (Springer, Berlin, 2008).
- [24] P. Holme and J. Saramäki, *Temporal Network Theory*, Computational Social Sciences (Springer International Publishing, Cham, 2019).
- [25] A. Mellor, The temporal event graph, *J. Complex Netw.* **6**, 639 (2018).
- [26] J. Saramäki, M. Kivelä, and M. Karsai, Weighted temporal event graphs, in *Temporal Network Theory* (Springer, Berlin, 2019), pp. 107–128.
- [27] H.-H. Jo, T. Hiraoka, and M. Kivelä, Burst-tree decomposition of time series reveals the structure of temporal correlations, *Sci. Rep.* **10**, 1 (2020).
- [28] J. Ureña-Carrion, J. Saramäki, and M. Kivelä, Estimating tie strength in social networks using temporal communication data, *EPJ Data Sci.* **9**, 37 (2020).
- [29] L. Kovanen, M. Karsai, K. Kaski, J. Kertész, and J. Saramäki, Temporal motifs in time-dependent networks, *J. Stat. Mech.: Theory Exp.* (2011) P11005.
- [30] T. Aledavood, S. Lehmann, and J. Saramäki, Social network differences of chronotypes identified from mobile phone data, *EPJ Data Sci.* **7**, 46 (2018).
- [31] T. Takaguchi, N. Masuda, and P. Holme, Bursty communication patterns facilitate spreading in a threshold-based epidemic dynamics, *PLoS One* **8**, e68629 (2013).
- [32] S. Sajjadi, M. R. Eftehadi, and F. Ghanbarnejad, Impact of temporal correlations on high risk outbreaks of independent and cooperative sir dynamics, *PLoS One* **16**, e0253563 (2021).
- [33] P. Holme, Network reachability of real-world contact sequences, *Phys. Rev. E* **71**, 046119 (2005).
- [34] E. Lee, S. Emmons, R. Gibson, J. Moody, and P. J. Mucha, Concurrency and reachability in treelike temporal networks, *Phys. Rev. E* **100**, 062305 (2019).
- [35] J. Moody and R. A. Benton, Interdependent effects of cohesion and concurrency for epidemic potential, *Ann. Epidemiol.* **26**, 241 (2016).
- [36] K. Garimella, Polarization on Social Media, thesis, Aalto University, 2018.
- [37] R. Lambiotte and N. Masuda, *A Guide to Temporal Networks*, Vol. 4 (World Scientific, Singapore, 2016).
- [38] P. Holme and J. Saramäki, Temporal networks, *Phys. Rep.* **519**, 97 (2012).
- [39] P. Holme, Modern temporal network theory: A colloquium, *Eur. Phys. J. B* **88**, 234 (2015).
- [40] D. J. Daley and D. G. Kendall, Epidemics and rumours, *Nature (Lond.)* **204**, 1118 (1964).
- [41] C. Castellano, S. Fortunato, and V. Loreto, Statistical physics of social dynamics, *Rev. Mod. Phys.* **81**, 591 (2009).
- [42] S. Unicomb, G. Iniguez, J. P. Gleeson, and M. Karsai, Dynamics of cascades on burstiness-controlled temporal networks, *Nat. Commun.* **12**, 133 (2021).
- [43] C. Tripp-Barba, C. Alcaraz, and M. A. Igartua, Special issue on “modeling and performance evaluation of wireless ad-hoc networks,” *Ad Hoc Netw.* **52**, 1 (2016).

- [44] N. Nassir, M. Hickman, A. Malekzadeh, and E. Irannezhad, A utility-based travel impedance measure for public transit network accessibility, *Transport. Res. A: Policy Pract.* **88**, 26 (2016).
- [45] A. Badie-Modiri, M. Karsai, and M. Kivelä, Efficient limited-time reachability estimation in temporal networks, *Phys. Rev. E* **101**, 052303 (2020).
- [46] H. Hinrichsen, Non-equilibrium critical phenomena and phase transitions into absorbing states, *Adv. Phys.* **49**, 815 (2000).
- [47] G. Ódor, Universality classes in nonequilibrium lattice systems, *Rev. Mod. Phys.* **76**, 663 (2004).
- [48] H. Hinrichsen, Non-equilibrium phase transitions, *Physica A* **369**, 1 (2006).
- [49] S. R. Broadbent and J. M. Hammersley, Percolation processes: I. Crystals and mazes, in *Mathematical Proceedings of the Cambridge Philosophical Society*, Vol. 53 (Cambridge University Press, Cambridge, UK, 1957), pp. 629–641.
- [50] J. Blease, Directed-bond percolation on hypercubic lattices, *J. Phys. C* **10**, 925 (1977).
- [51] F. Schlögl, Chemical reaction models for non-equilibrium phase transitions, *Z. Phys.* **253**, 147 (1972).
- [52] H. Gerola, P. Seiden, and L. Schulman, Theory of dwarf galaxies, *Astrophys. J.* **242**, 517 (1980).
- [53] N. Van Lien and B. Shklovskii, Hopping conduction in strong electric fields and directed percolation, *Solid State Commun.* **38**, 99 (1981).
- [54] P. Bak and K. Sneppen, Punctuated Equilibrium and Criticality in a Simple Model of Evolution, *Phys. Rev. Lett.* **71**, 4083 (1993).
- [55] E. Domany and W. Kinzel, Equivalence of Cellular Automata to Ising Models and Directed Percolation, *Phys. Rev. Lett.* **53**, 311 (1984).
- [56] W. Kinzel, Phase transitions of cellular automata, *Z. Phys. B* **58**, 229 (1985).
- [57] T. E. Harris, Contact interactions on a lattice, *Ann. Probab.* **2**, 969 (1974).
- [58] I. Jensen, Critical Behavior of the Pair Contact Process, *Phys. Rev. Lett.* **70**, 1465 (1993).
- [59] J. F. F. Mendes, R. Dickman, M. Henkel, and M. C. Marques, Generalized scaling for models with multiple absorbing states, *J. Phys. A: Math. Gen.* **27**, 3019 (1994).
- [60] R. M. Ziff, E. Gulari, and Y. Barshad, Kinetic Phase Transitions in an Irreversible Surface-Reaction Model, *Phys. Rev. Lett.* **56**, 2553 (1986).
- [61] D. Dhar, The collapse of directed animals, *J. Phys. A: Math. Gen.* **20**, L847 (1987).
- [62] H. Hinrichsen, On possible experimental realizations of directed percolation, *Braz. J. Phys.* **30**, 69 (2000).
- [63] K. A. Takeuchi, M. Kuroda, H. Chaté, and M. Sano, Directed Percolation Criticality in Turbulent Liquid Crystals, *Phys. Rev. Lett.* **99**, 234503 (2007).
- [64] G. Lemoult, L. Shi, K. Avila, S. V. Jalikop, M. Avila, and B. Hof, Directed percolation phase transition to sustained turbulence in couette flow, *Nat. Phys.* **12**, 254 (2016).
- [65] A. Barrat, M. Barthelemy, and A. Vespignani, *Dynamical Processes on Complex Networks* (Cambridge University Press, Cambridge, UK, 2008).
- [66] D. Kempe, J. Kleinberg, and A. Kumar, Connectivity and inference problems for temporal networks, *J. Comput. Syst. Sci.* **64**, 820 (2002).
- [67] J. Moody, The importance of relationship timing for diffusion, *Soc. Forces* **81**, 25 (2002).
- [68] R. K. Pan and J. Saramäki, Path lengths, correlations, and centrality in temporal networks, *Phys. Rev. E* **84**, 016105 (2011).
- [69] I. Scholtes, N. Wider, R. Pfitzner, A. Garas, C. J. Tessone, and F. Schweitzer, Causality-driven slow-down and speed-up of diffusion in non-markovian temporal networks, *Nat. Commun.* **5**, 5024 (2014).
- [70] J. Stehlé, N. Voirin, A. Barrat, C. Cattuto, L. Isella, J.-F. Pinton, M. Quaggiotto, W. Van den Broeck, C. Régis, B. Lina *et al.*, High-resolution measurements of face-to-face contact patterns in a primary school, *PLoS One* **6**, e23176 (2011).
- [71] S. Dai, H. Bouchet, A. Nardy, E. Fleury, J.-P. Chevrot, and M. Karsai, Temporal social network reconstruction using wireless proximity sensors: Model selection and consequences, *EPJ Data Sci.* **9**, 19 (2020).
- [72] A. Aleta, G. F. de Arruda, and Y. Moreno, Data-driven contact structures: from homogeneous mixing to multilayer networks, *PLoS Comput. Biol.* **16**, e1008035 (2020).
- [73] A. A. Saberi, Recent advances in percolation theory and its applications, *Phys. Rep.* **578**, 1 (2015).
- [74] M. Li, R.-R. Liu, L. Lü, M.-B. Hu, S. Xu, and Y.-C. Zhang, Percolation on complex networks: Theory and application, *Phys. Rep.* **907**, 1 (2021).
- [75] P. Grassberger and A. De La Torre, Reggeon field theory (schlögl's first model) on a lattice: Monte carlo calculations of critical behaviour, *Ann. Phys.* **122**, 373 (1979).
- [76] P. Grassberger, On phase transitions in Schlögl's second model, *Z. Phys. B* **47**, 365 (1982).
- [77] H. K. Janssen, On the nonequilibrium phase transition in reaction-diffusion systems with an absorbing stationary state, *Z. Phys. B* **42**, 151 (1981).
- [78] E. L. Kaplan and P. Meier, Nonparametric estimation from incomplete observations, *J. Am. Stat. Assoc.* **53**, 457 (1958).
- [79] See Supplemental Material at <http://link.aps.org/supplemental/10.1103/PhysRevE.105.054313> for details of empirical analysis and the full suit of empirical results.
- [80] I. Jensen, Low-density series expansions for directed percolation: I. A new efficient algorithm with applications to the square lattice, *J. Phys. A: Math. Gen.* **32**, 5233 (1999).
- [81] C. A. Voigt and R. M. Ziff, Epidemic analysis of the second-order transition in the Ziff-Gulari-Barshad surface-reaction model, *Phys. Rev. E* **56**, R6241 (1997).
- [82] P. Grassberger and Y.-C. Zhang, "self-organized" formulation of standard percolation phenomena, *Physica A* **224**, 169 (1996).
- [83] I. Jensen, Critical behavior of the three-dimensional contact process, *Phys. Rev. A* **45**, R563 (1992).
- [84] A. Badie-Modiri, A. K. Rizi, M. Karsai, and M. Kivelä, Source code and for "Directed Percolation in Temporal Networks" and "Directed Percolation in Random Temporal Network Models with Heterogeneities" (2021), <https://doi.org/10.5281/zenodo.5570746>.
- [85] R. Kujala, C. Weckström, R. K. Darst, M. N. Mladenović, and J. Saramäki, A collection of public transport network data sets for 25 cities, *Sci. Data* **5**, 180089 (2018).
- [86] Bureau of Transportation Statistics, Bureau of transportation statistics website (2017).

- [87] J. H. Kim and V. H. Vu, Generating random regular graphs, in *Proceedings of the 35th Annual ACM Symposium on Theory of Computing* (Association for Computing Machinery, San Diego, CA, USA, 2003), pp. 213–222.
- [88] A. Steger and N. C. Wormald, Generating random regular graphs quickly, *Comb. Probab. Comput.* **8**, 377 (1999).
- [89] V. Batagelj and U. Brandes, Efficient generation of large random networks, *Phys. Rev. E* **71**, 036113 (2005).
- [90] A. G. Hawkes, Point spectra of some mutually exciting point processes, *J. Roy. Stat. Soc. Ser. B (Methodol.)* **33**, 438 (1971).
- [91] P. J. Laub, T. Taimre, and P. K. Pollett, Hawkes processes, [arXiv:1507.02822](https://arxiv.org/abs/1507.02822).
- [92] A. Casteigts, A.-S. Himmel, H. Molter, and P. Zschoche, *Finding Temporal Paths Under Waiting Time Constraints* (Springer, 2021), Vol. 83, pp. 2754–2802.

*The thesis focuses on epidemic spreading and the relation between the underlying network structure and the spread of the epidemic but has a broad scope. **The introductory chapters, in particular, give a very nice summary of the state of the art in network epidemiology, making the thesis accessible for researchers or students who have never worked with epidemiology before.***

Clara Stegehuis, Mathematician & Associate Professor at Twente University

*The dissertation begins with a short introduction motivating the thesis (which includes a couple of great quotes that I will steal), followed by **three pedagogical chapters preparing any reader with a solid scientific background to understand the papers presented in the final part of the dissertation.** These three "micro-courses" cover i) mathematical epidemiology, ii) network theory, and iii) the integration of these two subjects in the third chapter. **The writing is engaging, and I sincerely appreciate the effort to render the reading of this extensive body of text a more pleasant journey.***

Riccardo Gallotti, Head of the Complex Human Behaviour Lab, FBK



ISBN 978-952-64-1704-2 (printed)
 ISBN 978-952-64-1705-9 (pdf)
 ISSN 1799-4934 (printed)
 ISSN 1799-4942 (pdf)

Aalto University
 School of Science
 Department of Computer Science
www.aalto.fi

BUSINESS +
 ECONOMY

ART +
 DESIGN +
 ARCHITECTURE

SCIENCE +
 TECHNOLOGY

CROSSOVER

DOCTORAL
 THESES